

DEVELOPMENT OF SENSITIVE BIOMOLECULE DETECTION STRATEGIES
FOR LOW-RESOURCE SETTINGS

By
Lauren Elizabeth Gibson

Dissertation

Submitted to the Faculty of the
Graduate School of Vanderbilt University
in partial fulfillment of the requirements

for the degree of

DOCTOR OF PHILOSOPHY

in

Chemistry

May, 2017

Nashville, Tennessee

Approved:

David W. Wright, Ph.D.

David E. Cliffl, Ph.D.

Craig L. Duvall, Ph.D.

Timothy P. Hanusa, Ph.D.

“To Him who is able to do far more abundantly beyond all that we ask or think,
according to the power that works within us...” Ephesians 3:20

Acknowledgements

As I think back over my time in graduate school, I am amazed at the incredible adventure it has been. If you would have asked me when I first decided to attend Vanderbilt University if I would work on low-resource diagnostics with Dr. David Wright, the answer would have been “no”, but I am so glad that I discovered that was exactly what I wanted to do. David, thanks for walking in one day with a paper about nanoparticle-based signal amplification, telling me to do it and then walking away. That project taught me to be a scientist. What an experience to get to start a project on my own, from scratch, and see it succeed. Thanks for challenging me and encouraging me in my work. Also, thank you for being my advocate during my time at Vanderbilt and as I pursued the next step in my career. Most of all, thanks for having a passion for global health and providing a place for me to pursue chemistry and my love for people around the world. The opportunities I have had in your lab have been life changing.

To the rest of my committee, Dr. David Cliffel, Dr. Craig Duvall, and Dr. Timothy Hanusa. Thanks for making it to every one of my exams and for encouraging me to look at my science from different perspectives. Dr. Cliffel, thank you for challenging me to become a better analytical chemist. Dr. Duvall, thank you for encouraging me to go for my dreams when it came time to look for a job. Dr. Hanusa, thank you for challenging me to figure out the inorganic chemistry problems in my work.

The Wright lab... how do I even start? I wouldn't have made it through graduate school without you all and you have all become some of my best friends. Keersten Ricks, thanks for being a knowledgeable and fun mentor. Your laugh is contagious and a constant reminder that there is always joy in life. Also, traveling Europe with you was a blast. Thanks for being my

adventure partner. Alexis Wong, I am so glad we met at a graduate school visit to UNC Chapel Hill and then both decided to come to Vanderbilt. You have been a most faithful friend, walking through these last five years with me as a roommate and a fellow lab member. Kim Fong, thanks for always caring about my life and pointing me to Jesus. Christine Markwalter, the Wright lab is so much better because you are a part of it. You are a great scientist and your care for people is amazing. Thanks for helping me with statistics, being the sounding board for all my research ideas and problems, and most of all for being a friend. Wes Bauer, thanks for being my sports buddy, whether that meant playing spikeball or doing a triathlon. And don't worry, I will never forget you since I will always have scars on my leg from the time you threw a Frisbee into that bush in Zambia. Anna Bitting, thanks for being a strong leader in lab. Also, I'm glad we got to share Zambian adventures together, like spiders running across my toes. Andrew Kantor, your positive attitude changes the atmosphere around you and it will get you far in life. Keep fighting. Matthew Park, you were an awesome undergraduate research student. You have an exceptional attitude and work ethic and made a great contribution to this scientific work. You also taught me how to be mentor, and for that I am very grateful. Whatever you decide to do in the future, I know you will have a great impact on the people around you. Danielle Kimmel, thanks for the fun times in Zambia, especially the 25 birthday presents and Kinder Egg bowling. Thomas Scherr, you have been an amazing addition to our lab. We needed an engineer! Chris Gulka, everyone knows the "Sweet and Sour" bay is the best! Also, even though it was frustrating at times, thanks for asking a lot of questions and challenging me to become a better scientist. Stevie Jackson, thanks for caring about basketball. I'm sorry, but UK will always be better than Arkansas. And Greg, our 8th floor custodian, you have encouraged me more than you know; thanks for bringing something positive to every day. To the rest of the Wright lab: Nicholas

Adams, Joseph Conrad, Mindy Leelawong, Lwiindi Mudenda, Jenny Nesbitt, Kelly Richardson and Adam Ryan Travis, it's been a privilege to work with you all. Carson Moore, Armin Nourani, and Megan van der Horst, I'm so glad that you have joined the lab. Carry on the Wright lab traditions and do some great science!

There are also many people outside of that Wright lab that had a great impact on my graduate school career. Allison Galassie, Brad Durbin and Bryson Howard, from my first-year class, thanks for being my first friends in Nashville. I would not have wanted to walk through the beginning of classes and teaching with anyone else. The Chemistry Department at Murray State University, thanks for giving me an excellent and personalized education. Dr. Revell, thanks for being an amazing teacher, you inspired me to be a chemistry major. And Dr. Johnson, thanks for sitting me down in your office one afternoon and telling me I should go to graduate school. I would have missed this adventure if you hadn't done so. Also, thanks for always being there to teach me and give me advice, even during my time at Vanderbilt. Finally, Dr. and Mrs. Howell Clark, thanks for always believing in me. Furthermore, I want to thank Dr. Phil Thuma, from Macha Research Trust. Dr. Thuma, what God has allowed you to do in Macha is amazing. I will never forget how beautifully science and faith come together in your life and how that has changed the world around you. Thanks for your example, I am ever grateful for the opportunities I have had to travel to Macha and work with you.

I would be remiss if I did not thank my wonderful Nashville community. Green Hills Church, when I came to Nashville I would have never guessed what a blessing you all would be. Your friendships have literally changed my life. Thank you for pointing me back to the truth and reminding me that the world is bigger than chemistry research. Thanks also for being a constant source of encouragement, writing this dissertation has been much easier with you all lifting me

up in prayer and being my cheerleaders. Really, you all are the best. Thanks for loving Jesus and me.

Finally, to my family. Everyone knows how much I love home and being with you all. I am so thankful I have gotten to walk through all of life with you. Grandpaw and Grandmom, you all have believed in me in such a way that inspires confidence and joy in everything I do. Granddaddy and Grandmomma, you all have been great a motivation to me through this journey as you have challenged and encouraged me. Granddaddy, your work ethic constantly inspires me. Whether it's that fact that you taught at the University of Kentucky for 50 years, or that you are traveling the world after battling leukemia, or that you are still doing research at 80 years old, I know I have no excuse to not be my best. Both you and Grandmomma have shown me that two of the most beautiful things in life are constantly learning and spending time with those you love the most. To my siblings, Nathan, I am so glad we got to be Commodores together. I wouldn't trade that time or your friendship for the world. Graham, you make me laugh and that's one of the best parts of life. Thanks for loving me. Hannah, thanks for putting up with me and believing in me. I can't think of anything better than being your sister. Mom and Dad, I don't even know how to put into words how well you have supported me throughout my life. In every new season, you all have always been right behind me to help me through. You all have shown me what love looks like by how you love others, Jesus and me. Your example has allowed me to walk through graduate school trusting in a faithful God. It's been a hard journey at times but He's made it beautiful. The following is the result. I love you all.

TABLE OF CONTENTS

	Page
DEDICATION	ii
ACKNOWLEDGMENTS	iii
LIST OF TABLES	xi
LIST OF FIGURES	xii
Chapter	
I. INTRODUCTION	1
The Challenges of Low-Resource Settings	1
Malaria: Disease and Diagnosis	4
Toward Sensitive Low-Resource Diagnostics	9
II. DRIED BLOOD SPOT ELISA FOR DETECTION OF A MALARIAL BIOMARKER IN PATIENT SAMPLES FROM RURAL ZAMBIA	12
Introduction	12
Experimental	13
Materials	13
<i>pf</i> HRP II ELISA Protocol	14
Dried Blood Spot Extraction	14
Dried Blood Spot <i>pf</i> HRP II ELISA	15
Percent Recovery Calculation	15
Stability Study	15
Study Setting	15
Patient Recruitment and Ethics	16
Patient Samples	16
Dried Blood Spot <i>pf</i> HRP II ELISA for Patient Samples	17
Sample Size Calculation	17
Data Analysis	18
Result and Discussion	18
Optimization of Extraction Parameters	18
DBS Card Type and <i>pf</i> HRP II Recovery and Stability	20
Comparison to Traditional <i>pf</i> HRP II ELISA	22
Analysis of Patient Samples from Rural Zambia	22
<i>pf</i> HRP II Clearance	24
Association Between Parasite and Biomarker Levels	27
Conclusion	28
Acknowledgements	29

III. MALARIA RAPID DIAGNOSTIC TEST ENHANCEMENT	30
Introduction	30
Experimental	32
Materials	32
Blood Sample Preparation	33
Extraction and Analysis with RDTs	34
Image Analysis	35
Results and Discussion	36
Enhancement in RDT Performance	36
Limit of Detection of Enhanced RDT Signal	39
Effect of Individual Donor Samples on RDT Performance	41
Conclusion	43
Acknowledgements	44
IV. SIGNAL AMPLIFICATION WITH TETRA(4-CARBOXYPHENYL) PORPHYRIN NANOPARTICLES FOR SENSITIVE BIOMOLECULE DETECTION.....	45
Introduction	45
Experimental	47
Materials	47
Instrumentation	47
Tetra(4-carboxyphenyl)porphyrin Nanoparticle Synthesis	48
Nanoparticle Concentration Measurements	48
Antibody Conjugation to TCPP Nanoparticles	49
Detection of Rabbit IgG and <i>p</i> fHRPII with TCPP Nanoparticles	49
Results and Discussion	51
Characterization of TCPP Nanoparticles.....	51
Conjugation of Antibodies to TCPP Nanoparticles.....	55
Optimization and Detection of Rabbit IgG	56
Optimization and Detection of <i>p</i> fHRPII in Diluted Whole Blood	58
Conclusion	61
Acknowledgements	62
V. HEMIN NANOPARTICLE ENZYME MIMIC FOR BIOMOLECULE DETECTION IN LOW-RESOURCE SETTINGS	63
Introduction	63
Experimental	66
Materials	66
Instrumentation	66
Hemin Nanoparticle Synthesis	67
Hemin Molecules per Nanoparticle.....	67
Hemin Nanoparticle Size Stability Study	68
Nanoparticle Synthesis for Additional Metal Protoporphyrin IX Derivatives	68

pH and Temperature Stability Studies.....	68
Ligand Optimization for Catalytic Turnover.....	69
Cyclic Voltammetry of Hemin-Pyridine Complex.....	69
Kinetic Analysis	70
Stability of Hemin Nanoparticle Catalytic Properties	71
Detection of Rabbit IgG	71
Detection of <i>Plasmodium</i> Lactate Dehydrogenase.....	72
Results and Discussion.....	73
Hemin Nanoparticle Synthesis Optimization	73
Stability of Hemin Nanoparticles	78
Hemin-Pyridine Catalytic Complex	80
Kinetic Properties of Hemin NPs and Comparison to Horseradish Peroxidase	84
Detection of Rabbit IgG	87
Detection of <i>Plasmodium</i> Lactate Dehydrogenase.....	89
Conclusion.....	91
Acknowledgements	92
VI. CELLULOSE MEMBRANES MODIFIED WITH METAL AFFINITY LIGAND FOR CAPTURE AND DETECTION OF MALARIAL BIOMARKERS.....	93
Introduction.....	93
Experimental	96
Materials	96
Instrumentation.....	97
Membrane Synthesis	97
Zinc Quantification with ICP-OES	98
Capture Efficiency.....	98
<i>pf</i> HRP II ELISA Protocol.....	99
Membrane Selection Study.....	99
Antibody Conjugation to Hemin Nanoparticles	99
Hemin Nanoparticle Lyophilization	100
On-Membrane Detection of <i>pf</i> HRP II	100
Image Analysis	101
Results and Discussion.....	101
Membrane Selection Study.....	101
<i>pf</i> HRP II Capture by Zn-IDA Membranes	103
Optimization of Hemin Nanoparticle Lyophilization.....	106
On-Membrane Detection of <i>pf</i> HRP II	107
Detection Limit of the <i>pf</i> HRP II Flow-Through Assay	109
Conclusion.....	111
Future Directions	111
Acknowledgements	117
REFERENCES	118

Appendix

A. SUPPORTING INFORMATION: CHAPTER II.....133

B. SUPPORTING INFORMATION: CHAPTER V.....139

C. DETECTION OF MALARIAL DNA WITH HEMIN NANOPARTICLES150

D. SELECTION OF X-APTAMERS AGAINST INFECTIOUS DISEASE BIOMARKERS...157

E. SURFACE TENSION VALVES AS SEPARATION BARRIERS FOR A SERUM
CREATININE ASSAY168

LIST OF TABLES

Table	Page
II.1. Extraction buffer compositions.....	19
III.1. RDT brand specifications	33
III.2. Limits of detection for RDTs with unextracted and extracted samples.....	40
V.1. Catalytic properties of Hemin NPs and HRP _x	85
VI.1. Characteristics of the cellulose membranes modified with Zn-IDA	103

LIST OF FIGURES

Figure	Page
I.1. Disability-adjusted life years in 2015	1
I.2. Testing for malaria in Zambia.....	3
I.3. Lifecycle of the malaria parasite.....	5
I.4. Rapid diagnostic test workflow	7
I.5. Proportion of malaria cases detected by PCR that were also detected by RDT	8
II.1. Optimization of DBS extraction parameters.....	20
II.2. <i>pf</i> HRP2 stability in DBS	21
II.3. DBS <i>pf</i> HRP2 ELISA reproducibility and comparison to traditional ELISA.....	22
II.4. ROC curve for DBS <i>pf</i> HRP2 ELISA.....	23
II.5. <i>pf</i> HRP2 clearance trends in patient samples	26
II.6. Correlation between parasite and <i>pf</i> HRP2 levels.....	27
III.1. Workflow for quantitation of RDT signal	35
III.2. RDT signal from unextracted samples.....	36
III.3. RDT signal as a function of parasitemia.....	38
III.4. RDT enhancement as a result of extraction	39
III.5. Signal from low, medium, and high performing RDTs	41
III.6. RDT signal from individual sample donors.....	42
IV.1. Workflow for porphyrin nanoparticle-based signal amplification assay	50
IV.2. Size characterization of TCPP NPs.....	51
IV.3. Size stability of TCPP NPs	52

IV.4.	TCPP NP stability as a function of pH	53
IV.5.	Absorbance and fluorescence spectra of TCPP NP dissolution.....	54
IV.6.	Stability of TCPP fluorescent signal.....	55
IV.7.	Optimization of the TCPP NP assay for detection of IgG	57
IV.8.	Standard curve for detection of IgG with TCPP NPs	58
IV.9.	Optimization of the TCPP NP assay for detection of <i>pf</i> HRP II.....	59
IV.10.	Standard curve for detection of <i>pf</i> HRP II with TCPP NPs.....	60
V.1.	Signal amplification scheme for Hemin NP detection method.....	65
V.2.	Hemin NP synthesis optimization.....	75
V.3.	Size distribution of Hemin NPs	77
V.4.	The effect of pH on Hemin NPs	79
V.5.	Horseradish peroxidase active site.....	80
V.6.	Hemin NP turnover of various ligands	81
V.7.	Absorbance spectra of Hemin NPs with various concentrations of pyridine	83
V.8.	Oxidation and reduction potentials of hemin with various concentration of pyridine	84
V.9.	Stability of the catalytic activity of Hemin NPs and HRPx.....	87
V.10.	IgG standard curves with Hemin NPs and HRPx detection	89
V.11.	Detection of <i>p</i> LDH with Hemin NPs.....	90
VI.1.	Synthesis scheme for functionalization of cellulose membranes with Zn-IDA	102
VI.2.	Zinc loading and <i>pf</i> HRP II capture with Zn-IDA membranes.....	104
VI.3.	Capture of <i>pf</i> HRP II from large sample volumes	105
VI.4.	Optimization of trehalose concentration for Hemin NP lyophilization	106
VI.5.	Detection of <i>pf</i> HRP II with Hemin NPs in a plate assay	108

VI.6. Optimization of Hemin NP concentration for flow-through assay	109
VI.7. Standard curve for detection of <i>pf</i> HRP II with flow-through assay	110
VI.8. Origami RDT workflow.....	112
VI.9. <i>pf</i> HRP II release from Zn-IDA membranes.....	114
VI.10. Capture and release reagent	115
VI.11. Test outcomes for the origami RDT	116

CHAPTER I

INTRODUCTION

The Challenges of Low-Resource Settings

One of the greatest challenges facing our world today is the interdependent, detrimental effect that poverty and disease have on a large portion of the population. For example, in Sub-Saharan Africa, 73% of the population lives on less than \$2 a day.¹ In this same region, disability-adjusted life years (DALY), which are the sum of the years of life lost due to premature death and those lost to disability, is the highest in the world (Figure I.1).² These two situations are linked, as high DALY places a huge burden on a population, keeping it in poverty, while poverty limits access to adequate healthcare that would minimize this loss of life. The lack of effective

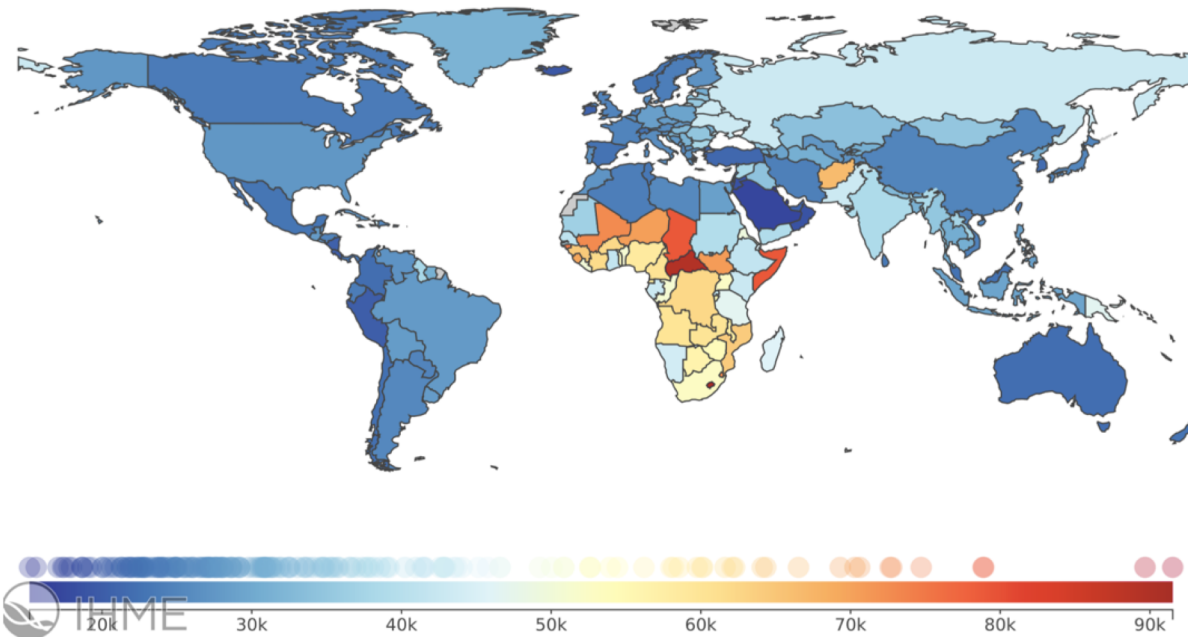


Figure I.1. The disability-adjusted life years (DALY) per 100,000 in 2015. It can be seen that the majority of years lost are in the region of Sub-Saharan Africa.²

healthcare is demonstrated by the fact that developing (low-resource) countries account for only 12% of the world's total healthcare spending, despite the fact that they carry 90% of the disease burden.^{3, 4}

As a result, the healthcare systems in low-resource areas look much different than those in high-resource areas of the world. In general, facilities in developing countries can be broken into three major types: (1) major-city hospitals, (2) district-level clinics and (3) village-level health outposts. Hospitals in major cities have reliable electricity, clean water and many other resources commonly found in high-resource health facilities. In district-level clinics, electricity is intermittent and there may or may not be access to clean water. Additionally, the environment is often windy and dusty, and ambient temperatures can reach 40°C. Finally, in the village setting, electricity and clean water are not available and healthcare workers are minimally trained (Figure I.2).⁵ Consequently, providing adequate medical diagnosis or care to people in these areas is not possible. This situation is only made worse by the fact that access even to these inadequate facilities is limited, as many patients have to walk for hours to reach them.⁶ Additionally, there is often distrust in the efficacy of diagnostic tests or the government, which is often responsible for implementation of disease control efforts.^{7, 8} It is also common for non-prescribed and traditional medication to be used by populations in these areas.⁹ Despite these situations, there is hope for increasing the availability of effective healthcare in these regions and closing the gap in DALY between low and high-resource areas. This prospect is based upon the fact that many of the diseases that currently plague low-resource areas are treatable. Therefore, disease prevalence could be reduced through accurate disease diagnosis and accurate diagnosis could occur with the implementation of diagnostics that are effective in low-resource settings.¹⁰



Figure I.2. Testing of individuals for malaria with rapid diagnostic tests in a village-level healthcare setting in the Southern Province of Zambia. Photo provided by Westley Bauer.

Considering the characteristics of the healthcare facilities in low-resource settings, it is evident that the diagnostic tests used in hospitals in the developed world will not be practical or useful. This has led to large push for the development of point-of-care or low-resource diagnostics that are designed to take into account the challenges associated with low-resource settings. One of the first point-of-care diagnostics was the home pregnancy test.¹¹ These tests are simple and inexpensive and can be performed by the general population. To direct the development of other low-resource diagnostics, the World Health Organization (WHO) summarized necessary characteristics through the acronym, ASSURED (Affordable, Sensitive, Specific, User-Friendly, Rapid, Equipment-free, Deliverable). The need for affordable diagnostics is evidenced by the small healthcare budget in low-resource areas. Furthermore,

sensitive and specific diagnostics are needed to produce accurate results. User-friendly is a necessary characteristic as the tests will likely be run by minimally trained individuals, as there is little incentive for trained healthcare workers to remain in rural areas.⁷ Rapid time to result allows for the patient to receive diagnosis and treatment in one visit. Finally, the ideal diagnostic would be equipment-free and deliverable as electricity is intermittent at best, meaning power sources and controlled environmental conditions are not available. The development of diagnostics with these characteristics is not an easy task. As a result, many low-resource diagnostics are unreliable and the challenge of providing patients with proper diagnosis and care still needs to be addressed.

Malaria: Disease and Diagnosis

The difficulty of diagnosing disease in low-resource settings can be highlighted through exploration of the biology and diagnosis of the common infectious disease, malaria. Malaria is a parasitic disease and the parasite life cycle alternates between two hosts: the female *Anopheles* mosquito and vertebrates. There were 212 million cases of malaria in 2015 and 90% occurred in the African region.¹² Five *Plasmodium* species are known to be a threat to humans; the deadliest being *P. falciparum*. Significant illness is also caused by *P. vivax*. The other species, *P. ovale*, *P. malariae*, and *P. knowlesi* are much less common.¹³ The life cycle of the *plasmodium* parasite is shown in Figure I.3.¹⁴ It can be seen that humans are infected by the bite of *Anopheles* mosquitos as sporozoites, in the mosquito salivary glands, enter the dermis and then infect liver cells. Following asexual reproduction, the liver cells rupture releasing merozoites that infect red blood cells. In the blood stage infection, the parasite again asexually reproduces, resulting in repeated rupture and infection of red blood cells. This cycle produces the symptoms normally

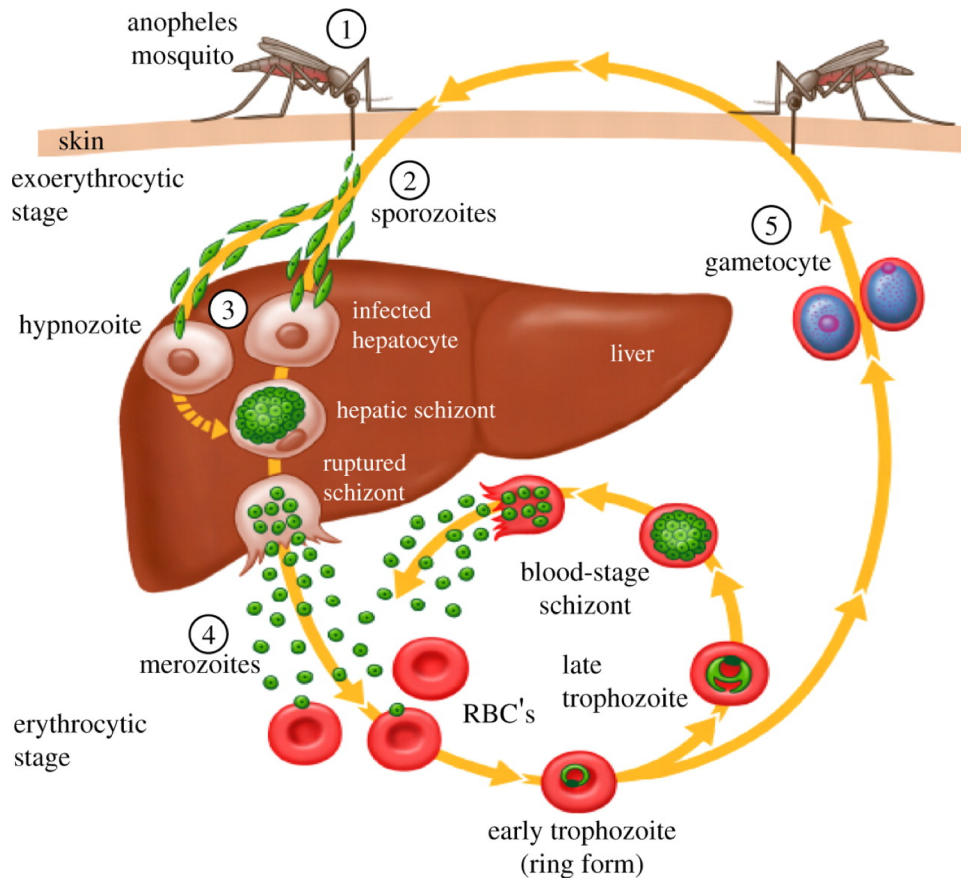


Figure I.3. Lifecycle of the malaria parasite.¹⁴

associated with malaria such as fever, nausea and muscle pains. The cycle is completed when some of the merozoites in the blood stage are reprogrammed to form gametocytes which infect mosquitoes and sexually reproduce in the mosquito gut.¹³

There are treatments available for malaria, though their efficacy has changed over time. Chloroquine, one of the first and most extensively used malaria drugs became ineffective in many areas of the world as the parasite developed resistance to this drug. This resistance came to a head in the 1980s and 90s, resulting in an increase in the global burden of malaria. Consequently, there was an increase in global spending towards malaria control, which emphasized artemisinin combination drug therapies.¹³ As a result, since 2000, death rates due to malaria have fallen 60% worldwide and 66% in Africa.¹⁵ In order to allow these drugs to remain

effective, current treatment strategies need to be designed in order to minimize the development of drug resistance.

In the treatment of malaria, two things must be considered. First, diagnosis of malaria based on the generic, flu-like symptoms is not reliable. Second, to prevent the spread of disease, the parasite must be eliminated from all human hosts. Taking into account these facts, a couple different treatment and elimination strategies have been employed. One method, mass drug administration, treats an entire population in a specific location. As a result, treatment is received regardless of whether an individual has malaria. This strategy removes the need for diagnosis and should eliminate the parasite from all human hosts. Unfortunately, many people do not take the full treatment, resulting in an ineffective dose. Also, the excessive use of the drug can be expensive and result in quick development of drug resistance.^{16, 17} This loss of drug efficacy is extremely dangerous as there are only a limited number of drugs available for treatment of the disease.

A second strategy looks to limit the development of drug resistance by only treating patients that have been diagnosed with malaria, thus reducing drug use. This method is often called mass screening and treatment (MSAT).¹⁶ MSAT should effectively eliminate the parasite from the human host, assuming patients are accurately diagnosed. At this point, the fact that malaria cannot be reliably diagnosed based upon symptoms becomes a problem. Furthermore, there are asymptomatic malaria infections that must be treated.¹⁸ Thus, in order for MSAT to be effective, malaria diagnostic tests must be available for a large portion of the population. Essentially, a diagnostic that is reliable in low-resource settings is required. For many years, microscopy was exclusively used for malaria diagnosis in low-resource settings but this was less than ideal as trained personnel and purchase of microscopes was required. Furthermore,

microscope slides are not easily read in dusty and windy environments.¹⁹ Recently, the face of low-resource malaria diagnostics completely changed with the implementation of rapid diagnostic tests (RDTs). RDTs are lateral flow immunoassays and to run these tests a small blood sample is added to one end of a nitrocellulose strip, followed by addition of buffer. Capillary action then pulls the sample down the strip toward an absorbent pad. Detection occurs through antibody-conjugated gold nanoparticles that bind to the biomarker and this complex is captured by a line of immobilized antibody called the test line. Therefore, a pink line is visible from the bound biomarker/gold nanoparticle complex, when a patient is infected with malaria (Figure I.4). RDTs have been widely distributed throughout the world as they detect malaria in a simple to use, cost effective and relatively stable format.²⁰

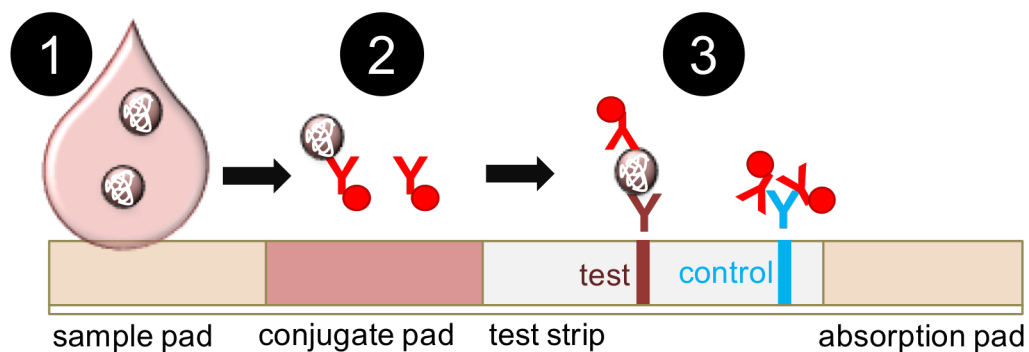


Figure I.4. The workflow of a rapid diagnostic test. 1) Sample is added to initiate flow. 2) Gold nanoparticle conjugates bind to biomarker. 3) Biomarker is captured to form test line. Figure provided by Westley Bauer.

RDTs can successfully diagnose symptomatic malaria infections and inform malaria treatment but as malaria death rates have dropped an ever-growing percentage of infections are low-level and asymptomatic.^{16, 21} Unfortunately, RDTs lack the sensitivity required to detect these infections levels, which have been reported to average around 5 parasites/ μL .²² The number of malaria infections that go undetected by RDTs is highlighted by the results of samples analyzed by both RDT and polymerase chain reaction (PCR), an extremely sensitive method for

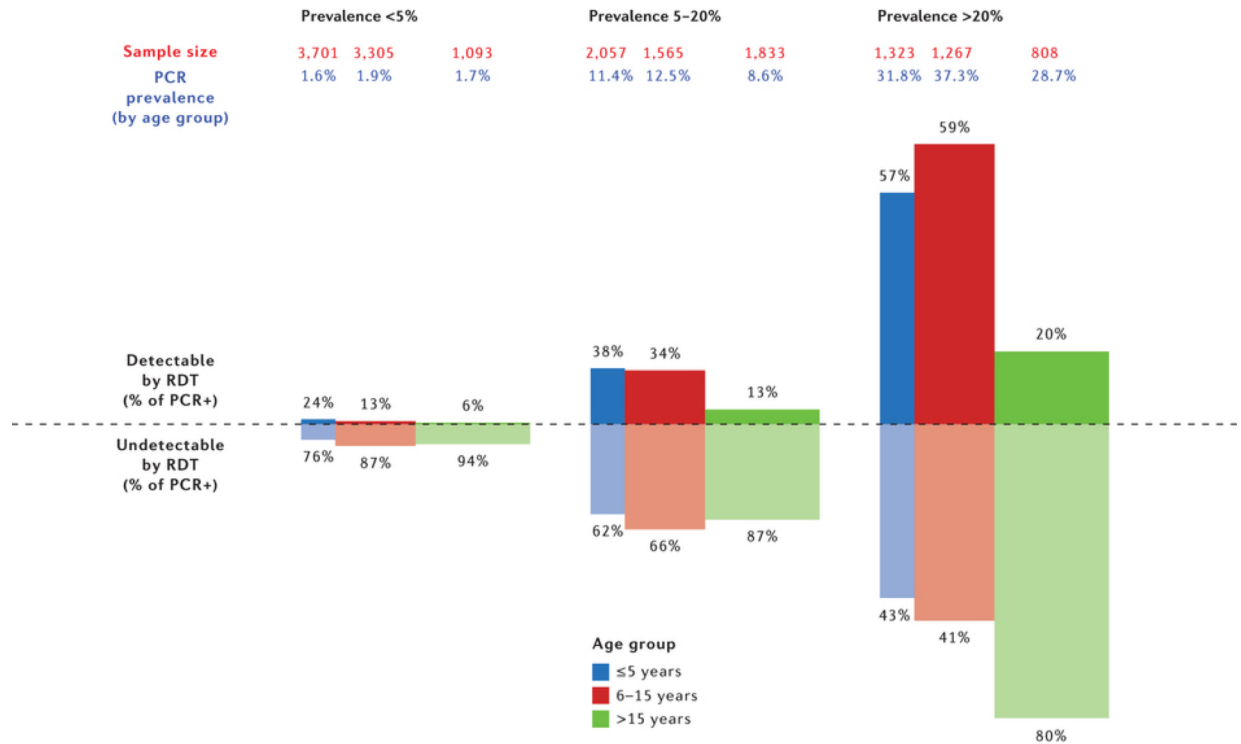


Figure I.5. The proportion of detectable and undetectable malaria infections by RDT relative to PCR (indicated by the height of the bar). The proportion of the population in each age group is reflected by the width of the bars.¹⁶

malaria detection that is not viable in low-resource settings (Figure I.5). Reports have shown that in some cases RDTs only detect 1/6 of all PCR positive infections.^{16, 19} Consequently, several MSAT campaigns based on RDT diagnosis have been ineffective as many patients are left untreated, leaving a reservoir of disease that undermines control and elimination efforts.^{23, 24} Additionally, there is evidence that long-term infections, even if asymptomatic, have deleterious effects on patient health.¹⁸ As a result, it is essential for sensitive, low-resource diagnostics to be developed. Use of these tests will improve patient health and move control efforts toward elimination of the disease without the development of drug resistance.²⁵

Toward Sensitive Low-Resource Diagnostics

Low-resource diagnostics that are sensitive are essential for accurate malaria diagnosis and elimination of the disease. One approach to the development of more sensitive diagnostics is the enhancement of currently used RDTs. A major strength of this method is that a completely new system is not required. As a result, use and interpretation of the tests is familiar to healthcare workers reducing confusion and the cost of implementation required with the use of a completely new test. Enhancement of commercially available RDTs has been achieved and is discussed in Chapter III of this work.²⁶⁻²⁹ There are disadvantages to this method, though, as the enhancement is limited by the manufacturing and design of the current tests. Thus common downfalls of RDTs, such as sample volume limitations, incomplete test clearance and inconsistent manufacturing, still remain.²⁷

These disadvantages have motivated the design of entirely new diagnostics. In the development of a diagnostic, there are four major components that need to be considered: (1) sample preparation, (2) diagnostic workflow, (3) molecular recognition element and (4) detection method. By careful design of each component followed by implementation into a complete diagnostic, the result can be a sensitive test that avoids the pitfalls of currently used RDTs. Thus, the end product would be stable in extreme environmental conditions, simple, inexpensive, and sensitive. Several groups have taken on the challenge of developing diagnostics with these characteristics and many different strategies have resulted. For sample preparation, methods comprise biomarker separation from whole blood and collection of plasma without centrifugation.^{26,30} Diagnostic workflows have included lateral and vertical flow assays.^{31,32} For molecular recognition elements, more stable alternatives to antibodies, such as aptamers, have been considered.³³ Finally, a wide variety of detection strategies have been designed, especially

as the field of materials science has grown. Detection has been achieved with proteins, nanoparticles and polymers. Additionally, these methods have been designed to implement signal amplification strategies to further increase sensitivity.³⁴⁻³⁶

This work explores each of the approaches addressed above. In Chapters II and III, currently used diagnostics are enhanced for use in low-resource settings. In Chapter II, an ELISA for the malarial biomarker *Plasmodium falciparum* histidine-rich protein II (*pfHRP*II), is modified for use with dried blood spot samples. Dried blood spots are an extensively employed sample collection method in low-resource settings. Furthermore, the collected data is used to gain new understanding of the characteristics of *pfHRP*II as a diagnostic biomarker. In Chapter III, a simple sample preparation step that purifies and concentrates *pfHRP*II using magnetic beads is shown to greatly increase the sensitivity of commercially available malaria RDTs. Unfortunately, it was observed that variations in RDT manufacturing limited the reliability of this method.

Thus, Chapters IV-VI pursue the second approach to development of sensitive diagnostics by looking at individual diagnostic components and designing new methods specifically for low-resource settings. Chapters IV and V explore new detection methods through the development of unique nanoparticle-based signal amplification strategies. These methods utilize porphyrin nanoparticles that are broken into thousands of constituent porphyrin molecules in the detection step. These molecules produce either a fluorescent or absorbent assay signal. The use of nanoparticle-based signal amplification produced sensitive detection strategies that show increased stability over commonly used protein enzyme detection methods. In this work, they are used to detect common malarial biomarkers but they can be easily modified for detection of other diseases. In Chapter VI, a vertical flow assay is developed based upon cellulose

membranes functionalized with metal affinity ligands. This diagnostic setup concentrates the biomarker on the test and allows for the use of large sample volumes, increasing the amount of biomarker available for detection. Additionally, the use of metal affinity ligands for biomarker capture is an environmentally stable method. Finally, the porphyrin nanoparticle detection method in Chapter V was used for biomarker detection on these membranes. As a result, through combination of the individually developed diagnostic components, a new diagnostic test was produced that accounts for the specific challenges of a low-resource setting. The projects presented in this work look to solve the problem of inaccurate disease diagnosis in low-resource settings. From enhancement of current diagnostics to the design and optimization of new ones, the goal is to provide inexpensive, simple, stable and sensitive diagnostics to low-resource areas. These diagnostics have the potential to provide patients with accurate diagnoses and thus treatment, a contribution that can lead to a better quality of life and assist in disease elimination campaigns.

CHAPTER II

DRIED BLOOD SPOT ELISA FOR DETECTION OF A MALARIAL BIOMARKER IN PATIENT SAMPLES FROM RURAL ZAMBIA

Introduction

Sample collection is a major challenge for disease diagnosis in low-resource settings. In these areas, the collection of venous blood is not always feasible, so a blood sample is often collected via finger prick and stored on filter paper cards. These samples, called dried blood spots (DBS), have increased sample stability compared to liquid samples, as they can be stored in ambient conditions. Additionally, DBS samples have a low biohazard risk and thus can be easily shipped.^{37, 38} These advantages have led to the availability of several types of DBS collection cards with different features including easy labeling and incorporated reagents for blood lysis or biomarker stability.³⁹

Dried blood spot samples have proven useful for the analysis of a variety of markers including proteins, nucleic acids, and drugs. Methods employing DBS require an extraction procedure followed by techniques such as enzyme-linked immunosorbent assay (ELISA) or polymerase chain reaction (PCR) to analyze the extracted samples.⁴⁰ For example, detection methods for hepatitis C, a measles specific antibody, and *Streptococcus pneumoniae* from DBS samples have been developed and were reliable when validated against gold standards.⁴¹⁻⁴³

In this work, dried blood spots samples were analyzed for *Plasmodium falciparum* histidine-rich protein II (*pf*HRPII), a uniquely structured and highly stable protein biomarker of malaria.⁴⁴ Malaria, a parasitic disease transmitted through mosquitos, is primarily found in

Africa where access to clinical laboratories is limited.¹² Through optimization of a method for the extraction of *pf*HRP II from dried blood spots, an ELISA protocol could be modified for analysis of these samples commonly collected in low-resource settings. Additionally, through analysis of *pf*HRP II in patient samples, biomarker levels, clearance trends and reliability can be determined and the advantages and disadvantages of *pf*HRP II for malaria diagnosis assessed. This knowledge could then contribute to the development of more effective diagnostics. In this work, particular parameters explored in the development of the extraction method include extraction buffer, mixing method and extraction time. Additionally, the percent recovery of *pf*HRP II and the biomarker stability were studied. Following extraction, a *pf*HRP II ELISA was used for biomarker detection, as this technique can detect low-level or asymptomatic infections that may otherwise be undetectable, and its high-throughput nature is useful for epidemiological studies.⁴⁵ The coupling of the developed extraction method with this ELISA allowed for detection of *pf*HRP II from DBS; a procedure that was then used to test patient samples in rural Zambia. This study allowed for determination of the method sensitivity, specificity, and reproducibility, as well as biomarker clearance characteristics, giving more clear understanding to the requirements of a *pf*HRP II diagnostic.

Experimental

Materials

Human Whole Blood (K3 EDTA) was purchased from Bioreclamation IVT (catalog no. HMWBEDTA3). *Plasmodium falciparum* D6 parasite was cultured in house. Recombinant HRP II protein for traditional ELISA standard curve was purchased from Immunology Consultants Laboratory Inc. (catalog no. AGPF-55). ELISA capture and detection antibodies

were acquired from Abcam Inc. (catalog nos. ab9206 and ab30384). Immulon 2HB ELISA plates (catalog no. 14-245-61) and Promega 3,3',5,5'-tetramethylbenzidine (TMB) One ELISA substrate (catalog no. PR-G7431) were purchased from Fisher Scientific. 903 Protein Saver Cards and Whatman 3 filter paper, were purchased from GE Healthcare Life Sciences (catalog nos. 10534612 and 1003-055). Biopunches, 6 mm, were acquired from Ted Pella Inc. (catalog no. 15111-60). All other reagents were purchased from either Fisher Scientific or Sigma Aldrich. DBS extraction was performed with a Fisher Scientific Analog Vortex Mixer (catalog no. 02-215-365). Absorbance measurements were collected on Biotek microplate readers.

pfHRP II ELISA Protocol

The *pfHRP II* ELISA protocol has been reported previously.²⁶ Briefly, 1 µg/mL of anti-*HRP II* IgM (ab9206) in PBS was immobilized in a 96-well plate, which was then blocked with 5% BSA in PBST (1X PBS, 0.1% Tween-20). Samples were then diluted in sample buffer (PBST, 0.1% BSA) and added to the plate. Finally, horseradish peroxidase conjugated detection antibody (ab30384) was added at 0.5 µg/mL in PBST with 0.5% BSA. Signal was visualized with TMB-One, a commercially available 3,3',5,5'-tetramethylbenzidine (TMB) substrate and stopped with 2M sulfuric acid. Absorbance was read at 450 nm.

Dried Blood Spot Extraction

DBS were prepared by spiking *Plasmodium falciparum* D6 parasite culture into whole blood and spotting 10 µL onto 903 Protein Saver cards (903 cards) or Whatman 3 filter paper (W3). Cards were allowed to dry overnight. Extraction was performed by cutting 6 mm spots with a biopunch and then placing two spots for each sample, in one, 2-mL microcentrifuge tube with 300 µL (unless otherwise specified) extraction buffer (PBST). The tubes were vortexed, with continuous shaking at maximum speed (3200 rpm) for 10 minutes. Afterwards, the tubes

were put in a mini-centrifuge to remove bubbles and spin down the DBS paper. The supernatant was then removed and analyzed by ELISA.

Dried Blood Spot pfHRP II ELISA

The previously reported *pfHRP II* ELISA was performed with the following modifications for analysis of dried blood spots. First, the standard curve was made from DBS standards to incorporate extraction conditions into the standard curve. Second, samples were directly added to the plate in the PBST extraction buffer instead of being diluted in sample buffer.

Percent Recovery Calculation

Percent recovery was determined by comparing ELISA signal from a blank (whole blood diluted 1:15 in PBST) and a positive control (whole blood spiked with parasite to 200 parasites/ μ L, diluted 1:15 in PBST), to ELISA signal from an extracted DBS sample. For example, percent recovery for a 200 parasite/ μ L DBS sample was calculated by the following equation.

$$\% \text{ Recovery } pfHRP II = \left(\frac{A_{DBS} - A_{blank}}{A_{positive} - A_{blank}} \right) \times 100$$

Stability Study

Dried blood spots were prepared on 903 cards and W3. The spots were stored in Ziploc bags containing desiccant at the following temperatures: room temperature (RT), 4°C, -20°C and -80°C. Samples were stored for various lengths of time, extending up to 6 months, and analyzed for percent recovery of *pfHRP II*.

Study Setting

Patient samples were collected during a separate study carried out in the Nchelenge District of Zambia, an area where malaria transmission has been sustained at a high level despite interventions.⁴⁶ The original study was designed to determine parasite clearance rates after

treatment with artemisinin combination therapy (ACT) in children under 5 years of age presenting with uncomplicated malaria to the local clinic. The anonymized samples were made available for the current study to determine if *pf*HRP2 clearance could be used as a proxy for parasite clearance rates.

Patient Recruitment and Ethics

Children who arrived at the clinic and tested positive for malaria according to SD Bioline *pf*HRP2 malaria RDTs were recruited for this study after the parent or guardian provided signed informed consent. The study and samples were collected under IRB approval TDRC/C4/09/2014 as well as after approval was granted by the Zambian National Health Research Authority (MH/101/17/6).

Patient Samples

Patient finger-prick blood samples were collected on 903 cards between December 2014 and August 2015. DBS *pf*HRP2 ELISA analysis was done in July 2016. In the interim between collection and analysis, the DBS samples were stored at -20 °C. At the time of collection, finger-prick samples were analyzed by thick smear microscopy to determine quantitative parasite levels by counting parasites per 200 white blood cells (WBC) and then using an estimate of 8,000 WBC/ μ L to obtain the parasite count for that particular time point. This analysis was used as the gold standard in this study. After diagnosis by RDT and *Plasmodium falciparum* parasitemia confirmed by a malaria smear, patients were enrolled and treated with artemether-lumefantrine (Coartem). Thick blood film malaria smears and DBS samples were collected at 15 time points: 0, 6, 12, 18, 24, 30, 36, 42, and 48 hours and days 3, 7, 14, 21, 28, and 35. In the current study, samples from time points 0, 6, 12 and 18 hours as well as days 28 and/or 35 were made available and analyzed for 35 patients. Additionally, all 15 time points were studied for 10 patients.

Dried Blood Spot pfHRP II ELISA for Patient Samples

Before analysis, patient samples were coded to ensure assays were performed blinded to microscopy results. To begin, one, 6-mm DBS spot was placed in a 2 mL microcentrifuge tube with 300 μ L of PBST extraction buffer. After vortexing for 10 minutes, the supernatants were removed for analysis by pfHRP II ELISA with two modifications. First, the standard curve (0-20 parasites/ μ L or 0-34 pM pfHRP II) was made from D6 parasite culture spiked into diluted whole blood (whole blood mixed 1:30 (v:v) with PBST). Second, after extraction, the samples were diluted 10-fold in PBST before addition to the plate. After completion of the assay, samples that did not produce a signal were analyzed a second time without dilution, and samples that exceeded the linear range were analyzed at a greater dilution. This second ELISA was performed on the same day, and samples were refrigerated between assays.

Sample Size Calculation

Appropriate sample size is essential for validation of diagnostic tests. Buderer reported an equation for calculation of sample size to ensure that a planned study would have sufficient power.^{47, 48} This number is dependent on sensitivity or specificity, so equations for each are shown below. To ensure sufficient sample size, the larger of the two was chosen.

$$n_{Se} = \frac{Z_{\alpha}^2 Se(1-Se)}{d^2 \times Prev} \quad n_{Sp} = \frac{Z_{\alpha}^2 Sp(1-Sp)}{d^2 \times (1-Prev)}$$

Variables are defined as: n = number of samples, Se = sensitivity, Sp = specificity, Z = Z score (1.96 for this analysis), d = confidence interval, and Prev = prevalence of disease. For this study, we chose d = 0.1. Considering the samples that were available for analysis, the prevalence was approximated at 70%. Additionally the desired sensitivity of the test was 90% and specificity 80%. When these values were incorporated $n_{Se} = 49$ samples and $n_{Sp} = 205$ samples. In this study, a sufficient sample size of 238 DBS was analyzed.

Data Analysis

For DBS samples, the concentration of *pf*HRP_{II} extracted was determined via standard curves. For the standard D6 parasite culture, 1 parasite/ μ L = 1.7 pM *pf*HRP_{II}. Intra-assay variability was calculated by finding the standard deviation of replicates run at a single concentration, in a single assay, and dividing by the mean of the replicates. Inter-assay variability was found by determining the standard deviation of a single concentration for assays run on different days and dividing by the mean value for that concentration. The sensitivity and specificity of the DBS *pf*HRP_{II} ELISA method was determined through a receiver operating characteristic (ROC) curve analysis using microscopy results as the gold standard.

Results and Discussion

Optimization of Extraction Parameters

In order to analyze the *pf*HRP_{II} in a DBS sample, the extraction method had to first be optimized. The technique used for mixing was chosen by extraction into PBST with mixing using a rotisserie, vortex, and sonicator and without mixing. It was found that recovery of *pf*HRP_{II} increased as the energy imparted by mixing method increased (Figure II.1A). Vortex mixing was selected as it resulted in a high recovery and is also feasible in low resource settings.⁴⁹ No difference in recovery was seen between 10 and 30 minutes of mixing (Figure SI II.1).

Extraction buffer compositions with varying salt concentrations and lysis reagents were also explored. The composition of the buffers analyzed are listed in Table II.1. Three different surfactants were tested, non-ionic surfactants Tween-20 and Triton X-100 and the ionic surfactant sodium deoxycholate. A greater recovery of *pf*HRP_{II} was observed with buffers which

contained nonionic surfactants, likely due to greater solubilization of the protein by the long polyethylene glycol chains. It was found that salt concentration did not affect recovery (Figure II.1B). Considering these results, PBST (Buffer 1) was chosen as the extraction buffer.

Buffer	Composition
1	10 mM PB pH=7.4, 150 mM NaCl, 0.1% Tween-20
2	50 mM PB pH=8, 150 mM NaCl, 1% Triton X-100
3	50 mM PB pH=8, 150 mM NaCl, 0.5% sodium deoxycholate
4	50 mM PB pH=8, 150 mM NaCl, 1% Triton X-100, 0.5% sodium deoxycholate
5	50 mM PB pH=8, 300 mM NaCl, 1% Triton X-100

Table II.1. Composition of the various extraction buffers that were tested.

The ratio of extraction buffer to 6 mm DBS was also examined for impact on *pf*HRPII recovery. Our study showed no significant difference in recovery for volumes of 150-250 μ L per 6 mm DBS (Figure SI II.2). Furthermore, an inherent challenge in DBS analysis is the sample dilution that occurs upon extraction of the protein from the card. For example, a 6 mm DBS punch contains approximately 10 μ L of sample, so if 100 μ L of extraction buffer is used then a 10-fold dilution results.⁵⁰ The DBS *pf*HRPII ELISA was designed to balance required sample volume and assay sensitivity. It was found that extracting two, 6 mm DBS in 300 μ L of buffer compared to one, 6 mm DBS doubled the slope of the standard curve, increasing assay sensitivity while still providing sufficient sample (Figure SI II.3).

Finally, the effect of heating was analyzed by placing DBS in extraction buffer and then in a heat block at 40°C, 60°C and 80°C for 10 minutes. The samples were then vortexed for 10 minutes before analysis by ELISA. Heating at 60°C increased recovery of *pf*HRPII from approximately 70% to 90% (Figure II.1C). A decrease was observed at 80°C, possibly due to

degradation of the protein. For this method, room temperature was chosen to reduce required instrumentation, but a heating step can be added if increased assay sensitivity is required.

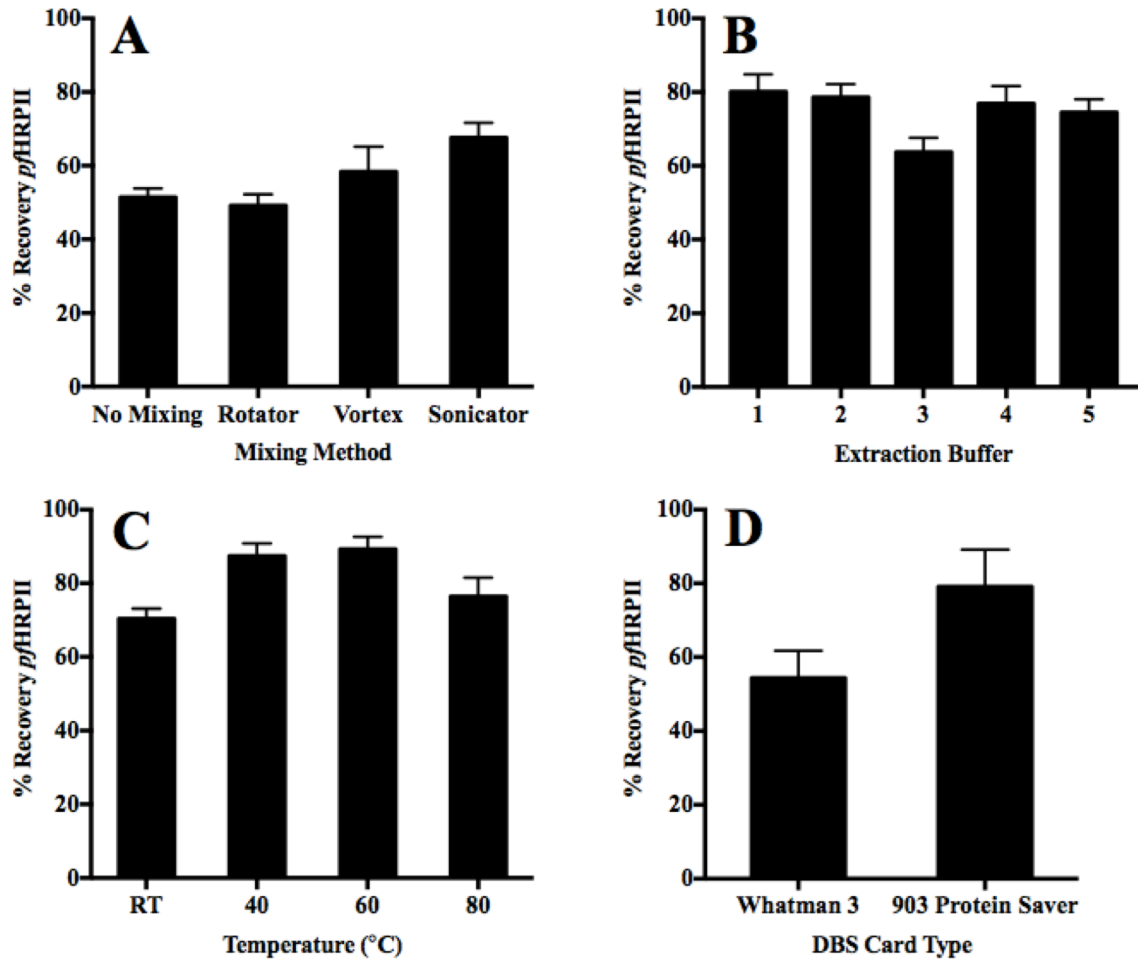


Figure II.1. Optimization of parameters for the extraction of *pfHRP II* from dried blood spot samples. A) mixing method, B) extraction buffer, C) temperature and D) dried blood spot card type.

*DBS Card Type and *pfHRP II* Recovery and Stability*

903 cards are designed for DBS collection with strict quality control in manufacturing to ensure reproducible absorbency and incorporated cover for storage and labeling. W3 is made for filtration but its thickness and pore size allow for retention and storage of dried blood samples. Because 903 cards cost up to 8 time more than W3, many field studies with limited budgets have

employed W3 for sample collection. To determine if the paper type has an effect on *pf*HRP II recovery, DBS samples were prepared on each card type. It was found that recovery of *pf*HRP II from 903 cards was consistently 20% greater than recovery from samples on W3 (Figure II.1D). *pf*HRP II stability was also assessed with both card types. It was observed that *pf*HRP II was less stable in W3 samples with only 30% of the initial *pf*HRP II recovery observed after being stored at room temperature for 6 months. Samples on 903 cards retained 50% of the initial recovery after being stored for 6 months at room temperature. Additionally, samples on 903 cards retained 100% of the original recovery after storage for 6 months at -20 and -80°C (Figure II.2).

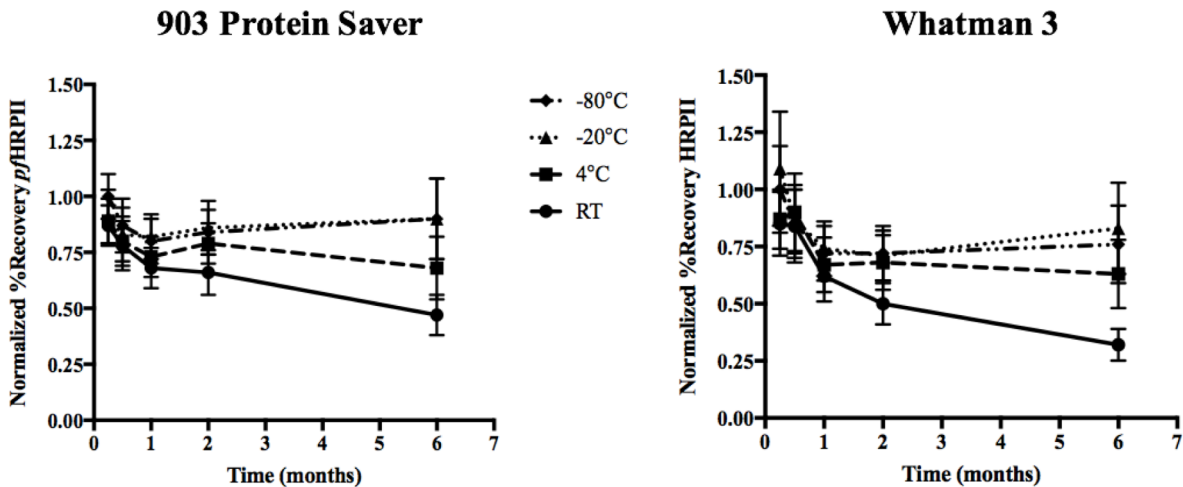


Figure II.2. The stability of *pf*HRP II in dried blood spots, over time, in different storage conditions. Stability on 903 Protein Saver Cards (left) and Whatman 3 filter paper (right).

Thus, though extraction of *pf*HRP II from DBS was achieved reproducibly, several factors affected its efficiency, most notably the type of paper on which the DBS was prepared. Since 903 cards had up to a 20% greater recovery of *pf*HRP II, and *pf*HRP II did not degrade in these cards when stored frozen for 6 months (Figures II.1D, II.2), the extra cost is justifiable as it enhances method performance. We conclude that 903 cards most likely provide a more stable matrix for

protein storage, and their increased thickness allows for greater protein recovery from a specific DBS area.

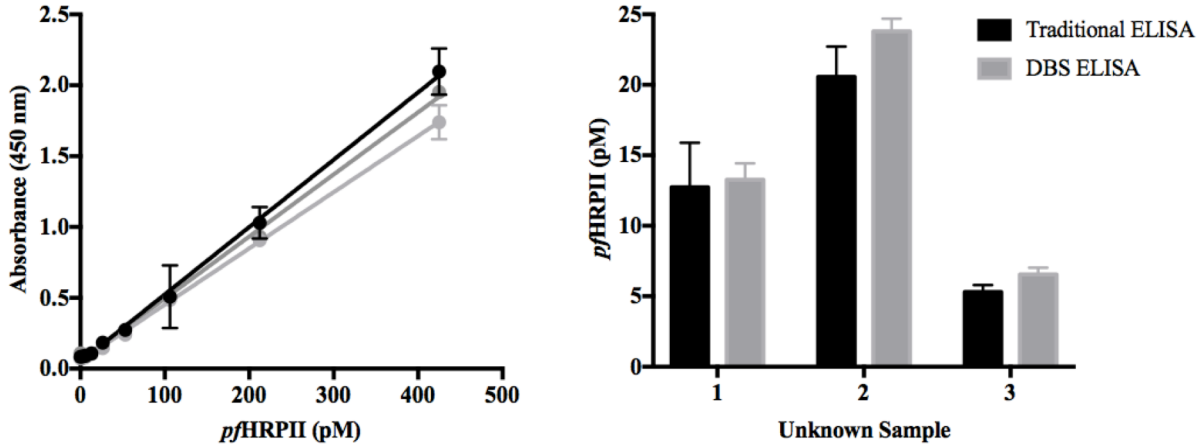


Figure II.3. The reproducibility and accuracy of the developed DBS *pfHRP II* ELISA. DBS standard curves run on three different days (left) and comparison of *pfHRP II* values between the DBS ELISA and a traditional ELISA (right).

*Comparison to Traditional *pfHRP II* ELISA*

Using the optimized protocol for extraction of two, 6 mm DBS in 300 μ L of PBST, with vortex mixing for 10 minutes, standard curves were generated from parasite spiked DBS samples on 903 cards. The resulting curves were highly reproducible with an intra-assay variability of 7% and inter-assay variability of 10% ($n=3$) (Figure II.3). The limit of detection (LOD), defined as $3\sigma_{\text{blank}}/\text{slope}$, was 4 ± 5 parasites/ μ L (8 ± 8 pM *pfHRP II*). Samples were then analyzed simultaneously on the traditional *pfHRP II* ELISA and the DBS *pfHRP II* ELISA. A paired t-test showed no statistical difference between the *pfHRP II* levels found by the two methods ($p = 0.1746$) (Figure II.3).

Analysis of Patient Samples from Rural Zambia

The standard curves used for analysis of DBS patient samples were made from parasite-spiked diluted whole blood. These assays, performed at Macha Research Trust, had an intra-

assay variability of 6% and an inter-assay variability of 18% (n=14). The LOD determined by $3\sigma_{\text{blank}}/\text{slope}$ was 0.165 ± 0.003 pM *pfHRP*II (Figure SI II.4). 238 DBS patient samples collected within 24 hours or at least 28 days after malaria diagnosis and treatment were analyzed by DBS *pfHRP*II ELISA (Table SI II.1). Using microscopy as the gold standard, a ROC curve was used to determine the sensitivity and specificity of the assay. An ideal ROC curve forms an approximately 90° angle in the left corner of the graph, which corresponds to a test with 100% sensitivity and 100% specificity. In this analysis, the DBS *pfHRP*II ELISA was found to have a sensitivity of 94% (CI: 89-97%) and a specificity of 89% (CI: 79-95%), with a threshold of 3.5 pM *pfHRP*II (Figure II.4). This demonstrates the developed DBS *pfHRP*II ELISA is a reliable diagnostic for malaria. Additionally, the area under the ROC curve was 0.96, indicating excellent accuracy of the method and the usefulness of *pfHRP*II as a diagnostic biomarker. Finally, using this threshold, the positive predictive value (PPV) for the assay was 95% and the negative predictive value (NPV) was 86%.

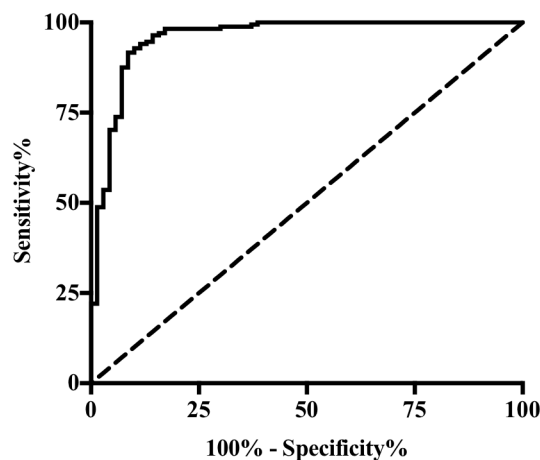


Figure II.4. Receiver operating characteristics curve for DBS *pfHRP*II ELISA when compared to clinical microscopy values for patient samples from rural Zambia. Sensitivity of the assay was 94% (CI: 89-97%) and specificity was 89% (CI: 79-95%) when the threshold was set at 3.5 pM *pfHRP*II.

The reduced specificity compared to sensitivity that was observed can be attributed to the fact that the gold standard for malaria diagnosis (microscopy) detects the malaria parasite rather than the protein biomarker detected with the DBS *pfHRP*II ELISA. This discrepancy can result in false positives by DBS ELISA because *pfHRP*II can persist in the blood stream days to weeks after parasite clearance.^{51, 52} So, while a patient may not have an active malaria infection, the DBS *pfHRP*II ELISA may detect residual *pfHRP*II in the blood, not a non-specific signal. Furthermore, microscopy has shortcomings of its own, including a lack of sensitivity. In general, ELISA is more sensitive than microscopy.⁵³ As a result, false positives could come from the ability of the DBS *pfHRP*II ELISA to detect malaria infections that are not seen by microscopy.

While a lower threshold could allow for detection of more truly *pfHRP*II-positive samples, it will also result in detection of *pfHRP*II that is not the result of an active malaria infection. This observation points to a disadvantage of *pfHRP*II as a biomarker, as its persistence can result in misdiagnosis of patients and improper treatment.⁵⁴ Consequently, there is a need for an alternative protein biomarker for malaria that quickly clears from the bloodstream.

Plasmodium lactate dehydrogenase (*pLDH*) is one such biomarker that is being further explored in our lab.^{36, 52} Nonetheless, the importance of detection of *pfHRP*II remains, as it continues to be the most sensitive and prevalently used protein biomarker for detection of *falciparum* malaria infections.⁴⁴

*pfHRP*II Clearance

For 10 patients, all 15 time points were analyzed and used to study the clearance of parasite and *pfHRP*II after treatment (Figure II.5). For these ten patients, the median clearance time was 1.38 days (33 hours) for the parasite and 3 days for *pfHRP*II. Various *pfHRP*II clearance trends were observed when looking at each patient individually, indicating many

difference response to the disease and treatment. Two patients with low initial parasitemias (Figures II.5A, II.5B), were negative for *pfHRP2* according to the threshold set by the ROC curve analysis. Patient 51 (Figure II.5C) had relatively low *pfHRP2* levels before a large spike at $t=1$ day. The level of *pfHRP2* in Patient 43 (Figure II.5D) spiked and fell throughout the study but was cleared by the last time point. Patients 25, 27 and 45 (Figures II.5E, II.5F, and II.5G respectively) all showed *pfHRP2* levels which corresponded with parasite load but with a lag in clearance time, demonstrating *pfHRP2* persistence. Patients 49 (Figure II.5H) and 50 (Figure II.5I) displayed the same trend except for a couple of spikes corresponding to a decrease in parasite levels, likely caused by the release of *pfHRP2* upon parasite death⁵⁵. Patient 44 (Figure II.5J) was also similar, but at the last three time points *pfHRP2* levels began to rise, while parasite levels remained negative, indicating reinfection or recrudescence may have occurred. Reinfection is when an individual is successfully treated for malaria but then becomes sick again with an entirely new malaria infection. This process is most common in high transmission areas.⁵⁶ Recrudescence occurs when the same malaria infection is never fully eliminated by treatment and reappears.⁵⁷ As sample genotyping was not performed on these samples, the cause of the spike in *pfHRP2* levels cannot be known for certain.^{58, 59}

As mentioned previously, the commonly observed trend in the patient samples of delayed *pfHRP2* clearance compared to parasite clearance, is an example of the persistence of *pfHRP2*.⁶⁰ The stability of *pfHRP2* allows it to remain in circulation for several days or even weeks after effective treatment, which can result in false positive diagnostic results. Using the ROC curve threshold, information can be gathered about infection levels and *pfHRP2* persistence in the blood. For the purposes of this study, infections levels were classified as follows: low (0-14,999 parasites/ μ L), medium (15,000-75,000 parasites/ μ L) and high (\geq 75,000 parasites/ μ L).

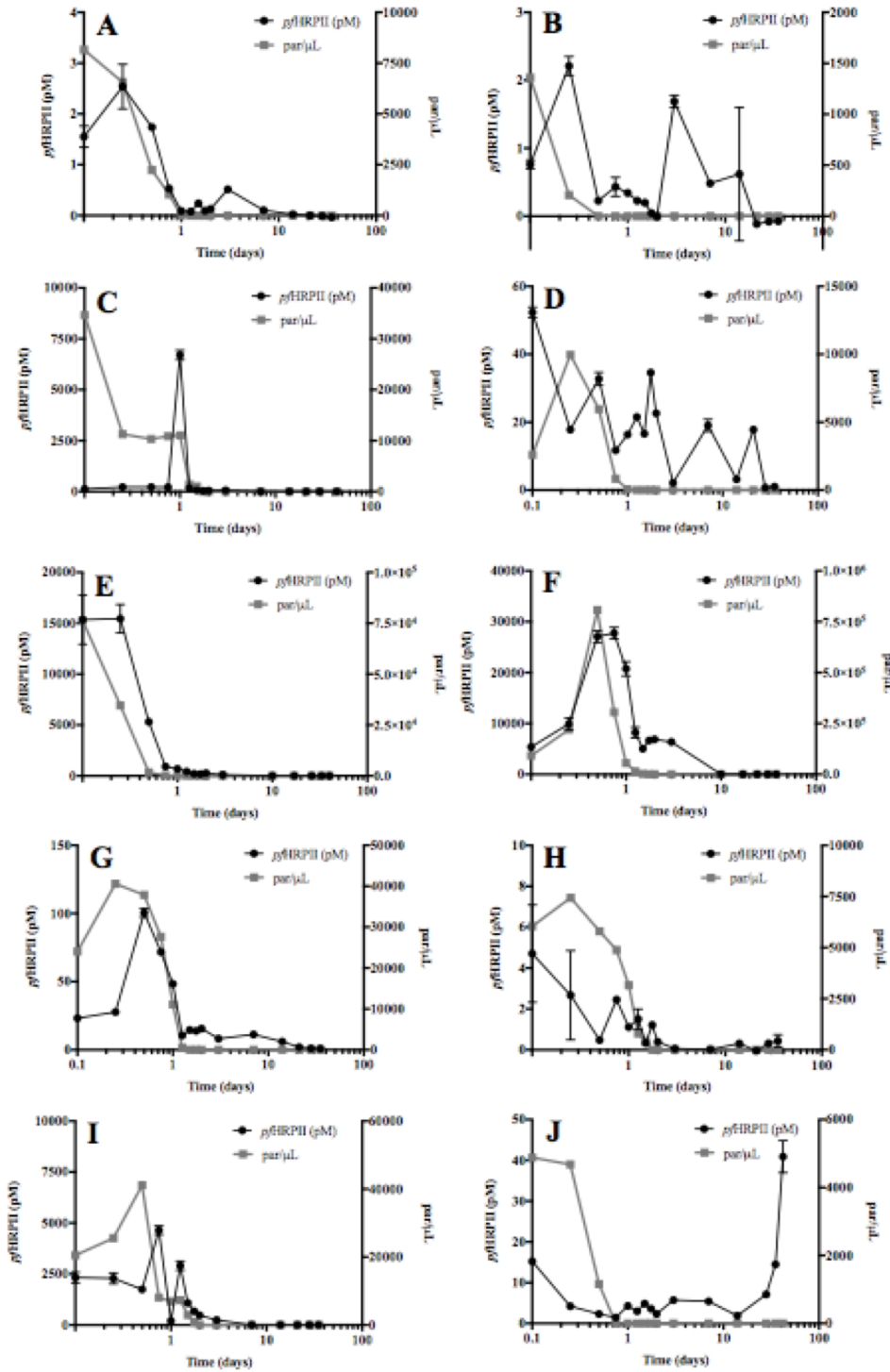


Figure II.5. The *pfHRP2I* clearance trends observed in patient samples collected at 15 time points, over a 35-day period. The concentration of *pfHRP2I* extracted from the DBS samples and the parasitemia determined by microscopy are plotted against time. A) Patient 46, B) Patient 53, C) Patient 51 and D) Patient 43, E) Patient 25, F) Patient 27, G) Patient 45, H) Patient 49, I) Patient 50 and J) Patient 44.

Besides the case of possible recrudescence, Patients 3 and 37 (Table SI II.1) had *pf*HRP II levels that were still positive at the end of the time study, meaning these samples contained *pf*HRP II as long as 30 days after the beginning of treatment. Furthermore, samples from Patients 43 and 45 (Figures II.5D and II.5G), which were analyzed for the full time study, retained *pf*HRP II past the median time-to-clearance of 3 days. It was found that the initial parasite level for each of these patients was below 25,000 parasites/ μ L, suggesting that persistence of *pf*HRP II was a result of chronic infection not the level of infection. In chronic infections, low-level parasitemias can persist in a patient for years, with minimal symptoms, and then become symptomatic.⁶¹⁻⁶³ The longevity of the infection can allow for build-up of *pf*HRP II over time, so even though the parasite load is low, a significant amount of *pf*HRP II persists in the blood.

Association Between Parasite and Biomarker Levels

To ascertain whether there was a correlation between parasite and *pf*HRP II levels, the DBS *pf*HRP II ELISA results for all 328 patient samples were compared to microscopy. A positive, linear correlation was observed, with a Spearman correlation coefficient (ρ) equal to

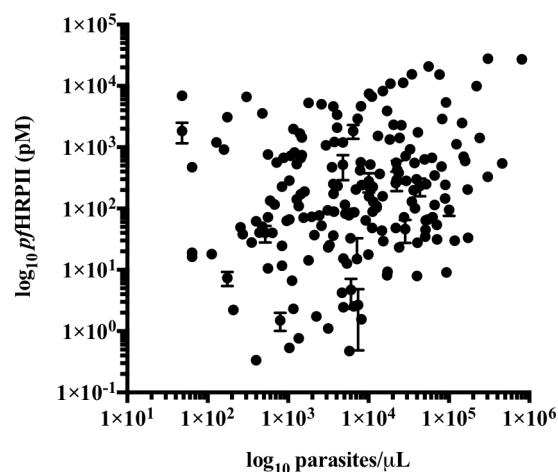


Figure II.6. Correlation between parasite and *pf*HRP II levels that were observed in the 328 patient samples from rural Zambia. Spearman correlation coefficient (ρ) = 0.70 (95% CI 0.63-0.75, $p < 0.0001$).

0.70 (95% CI 0.63-0.75, $p < 0.0001$) (Figure II.6). Statistically, this result proves an association between these two variables and the strength of the association is considered to be moderate ($\rho = 0.5-0.7$) to high ($\rho = 0.7-0.9$).⁶⁴ As was demonstrated by the DBS standard curves made from samples spiked with parasite, there is a direct correlation between *pfHRP2* and parasite levels in parasite culture (Figure II.3). Several different factors could have contributed to the decrease in the strength of association observed with patient samples. For example, the lack of strictly controlled storage conditions for the DBS samples likely caused protein degradation and variability in extraction efficiency. As a result, in the analysis of the patient samples there were other influences on protein recovery besides the initial parasitemia of the sample. Additionally, the amount of *pfHRP2* produced by the parasite is dependent on the life stage and strain.^{55, 65} Patient samples have much greater variety in these parameters than parasite culture, resulting in a weaker association between *pfHRP2* and parasite levels. Other literature reports have seen similar discrepancies in patient samples, as some report correlation between *pfHRP2* levels and disease severity, while others do not.^{66, 67} Nonetheless, in this work a positive association between *pfHRP2* and parasite levels was observed, indicating the usefulness of the *pfHRP2* biomarker in malaria diagnosis.

Conclusion

Dried blood spots represent a common and simple sample collection method in low-resource areas. Samples stored in this way are stable and easily shipped. In order to analyze these samples, methods must be optimized for extraction of specific biomarkers and subsequent analysis. Here, we report a highly reproducible procedure for extraction of the malarial biomarker *pfHRP2* and subsequent analysis of the protein by ELISA. This assay was then used to analyze patient samples in rural Zambia and was found to have a 94% sensitivity and 89%

specificity. Examination of patient samples also revealed trends in biomarker clearance, showing sustained *pf*HRP II in the blood and an instance of possible recrudescence. Furthermore, the a positive association between parasite and *pf*HRP II levels was observed. Thus, a protocol was developed that allowed the ELISA technique to be used for analysis of samples from low-resource setting. Additionally, the reported method is reliable and the results obtained give further insight into the both the strengths and drawbacks of *pf*HRP II as a diagnostic biomarker for malaria.

Acknowledgements

I would like to acknowledge Christine Markwalter, Danielle Kimmel, Lwiindi Mudenda, Saidon Mbambara, and Phil Thuma for their contributions to this work. Also, we thank the children and guardians who agreed to participate in the clinical aspect of this study, as well as Macha Research Trust for collection of the dried blood spot samples and for access to the samples and their on-site laboratories. This work was supported by the National Institute of Health/Fogarty International Center [D43 TW009348] and Vanderbilt University through Laboratories for Innovation in Global Health Technologies and the Mitchum E. Warren, Jr. Graduate Research Fellowship (L.E.G.). The clinical aspect of the study was supported by the National Institutes of Health as part of the International Centers of Excellence for Malaria Research (U19 AI089680).

CHAPTER III

MALARIA RAPID DIAGNOSTIC TEST ENHANCEMENT

Introduction

The advent of point-of-care (POC) diagnostic tools has changed the face of healthcare in nations affected by the ongoing spread of infectious diseases, including malaria.⁷ These underdeveloped, remote areas are often characterized by poverty, absent or intermittent electricity, hot and humid environmental conditions as well as a lack of skilled clinicians. Molecular based diagnostic methods such as enzyme-linked immunosorbent assays (ELISA), used in Chapter II, and quantitative polymerase chain reaction (qPCR) are powerful tools for the detection of protein and nucleic acid biomarkers of infectious diseases. However, reagent instability and cost of these assays, in addition to time and expertise needed to perform the tests, limits their use in low-resource areas.⁶⁸ For malaria, light microscopy is the gold standard for detection, but limited access to functional microscopes and trained microscopists prevents its widespread use at the point of care. Lateral flow immunochromatographic rapid diagnostic tests (RDTs), which operate much like commercial pregnancy tests, were developed to circumvent these challenges and bring affordable disease diagnosis to low-resource areas.^{69, 70} Several advantages of RDTs include low-cost, rapid time to result, and ease of use and interpretability.⁷¹ Additionally, these tests have been widely used in public health programs to aid with patient management, disease surveillance and treatment campaigns.²⁰ In 2010, 88 million RDTs were used in endemic countries for the detection of malaria alone.⁷²

Malaria RDTs detect protein biomarkers of the malarial parasite. The predominant biomarker used in RDTs for detection of *Plasmodium falciparum* infection is histidine-rich protein II (*pfHRP*II).⁶⁹ This biomarker was explored in Chapter II and was shown to be a reliable and accurate diagnostic biomarker for malaria. Detection of *pfHRP*II in an RDT format allows for a simple detection procedure opposed to ELISA. Unfortunately, despite the many advantages of RDTs, the need for these tests to have improved sensitivity and reliability has become apparent. The World Health Organization (WHO) periodically reviews all malaria RDTs manufactured for diagnostic use, and sets the limit of detection for these tests at 200 parasites/ μ L.⁷³ While this limit of detection is sufficient for the diagnosis of symptomatic malaria infections, many asymptomatic patients are not diagnosed and continue to be transmission reservoirs of the disease as current RDTs fail to identify these carriers. Additionally, poor manufacturing standards and storage conditions render many brands of malaria RDTs inoperable and unreliable.⁷⁴ According to the WHO, in 2011, less than 10% of the 60 brands and 200 types of tests manufactured were effective at detecting 200 parasites/ μ L parasite densities.⁷³ Unfortunately, tests are often acquired based on government sanctions, history of use, and cost instead of acquisition based on reliability of the brand.⁷⁵ This variability in test performance, sensitivity and reliability undermines the progress in malaria diagnosis and prevention.⁷⁶

We have recently reported the development of a low-resource extraction cassette that can extract, purify and concentrate *Plasmodium falciparum* histidine-rich protein II (*pfHRP*II) from a blood sample in less than 30 minutes.²⁶ In this study, a series of aqueous buffer solutions separated by oil surface tension valves were preloaded into a single length of tubing. We were able to purify the protein biomarker from blood by processing biomarker bound magnetic

particles through the cassette using a handheld magnet. At least 50% extraction efficiency was demonstrated for samples with parasitemias as low as 12.5 parasites/ μ L. As a result of this technique, a commercial RDT brand was qualitatively improved over 8-fold. In this current study, we describe the utility of this extraction cassette for the improvement of a wide range of RDT brands of variable performance, providing a method to increase the sensitivity of commercially available tests for detection of *pf*HRP II. The use of commercial tests is a strength of this method, as it results in a diagnostic readout that healthcare workers are accustomed to analyzing. Furthermore, the improvement in RDT sensitivity was quantitated at parasitemias below the 200 parasites/ μ L regime, where many RDTs are ineffective. Finally, we describe the effect of individual donor samples on low, medium and high performing RDT brands at various parasite loads.

Experimental

Materials

Both pooled and individual donor human whole blood in citrate phosphate dextrose (catalog no. HMWBPCPD) were purchased from Bioreclamation LLC. For the enhancement study, pooled blood was used. For the individual donor effect study, individual donor blood was used. This study was blinded, as we did not know the identity of the donors. *Plasmodium falciparum* D6 strain was cultured in the lab. Tygon tubing was purchased from McMaster Carr (catalog no. ACF00002). Ni-NTA Magnetic Agarose Beads (catalog no. 36113) were purchased from Qiagen Inc. Donut magnet used in this study was purchased from Emovendo LCC. Paracheck (Pck), ParaHit Dipstick (PDip), ParaHit Total (PTot), ICT Pf (IPf), ICT Dual (IDual) and Blue Cross One Step Pf (OsPf) rapid diagnostic tests were acquired from their respective

manufacturers (Table III.1). Hewlett Packard Color LaserJet CM3530fs MFP scanner was used to image the RDTs. Image J software was downloaded from the National Institute of Health website (<http://rsbweb.nih.gov/ij/>). OriginPro 9.0 Software was employed for RDT analysis. The remaining products were purchased from either Fisher Scientific or Sigma Aldrich.

Brand	WHO PDS	Catalog #	Lot #	Manufacturer
Paracheck Pf	96.0	30301025	311310	Orchid Biomedical Systems
One Step Pf	67.7	522352	201209025	Blue Cross Biomedical
ParaHit Pf	80.8	551C101-50	4000006366	Span Diagnostics
ParaHit Total	35.4	551C204-50	4000007699	Span Diagnostics
			4000010071	Span Diagnostics
ICT Dual	78.8	ML03	50130	ICT Diagnostics
ICT Pf	86.9	ML01	10006	ICT Diagnostics
			50131	ICT Diagnostics

Table III.1. Specifications of the RDTs used for this study.

Blood Sample Preparation

Human whole blood samples were combined in 1:1 (v:v) ratio with 2X lysis buffer (100 mM potassium phosphate pH = 8.0, 600 mM NaCl, 250 mM imidazole, 2% Triton X-100). Subsequently, the blood sample was filtered through glass wool that was placed in the bottom of a plastic syringe. Following filtration, a 200 parasite/ μ L stock blood sample was made by adding

a specific amount of D6 *Plasmodium falciparum* culture (at ~52000 parasites/ μ L) to the lysed and filtered sample. The remaining parasitemias were achieved by serial dilution of the 200 parasite/ μ L stock. For the mimic patient study, this process was modified slightly in that the specific amount *P. falciparum* culture required for the desired parasitemia was spiked into the sample before filtration.

Extraction and Analysis with RDTs

Extraction devices were constructed and prepared blood samples were purified and concentrated as described previously.²⁶ Briefly, a 9-inch piece of Tygon tubing was injected with three 100 μ L wash chambers (50 mM PB, pH 8.0, 300 mM NaCl, 125 mM imidazole, and 0.05% Tween-20) each separated by a 0.25 μ L mineral oil valve. An elution chamber consisting of 10 μ L of elution buffer (50 mM potassium phosphate (PB), pH 8.0, 300 mM NaCl, 500 mM imidazole, 0.05% Tween-20) was injected at the end of the tube. One end of the Tygon tube was blocked with a capillary tube and a PCR tube was placed on the other end as the sample chamber. 200 μ L of the blood sample were placed into this chamber with 10 μ L of Ni-NTA magnetic agarose beads. After incubation in the chamber, the beads were pulled through the wash chambers into the elution chamber with a magnet. After incubating in the elution chamber the beads were pulled back into the adjacent oil valve. The elution chamber was then cut off with a razor and the contents were spotted onto an RDT. In the enhancement study, this process was done, in triplicate, on six types of RDTs, at six parasitemias (0, 12.5, 25, 50, 100 and 200 parasites/ μ L). For the individual donor effect study, the process was done in triplicate for three parasitemias (0, 10 and 100 parasites/ μ L) with each donor sample, on three RDT brands, PTot, IPf and Pck, of low to high performance, respectively. For both studies, standard analysis of the blood samples that were not extracted consisted of spotting 5 μ L of parasite spiked blood sample

directly onto the RDT and processing according to manufacturer's specifications. These unextracted samples served as reference standards.

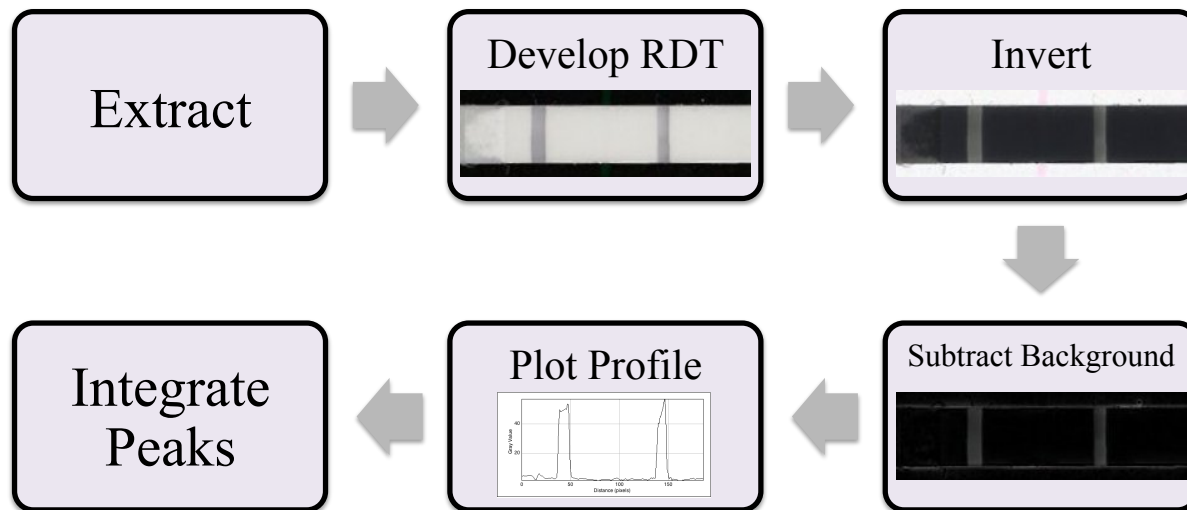


Figure III.1. The workflow used to quantitate the RDT signals.

Image Analysis

The process used for analysis of the RDTs is outlined in Figure III.1. To begin the image analysis portion of this workflow the lateral flow test strip, housed within the plastic cassette of the RDT, was removed. The absorption pad at the end of the strip was detached to aid in the drying of the strip. The strips were dried overnight prior to imaging with a Hewlett Packard Color LaserJet CM3530fs MFP scanner. This drying step did not affect peak signal over time (data not shown). Specific settings were used (darkness = 8, background = 1, sharpness = 4) and the highest image quality was selected. The image was then manipulated in Image J. First, the image was inverted. This is a processing step commonly performed in RDT reader algorithms to present the data in an intuitive manner.⁷⁷ Secondly, the background was subtracted (rolling ball radius = 15 pixels, smoothing disabled). Once this was accomplished, a plot profile containing the test and control line was generated. This profile was imported into Origin® software, where

the peak in the plot profile associated with the test line was integrated using the Peak Analysis tool. When using this tool, the automatic background line was used. A test was considered positive if the height of the test line peak on the plot profile was at least 3% of the control peak. Peak width was determined manually by the user, and the result of the integration was generated by the software. This result was used to quantitate the intensity of the test line in the form of an integrated area.

Results and Discussion

Enhancement in RDT Performance

The advent and implementation of rapid diagnostic tests, which detect *p*fHRP_{II}, have made an invaluable impact on the diagnosis and treatment of malaria in low-resource settings. The efficacy of these tests at high parasitemia was demonstrated in this study, as all RDT brands

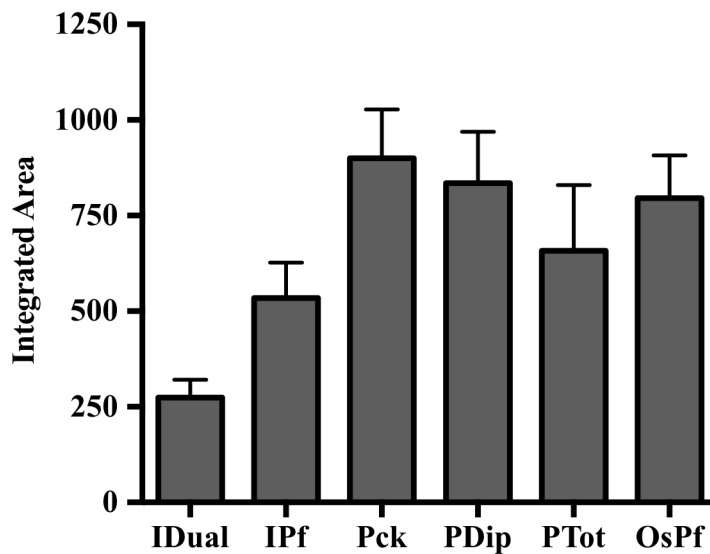


Figure III.2. The integrated area of the RDT signal for unextracted samples at 2000 parasites/ μ L. All brands, ICT Dual (IDual), ICT Pf (IPf), Paracheck (Pck), Parahit Dipstick (PDip), Parahit Total (PTot) and One Step Pf (OsPf) are able to detect *p*fHRP_{II} at this level of parasitemia.

analyzed were found to produce detectable signal given unextracted samples at a parasite density of 2000 parasites/ μL (Figure III.2). But as discussions about eradication strategies begin in earnest, the challenge becomes how to effectively identify the untreated asymptomatic patient reservoir. Management of submicroscopic malarial infections has become a challenge in the field, as current rapid diagnostics are unable to detect these patients.⁷⁸⁻⁸⁰ Thus, for this study we set our desired detection limit to less than 20 parasites/ μL as this will allow for detection of parasite at submicroscopic levels and lead to the diagnosis of more asymptomatic infections.⁷⁸

The RDT diagnostic process was modified by adding a simple sample preparation step which consists of a self-contained extraction device that purifies and concentrates the malaria biomarker *pfHRP2*, enhancing RDT performance. Improvement in test performance was benchmarked on changes in the signal intensity of the *pfHRP2* test line. The RDT brands evaluated in this study were chosen based on performance as indicated in the WHO report on all manufactured malaria RDTs. The brands used were representative of low, medium and high performing tests (Table III.1).

The effect of sample preprocessing on RDT performance can be seen in Figure III.3. This analysis showed five of the six RDT brands tested were able to detect 200 parasites/ μL from an unextracted sample. Four brands detected 100 parasites/ μL , as compared to only two at 50 parasites/ μL . Only IDual detected unextracted samples at 25 and 12.5 parasites/ μL . After extraction, all brands were improved to detect parasite concentrations of 12.5 parasites/ μL and higher, with the exception of OsPf.

To quantitate performance, the lateral flow strips within each cassette for all brands were scanned and the corresponding plot profiles analyzed using peak integration software. Analysis methods of this type are common in recently developed RDT readers.⁷⁷ The degree of

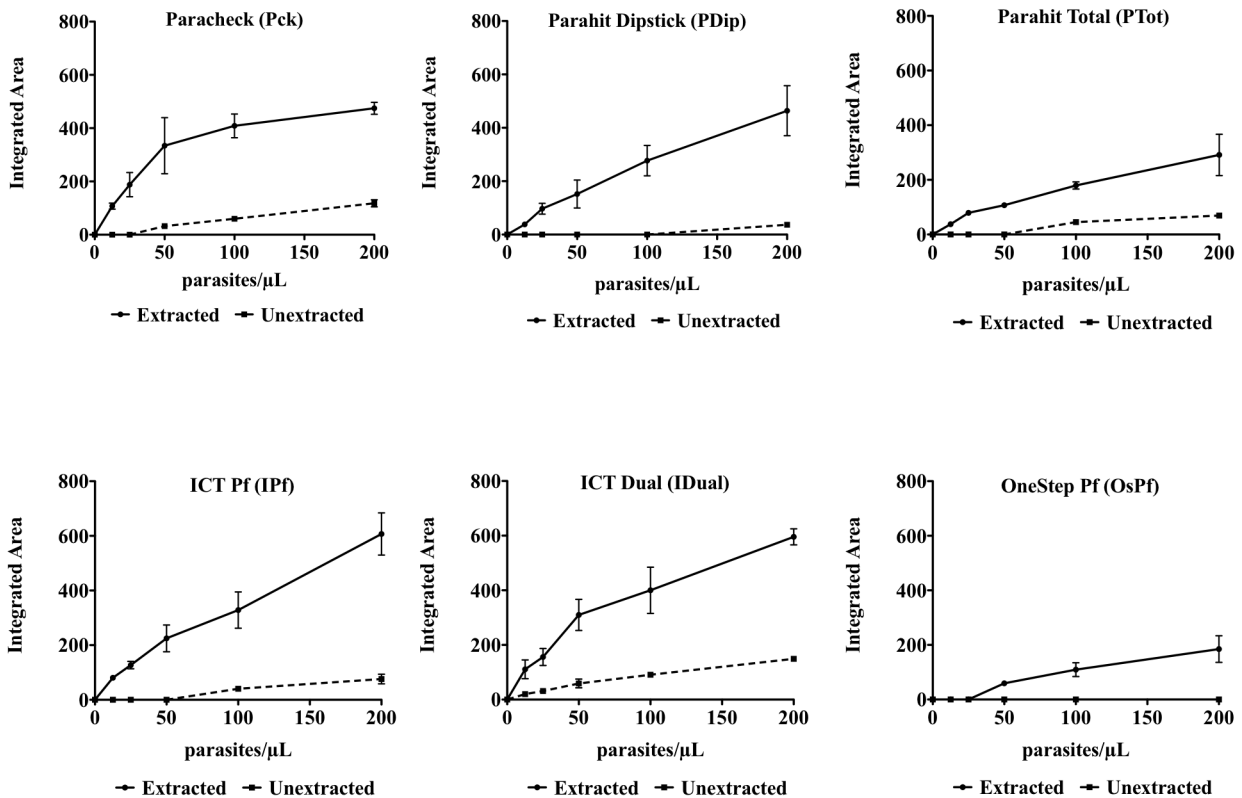


Figure III.3. Integrated area of the RDT signal as a function of parasitemia, extraction and RDT brand. Curves for extracted (black lines) and unextracted (dashed line) samples are shown and the signal increase gained from extraction can be seen. The diagnostic threshold for all tests analyzed was 200 parasites/ μL , as set by the World Health Organization.

enhancement in RDT signal that occurs with extraction of the sample (enhancement factor) was calculated for 200 parasites/ μL by the following relationship:

$$\text{Integrated Area}_{\text{Extracted}} / \text{Integrated Area}_{\text{Unextracted}}$$

This enhancement factor ranged from 4 to 13 among the five brands that produced a detectable signal at 200 parasites/ μL unextracted (Figure III.4). The greatest enhancement was observed for those tests that gave minimal or undetectable results when the samples were unextracted. For example, the enhancement of OsPf was practically infinite, as the unextracted sample was not detected at 200 parasites/ μL (Figure III.4).

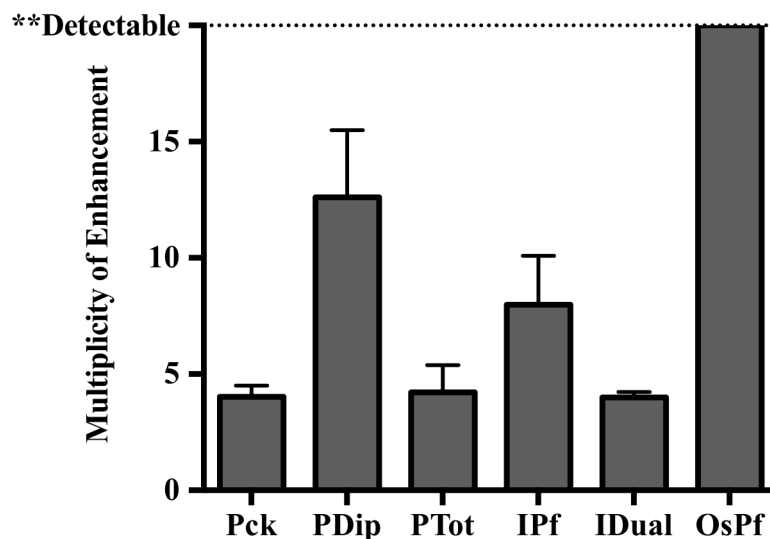


Figure III.4. The multiplicity of enhancement observed at 200 parasites/ μ L for each RDT brand, as a result of extraction.

Despite the observed enhancement, visual and pixel analysis of the tested brands revealed several brand-to-brand discrepancies. The most noted was in the case of OsPf, where smearing of the sample and RDT components on the test strip increased the background, preventing detection of low parasitemias in this brand. This failure of the test strip to clear the sample and reagents prevented proper development of the test line and peak identification. Other brand-to-brand differences were observed by comparing the shape of the titration curves. Pck reached saturation in signal intensity after 100 parasites/ μ L, whereas PTot and IPf remained linear through 200 parasites/ μ L, where our analysis stopped (Figure III.3). These differing trends suggest a greater concentration of active antibody on the test line of IPf and PTot RDTs, thus providing a wider linear range for calculations made through our algorithm.

Limit of Detection of Enhanced RDT Signal

Given the nature of the algorithm used to detect the peaks on the scanned RDT image, the limit of detection was found as a percentage of the control peak (threshold height). For each

	Unextracted	Extracted
Paracheck (Pck)	21.7 ± 7.4	3 ± 0.2
Parahit Dipstick (PDip)	143.7 ± 39.5	10.7 ± 0.9
Parahit Total (PTot)	70.2 ± 12.4	17.3 ± 1.5
ICT Pf (IPf)	51.1 ± 7.9	5.6 ± 0.8
ICT Dual (IDual)	15 ± 1	2.9 ± 0.2
One Step Pf (OsPf)	ND	32.6 ± 4.5

Table III.2. Limit of detection (in parasites/ μ L) for all brands of RDTs tested with unextracted and extracted samples.

brand tested, the integrated area for all of the control lines analyzed were averaged and converted to the 3% threshold height maximum. Given this threshold height, the LOD was found for extracted and unextracted samples of each brand.

According to the WHO, the limit of detection for malaria RDTs is required to be at least 200 parasites/ μ L.⁷³ We found five out of six of these brands to have limits of detection ranging from 15-150 parasites/ μ L given an unextracted sample. OsPf did not detect unextracted samples within the LOD recommended by the WHO. When samples were extracted, the limits of detection were found to be between 3-33 parasites/ μ L (Table III.2). Both Pck and IDual had LODs of 3 parasites/ μ L after extraction and of the six brands tested, five were enhanced to detect below the set detection limit of 20 parasites/ μ L, which is representative of asymptomatic and submicroscopic levels of malaria infection. IDual was the only brand tested that was able to detect at this level before extraction. To our knowledge, no previously developed method for RDT analysis has allowed for the detection of such low parasitemias. Furthermore, the desired

detection limits were reached through modification of the current RDT diagnostic process, which has allowed our method to be simple, rapid and affordable.

Effect of Individual Donor Samples on RDT Performance

After quantifying the LOD of these brands, we focused the study to three brands (Pck, PTot and IPf) analyzing individual donor blood samples to examine the influence of individual donor background. The three brands were selected by their WHO panel detection score (PDS), which is established by the RDT brand's inter-test and inter-lot consistency.⁷³ Pck fell in the high (>90%), IPf in the medium (50-90%) and PTot in the low (10-40%) range. These three brands were tested with unextracted and extracted samples at 0, 10 and 100 parasites/ μ L to demonstrate their utility at low parasitemias. As can be observed in Figure III.5, the extracted donor samples at 100 parasites/ μ L had average signal intensities that were statistically different among brands and trended with their respective PDS. The highest signal intensities for the extracted samples

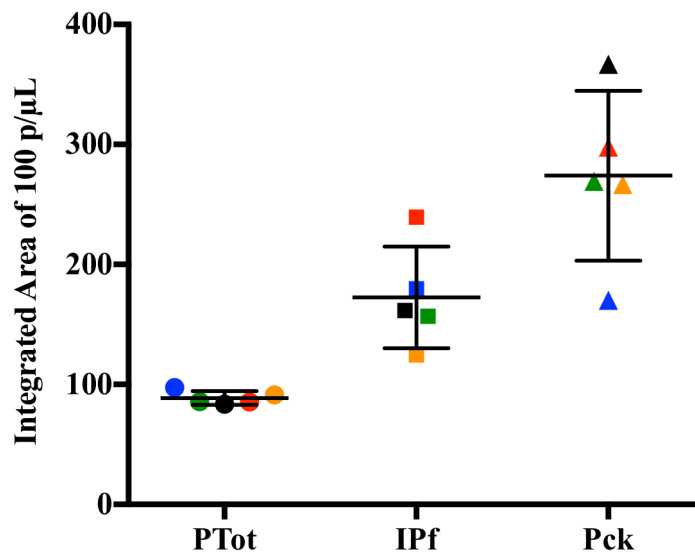


Figure III.5. Quantitative performance of three RDT brands for 100 parasites/ μ L extracted samples. Five blood donor samples were analyzed. Donor 1 (red), Donor 2 (green), Donor 3 (yellow), Donor 4 (black), Donor 5 (blue). The WHO panel detection scores for Parahit Total (PTot), ICT Pf (IPf) and Paracheck (Pck) are 35.4%, 86.9% and 96.0%, respectively.

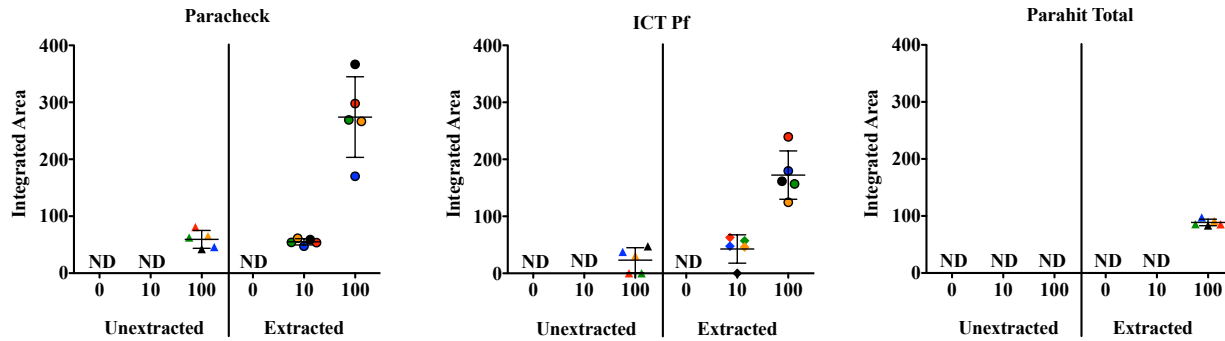


Figure III.6. Plots of the average peak areas from the RDT test lines for each surrogate patient sample, extracted and unextracted, at all parasitemias. Donor 1 (red), Donor 2 (green), Donor 3 (yellow), Donor 4 (black), Donor 5 (blue).

were observed for Pck, which had a PDS of 96.0%. Signal intensity decreased for IPf followed by PTot, whose detection scores were 86.9% and 35.4%, respectively. Generally, all samples of the same parasitemia, analyzed by the same RDT brand, experienced similar enhancements (Figure III.6). Thus, the test performance at 10 and 100 parasites/μL was not affected by individual blood donors for the three brands evaluated. As a result, any variations in signal intensity of a given RDT observed for samples with the same preparation and parasitemia were attributed to manufacturing and brand differences.

It can also be seen in Figure III.6 that when unextracted donor samples were applied to Pck, 5/5 were detected at 100 parasites/μL, while 0/5 were detected at 10 parasites/μL. When extracted donor samples were applied to Pck, 5/5 were detected at 100 and 10 parasites/μL. When unextracted donor samples were applied to IPf, 3/5 were detected at 100 parasite/μL and 0/5 were detected 10 parasites/μL. When extracted donor samples were applied to IPf, 5/5 were detected at 100 parasites/μL and 4/5 were detected at 10 parasites/μL. When unextracted donor samples were applied to PTot 0/5 were detected at 100 and 10 parasites/μL. When extracted donor samples were applied to PTot 5/5, were detected at 100 parasites/μL and 0/5 were detected at 10 parasites/μL. This data shows that sample extraction reduced the incidence of false

negative test results as more donor samples produced detectable signal when extracted than when not extracted (Figure III.6). Thus, the inclusion of the extraction step makes seemingly bad RDTs work better, by increasing signal and thus reducing false negatives. This method be invaluable to malaria management programs to enhance the performance of brands available for use.

Conclusion

We have described a method of improving existing rapid diagnostic tests for the detection of malaria by adding a simple sample preparation step prior to performing the test. Thus, this method enhances tests familiar to healthcare workers. Regardless of the panel detection scores assigned to the selected brands by the World Health Organization, we found five of six brands were improved and detected parasitemia within submicroscopic levels of infection, a regime of diagnosis that RDTs have traditionally been unable to detect. Both the visual signal and limit of detection gained a 4-fold and in some cases 100-fold enhancement. Limits of detection, after extraction, were estimated to be as low as 3 parasites/ μ L for two brands. Several labs are currently developing cell phone RDT readers, which use an algorithm similar to that described here to convert the visual test signal to a quantitative one.^{77, 81, 82} By combining our extraction technology with these developing resources, the positive impact of *p*/HRPII RDTs for malaria control could become an important tool for diagnosing symptomatic and asymptomatic carriers in low-resource settings.

Acknowledgements

Reproduced from Davis, K.M., Gibson, L. E., Haselton, F. R. and Wright, D. W. *Analyst*, **2014**, *139*, 3026-3031 – Published by The Royal Society of Chemistry and Davis, K. M. Development of Rapid Immunoassays for Improved Point-of-Care Malaria Diagnostics. Ph.D. Dissertation, Vanderbilt University, Nashville, TN, 2015.

We thank Dr. Phil Thuma and Dr. Sungano Mharakurwa for their assistance with this work. Partial support for this work was provided by the Bill and Melinda Gates Foundation Grand Challenges in Global Health: Develop Technologies that Allow Assessment of Multiple Conditions and Pathogens at Point-of-Care. Additional support was provided through the Vanderbilt-Zambia Network for Innovations in Global Health Technologies (NIH D43 TW009348). Support for K.M.D. was provided by an NSF Graduate Research Fellowship (GRFP2012095464).

CHAPTER IV

SIGNAL AMPLIFICATION WITH TETRA(4-CARBOXYPHENYL) PORPHYRIN NANOPARTICLES FOR SENSITIVE BIOMOLECULE DETECTION

Introduction

Methods for signal amplification improvements are driven by the fact that more sensitive diagnostics result from the detection of ever smaller quantities of biomarker. The problem of detecting minute amounts of nucleic acids was surmounted by the development of polymerase chain reaction (PCR) in 1980s.⁸³ In this method, through the use of a DNA polymerase, a nucleic acid sequence of interest can be exponentially replicated producing a detectable amount of biomarker. Additionally, the sensitivity and ease with which detection of protein biomarkers was performed was greatly increased by the origination of the enzyme-linked immunosorbent assay (ELISA).^{84, 85} In this assay, a detection antibody is conjugated to an enzyme, typically horseradish peroxidase, and signal amplification is achieved through the enzymatic turnover of a colorimetric substrate in the presence of peroxide.

Though the discoveries of these signal amplification methods were groundbreaking and the methods are prolifically employed, they do not solve the problems facing disease diagnosis in low-resource settings. As was seen in Chapter III, current malaria diagnostics suffer from a lack of sensitivity. While this shortcoming was surmounted by the introduction of a simple sample processing step, this method was still limited by variability in RDT manufacturing and the addition of extra user steps. So, the design of a completely new diagnostic was considered with implementation of a signal amplification detection strategy for increased sensitivity.

Unfortunately, the signal amplification methods mentioned earlier lack stability and are not cost effective, preventing their use in low-resource diagnostics. To address this problem, several signal amplification methods with increased stability have been developed. These methods include metal enhancement of gold nanoparticles by increasing the nanoparticle size,³² polymerization-based signal amplification³⁵ and nanocrystal-based signal amplification.³⁴ In the nanocrystal-based signal amplification method, Tong *et al.* reported that metal-oxide nanoparticles attached to detection antibodies produced amplification by dissolution of the nanoparticles and visualization of the metal ions through addition of a chromogenic reagent.³⁴ The result was that for every biomolecule, there were thousands of signal producing metal ions. The assay was found to be more reliable and have comparable sensitivity to ELISA.³⁴

We found nanocrystal-based signal amplification to be an intriguing method for further development and implementation into more sensitive low-resources diagnostics. So, in this work, we applied the principle of nanocrystal-based signal amplification to tetra(4-carboxylphenyl)porphyrin nanoparticles (TCPP NPs). When TCPP is incorporated into the nanoparticle structure, its inherent fluorescence is quenched. However, when the nanoparticle structure is disrupted by the addition of base, the individual TCPP molecules are released into solution and fluorescence is activated. Thus, a “fluorescent on” nanoparticle amplification system results. In addition to the signal amplification component of this system, further advantages, relative to other nanoparticle-based detection methods, include simple synthesis and bioconjugation procedures, environmentally stable reagents, and readily available instrumentation for signal readout. These advantages make this particular nanoparticle amplification strategy uniquely suited for the low resource setting. Herein, we optimized the TCPP NP method for detection of rabbit-IgG (Rab-IgG) in a standard sandwich ELISA format.

The assay was then applied to the detection of the malarial biomarker, *p*fHRP II, from a complex matrix.

Experimental

Materials

Meso-tetra(4-carboxyphenyl)porphyrin, 98% (catalog no. 07-1970), was purchased from STREM Chemicals. Tetraethyleneglycol monomethyl ether (catalog no. 4200350050), Pierce™ Sulfo-NHS-LC diazirine photoreactive crosslinker (catalog no. PI-26174), 10 kDa SnakeSkin™ dialysis tubing, 33 mm (pore size 0.45 μm) PVDF syringe filters, 0.5 mL Zeba™ Spin Desalting Columns (7K MWCO) were acquired from Fisher Scientific. Goat anti-rabbit IgG antibody (pAb) and rabbit IgG control (whole molecule) were purchased from Genscript Inc (catalog nos. A00131 and A01008 respectively). Anti-*Plasmodium falciparum* antibodies were acquired from Abcam (catalog nos. ab9206 and ab9203). *Plasmodium falciparum* D6 strain was cultured in house. Human Whole Blood (CPD) was purchased from Bioreclamation IVT (catalog no. HMWBPCPD). 1000 kDa Spectra/Por® Float-A-Lyzer® G2 dialysis devices (catalog no. G235062) and Spectra/Gel® absorbent (catalog no. 292600) were purchased from Spectrum Laboratories Inc. All other reagents were obtained from either Sigma-Aldrich or Fisher Scientific.

Instrumentation

Dynamic light scattering measurements were performed using a Malvern Instruments Nano Zetasizer. TEM images were taken using an FEI Tecnai Osiris™ transmission electron microscope, on formvar coated copper grids, at 200 kV. Nanoparticle concentration measurements were made on a ZetaView PMX110. A Spectroline handheld UV light (Model

ENF-260C) with irradiation at 365 nm was used to initiate the photoreactive crosslinker. Absorbance and fluorescence measurements were collected on a Biotek Synergy™ H4 microplate reader.

Tetra(4-carboxyphenyl)porphyrin Nanoparticle Synthesis

TCPP NPs were synthesized as previously reported.⁸⁶ Briefly, 400 μ L of a 1.56 mM solution of TCPP in THF was added to a glass vial and combined with 50 μ L of tetraethyleneglycol monomethyl ether. After stirring with a magnetic stir bar for 30 seconds, 5 mL of deionized water was quickly added. The solution was then mixed for 1 hour with a stir bar. The resulting particles were dialyzed overnight to remove excess reagents and filtered through a 0.45 μ m syringe filter to eliminate large aggregates. For larger batches of TCPP NPs the synthesis was doubled and the result was nanoparticles of the same size as a single batch.

Nanoparticle Concentration Measurements

The number of TCPP molecules within one nanoparticle was determined using a ZetaView PMX110 analyzer. This instrument employs a laser scattering video microscope for nanoparticle tracking analysis. A 1 mL sample, in DI water, was injected into the ZetaView cell. It was analyzed at 11 positions within the cell, with two cycles of readings per position. 100 nm polystyrene particles were used to calibrate the instrument. The sample was a solution of dialyzed TCPP NPs, with a known TCPP concentration (determined by $\epsilon_{415} = 170,000$ L/mol-cm). A 10,000-fold dilution was made to reach the particle concentration range required by the ZetaView instrument. After analysis, the nanoparticle concentration and TCPP concentration were known, so the number of TCPP molecules per nanoparticle could be determined.

Antibody Conjugation to TCPP Nanoparticles

Goat anti-rabbit IgG antibodies were conjugated to TCPP NPs through a sulfo-NHS-LC-diazirine photoreactive linker. The linker was attached to the antibodies according to manufacturer instructions. Then a spin column (7K MWCO) was used to exchange the modified antibodies into phosphate buffer pH 5.7. The concentration of antibody was determined by light absorption using a Take3 microvolume plate and the molar extinction coefficient of IgG at 280 nm ($\epsilon_{280} = 13.7 \text{ L/gm}\cdot\text{cm}$). For the conjugation reaction, 36 μg of modified antibody was added for every 1000 μg of TCPP (mole ratio approximately 100:1 IgG:TCPP NP). The concentration of TCPP NPs for conjugation was 130 μg TCPP/mL. This concentration was achieved through use of an absorbent. The concentration of TCPP in a nanoparticle solution was found by breaking the TCPP NPs apart into individual TCPP molecules with 0.1 M NaOH and measuring the absorbance at 415 nm ($\epsilon_{415} = 170,000 \text{ L/mol}\cdot\text{cm}$). The modified antibody solution was added to the TCPP NPs and 150 μL of this solution was added to each well of a 96-well plate. A handheld UV light was then placed on top of the plate and the solutions were irradiated at 365 nm for 20 minutes, promoting coupling of the antibody to the TCPP NPs. Excess antibody was removed through dialysis with a 1000 kDa dialysis device. Conjugation of the anti-*Plasmodium falciparum* antibody (ab9203) to the TCPP NPs was done by the same procedure except 180 μg of modified antibody was added for every 1000 μg of TCPP.

Detection of Rabbit IgG and pfHRP II with TCPP Nanoparticles

The detection of rabbit IgG control protein (Rab-IgG) with goat anti-rabbit antibody conjugated TCPP NPs (Ab-TCPP NPs) was carried out in a sandwich plate assay format. First, 100 μL of 4 $\mu\text{g}/\text{mL}$ goat anti-rabbit IgG in 1X PBS was incubated in an Immulon 96-well plate for 1 hour at room temperature. Next, the plate was washed five times with PBST (1X PBS,

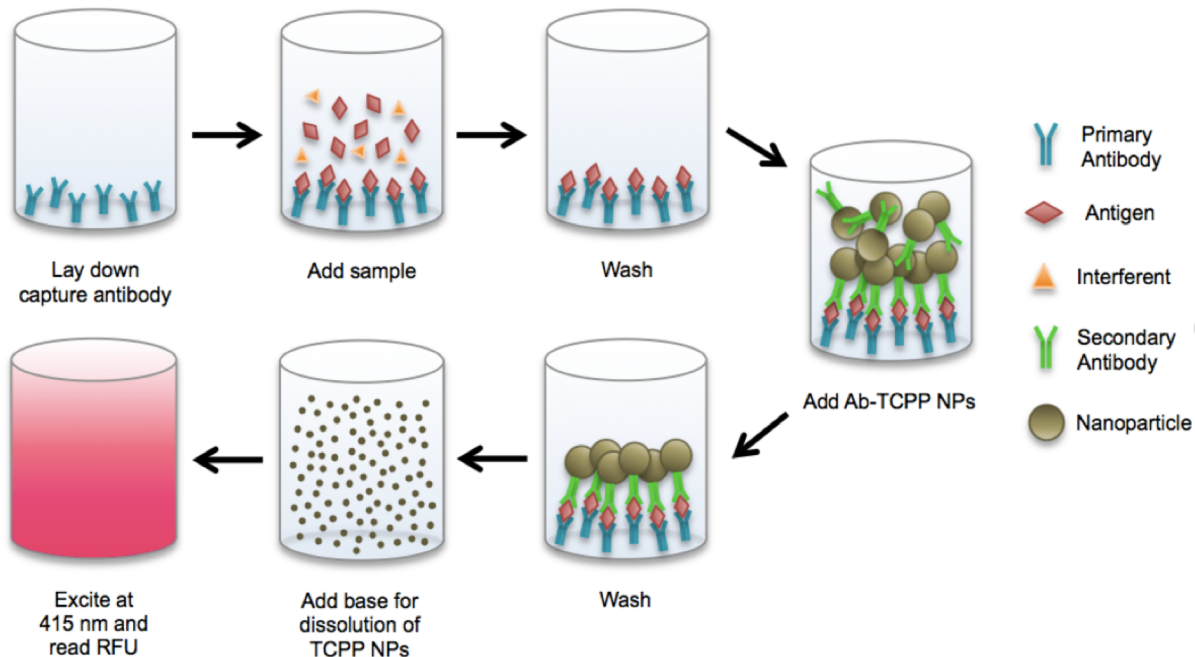


Figure IV.1. The workflow of porphyrin nanoparticle-based signal amplification sandwich assays for the detection of biomolecules.

0.1% Tween-20). The plate was then blocked by incubating 300 μL of 2% BSA in PBST on the plate for 2 hours. Afterward, the plate was again washed with PBST and then 100 μL samples of Rab-IgG in 2% BSA were added and incubated for 2 hours. The plate was then washed with PBST but the pH of the buffer was adjusted to 5.7 to prevent degradation of the Ab-TCPP NPs in the next step. Finally, 100 μL of Ab-TCPP NPs in 10% BSA, at a concentration of 100 μg TCPP/mL, were added to the plate and it was incubated on a shaker for 1 hour. Following five more washes with PBST (pH 5.7), 100 μL of 0.1 M NaOH was added to each well. After shaking the plate for 5 minutes, the solutions were transferred to a black plate and the fluorescence was read with an excitation wavelength of 415 nm and an emission wavelength of 648 nm (Figure IV.1).

Detection of *pfHRP*II was performed in a similar manner. In this assay, *pfHRP*II from *Plasmodium falciparum* culture was detected by anti-*Plasmodium falciparum* antibody conjugated TCPP NPs (*pfAb*-TCPP NPs). First, 100 μL of 2 $\mu\text{g}/\text{mL}$ anti-*Plasmodium falciparum*

capture antibody (ab9206) in 1X PBS was incubated on the plate for 1 hour. This step was followed by five washes with PBST and then the plate was blocked with 2% BSA. Next, the plate was washed and 100 μ L diluted whole blood (whole blood mixed 1:1 (v:v) with 2% BSA in 1X PBS) spiked with *Plasmodium falciparum* culture, were added and incubated for 2 hours. The plate was again washed with PBST pH 5.7, and *pf*Ab-TCPP NPs in 10% BSA were added to the plate at a concentration of 75 μ g TCPP/mL and incubated on a shaker for 1 hour. Finally, the plate was washed, 0.1 M NaOH was added and the fluorescence was read. The limit of detection was determined by the following equation: $3\sigma_{\text{blank}}/\text{slope}$.

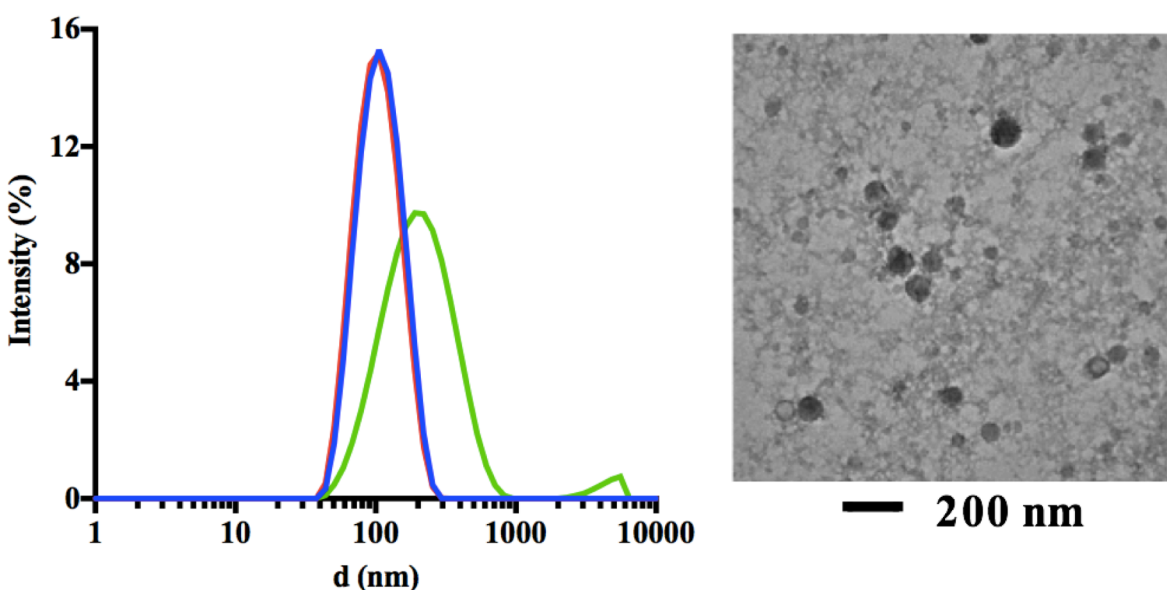


Figure IV.2. DLS size distributions of filtered (blue), concentrated (red), antibody conjugated (green) TCPP NPs (left). TEM image of TCPP NPs (right).

Results and Discussion

Characterization of TCPP Nanoparticles

TCPP NPs were synthesized as reported by Drain *et al.*^{86, 87} The NP size was evaluated by DLS and a single peak centered around 100 nm was observed. The synthesis was very reproducible as the average hydrodynamic diameter over several batches (n=14) was found to be

110 ± 9 nm with a polydispersity index of 0.11 ± 0.01 . Upon concentration of the TCPP NPs, the size distribution did not significantly change. When antibodies were coupled to TCPP NPs, an increase of approximately 75 nm in hydrodynamic diameter was seen, consistent with antibody conjugation (Figure IV.2). TEM images showed spherical nanoparticles with a background of TEGME from nanoparticles that collapsed when the sample was dried on the grid. The spherical nanoparticles have diameters within the range specified by DLS (Figure IV.2). TCPP NP size remained constant for over 60 days. After 90 days, large aggregates began to form (Figure IV.3). The number of TCPP molecules per NP was determined by finding the NP concentration with ZetaView instrumentation and the TCPP concentration by absorbance. It was determined that there was on the order of magnitude of 100,000 TCPP molecules/nanoparticle. This number highlights the advantage of this signal amplification strategy, because upon nanoparticle

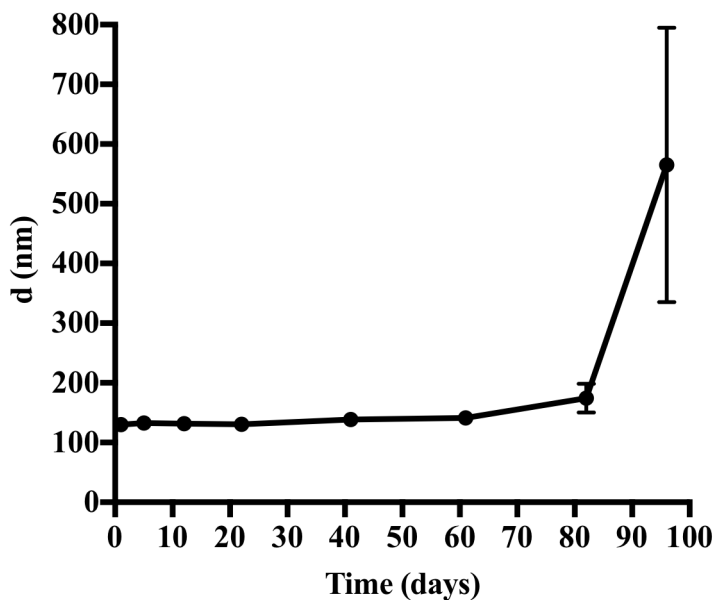


Figure IV.3. The increase in diameter of the TCPP NPs over time. Aggregation of the TCPP NPs is observed after 90 days.

dissolution there are hundreds of thousands of signal-producing, fluorescent molecules that result from one nanoparticle.

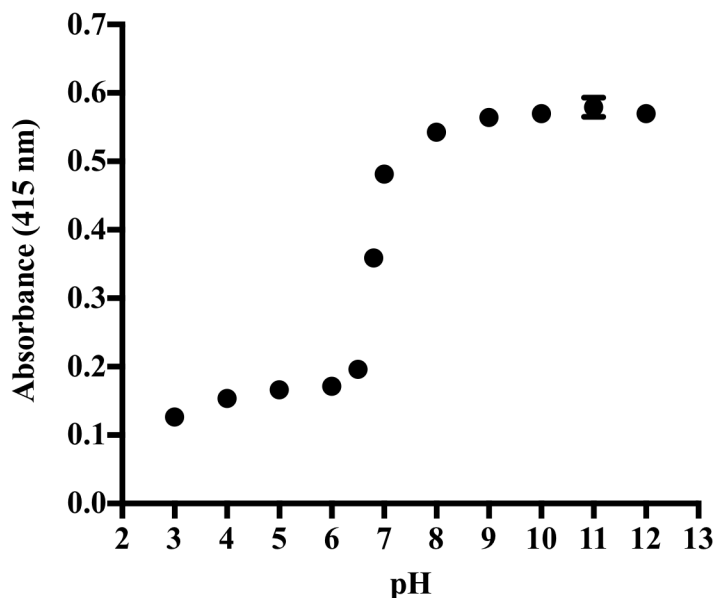


Figure IV.4. Titration curve displaying the breakdown of TCPP NPs as a function of pH.

Dissolution conditions for TCPP NPs were examined as a function of pH. TCPP NPs were placed in buffers that covered a range of pH values (citrate/phosphate pH 3-5, phosphate pH 6-8, borate pH 9-12) and the absorption of the Soret band was observed. An increase in absorption of this band indicates more, free TCPP in solution. It was found that the TCPP NPs quickly broke apart at pH 6.5 as shown in the titration curve in Figure IV.4. We conclude that the inflection point at pH 6.75 corresponds to the pKa of the carboxylic acid groups on TCPP, as it is near the value previously reported.⁸⁸ Thus, as the acid groups become deprotonated the non-covalent forces holding the particles together are disrupted. Additionally, interaction of TCPP with the solvent is increased and the result is dissolution of the TCPP NPs. Thus, nanoparticle-based signal amplification could be achieved through addition of sodium hydroxide (NaOH), for TCPP NPs.

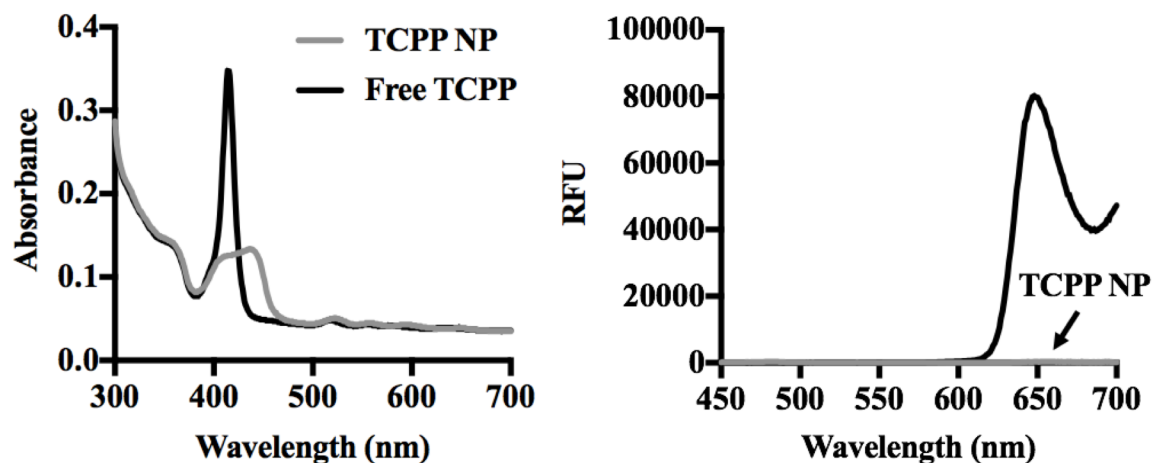


Figure IV.5. The increase in absorbance (left) and fluorescence (right) that is seen with TCPP NP dissolution by NaOH.

Optical characterization of porphyrin nanoparticles displays broadened and often split Soret bands.⁸⁶ The TCPP NP absorption spectrum revealed both of these characteristics (Figure IV.5). The direction of the shift, either hypsochromic or bathochromic, indicates the type of interactions between porphyrins in the nanoparticles. Free TCPP has a maximum wavelength of the Soret band at 415 nm. The TCPP NP spectrum showed a Soret band with a bathochromic shift, indicative of J-type aggregates (edge-to-edge interactions) of the porphyrins in the nanoparticle.^{86, 87, 89, 90}

The formation of J-aggregates in the nanoparticle reduces the absorption intensity of the Soret band. Additionally, static quenching of the porphyrin fluorescence is observed.⁹¹ Upon the addition of NaOH, which results in free porphyrin in solution, the intensity of these properties was restored and a 3-fold rise in absorption and 240-fold increase in fluorescence were seen (Figure IV.5). The magnitude of the enhancement and intensity of the fluorescent signal, upon nanoparticle dissolution, made fluorescence the best signal readout for this assay. This signal was found to be stable on the benchtop for at least 4 hours (Figure IV.6). The longevity of the

fluorescent signal increases the assay stability relative to other colorimetric products that often degrade within an hour or are light sensitive.

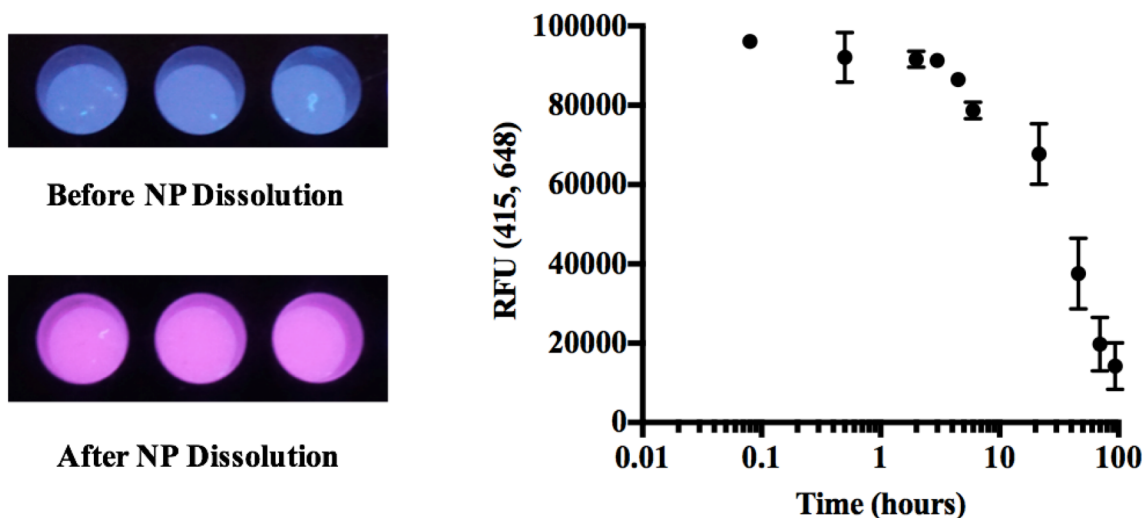


Figure IV.6. TCPP NP fluorescence before and after dissolution with base. Fluorescence is quenched in the nanoparticle form but is very strong after the dissolution to TCPP molecules (left). Degradation of the fluorescent signal of TCPP molecules in 0.1 M NaOH after TCPP NP dissolution. The fluorescent signal did not decrease for 4.5 hours when left on the benchtop (right).

Conjugation of Antibodies to TCPP Nanoparticles

To utilize TCPP NPs in an amplification strategy, an antibody was coupled to the nanoparticles to impart biomarker specificity. Studies began with the detection of a model biomarker, Rab-IgG. Anti-rabbit IgG antibody was coupled to the TCPP NPs through a photoreactive linker. The diazirine-based photoreactive linker was chosen because coupling could efficiently occur at pH 5.7, where the TCPP NPs are stable (Figure IV.4). Coupling was achieved by applying UV light to a mixture of TCPP NPs and antibodies modified with the photoreactive linker. The UV light promotes the release of nitrogen from the diazirine producing a carbene that forms a covalent bond to the nanoparticle. Carbene groups quickly react with nucleophiles, and in certain circumstances, addition to hydrocarbons occurs.⁹² Considering that the reaction between TCPP NPs and the modified antibody takes place in aqueous conditions, the

covalent bond is most likely formed between the carbene and the OH groups on the TEGME or TCPP components of the nanoparticles. Conjugation of the antibody was confirmed by detecting Rab-IgG on a plate. Fluorescent signal was observed when Rab-IgG was present, but when Rab-IgG was not present a signal was not observed. Additionally, little non-specific signal was seen, as TCPP NPs without antibodies conjugated did not show signal in the presence of Rab-IgG. Similar results were observed for TCPP NPs conjugated to anti-*Plasmodium falciparum* antibodies.

Optimization and Detection of Rabbit IgG

The TCPP NP detection method was used to detect Rab-IgG in a sandwich assay format (Figure IV.1), where a capture antibody was immobilized onto the plate, followed by a blocking step. A sample containing Rab-IgG was then added and the Rab-IgG was captured by the antibody out of the sample matrix. After capture of the biomarker the Ab-TCPP NPs were added to the plate as the detection element. After several wash steps, NaOH was added to promote dissolution of the nanoparticles. The result was signal amplification as each nanoparticle broke into hundreds of thousands of signal-producing, porphyrin molecules for each Rab-IgG protein. Release of the porphyrins from the nanoparticle matrix eliminated fluorescence quenching, so the fluorescent signal of TCPP was read without the addition of any other chromogenic reagents.

To begin the optimization of this assay, the capture antibody concentration that gave the best signal intensity while minimizing background signal was determined. Background signal can often increase with capture antibody concentration as a result of non-specific binding. 4 $\mu\text{g/mL}$ of capture antibody produced optimal signal-to-noise performance (Figure IV.7A). Additionally, a common blocking buffer containing 2% BSA was used for the assay to prevent nonspecific binding of proteins to the plate. The concentration of detection element, Ab-TCPP

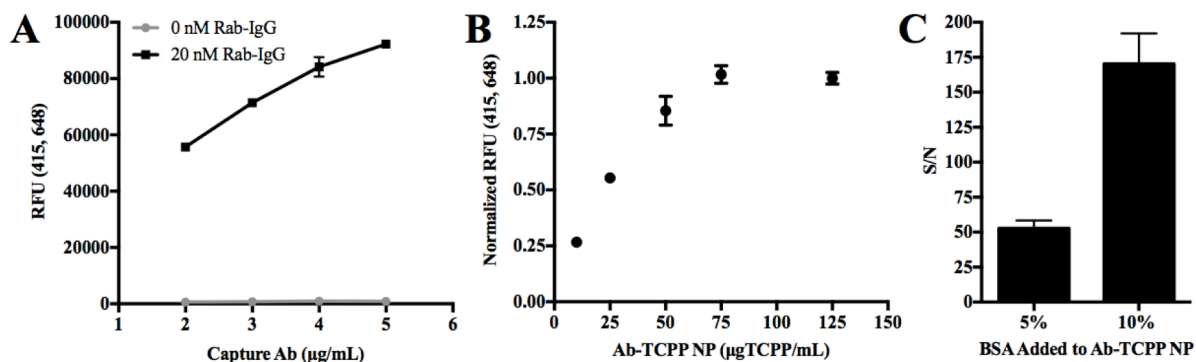


Figure IV.7. Optimization of assay conditions for the sandwich detection of Rab-IgG. Parameters analyzed include: A) capture antibody concentration, B) Ab-TCPP NP concentration and C) Ab-TCPP NP blocking. Concentrations chosen for the assay were 4 µg/mL capture antibody, 100 µg TCPP/mL and 10% BSA.

NPs, needed to achieve maximum signal was also determined. As can be seen in Figure IV.7B, the signal against constant Rab-IgG saturates at a concentration of 75 µg TCPP/mL. At this point the signal is limited by the amount of Rab-IgG in the well, not by the amount of detection element. To ensure saturation was reached, 100 µg TCPP/mL of Ab-TCPP NPs were used in the assay. Finally, blocking of the Ab-TCPP NPs was explored. It was found that increasing the amount of BSA used to block the Ab-TCPP NPs greatly improved the signal-to-noise of the assay. This observation is thought to be a result of the TCPP NPs having a weak attraction to the capture antibody but upon blocking with BSA, this nonspecific binding is eliminated. A BSA blocking concentration of 10% was used for this assay (Figure IV.7C). The optimized sandwich assay produced a linear, concentration dependent response from 10 to 1000 pM. This linear range is greater than that observed for ELISAs because enzyme catalysis is not a linear process. In contrast, when TCPP NPs are used for signal amplification, signal is dictated by the number of porphyrin molecules in solution; this is linear with respect to the number of Rab-IgG proteins until saturation of the surface area of the well occurs.³⁴ The limit of detection of the assay was found to be 2.05 ± 0.03 pM (Figure IV.8).

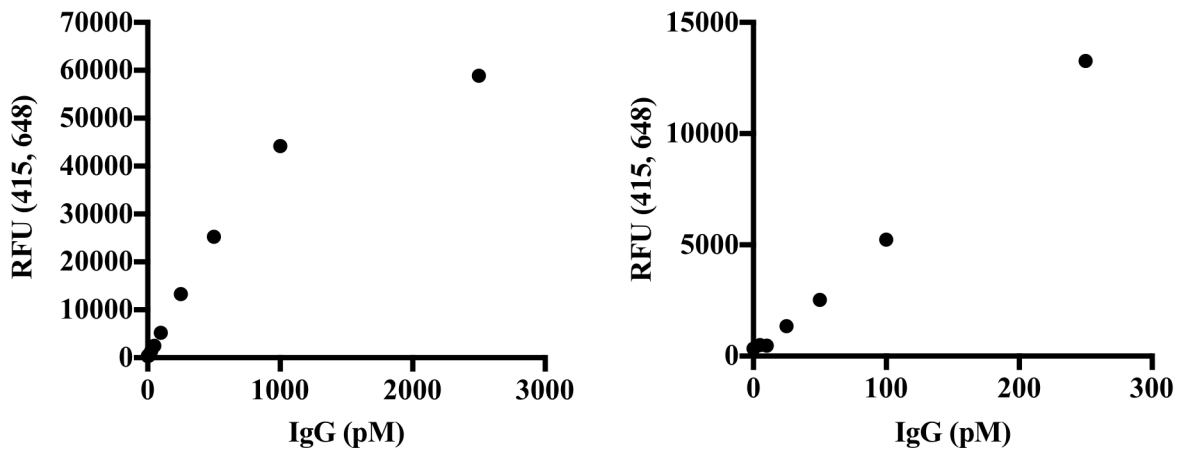


Figure IV.8. Detection of Rab-IgG using Ab-TCPP NPs in sandwich assay format. Linear concentration dependent response observed from 10-1000 pM. Full titration (left) and enlargement of low concentrations (right).

Optimization and Detection of pfHRP II in Diluted Whole Blood

pfHRP II is a standard protein biomarker of malaria, a common disease in low-resource areas of the world. In these areas, as malaria eradication campaigns have begun, it has become increasingly important to detect low-level, asymptomatic infections (<200 parasites/ μ L).

Inaccurate detection and treatment of these infections results in a reservoir of the disease. As discussed in Chapter III, commonly used rapid diagnostic tests are not a viable solution to this problem as they do not have sufficient sensitivity.⁹³ Additionally, microscopy, though it has a lower limit of detection, suffers from a high false positive rate and lack of reproducibility. Thus, the TCPP NP detection method was optimized for *pfHRP II*, as incorporation of this detection strategy into a diagnostic has the potential to produce the sensitive, stable and reproducible test needed for malaria in low-resource settings.

For development of the *pfHRP II* TCPP NP detection strategy, the relevant parameters of the sandwich plate assay were re-optimized for the detection of *pfHRP II* from *Plasmodium falciparum* culture. It was found that the best signal-to-noise performance occurred with 2 μ g/mL

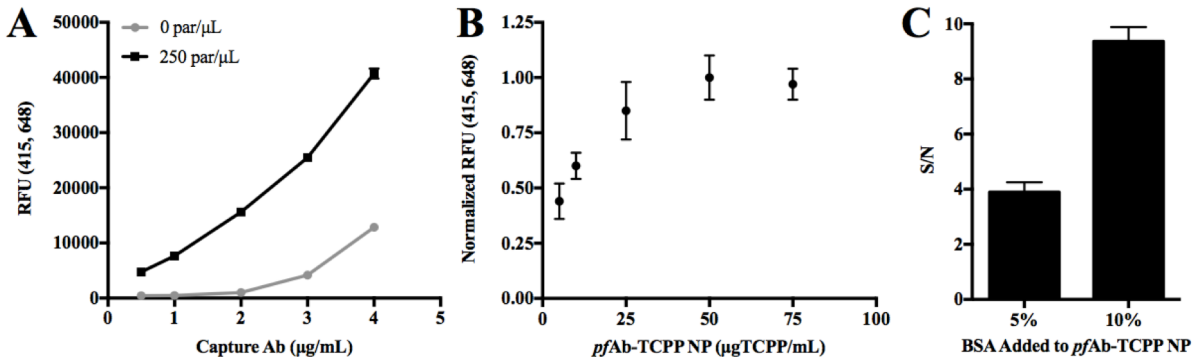


Figure IV.9. Optimization of assay conditions for the sandwich detection of *pfHRP* II. Parameters analyzed include: A) capture antibody concentration, B) *pfAb*-TCPP NP concentration, and C) *pfAb*-TCPP NP blocking. Concentrations chosen for the assay were 2 µg/mL capture antibody, 75 µg TCPP/mL and 10% BSA.

of anti-*Plasmodium falciparum* capture antibody (Figure IV.9A). Furthermore, the signal was no longer limited by the *pfAb*-TCPP NPs at 50 µg TCPP/mL, so 75 µg TCPP/mL *pfAb*-TCPP NPs were used in the assay (Figure IV.9B). Additionally, as seen with the Ab-TCPP NPs, non-specific binding of the *pfAb*-TCPP NPs was greatly reduced when the NPs were blocked with 10% BSA (Figure IV.9C).

Diluted whole blood spiked with clinically relevant amounts of *Plasmodium falciparum* culture was tested for *pfHRP* II. The assay workflow followed that of Figure IV.1. The result was an assay with a linear range of 16-250 parasites/µL and a limit of detection of 16.2 ± 0.5 parasites/µL or the equivalent of 21 pM *pfHRP* II (Figure IV.10). The assay was repeated in triplicate on four different days and the intra-assay variability (defined as the standard deviation of the triplicate divided by the mean of the triplicate) was 9%. The inter-assay variability (the standard deviation of the concentrations from the four different days divided by the mean concentration) was 16%. This data shows that the TCPP NP detection method is reproducible and has a lower limit of detection and a similar linear range to commercially available ELISA kits for *pfHRP* II.⁹⁴ Additionally, it is able to detect within the asymptomatic range of malaria

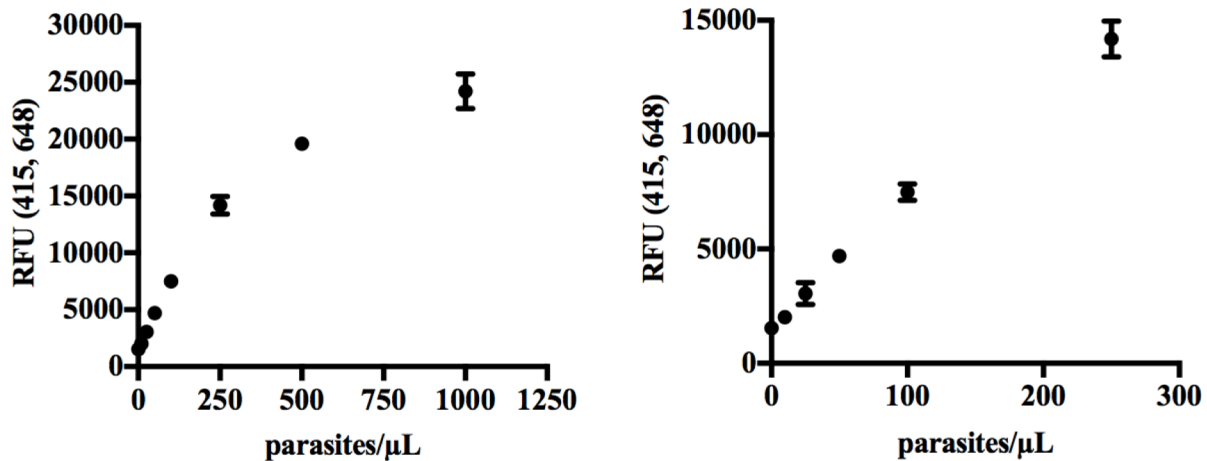


Figure IV.10. Detection of *pfHRP*II from *Plasmodium falciparum*-spiked diluted whole blood using *pfAb*-TCPP NPs. Linear concentration dependent response observed from 16-250 parasites/μL. Full titration (left) and enlargement of low concentrations (right).

infection. Thus, the TCPP NP detection method has the needed sensitivity as well as increased stability through replacement of the enzyme with a nanoparticle as the signal-generating moiety. These results show great potential for application of the TCPP NP detection method to low-resource settings. Furthermore, this detection strategy is a platform technology and can be used to detect a wide variety of biomarkers through conjugation to other antibodies. As was discussed in Chapter II, *pfHRP*II is not an ideal biomarker as it can remain in circulation days to weeks after effective treatment. If detection of different biomarker, such a *plasmodium* lactate dehydrogenase was desired, the TCPP NP detection strategy could be easily modified for this biomarker.

Conclusion

In this work, the principle of nanocrystal-based signal amplification reported by Tong et al. was employed to develop a new biomolecule detection method using TCPP NP signal amplification.³⁴ Amplification was achieved through dissolution of the TCPP NPs into hundreds of thousands of fluorescent TCPP molecules. The product was a sensitive assay that did not require the use of a protein enzyme, which makes TCPP NP detection a more stable method relative to ELISAs. The use of a porphyrin nanoparticle eliminates the susceptibility of the detection method to environmental conditions and produces a more stable signal. Furthermore, simplicity of the TCPP NP detection method relative to the original nanocrystal-based signal amplification method is increased by the inherent fluorescence of TCPP, which allows direct measurement of the assay signal without extra steps for neutralization and addition of a chromogenic reagent. Using the TCPP NP method, we were able to detect the Rab-IgG protein biomarker at low picomolar levels. Additionally, clinically relevant amounts of the malarial biomarker *p*fHRPII were detected out of diluted whole blood. This result also shows increased simplicity, as the original method was only able to detect low picomolar levels of biomolecule when multiple types of nanoparticles were added to the assay. The TCPP NP method only required one nanoparticle type. The sensitivity of the TCPP NP method, accompanied by its increased stability and simplicity relative to other methods, makes it an intriguing option for further development as a detection method for low-resource areas.

Acknowledgements

Reprinted with permission from Gibson, L. E., Wright, D. W. *Anal. Chem.*, **2016**, *88* (11), pp 5928-5933. Copyright (2016) American Chemical Society.

Partial support for this work was provided by the Bill and Melinda Gates Foundation (OPP1123092) and the Mitchum E. Warren, Jr. Graduate Research Fellowship (L.E.G.). Additionally, support for use of the Osiris TEM was provided by the National Science Foundation (NSF EPS 1004083). We would also like to thank the Vanderbilt Institute of Nanoscale Science and Engineering for access to DLS instrumentation and Dr. Alissa Weaver's lab for use of the ZetaView particle analyzer.

CHAPTER V

HEMIN NANOPARTICLE ENZYME MIMIC FOR BIOMOLECULE DETECTION IN LOW-RESOURCE SETTINGS

Introduction

Diagnostics for various applications are all plagued by one common problem: the most sensitive methods lack environmental stability. For example, the enzyme-linked immunosorbent assay (ELISA), a prevalently used protein detection assay, owes much of its sensitivity to the use of the horseradish peroxidase enzyme (HRPx) for signal generation.⁸⁴ HRPx comes from the horseradish plant and is an extremely efficient catalyst for the oxidation of colorimetric substrates.⁹⁵ As a result, signal amplification occurs in these assays because one HRPx molecule is associated with one disease molecule, but the signal results from the hundreds of thousands of colored, substrate molecules generated by HRPx. Thus, ELISAs are extensively used in disease diagnosis as they are able to detect the extremely small amounts of biomarker that are often indicative of a disease state.⁹⁶

While there are many advantages to ELISAs, there are several properties associated with the HRPx enzyme that are less than ideal. The HRPx enzyme is expensive due to challenges in production and purification. Furthermore, the activity of HRPx is very susceptible to different environmental conditions which result in the degradation of the protein.⁹⁷ While the requirement of HRPx to remain in a controlled climate is an inconvenience in modern laboratory settings, it prevents the use of the enzyme in low-resource settings, as electricity is intermittent in these

areas. Therefore, as mentioned previously, when designing more sensitive diagnostic for low-resource settings, signal amplification with HRPx is not a viable detection strategy.

As a result, many different materials have been developed that mimic HRPx through signal amplification by catalytic turnover of a substrate that are more cost effective and stable. These methods include simple inorganic materials which rely on metals for catalytic activity.⁹⁸⁻¹⁰³ Additionally, more complicated materials such as hybrid, shell or encapsulated nanoparticles have also been designed.¹⁰⁴⁻¹⁰⁷ Furthermore, supramolecular systems that aim to mimic the enzyme through incorporation of a hydrophobic environment and coordinating ligands have been developed.¹⁰⁸⁻¹¹⁰ These approaches had varying degrees of success. While they essentially all show increased stability, most are far from reaching the catalytic efficiency of HRPx. Of these materials, those that did shown comparable or improved efficiency required complicated synthesis schemes. Furthermore, complete development of these methods for protein detection from complex matrices has not been reported.

The porphyrin, hemin, is a tetrapyrrole with an iron center. This molecule serves a variety of biological functions. It is found in hemoglobin and serves as the molecular component responsible for oxygen binding.¹¹¹ It also is found in the active site of HRPx and is responsible for binding the substrate, hydrogen peroxide, for the initiation of the catalytic turnover of a colorimetric substrate.⁹⁵ It has been shown that hemin removed from the protein structure is still catalytically active.¹¹² Thus, this molecule can be used as a mimic of HRPx. The removal of hemin from the protein structure results in greater stability but also reduces catalytic efficiency.

In this chapter, we report a simple and fast synthesis for hemin nanoparticles (Hemin NP). By making nanoparticles out of hemin, we can exploit the catalytic properties of the molecule and combine thousands into one particle, compensating for the reduction in catalytic

efficiency that results from removal of the hemin from the protein structure. Thus, there are two types of signal amplification in this method. First, the nanoparticles are broken apart into their constituent hemin molecules. Consequently, one nanoparticle results in thousands of catalytic molecules. Second, each of these molecules then acts as an enzyme mimic to turnover a colorimetric substrate (Figure V.1). It is hypothesized that the combined activity of the hemin molecules in a nanoparticle would result in an enzyme mimic with comparable activity to HRPx but with increased environmental stability. Furthermore, in contrast to the fluorescent tetra(4-carboxyphenyl) porphyrin nanoparticle strategy reported in Chapter IV, an easily visualized, absorbent signal would be produced, which is ideal for low-resource settings. Thus, upon synthesis of the Hemin NPs, their size, stability and catalytic properties were characterized. Furthermore, this detection strategy was incorporated into an assay for the detection of a model protein biomarker and a malarial biomarker from a complex matrix.

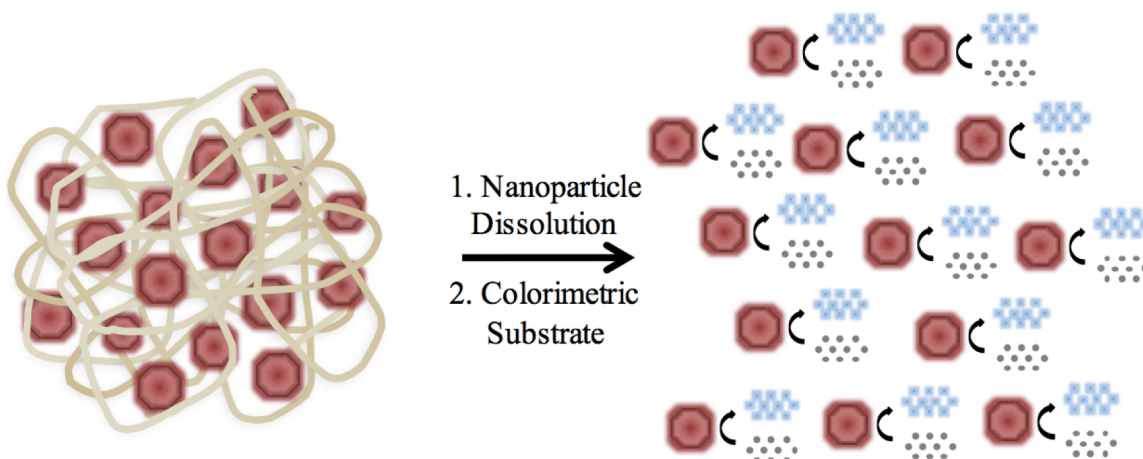


Figure V.1. The signal amplification scheme for the Hemin NP detection method. Hemin nanoparticles break apart into constituent hemin molecules, which subsequently catalytically turn over a colorimetric substrate.

Experimental

Materials

Hemin was purchased from MP Biomedicals (catalog no. 198820). Mn(III), Co(III), Cu(II), and Zn(II) protoporphyrin IX were acquired from Frontier Scientific (catalog nos. MnP562-9, Co654-9, P40769, Zn625-9). Promega 3,3',5,5'-tetramethylbenzidine (TMB) One ELISA substrate (catalog no. PR-G7431), horseradish peroxidase (HRP_x) (catalog no. P131490), Pierce™ Sulfo-NHS-LC diazirine photoreactive crosslinker (catalog no. PI-26174), 10 kDa SnakeSkin™ dialysis tubing, and 0.5 mL Zeba™ Spin Desalting Columns (7K MWCO) were purchased from Fisher Scientific. 3,3',5,5'-tetramethylbenzidine (TMB) tablets were purchased from Sigma Aldrich (catalog no. T55251000). 1000 kDa Spectra/Por® Float-A-Lyzer® G2 dialysis devices (catalog no. G235062) and Spectra/Gel® absorbent (catalog no. 292600) were acquired from Spectrum Laboratories Inc. Goat anti-rabbit IgG antibody (pAb) (catalog no. A00131), and rabbit IgG control (whole molecule) (catalog no. A01008) were purchased from Genscript Inc. Pan-malaria anti-pLDH (capture) (catalog no. 19g7) and pan-malaria anti-pLDH (conjugate) (catalog no. 1201) were acquired from Vista Diagnostics International. *Plasmodium falciparum* D6 strain was cultured in house. Human Whole Blood (CPD) was purchased from Bioreclamation IVT (catalog no. HMWBCPD). All other reagents were obtained from either Sigma-Aldrich or Fisher Scientific.

Instrumentation

Sonication during nanoparticle synthesis was carried out with an Ace Glass GEX 600-5 Ultrasonic Processor (600 Watts). Dynamic light scattering measurements were performed using a Malvern Instruments Nano Zetasizer. Nanoparticle concentration measurements were made on a ZetaView PMX110. Cyclic voltammetry measurements were made with a CH Instrument

Multichannel Analyzer with a glassy carbon working electrode, Ag/AgCl reference electrode, and a Pt wire/mesh counter electrode. A Spectroline handheld UV light (Model ENF-260C) with irradiation at 365 nm was used to initiate the photoreactive crosslinker. Absorbance measurements were collected on a Biotek Synergy™ H4 microplate reader.

Hemin Nanoparticle Synthesis

Hemin NPs were synthesized by combining 100 μL of 1.9 mM hemin in DMF with 80 μL of hexaethylene glycol monomethyl ether (HEGME). 6 mL of DI water were then quickly added to this solution followed by sonication for 2 minutes. Sonication was performed in an ice water bath, using a probe sonicator with an amplitude setting of 3%. The concentration of hemin was determined by measuring the absorbance of the Soret band in a 5% pyridine solution ($\epsilon_{405} = 92,297 \text{ L/mol}\cdot\text{cm}$). Optimization of each of these parameters is discussed in the results.

Hemin Molecules per Nanoparticle

The number of hemin molecules within one nanoparticle was determined using a ZetaView PMX110 analyzer. This instrument employs a laser scattering video microscope for nanoparticle tracking analysis. For sample analysis, a 1 mL sample in DI water was injected into the ZetaView cell. It was analyzed at 11 positions within the cell, with two cycles of readings per position. The analysis was run at 26.6 °C. The remaining settings included: sensitivity of 85, frames per second of 30, shutter speed of 70 and laser pulse duration of 3 seconds. A standard of 100 nm polystyrene particles was used to calibrate the instrument. The sample was a solution of dialyzed Hemin NPs, with a known hemin concentration (determined by $\epsilon_{405} = 92,297 \text{ L/mol}\cdot\text{cm}$ in 5% pyridine). A 10,000-fold dilution was made to reach the particle concentration range required by the ZetaView instrument. After analysis, the nanoparticle concentration and the

concentration of hemin were known, so the number of hemin molecules per nanoparticle could be calculated.

Hemin Nanoparticle Size Stability Study

Three batches of Hemin NPs were synthesized and stored at room temperature. Dynamic light scattering measurements were taken at various time points to determine how long the size and polydispersity of the particles remained constant.

Nanoparticle Synthesis Protocol for Additional Metal Protoporphyrin IX Derivatives

Nanoparticles were synthesized from other metal protoporphyrin IX (Me PPIX) derivatives besides hemin (Fe(III) PPIX), to determine if the metal center had an effect on nanoparticle formation and stability. Me PPIX analyzed included Mn(III), Co(III), Cu(II), and Zn(II) PPIX. These nanoparticles were synthesized by the same procedure used for Hemin NPs. Concentrations of each porphyrin were found under the following conditions: Mn(III) PPIX, $\epsilon_{462} = 25,000$; Fe(III) PPIX, $\epsilon_{385} = 58,400$; Co(III) PPIX, $\epsilon_{416} = 93,000$; Cu(II) PPIX, $\epsilon_{388} = 64,000$; and Zn(II) PPIX, $\epsilon_{412} = 87,400$ (all molar extinction coefficients are in units of L/mol-cm). The solvent used for determination of concentration for Fe(III), Mn(III) and Zn(II) derivatives was 0.1 M NaOH and 0.1 M Tris-Acetate buffer pH = 7.9 was used for Co(III) and Cu(II) derivatives. The concentration of each porphyrin solution in DMF, before addition to the nanoparticle synthesis reaction, was 1.7 mM. The resulting particles were analyzed by UV-Vis absorption spectroscopy and DLS (Table SI V.1).

pH and Temperature Stability Studies

The stability of the Hemin NPs from pH = 3-9 was analyzed by adding 30 μ L of nanoparticles to 170 μ L of the specified buffer. Solutions were then mixed for 5 minutes and the absorption spectrum taken. For pH = 3-5, citrate-phosphate buffer was used; pH = 6-8, phosphate

buffer; pH = 9-12, borate buffer. The pH dependent DLS samples were analyzed in buffers corresponding with the specified pH. The stability of the Hemin NPs at different temperatures was determined by DLS. The instrument was programmed to analyze the nanoparticles from 20°C-80°C. The Hemin NP sample was kept at the specified temperature for 20 minutes before size analysis.

Ligand Optimization for Catalytic Turnover

Dialyzed Hemin NPs were combined with each ligand in 200 mM PB pH = 7. Final concentrations were 0.3 M ligand and 200 nM hemin. 100 μ L of TMB-One was added and the absorbance was read at 650 nm every 30 seconds for 20 minutes. The same procedure was followed for the optimization of pyridine concentration, except pyridine solutions were made in 10 mM borate buffer pH=8 and the final hemin concentration was 300 nM. Absorbance was read after 10 minutes.

Cyclic Voltammetry of Hemin-Pyridine Complex

For the analysis of the hemin-pyridine complex by cyclic voltammetry, the working, reference and counter electrodes were rinsed in DI water before each experiment. The counter electrode was also flame cleaned. Samples with less than 30% pyridine contained 0.5 M NaNO₃, 30% v/v 190 proof ethanol, 0.05 M Tris buffer pH 8.0, 0.5-1.0 mM hemin and the specified concentration of pyridine. These solutions were made in a 25 mL volumetric flask and additional volume was filled with DI water. If a solution contained greater than 30% pyridine, then the same procedure was used except the ethanol concentration was 10% v/v. Measurements were made after degassing the solution for 20 minutes. The solution was then immediately added to the test cell and the electrodes immersed. The experiment was run in the negative direction from 0.4 V to -0.8 V to 0.4 V with a scan rate of 0.1 V/sec and a sensitivity of 1×10^{-5} A.

Kinetic Analysis

The catalytic properties of HRPx and Hemin NPs were examined with respect to the substrates hydrogen peroxide (H_2O_2) and TMB and then compared. The solvent for all TMB solutions was 10% DMSO in citrate-phosphate buffer as specified by the manufacturer. When HRPx was analyzed with respect to H_2O_2 , TMB was held constant at 0.4 mM and HRPx at 0.25 mM. When HRPx was analyzed with respect to TMB, H_2O_2 was held constant at 1 mM (final concentrations). The following volumes of each component were combined for a total reaction volume of 200 μL : 190 μL TMB, 8 μL H_2O_2 and 2 μL HRPx. The reaction was immediately analyzed by measuring the absorbance at 650 nm over time, with continuous plate shaking.

The catalytic properties of Hemin NPs were analyzed with pyridine in the same way except for the following modifications. Final concentration of pyridine was 0.3 M and that of hemin (from the Hemin NPs) was 42.8 nM. TMB was held constant at 0.4 mM when performing the analysis with respect to H_2O_2 , and H_2O_2 was held constant at 20 mM when analyzing with respect to TMB. The total volume of 200 μL was divided in the following way: 190 μL TMB, 2 μL H_2O_2 , 5 μL pyridine and 3 μL Hemin NPs.

When Hemin NP catalytic properties were analyzed without pyridine, the final concentration of hemin was 3.9 μM . The concentration of TMB was held constant at 0.4 mM when analyzing with respect to H_2O_2 and the H_2O_2 concentration held constant at 500 mM when analyzing with respect to TMB. In this experiment, the component volumes for the 200 μL reaction were 145 μL TMB, 10.5 μL H_2O_2 and 44.5 μL Hemin NPs. The final concentration of DMSO in the wells was 9.5% to align with the other kinetic experiments.

Kinetic data was acquired by measuring absorbance over time at different substrate concentrations. To determine kinetic properties, velocity curves were generated by first taking

these absorbance values and converting them to concentration of product through the molar absorptivity of TMB ($\epsilon_{650} = 39,000 \text{ L/mol}\cdot\text{cm}$). These concentration values were plotted versus time.¹¹³ The slope of the linear portion of these plots (the velocity) was then determined and plotted again the substrate concentration. The resulting plots were then fit to a Michaelis–Menten model using Prism software and k_{cat} and K_{M} were determined. Catalytic efficiency was defined as the ratio of the two.

Stability of Hemin Nanoparticle Catalytic Properties

Kinetic stability of the Hemin NPs was determined by storing the nanoparticles in the dark, at room temperature. At specified time points, portions of the nanoparticles were removed from the stock and analyzed for catalytic activity. Final concentrations of reactants were 42.8 nM hemin, 20 mM H_2O_2 , 0.4 M TMB and 0.3 M pyridine. The absorbance was read after 1.5 minutes at 650 nm. HRPx stability was analyzed by storing a 25 nM HRPx solution in a drawer. It was then analyzed at specific time points with reaction conditions of 2.27 nM HRPx combined with 100 μL of TMB-One. After 10 minutes the reaction was stopped with 2M H_2SO_4 and the absorbance read at 450 nm.

Detection of Rabbit IgG

Antibodies were conjugated to Hemin NPs for a protein detection assay. The conjugation of the antibody was carried out as previously reported.¹¹⁴ Briefly, a diazirine-based photoreactive linker was used for conjugation. The ratio of Hemin NPs to anti-rabbit IgG antibody (A00131) was 17 μg of anti-rabbit IgG antibody per 100 μg of hemin (mole ratio approximately 40:1 IgG:Hemin NP). The amount of hemin was determined by adding 5 μL of Hemin NPs to 195 μL of 5% pyridine. The absorbance of the solution was read at 405 nm ($\epsilon_{405} = 92,297 \text{ L/mol}\cdot\text{cm}$). After conjugation, the particles were dialyzed at 4°C to remove any excess antibody or reagents.

The plate assay for detection of the model biomarker, rabbit-IgG (Rab-IgG), was carried out according to the following procedure. In a 96-well Immulon plate, 100 μL of goat anti-rabbit IgG at 4 $\mu\text{g}/\text{mL}$ was immobilized in each well and incubated for 1 hour. The plate was then blocked with 300 μL of 1% BSA in PBST (1X PBS, 0.1% Tween-20) and incubated for 2 hours. 100 μL samples of Rab-IgG, in 1X PBS with 2% BSA, were then added and incubated 2 hours. In the detection step, 100 μL of anti-rabbit IgG conjugated Hemin NPs (Ab-Hemin NP) were added at a concentration of 40 μg hemin/ mL in 7% BSA and incubated on a shaker for 1 hour. After each of these steps the plate was washed 5 times with PBST. Following the last wash, 50 μL of 0.9 M pyridine in 10 mM borate buffer pH 8 was added and the plate shaken for an additional 5 minutes. Finally, 100 μL of TMB-One spiked with H_2O_2 to a final concentration of 8 mM was added and the absorbance was read at 650 nm after 4 minutes. All incubations were performed at room temperature.

For comparison, an identical assay was performed using HRPx conjugated anti-rabbit IgG as the detection element. To determine how much HRPx detection element to add to the assay, the number of Ab-Hemin NPs added per well was found based upon one Hemin NP containing 60,000 hemin molecules. The result was 6×10^{10} nanoparticles/well, so this number of HRPx anti-rabbit IgG molecules were added to each well. As a result, concentration of reagents used in this assay were: 4 $\mu\text{g}/\text{mL}$ anti-rabbit IgG for capture, 1% BSA in PBST for blocking, Rab-IgG samples in 2% BSA, 0.16 $\mu\text{g}/\text{mL}$ of HRPx anti-rabbit IgG in 7% BSA for detection. Absorbance at 650 nm was read after 4 minutes.

Detection of Plasmodium Lactate Dehydrogenase

Antibodies were coupled to Hemin NPs for detection of *pLDH* at the ratio of 32 μg anti-*pLDH* antibody (1209) for every 100 μg of hemin. These anti-*pLDH* Hemin NPs (*pLDH*-Hemin

NPs) were then used in a plate assay for detection of *p*LDH. The assay was performed as the Rab-IgG assay but with the following modifications. Capture antibody (19g7) was added at a concentration of 1 $\mu\text{g}/\text{mL}$ and the plate was blocked with 1% BSA in PBST. Samples were prepared in lysed whole blood (1:1 v/v whole blood:lysis buffer (100 mM PB pH=8, 300 mM NaCl, 2% Triton X-100)). The blood was then spiked with parasite culture to the specified concentration. In this culture, 1 parasite/ μL was equal to approximately 5 pM *p*LDH. After incubation of these samples, *p*LDH-Hemin NPs were added at 40 μg hemin/mL in 12% BSA. Finally, pyridine and the TMB-One substrate were added for signal generation.

Results and Discussion

Hemin Nanoparticle Synthesis

Nanoparticles made of the porphyrin, hemin (Fe(III) PPIX), were synthesized in the hope of developing an alternative detection strategy to the horseradish peroxidase enzyme (HRPx). HRPx is prevalently used in enzyme-linked immunosorbent assays (ELISA) for protein detection. These assays have great sensitivity as a result of the catalytic efficiency of HRPx in the turnover of colorimetric substrates producing signal amplification in the assay. As mentioned previously, HRPx is sensitive to heat, light, pH and other environmental conditions and as such is not practical for low-resource settings.⁹⁷ Hemin, found in the active site of HRPx, can also turnover a colorimetric substrate, so nanoparticles made from this molecule could result in a detection strategy that employs signal amplification but is environmentally stable. In a Hemin NP detection strategy, signal amplification would occur in two ways. In the first, Hemin NPs would be broken apart into individual hemin molecules, producing tens of thousands of signal-

generating, hemin molecules from one nanoparticle. Secondly, each of these hemin molecules would catalytically turnover a colorimetric substrate, amplifying the signal once again.

To develop this detection strategy, a synthesis method was optimized for 100 nm Hemin NPs. This synthesis was based upon the mixed solvent method, which has been previously reported for the synthesis of other porphyrin nanoparticles.⁸⁶ In this method, the porphyrin is dissolved in an organic solvent with a polyethylene glycol (PEG) stabilizer. The addition of a relatively large amount of water then forces the interaction of the porphyrin molecules with each other and these aggregates are stabilized by the PEG. Energy is then applied to the solution, in the form of mixing, resulting in a monodisperse solution of nanoparticles.⁸⁷ To our knowledge, Hemin NPs have never been synthesized using this method, so a protocol was developed.

The first parameter that was optimized was the mixing method. It was necessary to find a mixing method that was reproducible and also sufficiently strong to produce particles in the desired 100 nm size range. A probe sonicator was chosen as it provided consistent and sufficient energy. In general, nanoparticles composed of metal porphyrins require higher energy mixing than free porphyrin nanoparticles, as a result of the additional interactions introduced by the metal ions.⁸⁶ The optimum energy setting for the sonicator was found by varying the amplitude between 3% and 15%. It was found that with greater amplitude the particles size decreased but the polydispersity increased (Figure V.2A). Since previous experiments had shown low polydispersity to be the best indicator of nanoparticle stability, an amplitude of 3% was used for all further syntheses. The time of sonication was also examined but it was found to have no significant effect on particle size or polydispersity. Sonication for 2 minutes was found to be the most reproducible, so this parameter was used in the remaining syntheses (Figure V.2B).

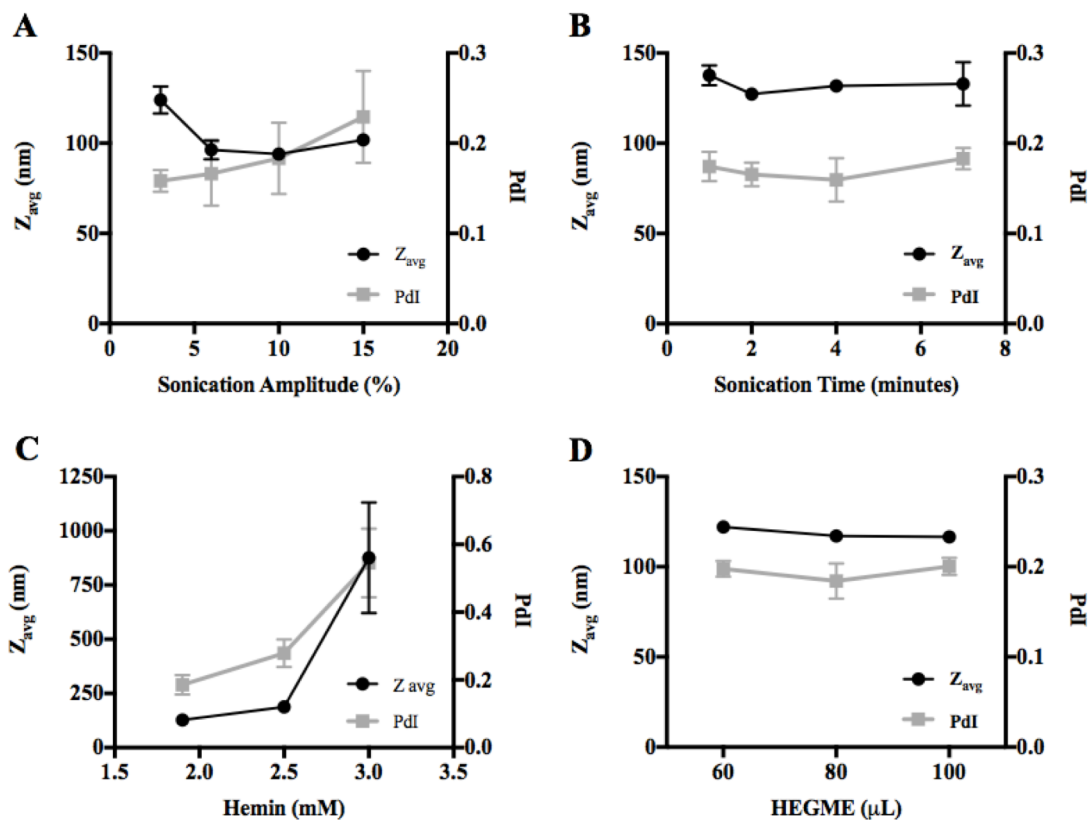


Figure V.2. Hemin nanoparticle synthesis optimization. A) Energy of mixing for synthesis. Sonication amplitude of 3% was chosen. B) Mixing time. Sonication time of 2 minutes was selected. C) Concentration of hemin added to synthesis. 1.9 mM hemin was chosen. D) Volume of stabilizer added to synthesis. 80 μ L of hexaethylene glycol monomethyl ether resulted in the most stable particles.

The concentration of hemin added to the reaction mixture was also optimized. Hemin concentrations between 1.9 mM and 3.0 mM were tested with 60 μ L of HEGME. It was observed that adding higher concentrations of hemin resulted in larger particles (Figure V.2C). The larger particles quickly fell out of solution indicating greater concentrations of hemin did not necessarily produce bigger particles but instead unstable particles that quickly aggregated. Furthermore, the amount of HEGME added to the reaction mixture was explored. The volumes of HEGME tested were 60, 80 and 100 μ L with 1.9 mM hemin. It was found that the particle size did not significantly change between these samples (Figure V.2D). Analysis of long term

stability showed that the particles made with 60 μL or 100 μL of HEGME fell out of solution within 20 days, while the Hemin NPs made with 80 μL HEGME remained stable. Thus, 80 μL of HEGME per 100 μL of 1.9 mM hemin in DMF was selected for all future syntheses.

Hexaethylene glycol, a stabilizer similar in structure to HEGME, was explored as a more cost-effective alternative for this synthesis. Unfortunately, use of this stabilizer resulted in large, polydisperse particles (Figure SI V.1). It has been previously observed that changing the type of stabilizer has a significant effect on nanoparticle synthesis when the porphyrin used has polar substituents. This is so because of greater interactions between the porphyrin, stabilizer and solvent. Since hemin contains polar substituents, it likely has significant interaction with the stabilizer which would explain the large effect the type of stabilizer had on the Hemin NP size⁸⁶.

It was also determined whether the temperature at which the synthesis was performed had an effect on Hemin NP size. The synthesis was performed at 0°C, 22°C and 50°C and no difference in nanoparticle size or polydispersity was observed (Figure SI V.2). Furthermore, scale up of the synthesis was tested. It was found that a 1.5x scale-up resulted in larger particles with greater polydispersity (Figure SI V.3). Thus, only 6 mL Hemin NPs batches were made in this study.

Using the optimized conditions of 100 μL of 1.9 mM hemin with 80 μL of HEGME and 6 mL of water at 0°C, the resulting Hemin NPs had a diameter of 110 ± 10 nm and $\text{PDI} = 0.20 \pm 0.03$ ($n = 10$) (Figure V.3). The number of hemin molecules per nanoparticle was determined through finding the particle concentration in a sample with a known hemin concentration using a ZetaView particle analyzer. It was found that there were approximately 60,000 hemin molecules/nanoparticle. This number indicates that a large amplification should be achieved through dissolution of the nanoparticles. Optical analysis of the Hemin NPs showed an

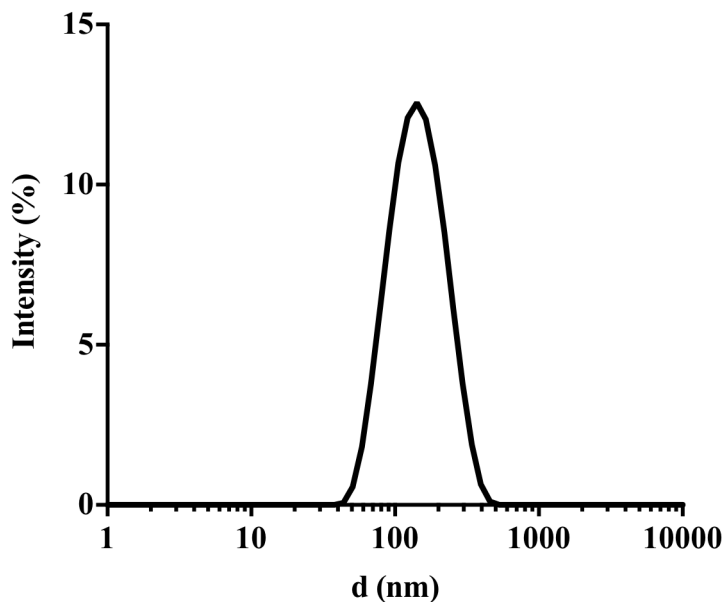


Figure V.3. Size distribution of Hemin NPs from the optimized synthesis procedure. These particles have a diameter of 110 ± 10 nm and polydispersity of 0.20 ± 0.03 .

absorbance spectrum with a broadened Soret band ($\lambda \approx 400$ nm) compared to free hemin (Table SI V.1). This broadening is a result of the interactions of the hemin molecules with each other producing a wider range of absorbed wavelengths. Thus, a broadened Soret band is indicative of nanoparticles and a sharp Soret band of free hemin.

Lastly, it has been previously reported that the identity of the metal ion in the porphyrin affects nanoparticle formation.⁸⁶ To explore this result in our system, nanoparticles were synthesized from the following PPIX derivatives: Mn(III) PPIX, Co(III) PPIX, Cu(II) PPIX and Zn(II) PPIX. The optical properties and size of the particles were then analyzed. Absorbance spectra showed broadened Soret bands for all particles. In the DLS analysis, a difference in particle size was seen corresponding to the oxidation state of the metal. Co(III) PPIX formed almost identical nanoparticles to hemin (Fe(III) PPIX). Mn(III) PPIX nanoparticles were larger than these particles but showed a similar size distribution. On the other hand, Zn(II) PPIX nanoparticles were much smaller with greater polydispersity. Cu(II) PPIX did not form stable

particles, as replicates varied greatly and the polydispersity was close to 1.0 (Table SI V.1). We hypothesize that the oxidation state affects the interplanar distance between the porphyrins upon pi-stacking. As a result, since interactions between the porphyrin molecules has change, re-optimization of the method is required for synthesis of stable nanoparticles from porphyrins with metal centers in the lower (+2) oxidation state.

Stability of Hemin Nanoparticles

The size stability of Hemin NPs was examined through analysis of the particles by dynamic light scatter at different time points. The nanoparticles were stored in solution, at room temperature. It was found that Hemin NP size remained stable for 57 days. By day 70, the Hemin NPs had fallen out of solution. Thus, these particles show great stability as they remain suspended in aqueous solution, when stored at room temperature, for nearly 2 months (Figure SI V.4).

It has been previously reported that basic conditions can result in the dissolution of porphyrin nanoparticles.¹¹⁴ To determine the pH stability of Hemin NPs, the absorbance spectrum of the particles was recorded in solutions of different pH. It was seen that the sharpness of the Soret band increased as the pH increased, indicating a decrease in aggregation of the hemin molecules. This increase in absorbance occurred at three distinct points (Figure V.4). The first was at pH 3-4, where the Soret band was broadened and the intensity of the absorbance was very low. From pH = 5-9, the intensity of the absorbance increased, while the shape of the spectrum remained the same. Finally, at pH = 10-12, a sharp peak Soret band began to be visible. The Hemin NPs were then analyzed by DLS at pH = 3, 7 and 10, to see if there was a change in particle size that corresponded with the absorption spectrum. It was seen that the Hemin NPs form large aggregates (1 μm) at pH = 3, which would be expected as absorbance intensity is

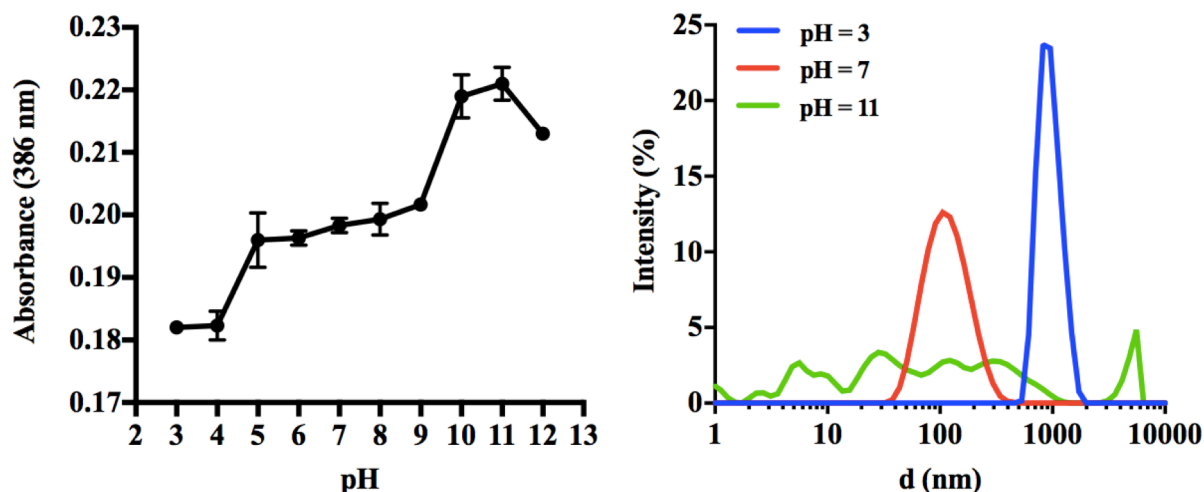


Figure V.4. The pH stability of Hemin NPs. Hemin NPs were placed in solutions of different pH and absorption of the Soret band was measured. As pH increased the absorbance the Soret band also increased (left). The size of the Hemin NPs was analyzed in acidic, neutral and basic environments and dissolution of the nanoparticles was observed at pH = 11 (right).

known to decrease with aggregation. At pH = 7, the Hemin NP size was around 100 nm as previously observed. The reduced aggregation accounts for the observed increase in absorbance. Finally, at pH = 11, the DLS spectrum did not show a clear size distribution pointing to the dissolution of the Hemin NPs which corresponds to the sharp Soret band seen in the absorption spectrum. We conclude that the Hemin NPs are stable up to pH = 9, after which they fall apart. This would be expected as previous reports have shown hemin to be soluble in aqueous conditions around pH = 9.5.¹¹⁵ At this point, the carboxylic acid groups are deprotonated and the chloride ion on the iron center has been replaced by a hydroxyl group.¹¹⁶ This result demonstrates that Hemin NPs are more pH stable than the free base porphyrin NPs analyzed in Chapter IV.

The size stability of Hemin NPs at different temperatures was also explored. It was seen that when incubated for 20 minutes at various temperatures, the size of the nanoparticles remained constant, even at 80°C (Figure SI V.5). This result indicates the capacity of Hemin NPs to remain stable even in harsh environmental conditions.

Hemin-Pyridine Catalytic Complex

The Hemin NP synthesis was developed in order to create a material which could mimic the signal amplification properties of HRPx but have increased stability. Once stable Hemin NPs were synthesized, their catalytic properties were explored. First, the ability of Hemin NPs to turn over a colorimetric substrate was determined. This property was tested by combining the Hemin NPs with a commercially available TMB substrate that contains hydrogen peroxide and measuring the absorbance over time. This turnover was tested without addition of a ligand and with addition of the following ligands: histidine, pyridine and imidazole. These specific ligands were tested because previous reports have demonstrated they increase the catalytic activity of hemin.^{108, 112, 117} This is so, because these ligands mimic the histidine residue found in the active site of HRPx (Figure V.5).¹¹⁸ In the active site, this histidine residue stabilizes the iron center of hemin for the formation of compound 1, the species responsible for oxidation of the colorimetric

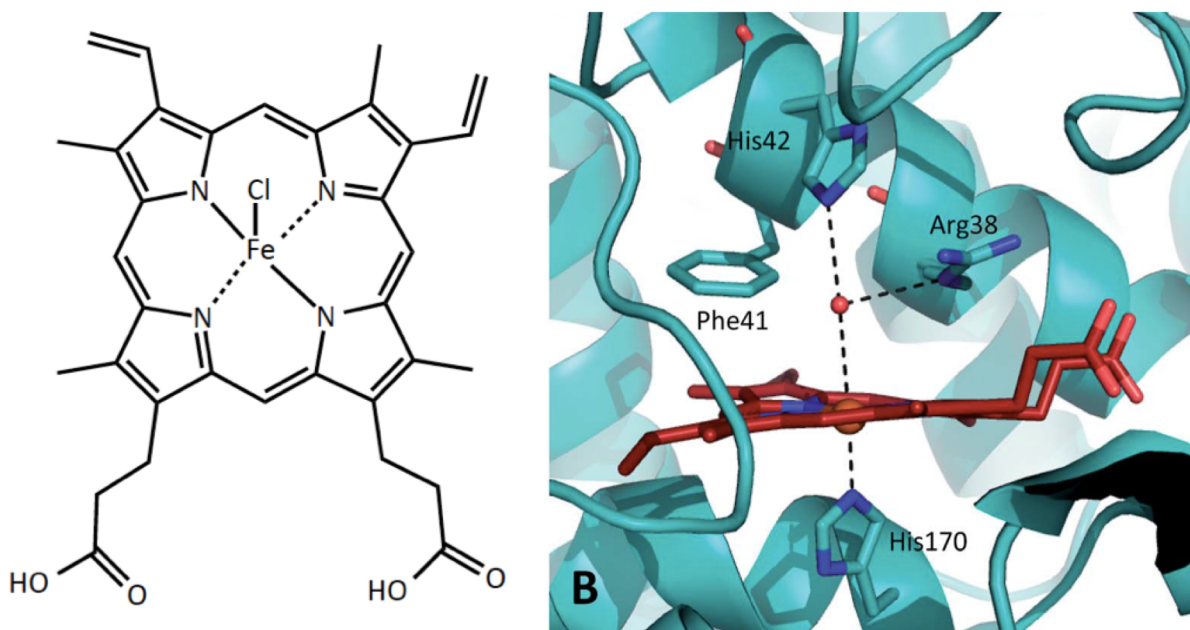


Figure V.5. Structure of the hemin molecule (left). The active site of the horseradish peroxidase enzyme. It can be seen that the iron center of the hemin molecule (in red) is stabilized by a histidine residue (right).¹¹⁸

substrate (Figure SI V.6).¹¹⁹ Thus, introducing these ligands to a solution of Hemin NPs provides stabilization of the intermediate species required for substrate turnover.

It was found that the turnover of the colorimetric substrate by Hemin NPs significantly increased with the addition of the ligands. Pyridine was found to have the largest impact on the turnover, and maximum turnover was observed with 2.4% (0.3 M) pyridine (Figure V.6). The addition of pyridine promotes dissolution of the Hemin NPs, the first type of signal amplification in this method (Figure SI V.7). Thus, this ligand break the Hemin NPs apart and assists in the catalytic turnover of the substrate.

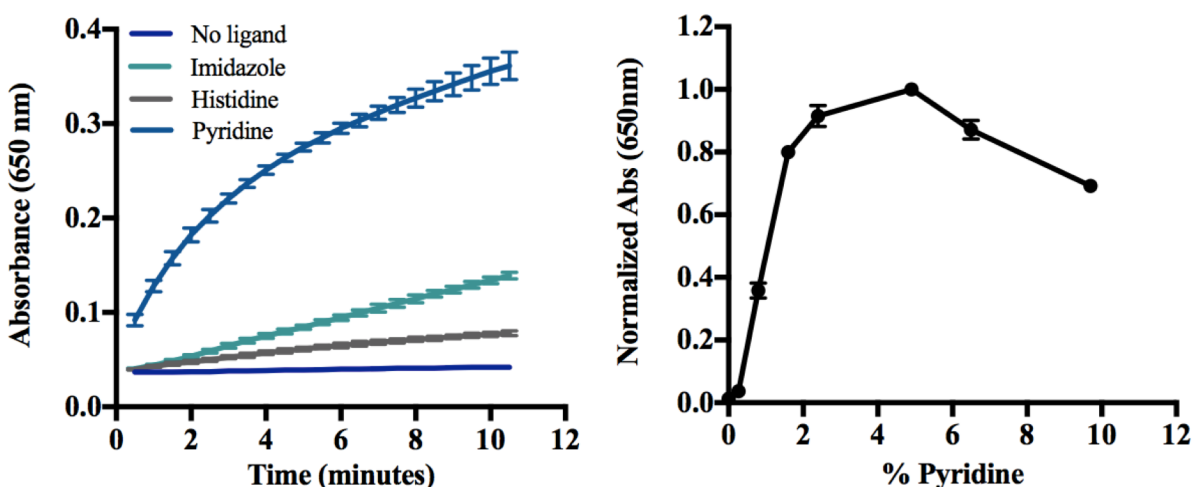


Figure V.6. Turnover of a colorimetric substrate (3,3',5,5'-tetramethylbenzidine) in the presence of various ligands (left). The greatest turnover was seen with pyridine. The concentration of pyridine that resulted in the best turnover was 2.4% (right).

The complex formed upon addition of pyridine to the Hemin NPs was further characterized to determine whether the iron center of hemin is mono or bis-ligated by pyridine. A bis-ligated species would be expected to have minimal catalytic turnover as the hydrogen peroxide binding site would be blocked by pyridine. Conversely the mono-ligated species would allow for hydrogen peroxide binding with a stabilized metal center. Since catalytic activity was observed, it was expected that the mono-ligated species was formed. Nonetheless, the amount of

pyridine added (2.4%) was in large molar excess to hemin, so the formation of the bis-ligated species was plausible. Therefore, the complex was analyzed further.

Literature reports have examined the hemin-pyridine complex in aqueous solutions by proton NMR. In these reports, the methyl resonances of the complex were monitored as increasing amounts of water were added to pyridine solutions containing hemin. It was found that in aqueous pyridine solutions containing 50% or less pyridine, the primary complex present in solution was mono-ligated with pyridine, and a water molecule was coordinated to the other side of iron center (aqua-pyridine complex). In solutions with more than 50% pyridine, a mixture of species were found, including the bis-ligated pyridine species and the aqua-pyridine complex.^{120, 121} These reports indicate that the catalytic complex observed in our system, at 2.4% pyridine, is mono-ligated. This hypothesis was further explored through analysis of the optical and electrochemical properties of the complex.

The absorbance spectrum of Hemin NPs was measured in the presence of aqueous pyridine solutions. When hemin is in the nanoparticle, it is aggregated, producing a broad absorption band. Upon addition of the ligand, pi-pi interactions between porphyrin molecules are reduced resulting in deaggregation of the molecules and a corresponding sharp absorption band.⁸⁹ Consequently, this band likely corresponds to breakdown of the Hemin NPs and binding of the pyridine to hemin. The sharp absorption band at 410 nm became visible at 1.0% pyridine and its maximum was reached at 7.2% pyridine (Figure V.7). We hypothesize that this range corresponds to mono-ligation of the hemin molecules with pyridine, forming the aqua-pyridine complex. Thus, the majority of hemin molecules are coordinated to one pyridine once a concentration of 7.2% pyridine is reached. Since the Hemin NP catalytic reaction is carried out at 2.4% pyridine, it follows that the catalytic complex is mono-ligated.

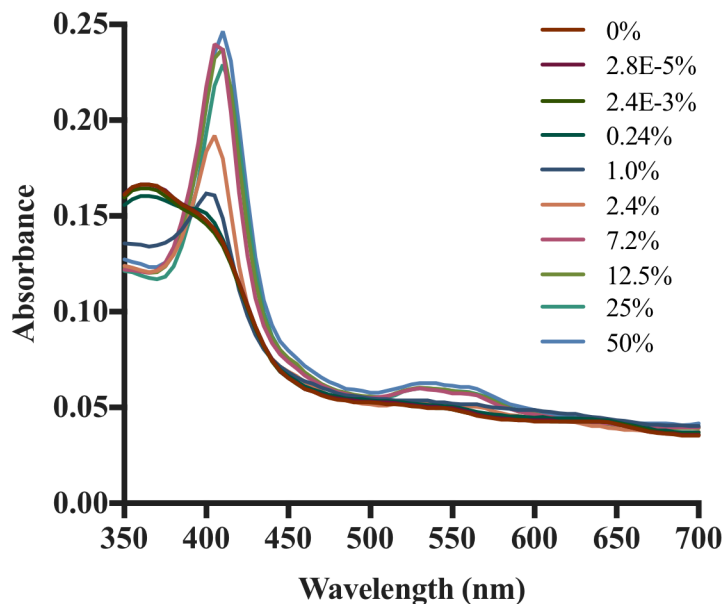


Figure V.7. The absorbance spectrum of Hemin NPs at various concentrations of pyridine. It can be seen there is an increasing sharpness of the Soret band with increasing pyridine concentration.

The hemin-pyridine complex was also analyzed by cyclic voltammetry, as ligand binding to the iron center affects its electrochemical properties. In these analyses, solutions of hemin in various concentrations of pyridine were evaluated. A large jump in oxidation and reduction potentials was observed between 0% and 4% pyridine, after which the potentials remained fairly consistent (Figure V.8). This positive shift in the reduction potential has been seen previously and it indicates that the reduction of the iron center occurs more easily upon binding of pyridine to hemin.¹²¹ This result would be expected as pyridine is less electron donating than the water/hydroxide ligand it replaces, allowing for easier reduction of the iron center upon binding. This change in reduction potential corresponding to mono-ligation of hemin is observed in the pyridine concentration range where the catalytic complex is formed. Thus, this result also confirms that the species present at 2.4% pyridine is mono-ligated. Therefore, the hemin-pyridine catalytic complex responsible for the turnover observed with the Hemin NP detection strategy has one pyridine coordinated to the iron center.

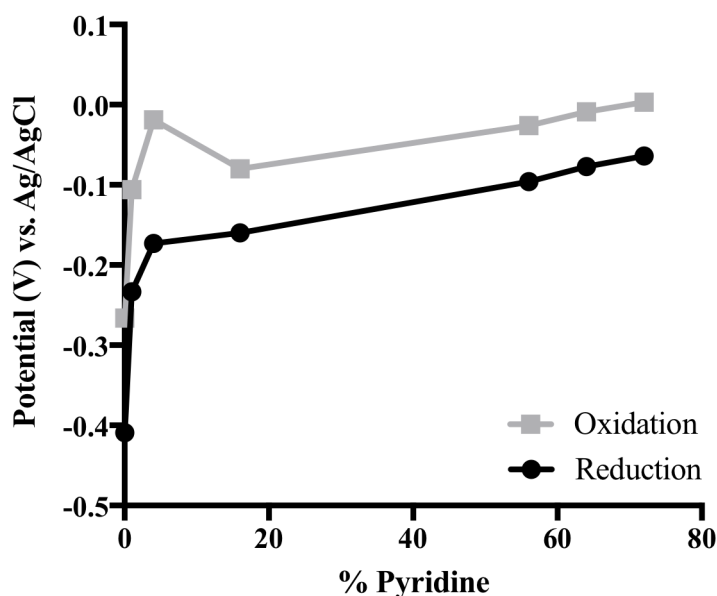


Figure V.8. The change in the oxidation and reduction potentials of the iron center of hemin with increasing concentrations of pyridine.

Kinetic Properties of Hemin NPs and Comparison to Horseradish Peroxidase

Once it was confirmed that Hemin NPs could be used to produce a colorimetric signal, their kinetic properties were compared to HRPx. Michaelis–Menten kinetic behavior was observed and substrate versus velocity curves were plotted for HRPx, Hemin NPs with pyridine and Hemin NPs (Figure SI V.8). The concentration of active sites for each sample was known, so k_{cat} values were calculated using Prism software. k_{cat} is a measure of the number of substrate molecules converted to product per unit time by one active site. Thus, a higher k_{cat} indicates a higher catalytic activity. As can be seen in Table V.1, Hemin NPs with pyridine have the greatest k_{cat} . The k_{cat} of the Hemin NPs with pyridine is 1,000x that of HRPx with respect to H_2O_2 and TMB. These k_{cat} values were calculated based upon the assessment that there are 60,000 hemin molecules per nanoparticle. Thus, the k_{cat} for a single hemin molecule within the nanoparticle is significantly lower (Table V.1, shown in parenthesis). Each horseradish peroxidase enzyme contains only one hemin molecule, so the fact that the k_{cat} for HRPx is up to 100x that of a single

hemin molecule from the nanoparticles in the presence of pyridine demonstrates how the protein structure, which is removed in the Hemin NPs, significantly enhances substrate turnover by hemin. Consequently, the combination of signal amplification by dissolution of the nanoparticles with the catalytic turnover is essential for the Hemin NP method to have significant catalytic activity.

	k_{cat} 1/min x 10^3		K_M mM		Catalytic Efficiency 1/(mM·min) x 10^3	
	H ₂ O ₂	TMB	H ₂ O ₂	TMB	H ₂ O ₂	TMB
Horseradish peroxidase	100 ± 19	160 ± 50	0.5 ± 0.3	0.5 ± 0.4	200 ± 130	300 ± 300
Hemin NP with pyridine	120,000 ± 40,000 (1.7 ± 0.5)	110,000 ± 20,000 (1.6 ± 0.2)	30 ± 20	0.8 ± 0.2	4,000 ± 3,000 (0.06 ± 0.04)	140,000 ± 50,000 (2.0 ± 0.6)
Hemin NP	270 ± 60 (0.0039 ± 0.0004)	280 ± 150 (0.004 ± 0.002)	330 ± 70	0.3 ± 0.3	0.82 ± 0.25 (0.000012 ± 0.000003)	900 ± 1000 (0.0013 ± 0.0015)
Value per hemin molecule shown in parenthesis						

Table V.1. A comparison of the catalytic properties of HRPx and Hemin NPs with and without pyridine.

Another interesting result of the kinetic characterization was the K_M values. K_M is defined as the concentration of substrate where half of the active sites are filled. As a result, K_M is an indirect measure of the affinity of the substrate for the active site. The substrate has high affinity for the active site when the K_M is small, indicating that a small amount of substrate is needed to reach this point. As can be seen in Table V.1, the K_M values for the H₂O₂ substrate increase significantly between HRPx, Hemin NPs with pyridine, and just Hemin NPs. This result shows that the enzyme has a much greater affinity for H₂O₂ than does hemin. Nevertheless, the addition of pyridine greatly decreased the K_M of Hemin NPs with respect to H₂O₂. This

observation suggests that the greater catalytic turnover observed upon addition of pyridine is a result of increased affinity for H₂O₂.

A more complete picture of the catalytic activity of the Hemin NPs can be seen when both k_{cat} and K_{M} are taken into account. These terms can be combined into a parameter called catalytic efficiency, which is defined as $k_{\text{cat}}/K_{\text{M}}$. Catalytic efficiency does not just look at the rate of turnover but also the amount of substrate required. As can be seen in Table V.1, the catalytic efficiency with respect to H₂O₂ of HRPx is 200×10^3 , while that for Hemin NPs with pyridine is $4,000 \times 10^3$. Thus, when considering the H₂O₂ substrate, the Hemin NP method is 20-fold more efficient than HRPx. The catalytic efficiencies with respect to TMB were 300×10^3 for HRPx and $140,000 \times 10^3$ for Hemin NPs with pyridine. In this instance, the Hemin NP method is 500 times more efficient. Thus, the developed Hemin NP method has a higher catalytic efficiency than HRPx. The difference between the efficiencies based upon H₂O₂ and TMB substrates is expected as higher K_{M} values were observed for H₂O₂ compared to TMB. The utility of these strategies to detect a protein biomarker is discussed in the next section and seen in Figure 10.

The stability of the catalytic activity of Hemin NPs was of great interest as one of the greatest downfalls of HRPx is that it quickly loses activity in non-ideal environmental conditions. To study this property, Hemin NPs were stored at room temperature and the absorbance generated by substrate turnover was measured at various time points. These values were compared to the initial signal. It was found that after 40 days, there was no statistical difference in the signal produced by the Hemin NPs compared to day 1 (Figure SI V.9). Thus, without refrigeration the Hemin NPs retain their catalytic activity, indicating the viability of this detection strategy in a low-resource setting. For comparison, a similar study was done with HRPx. By day 7, the signal produced had decreased by over 75%, and even within one day a

significant drop was seen (Figure V.9). The degradation of the protein structure is most likely the cause of this loss of signal. As there are no protein components in the Hemin NPs, a decrease in signal was not observed. Thus, the Hemin NP detection method has higher catalytic activity than HRPx and significantly greater environmental stability.

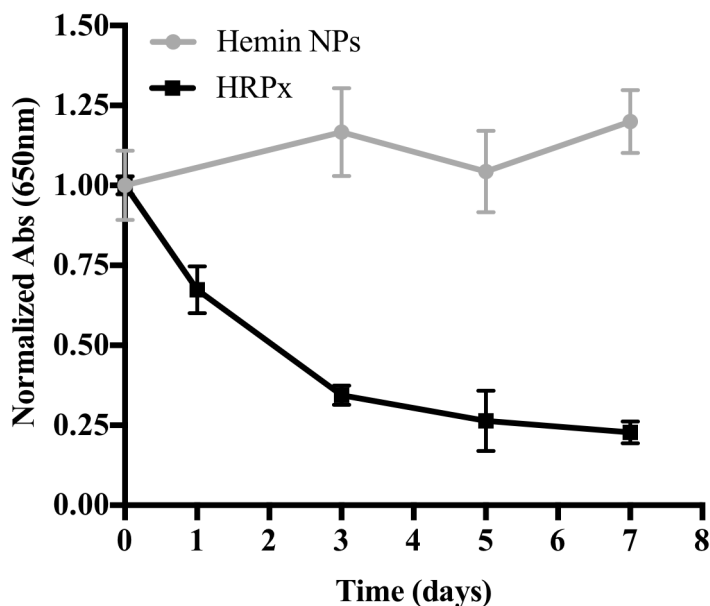


Figure V.9. The stability of the catalytic activity of Hemin NPs and HRPx. It can be seen that after seven days the ability of HRPx to turnover a substrate is lost.

Detection of Rabbit IgG

Up to this point it has been shown that Hemin NPs are an efficient and stable signal-generating material but the usefulness of this strategy for detection of biomolecules has not been demonstrated. To complete the Hemin NPs detection method, antibodies were coupled to Hemin NPs and these conjugates were used as the detection element in an ELISA-like assay for detection of the model biomarker, Rab-IgG. In this assay, a primary antibody was immobilized on a plate, followed by blocking and addition of the sample. The anti-rabbit IgG conjugated Hemin NPs (Ab-Hemin NPs) were then added as the detection element.

The primary antibody concentration was optimized for this assay based upon signal-to-noise, as too little primary antibody results in insufficient biomarker capture and too much can cause non-specific binding. It was found that 4 $\mu\text{g}/\text{mL}$ resulted in the highest signal-to-noise with the least variability, so this concentration was chosen for the assay (Figure SI V.10A). The amount of BSA needed to block the plate to prevent non-specific binding was also explored. It was found that 1% BSA resulted in the best signal-to-noise (Figure SI V.10B).

Optimal Ab-Hemin NP concentration and blocking were also determined. The concentration of Ab-Hemin NPs added to each well is important to ensure that the assay signal is dependent on the amount of biomarker present and not limited by the quantity of nanoparticles added. It was found the signal saturated at an Ab-Hemin NPs concentration of 40 $\mu\text{g}/\text{mL}$ (Figure SI V.10C). The amount of BSA required for sufficient blocking of the Ab-Hemin NPs was also an essential optimization, as Ab-Hemin NPs displayed significant non-specific binding. This non-specific binding was mitigated with 7% BSA (Figure SI V.10D).

A Rab-IgG standard curve was performed using the optimized protocol and the result was an assay with a linear range from 15 to 250 pM Rab-IgG (Figure V.10). The limit of detection, calculated by $3\sigma_{\text{blank}}/\text{slope}$, was 14.5 ± 0.8 pM Rab-IgG. An identical assay was then run with HRPx as the detection element allowing for comparison of the two strategies. The results showed a linear response over the concentration range of 10-100 pM Rab-IgG with a limit of detection of 0.27 ± 0.01 pM Rab-IgG. The Hemin NP assay had greater sensitivity than the HRPx assay as the slope of the linear regression was greater ($y = 0.0148x + 0.18$ compared to $y = 0.0064x + 0.07$). On the other hand, the HRPx assay had a lower background and was more precise, resulting in a lower calculated LOD (Figure V.10). This data shows that the combination of the two amplification strategies in the Hemin NP method produced a protein detection strategy with

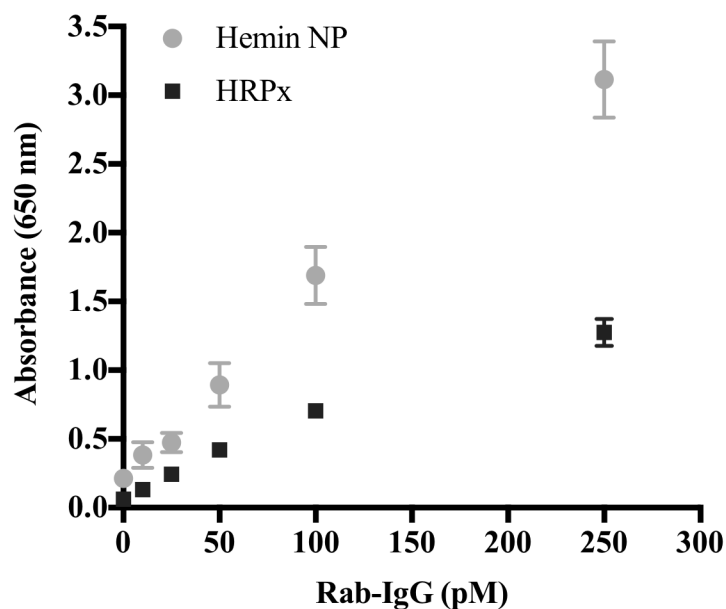


Figure V.10. A comparison of the standard curves generated when Rab-IgG was detected in a plate assay with Hemin NPs and HRPx.

greater sensitivity than HRPx, confirming the results of the kinetic analysis which showed the Hemin NP method had greater catalytic efficiency. Furthermore, it illustrates how signal amplification is profitable up to a point but then the corresponding amplification in error prevents a continued decrease in detection limits. Nonetheless, employing signal amplification with Hemin NP was shown to be both sensitive and stable. Furthermore, this method shows improvement over the fluorescent detection strategy developed in Chapter IV, as the absorbent signal easily read by the naked eye; an important characteristic for a low-resource diagnostic (Figure SI V.11).

Detection of Plasmodium Lactate Dehydrogenase

The Hemin NP strategy was then applied to the detection of a malarial biomarker in a whole blood matrix. As was discussed in Chapter II, there are two primary protein biomarkers used to detect malaria: (1) *Plasmodium falciparum* Histidine-Rich Protein II (*pfHRP*II) and (2) *plasmodium* lactate dehydrogenase (*pLDH*). It was found that there are downfalls associated

with using *p*/HRPII as a biomarker, including its persistence in the blood, which can result in false positive test results. Therefore, *p*LDH was selected as the target for this assay as it clears quickly from the bloodstream and is found in all species of malaria. The Hemin NP detection strategy was optimized for detection of *p*LDH in lysed whole blood samples spiked with parasite culture. The parameters that resulted in the best assay signal-to-noise were found to be 1 $\mu\text{g}/\text{mL}$ anti-*p*LDH antibody (19g7) for capture, 1% BSA for blocking of the plate, and 40 $\mu\text{g}/\text{mL}$ of *p*LDH-Hemin NPs blocked of 12% BSA (Figure SI V.12A-C).

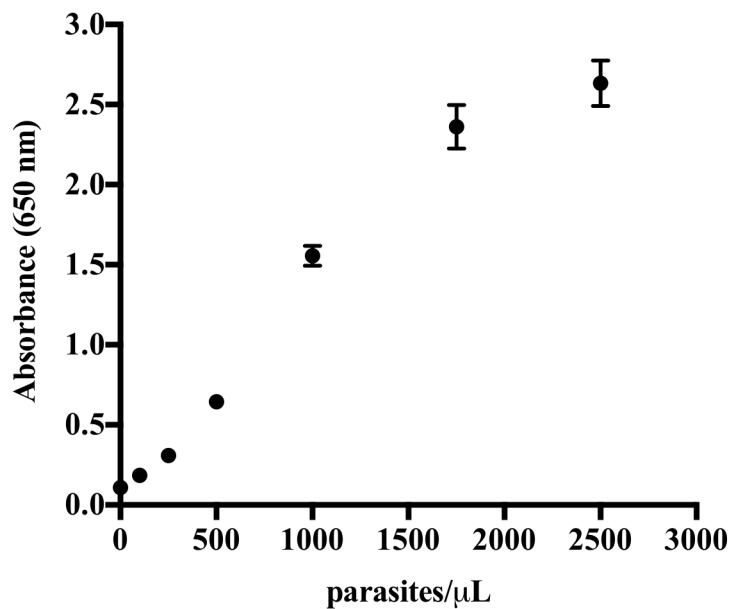


Figure V.11. Detection of *p*LDH from parasite-spiked lysed blood using *p*LDH-Hemin NPs. Linear concentration dependent response observed from 100-1750 parasites/ μL .

The optimized *p*LDH assay had a linear range from 100-1750 parasites/ μL and a calculated limit of detection of 18.6 ± 0.6 parasites/ μL (~ 90 pM *p*LDH) (Figure V.11). This limit of detection is well within the submicroscopic range of malaria infections and is of the same order of magnitude as commercially available ELISA kits for detection of *p*LDH.³⁶ This assay was also reproducible, as the inter-assay variability was found to be 5% and the intra-assay

variability between 250 and 1750 parasites/ μL was 18% ($n=3$). Thus, the Hemin NP detection strategy is stable, sensitive and reproducible and can be used to detect a malarial biomarker at clinically relevant concentrations from a complex matrix.

Conclusion

A novel, nanoparticle-based detection strategy using hemin nanoparticles has been reported. This method, which takes inspiration from the horseradish peroxidase enzyme, employs two-types of signal amplification. The first is dissolution of the Hemin NPs into tens of thousands of constituent hemin molecules and the second is catalytic turnover of a colorimetric substrate by each hemin molecule. A synthesis for Hemin NPs was developed and the catalytic properties of the resulting nanoparticles were optimized and characterized. The result was a detection element that showed great stability compared to HRP_x, maintaining catalytic activity even after storage at room temperature for 40 days. Furthermore, biomolecule detection by the Hemin NP strategy was found to have greater sensitivity than HRP_x and it detected picomolar levels of both the model biomarker, Rab-IgG and malarial biomarker, *p*LDH. This method could also easily be used for detection of protein biomarkers indicative of other diseases by changing the conjugated antibody. The easily observable signal, sensitivity, stability and versatility of the Hemin NP detection method makes it a very promising option for future incorporation into paper-based, low-resource diagnostics.

Acknowledgements

Special thanks to Matthew Park for assistance with the nanoparticle synthesis optimization experiments, as well as Dr. Aren Gerden for performing the cyclic voltammetry study. Partial support for this work was provided by the Bill and Melinda Gates Foundation (OPP1123092) and the Mitchum E. Warren, Jr. Graduate Research Fellowship (L.E.G.). Additionally, we would like to thank the Vanderbilt Institute of Nanoscale Science and Engineering for access to DLS instrumentation and Dr. Alissa Weaver's lab for access to the ZetaView particle analyzer.

CHAPTER VI

CELLULOSE MEMBRANES MODIFIED WITH METAL AFFINITY LIGAND FOR CAPTURE AND DETECTION OF MALARIAL BIOMARKERS

Introduction

One of the most effectively implemented low-resource diagnostics is the rapid diagnostic test (RDT).^{72, 122} These tests are easy to use, requiring minimal user steps and reducing the need for highly trained personnel. RDTs are also stable, allowing to shipment and storage in ambient conditions.^{72, 123} Thus, RDTs can withstand many of the rigors of low-resource environments. The low cost of RDTs has enabled their procurement on a mass scale and the lack of instrumentation allows their use at all levels of health facilities in low-resource settings.^{74, 124} As a result, RDTs have been extensively used in malaria elimination campaigns around the world. In certain areas of Sub-Saharan Africa, diagnosis by RDT with subsequent treatment has resulted in a significant decline in the prevalence of the malaria.^{20, 125}

Unfortunately, as discussed in Chapter III, RDTs still have limitations, namely a lack of sensitivity. This lack of sensitivity prevents RDTs from detecting submicroscopic malaria infections, many of which are asymptomatic, resulting in a sustained disease reservoir and preventing disease elimination.^{27, 70} In order to enhance the sensitivity of these tests, a simple sample processing step was introduced in Chapter III, which purifies and concentrates the malarial biomarker *Plasmodium falciparum* histidine-rich protein II (*pfHRP*II) using Ni-NTA magnetic beads which bind to the histidines in *pfHRP*II. Using this technique, the limit of

detection of a several RDT brands was decreased to single digit parasitemias, which is well within the submicroscopic infection range.²⁷

While this sample preparation procedure was very successful, it added several steps to the process of performing an RDT and required extract diagnostic components, a less than ideal characteristic in low-resource settings where trained personnel are limited. The efficacy of this sample preparation step was a result of the fact that it overcame the sample volume limitation of RDTs, a primary contributor to their lack of sensitivity. RDTs are sample volume limited in that the addition of large sample volumes, which present more biomarker to the test, is not feasible since blood volumes above those recommended by the manufacturer do not clear from the test.²⁸ In the sample processing step, the biomarker from a large sample volume is concentrated into a small volume that can be added to the RDT. Thus, more biomarker is presented to the test, allowing smaller infection levels to be detected.

In this chapter, we present an alternative method for concentration of *pf*HRP II that does not require the extra components and steps used in the previous method. This new design utilizes cellulose that is functionalized with metal affinity ligands to capture the biomarker. Similar materials have been synthesized previously with several different metal affinity ligands including iminodiacetic acid, nitrilotriacetic acid and N, N, N,-tris(carboxymethyl)ethylenediamine.^{126, 127} Application of these membranes included metal capture out of solution and protein purification.¹²⁸⁻¹³¹ In the following work, cellulose membranes were modified with the iminodiacetic acid (IDA) and zinc was subsequently coordinated to this ligand. These Zn-IDA cellulose membranes were used to capture *pf*HRP II, as the intrinsic histidines will bind to zinc.^{29,}¹³² A diagnostic which utilizes the Zn-IDA membrane will have a large sample volume capacity, as the sample can simply flow through the membrane which will capture the *pf*HRP II,

concentrating it for subsequent detection. A strength of this approach is that paper is the only material required for concentration of the biomarker, making this an inexpensive and simple option for low-resource settings.

Furthermore, the use of paper allows the sample preparation step and the diagnostic to be combined into one complete test. For example, the simple addition of a detection element, which binds to the biomarker captured on the cellulose membrane, would allow for biomarker detection on the membrane. Assays have been previously developed for detection of malaria, p24, and prostate-specific antigen, that utilize this flow-through diagnostic technique. These assays utilized aptamers or antibodies for capture of the biomarker and assay signals were produced by either gold nanoparticles or enzymes. Clinically relevant concentrations were detected by these methods and increased sensitivity was observed with greater sample volumes.^{31, 33, 133} In the following, we demonstrate how Zn-IDA membranes can be used for the effective capture of the malarial biomarker (*pfHRP*II). For detection, the hemin nanoparticle method developed in Chapter V was implemented because of its sensitivity and stability. Up to this point the Hemin NP method had only been implemented in a plate assay format, which is not feasible in low-resource settings. But through combination of this method with the Zn-IDA membranes, it will be utilized in a low-resource format. Thus, this work combines sample preparation and biomarker detection in one diagnostic device. The capture of *pfHRP*II by the Zn-IDA membranes is characterized. Furthermore, the hemin nanoparticle detection strategy is optimized for this paper-based method and the limit of detection for *pfHRP*II, using this flow-through diagnostic, is reported.

Experimental

Materials

Sharkskin (catalog no. 09800965), Whatman 2589A (catalog no. 09924374), Whatman 91 (catalog no. 09927547), and Whatman 3 (catalog no. 09-820H) cellulose membranes were purchased from Fisher Scientific. Regenerated cellulose membranes were acquired from Sartorius (catalog no. 18406--47-----N). (±)-Epichlorohydrin (catalog no. 45340) and ethylenediaminetetraacetic acid tripotassium salt dihydrate (catalog no. 03664) were purchased from Sigma Aldrich. Zinc sulfate heptahydrate (catalog no. Z68), nitric acid (TraceMetal™ Grade) (catalog no. A509P500) and 33 mm (pore size 0.45 μm) PVDF syringe filters (catalog no. 09-719-002) for preparation of ICP-OES samples were acquired from Fisher Scientific. PlasmaCAL multi-element standard (catalog no. 600-698-201) for ICP-OES analysis was purchased from SCP Science. For flow-through assays Norm-Ject™ 3 mL syringes were used. *Plasmodium falciparum* D6 strain (1 parasite/μL ≈ 2.9 pM *pfHRP*II) was cultured in house and Human Whole Blood (CPD) was purchased from Bioreclamation IVT (catalog no. HMWBCPD). *pfHRP*II ELISA capture and detection antibodies were acquired from Abcam Inc. (catalog nos. ab9206 and ab30384, respectively). Immulon 2HB ELISA plates (catalog no. 14-245-61) and Promega 3,3',5,5'-tetramethylbenzidine (TMB) One ELISA substrate (catalog no. PR-G7431) were purchased from Fisher Scientific. Hemin for nanoparticle synthesis was acquired from MP Biomedicals (catalog no. 198820). Pierce™ Sulfo-NHS-LC diazirine photoreactive crosslinker (catalog no. PI-26174), 10 kDa SnakeSkin™ dialysis tubing, and 0.5 mL Zeba™ Spin Desalting Columns (7K MWCO) were purchased from Fisher Scientific. 1000 kDa Spectra/Por® Float-A-Lyzer® G2 dialysis devices (catalog no. G235062) and Spectra/Gel® absorbent (catalog no. 292600) were acquired from Spectrum Laboratories Inc. Goat anti-rabbit

IgG antibody (pAb) (catalog no. A00131), goat anti-rabbit IgG antibody [HRP] (catalog no. A00098) and rabbit IgG control (whole molecule) (catalog no. A01008) were purchased from Genscript Inc. The anti-*Plasmodium falciparum* antibodies for conjugation to hemin nanoparticles and capture in the plate assay were acquired from Abcam (catalog nos. ab9203 and ab9206, respectively). All other reagents were obtained from either Sigma-Aldrich or Fisher Scientific.

Instrumentation

Zinc was quantified using an Optima 7000 DV inductively coupled plasma optical emission spectrometer (ICP-OES). Sonication during nanoparticle synthesis was carried out with an Ace Glass GEX 600-5 Ultrasonic Processor. A Spectroline handheld UV light (Model ENF-260C) with irradiation at 365 nm was used to initiate the photoreactive crosslinker. Absorbance measurements were collected on a Biotek Synergy™ H4 microplate reader. Membranes were imaged using a HP Color Laser Jet Pro MFP M476dw scanner.

Membrane Synthesis

Zn-IDA functionalized membranes were synthesized with slight modification to a previously reported procedure.¹³⁰ Briefly, a 25 mL solution containing 80% 1.6 M sodium hydroxide and 20% (\pm)-Epichlorohydrin (EPI) was added to a glass vessel with the cellulose membrane of choice. After 8 hours, the membrane was removed from the solution and washed three times with DI water. It was then added to a 25 mL solution of 1 M iminodiacetic acid (IDA) in 1 M sodium carbonate. This reaction was allowed to proceed overnight. Next, the membrane was washed with DI water three more times. Finally, the membrane was added to 25 mL of 25 mM zinc sulfate for 1 hour, washed again with DI water and then allowed to dry. IDA

control membranes were synthesized in the same way except the synthesis was terminated after reaction with IDA in sodium carbonate, so zinc was not coordinated to the membrane.

Zinc Quantification with ICP-OES

The amount of zinc bound to IDA on the membrane was quantified by ICP-OES. A piece of membrane with a known size was placed in a 1.5 mL microcentrifuge tube with 13.3% trace metal free nitric acid. This tube was placed on a shaker for 15 minutes before the solution was passed through a PVDP syringe filter to remove remaining cellulose. The solution was then diluted to a concentration of 2% nitric acid. If further dilution was required for the sample to be within the linear range of the instrument, this was done with 2% nitric acid. These samples were then analyzed against standards and zinc was measured at a wavelength of 206.2 nm.

Capture Efficiency

For determination of the amount of *pf*HRP II that could be captured by the Zn-IDA membrane, a $d = 1$ cm section of membrane was placed in the bottom of a 3 mL plastic syringe. A 500 μ L sample at 200 parasites/ μ L was then added to the syringe. Samples in buffer (50 mM phosphate buffer pH = 8, 300 mM NaCl, and 0.1% BSA), whole blood and lysed whole blood (1:1 v/v whole blood:lysis buffer (100 mM PB pH=8, 300 mM NaCl, 2% Triton X-100)) were analyzed. The samples were allowed to gravity flow through the membrane for 1 minute before the remaining sample was pushed through by the plunger. This sample was collected for analysis by *pf*HRP II ELISA to determine the amount of *pf*HRP II remaining in the solution after flow through the membrane. A positive and negative control were also analyzed. The amount of *pf*HRP II bound to the membrane was determined by subtracting the amount of *pf*HRP II in the sample that passed through the membrane from the amount of *pf*HRP II in the original sample (the positive control).

pfHRP II ELISA Protocol

The protocol for the ELISA used to quantify *pfHRP II* bound by the Zn-IDA membranes has been reported previously.²⁶ Briefly, 1 µg/mL of anti-*HRP II* IgM (ab9206) in PBS was immobilized in a 96-well plate, which was then blocked with 5% BSA in PBST (1X PBS, 0.1% Tween-20). Samples were diluted in sample buffer (PBST, 0.1% BSA) and added to the plate. Finally, horseradish peroxidase conjugated detection antibody (ab30384) was added at 0.5 µg/mL in PBST with 0.5% BSA. Signal was visualized with TMB-One and stopped with 2M sulfuric acid. Absorbance was read at 450 nm.

Membrane Selection Study

Sharkskin, Whatman 2589A, Whatman 91, and Whatman 3 cellulose membranes and a regenerated cellulose membrane from Sartorius were functionalized with Zn-IDA as described earlier in this section. After synthesis, each membrane was analyzed by ICP-OES to determine zinc binding. Additionally, the *pfHRP II* capture efficiency of each membrane was quantified by *pfHRP II* ELISA.

Antibody Conjugation to Hemin Nanoparticles

Hemin NPs were synthesized as described in Chapter V. For lyophilization studies, anti-rabbit IgG antibodies were conjugated to the nanoparticles (Ab-Hemin NPs) through a photoreactive linker. This procedure is also reported in Chapter V. In a similar manner, Hemin NPs for detection of *pfHRP II* in the flow-through assay were conjugated to anti-*Plasmodium falciparum* antibodies through a photoreactive linker. In this reaction, the ratio of antibody to hemin was 32 µg antibody per 100 µg hemin (*pfAb*-Hemin NPs). These particles were tested in a plate assay to confirm their ability to detect *pfHRP II* before they were used for on-membrane detection. The plate assay was performed by adding 100 µL of 2 µg/mL of capture antibody

(ab9206) to a plate for 1 hour, followed by the addition of 300 μL of 2% BSA in PBST for 2 hours. Next, 100 μL samples of D6 parasite culture spiked into 2% BSA were added. The final step included the addition of 100 μL of *pf*Ab-Hemin NP at 40 μg hemin/mL in 10% BSA. The plate was washed with PBST after each step. The signal was then visualized through the addition of 50 μL of 0.9 M pyridine and 100 μL TMB-One.

Hemin Nanoparticle Lyophilization

The stability of the Hemin NP detection strategy upon lyophilization was explored through analysis of the size distribution of the particles by DLS before and after lyophilization. The Hemin NPs were lyophilized in solutions of 0, 2, 5, 10 and 15% trehalose with 10 mM PB pH = 5.7. Before lyophilization, the nanoparticles were frozen at -80°C for 6 hours. The samples were then lyophilized for at least 24 hours. For size analysis after lyophilization, Hemin NPs were resuspended in DI water.

To test if Ab-Hemin NPs could still bind to their target and produce signal post-lyophilization, they were lyophilized in 15% trehalose with 10 mM PB pH=5.7 and stored in Ziploc bags with desiccant packs at room temperature. At various time points these Ab-Hemin NPs were resuspended and used as the detection element in the Rab-IgG detection assay described in Chapter V. The signal from the Ab-Hemin NPs was normalized to an HRPx conjugated anti-rabbit IgG detection antibody control. For the detection step in the control wells, 0.5 $\mu\text{g}/\text{mL}$ of anti-rabbit IgG HRPx in 1% BSA was added.

On-Membrane Detection of pfHRPII

For detection of *pf*HRPII on Zn-IDA membranes, a piece of membrane ($d = 1\text{ cm}$) was placed in the bottom of a 3 mL, plastic syringe. A 500 μL sample of parasite culture spiked in 10% BSA was added to the syringe. After 1 minute, any sample remaining in the syringe was

expelled. Next, 250 μL of *pf*Ab-Hemin NPs in 10% BSA were added at a concentration of 0.4 $\mu\text{g}/\text{mL}$. Again, after 1 minute the remaining solution was pushed through the membrane. The membrane was then washed with a 500 μL of 1X PBS (10 mM phosphate buffered saline, 150 mM NaCl). Finally, 100 μL of detection solution (2:1 v/v TMB-One:0.9 M pyridine in 10 mM borate buffer pH = 8) was added. Color was allowed to develop for 10 minutes before the membranes were scanned and the images analyzed by ImageJ.

Image Analysis

The signal on the membrane was quantified by scanning the membranes and analyzing these images with ImageJ software available on the National Institute of Health's website. When images were opened in this software, they were converted to the HSB (hue, saturation, brightness) color scheme. In this color scheme, saturation takes into account the intensity of the color. As a more intense blue color is indicative of higher biomarker concentrations, saturation of the images was measured. This analysis gave a quantitative result for the intensity of the signal on the membrane.

Results and Discussion

Membrane Selection Study

Zn-IDA cellulose membranes were made through modification of the membrane with the metal affinity ligand, iminodiacetic acid, and subsequent coordination of zinc to this ligand (Figure VI.1). Functionalization with Zn-IDA allowed the cellulose membranes to bind *pf*HRP II, a histidine-rich protein biomarker of malaria, as the histidines in *pf*HRP II have a high affinity for zinc.¹³² Biomarker capture on this membrane is essential for the development of a flow-through diagnostics. To determine the best membrane for *pf*HRP II capture, several different cellulose

membranes, with varying pore sizes and thicknesses, were tested. The specifications of the five membrane types that were modified with Zn-IDA are shown in Table VI.1.

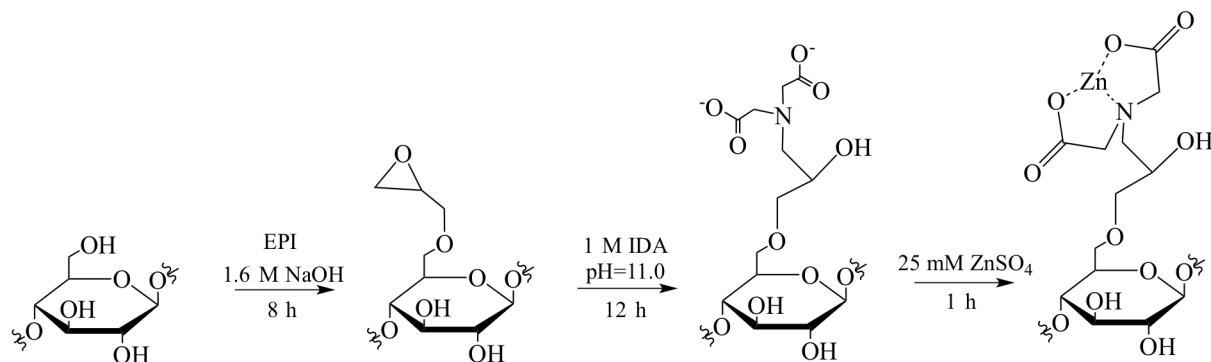


Figure VI.1. Synthesis scheme used for the functionalization of cellulose membranes with iminodiacetic acid coordinated to zinc (Zn-IDA). These membranes were used to capture and concentrate *pf*HRPII.

The modified membranes were analyzed for zinc content by ICP-OES. Zinc content was observed for all membranes indicating successful functionalization with Zn-IDA (Table VI.1). It can be seen that the amount of zinc loading corresponded to the surface area available on the membrane. Sharkskin and Whatman 91 had the lowest amount of zinc loading and were relatively thin with large pores. Whatman 3 and 2589A were much thicker membranes and high zinc loading was observed. The Sartorius regenerated cellulose (Sartorius RC) membranes had high zinc loading even though they were relatively thin, which must be the result of larger surface area for Zn-IDA functionalization from the smaller pore size and greater porosity of these membranes. The ability of these membranes to bind *pf*HRPII, in a flow-through format, was also analyzed. It was found that the three membrane types with the highest zinc loading were the ones that resulted in greatest capture of *pf*HRPII (Table VI.1).

As essentially complete capture of *pf*HRPII was observed for both Sartorius RC and Whatman 3 cellulose membranes, other characteristics were taken into account in selection of the

Membrane	Thickness (μm)	Pore Size (μm)	Zn Loading (μmol/cm ³)	% <i>pf</i> HRP ^{II} Bound
Sartorius RC	170	0.45	330 ± 17	98 ± 1
Whatman 3	390	6	100 ± 10	95 ± 1
Whatman 2589A	430	12	109 ± 6	90 ± 1
Whatman 91	205	10	92 ± 6	<80%
Sharkskin	170	12	90 ± 4	<80%

Table VI.1 Characteristics of the cellulose membranes that were modified with Zn-IDA. Zinc loading and *pf*HRP^{II} capture are also listed.

membrane type for the flow-through assay. The Sartorius RC membrane is made of regenerated cellulose which has a greater wet strength and solvent compatibility compared to cellulose, the material from which Whatman 3 is made. While this is a positive characteristic considering the harsh reaction conditions required for functionalization, upon drying, these membranes became very brittle and making handling difficult. Thus, for ease of use and compatibility with the flow-through assay format, Whatman 3 membranes were selected for this study. A more complete characterization of the Whatman 3 Zn-IDA membranes (W3-Zn-IDA) showed specific binding of zinc to IDA. The zinc content of non-functionalized Whatman 3 membranes, which were mixed in a zinc sulfate solution for 1 hour, was $0.031 \pm 0.009 \mu\text{mol}/\text{cm}^2$. After functionalization with IDA, zinc content was found to be $4.1 \pm 0.4 \mu\text{mol}/\text{cm}^2$.

*pf*HRP^{II} Capture by Zn-IDA Membranes

As it has been shown that W3-Zn-IDA binds essentially all of the *pf*HRP^{II} out of solution, it was then necessary to determine the specificity of this binding. This analysis was

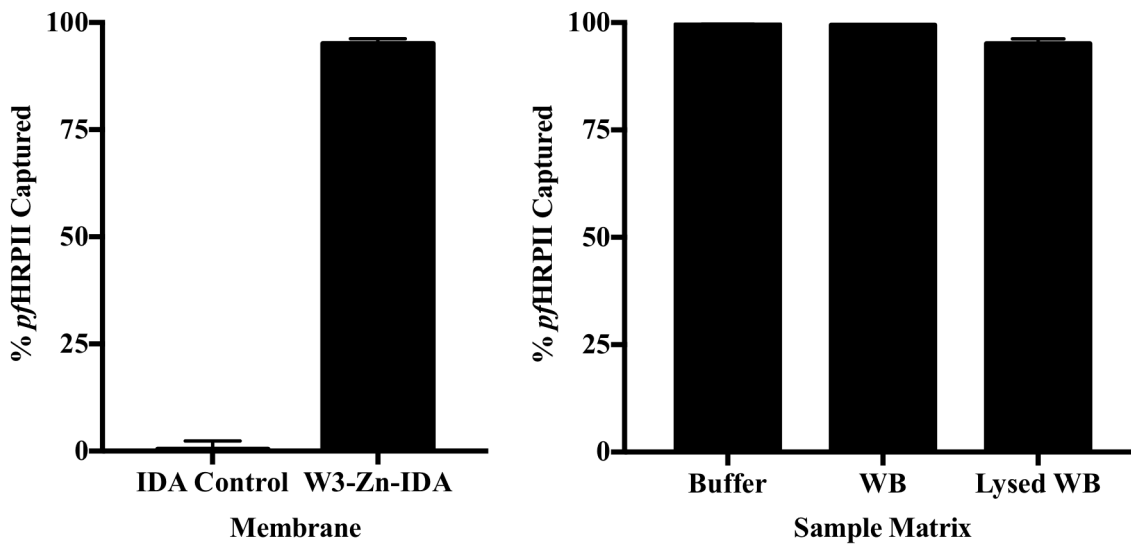


Figure VI.2. *pfHRP*II specifically binds to zinc on W3-Zn-IDA, as binding was only observed with the membrane to which zinc was coordinated. Binding occurs between the intrinsic histidines in *pfHRP*II and zinc (left). W3-Zn-IDA membranes show complete capture of *pfHRP*II out of various sample matrices (right).

done by quantitating *pfHRP*II binding to a membrane solely functionalized with IDA, thus the zinc atoms to which the *pfHRP*II should specifically bind were eliminated. The result showed no binding (0 ± 2 % *pfHRP*II) to the IDA control membrane indicating that the 95 ± 1 % *pfHRP*II was specifically bound by W3-Zn-IDA (Figure VI.2). The ability of the W3-Zn-IDA to bind *pfHRP*II from various matrices was also explored. It was seen that essentially complete capture was observed from buffer, whole blood and lysed whole blood (Figure VI.2). This result was excellent, as it demonstrated that *pfHRP*II could be directly captured from a patient sample without any additional preparation steps.

Additionally, in development of a diagnostic, the sensitivity is very important as it allows for the detection of low infections levels. In the case of malaria, these low, asymptomatic infections often go undiagnosed and untreated which is detrimental to patient health and leaves a reservoir of the disease.^{18, 22, 45} One of the strengths of a flow-through assay is the concentration of the biomarker that occurs on the membrane surface. This property can be used to detect lower

infection levels by simply increasing the sample volume that is analyzed. This is so because there is a greater total amount of biomarker in a large sample volume compared to a small sample volume, so more biomarker is captured as sample volume increases. To test whether or not this increased biomarker capture was observed in our system, samples with a constant concentration of *pf*HRP II but of varying volumes were analyzed. It was found that with an increase in sample volume there was a corresponding increase in *pf*HRP II captured (Figure VI.3). This indicates larger samples volumes could be incorporated into our system for detection of low level infections.

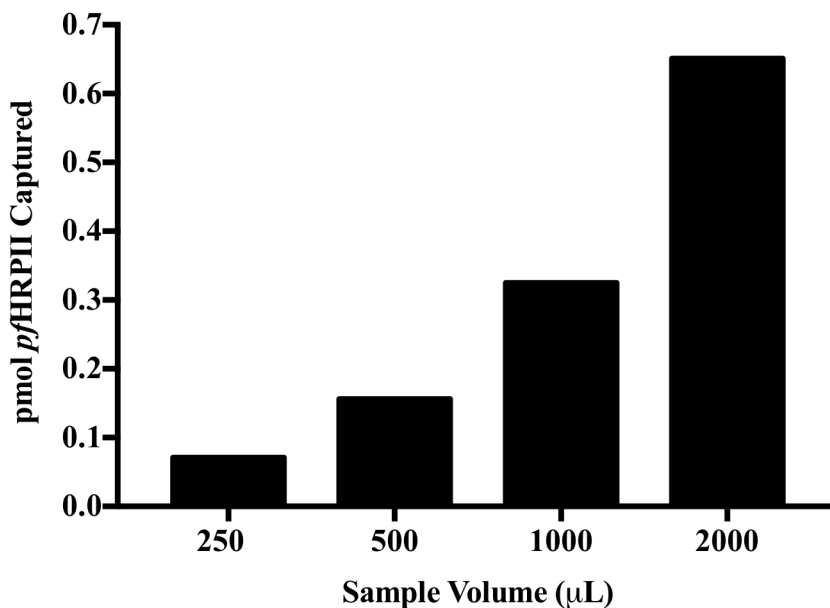


Figure VI.3. Increasing sample volume results in greater biomarker capture on the Zn-IDA functionalized Whatman 3 membrane.

The complete capture of *pf*HRP II from large sample volumes is possible because of the excess of zinc binding sites compared to the number of *pf*HRP II molecules within a sample. According to ICP-OES results, there are 2×10^{18} zinc atoms in a $d = 1$ cm section of membrane. In a 500 µL sample with a parasite concentration of 200 parasites/µL, there are 2×10^{14} *pf*HRP II molecules. Thus, there is a 10,000-fold excess of binding sites on the membrane, meaning the 4-

fold increase in sample volume did not come close to saturating the number of available binding sites. As a result, all of the *pf*HRP_{II} was bound. Additionally, the large excess of binding sites increases the rate of *pf*HRP_{II} capture allowing all of the *pf*HRP_{II} to be bound within one minute. This is very amenable to a low-resource setting, considering fast assay time is often a necessity.

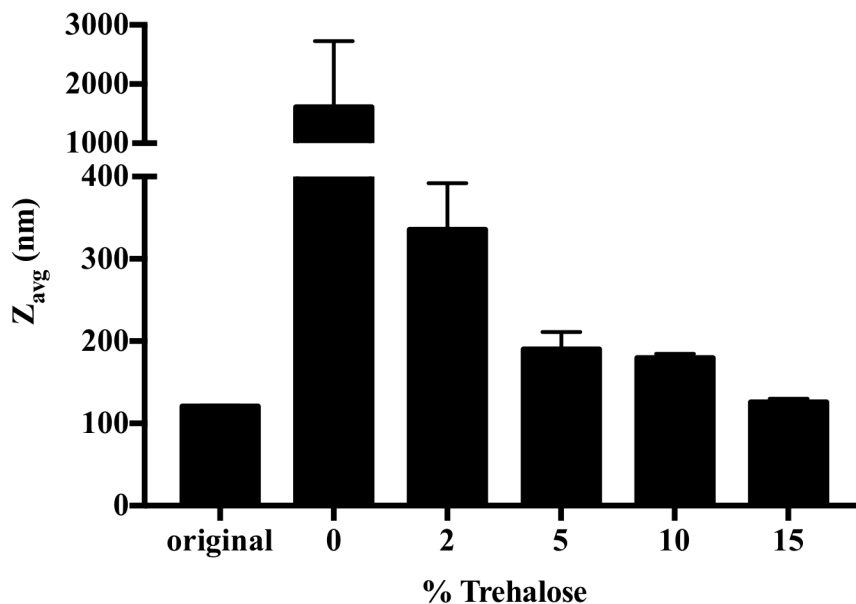


Figure VI.4. The size of Hemin NPs after lyophilization and resuspension. It can be seen that nanoparticle structure was retained (compared to the original sample), when lyophilization was performed in 15% trehalose.

Optimization of Hemin Nanoparticle Lyophilization

After it was determined that *pf*HRP_{II} could be effectively captured by W3-Zn-IDA, a method for detection of the biomarker, on the membrane, was developed. The nanoparticle-based detection strategy developed in Chapter V was both sensitive and stable and as such it seemed ideal for incorporation into the Zn-IDA flow-through assay. One important characteristic to determine for the selected detection strategy was whether the detection element could be lyophilized, resuspended and still successfully detect a biomarker. Since effective paper-based

diagnostic strategies require storage for long periods of time, this stability of the detection element is essential.

To test whether the Hemin NP detection element could be lyophilized and remain effective, several lyophilization conditions were tested. Initially, it was determined which conditions resulting in Hemin NPs of the original size after resuspension. To perform this experiment, Hemin NPs were placed in solutions of varying concentrations of trehalose. Trehalose was chosen as it is a sugar that has been shown to greatly stabilize materials and antibodies upon lyophilization. The crystalline sugar structure that forms around the nanoparticles prevents collapse of the particle during the lyophilization procedure.¹³⁴ Thus, Hemin NPs were lyophilized in these solution, resuspended in DI water and their size measured by DLS. It was found that at a concentration of 15% trehalose there was no difference in the Hemin NP size seen before and after lyophilization, indicating that the nanoparticles remained stable through the process (Figure VI.4).

As a result, 15% trehalose was used for lyophilization of Ab-Hemin NPs. These antibody-conjugated particles were tested to see if the detection capabilities of Hemin NPs remained stable in addition to Hemin NPs size. The lyophilized Ab-Hemin NPs were stored at room temperature and then resuspended for use in a sandwich assay for detection of Rab-IgG. It was found that after 1 month these nanoparticles were able to produce signal and specifically detect IgG.

On-Membrane Detection of pfHRP II

As the Hemin NP detection strategy was evidenced to be ideal for on-membrane detection of *pfHRP II* because of its sensitivity and stability, it was implemented into the flow-through diagnostic assay. To develop this assay for detection of *pfHRP II*, anti-*Plasmodium*

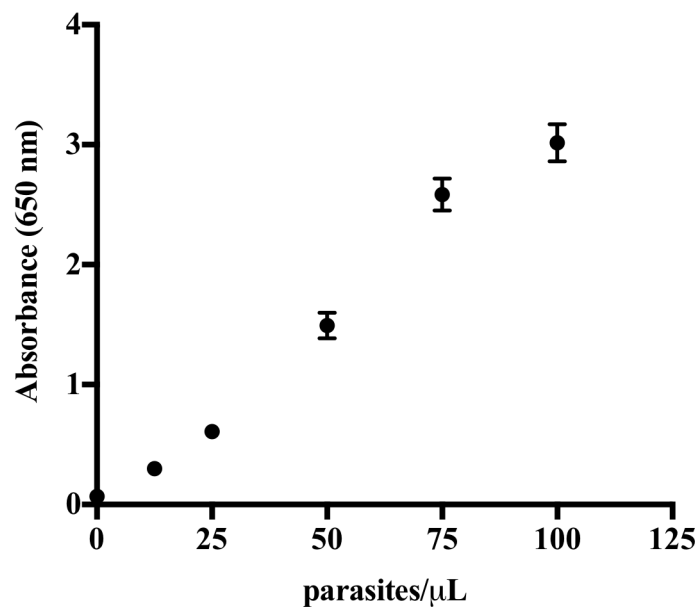


Figure VI.5. Detection of *pf*HRP_{II} using *pf*Ab-Hemin NPs in a plate assay.

falciparum antibodies had to be conjugated to the Hemin NPs. The *pf*Ab-Hemin NPs were first tested in a plate assay and the resulting standard curve had a LOD of 12.2 ± 0.7 parasites/ μL (~ 35 pM *pf*HRP_{II}) (Figure VI.5). These particles were then implemented into the flow-through assay, where *pf*HRP_{II} was captured on the membrane and then subsequently detected by the *pf*Ab-Hemin NPs through addition of the colorimetric substrate.

Initially, *pf*Ab-Hemin NPs were added at similar concentration to that required by the plate assay, but the result was a high background signal. It was found that as the concentration of *pf*Ab-Hemin NPs was decreased, the assay signal-to-noise increased (Figure VI.6). As a result, a particle concentration of $0.4 \mu\text{g}$ hemin/mL was chosen for the assay, as it gave large positive signal with minimal background. The fact that the flow-through assay required much less detection element is likely a result of the flow of the *pf*Ab-Hemin NPs through the membrane. This process concentrates the detection element at the membrane surface as well as forces interaction with the bound biomarker. This result is another great advantage of the flow-through

diagnostic strategy, as the cost of the assay is significantly decreased by reduction in the amount of *pf*Ab-Hemin NPs required.

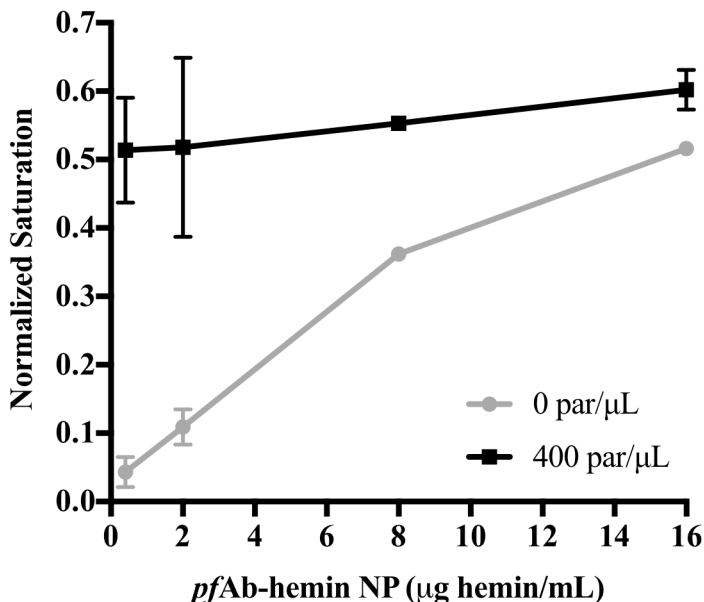


Figure VI.6. Optimization of the amount of *pf*Ab-Hemin NPs required for the flow-through assay. The concentration of *pf*Ab-Hemin NPs was significantly reduced compared to that used in the plate assay in order to minimize non-specific background signal.

Detection Limit of the pfHRP II Flow-Through Assay

Once signal was successfully achieved on-membrane for detection of *pf*HRP II, samples of various *pf*HRP II concentrations were analyzed to determine the limit of detection of the assay. As can be seen in Figure VI.7, samples between 0 and 200 parasites/ μL were analyzed and a visual signal was observed even at 12.5 parasites/ μL . Images of the membranes were analyzed by ImageJ for color saturation and a standard curve was produced (Figure VI.7). The limit of detection of the assay was determined from the linear portion of this curve ($3\sigma_{\text{blank}}/\text{slope}$). The result was a LOD of 2.2 ± 0.2 parasites/ μL (6.5 ± 0.5 pM *pf*HRP II). Thus, this method allows for detection of low infection levels within the range corresponding to asymptomatic patients. This outcome demonstrates that biomarker capture and concentration on the Zn-IDA membrane

combined with the Hemin NP detection strategy, resulted in a sensitive diagnostic using a format that is both stable and cost effective. Future work will look to design a user-friendly diagnostic housing.

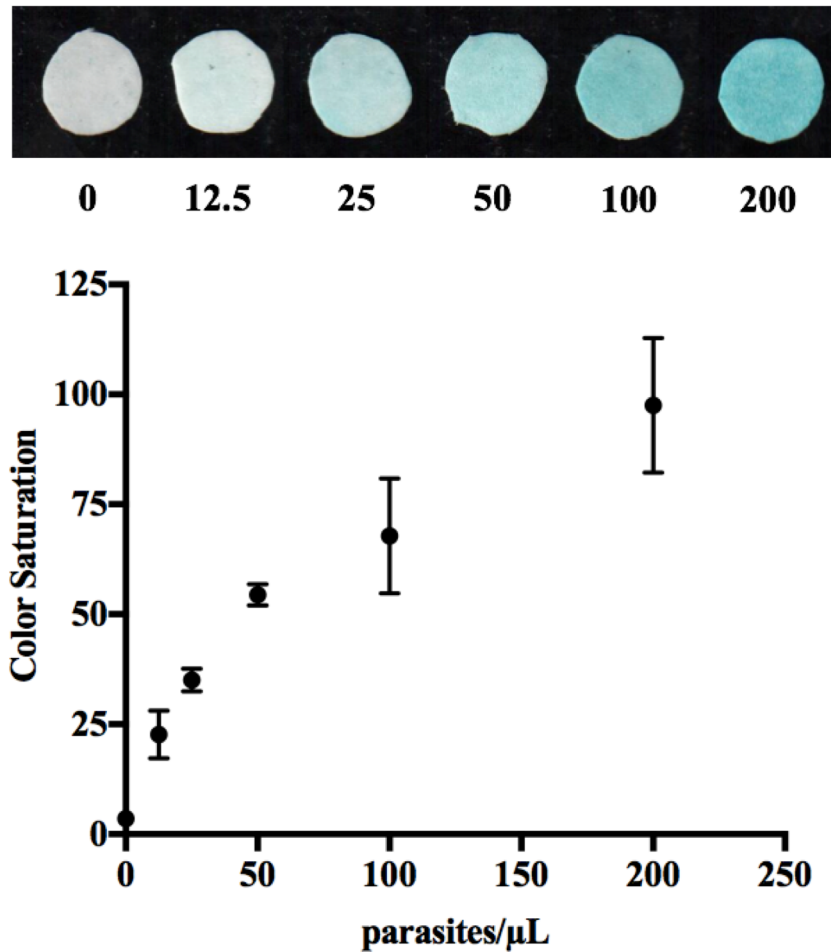


Figure VI.7. Detection of *pfHRP2* in the flow-through assay format using Zn-IDA functionalized Whatman 3 membranes for capture and *pfAb*-Hemin NPs for detection. A visual signal was observed as low as 12.5 parasites/μL and the calculated LOD after image analysis was 2.2 parasites/μL.

Conclusion

In this work, cellulose membranes were effectively modified with Zn-IDA ligands for the specific capture of a histidine-rich malarial biomarker, *pfHRP*II. Capture of this biomarker was achieved through interaction between the histidine moieties and the zinc atoms. It was found that these membranes could essentially capture all of the *pfHRP*II out sample volumes from 250-2000 μ L and in buffer and whole blood matrices. The Hemin NP detection strategy reported in Chapter V was used to detect the captured *pfHRP*II and produced a visual signal. The result was a flow-through diagnostic that was able to detect single digit parasitemias. Thus, the individual assay components developed throughout this work were combined to produce a simple, sensitive and stable low-resource diagnostic for malaria.

Future Directions

Zn-IDA cellulose membranes are very intriguing components in the design of diagnostics for low-resource settings. The fact that these membranes are cheap, disposable and have essentially complete biomarker capture ability, is very unique. It has been shown how this effective capture can be used to detect low-levels of biomarker on membrane and one could imagine there are other diagnostic strategies which could be greatly enhanced by use of these membranes.

As has been mentioned throughout this document, rapid diagnostic tests (RDT) are the most effectively implemented low-resource diagnostic throughout the world.⁷² These tests are cost-effective and stable, not to mention simple to perform and analyze. RDTs are widely distributed, so healthcare workers around the world are familiar with running and reading these tests. Thus, while a flow-through assay has many advantages, as was highlighted in the

beginning of this chapter, the necessity to re-train individuals in order to implement this strategy is not ideal. Furthermore, implementation of controls and multiplex detection into a flow-through test can be challenging. As a result, a lateral flow diagnostic similar to an RDT would be ideal

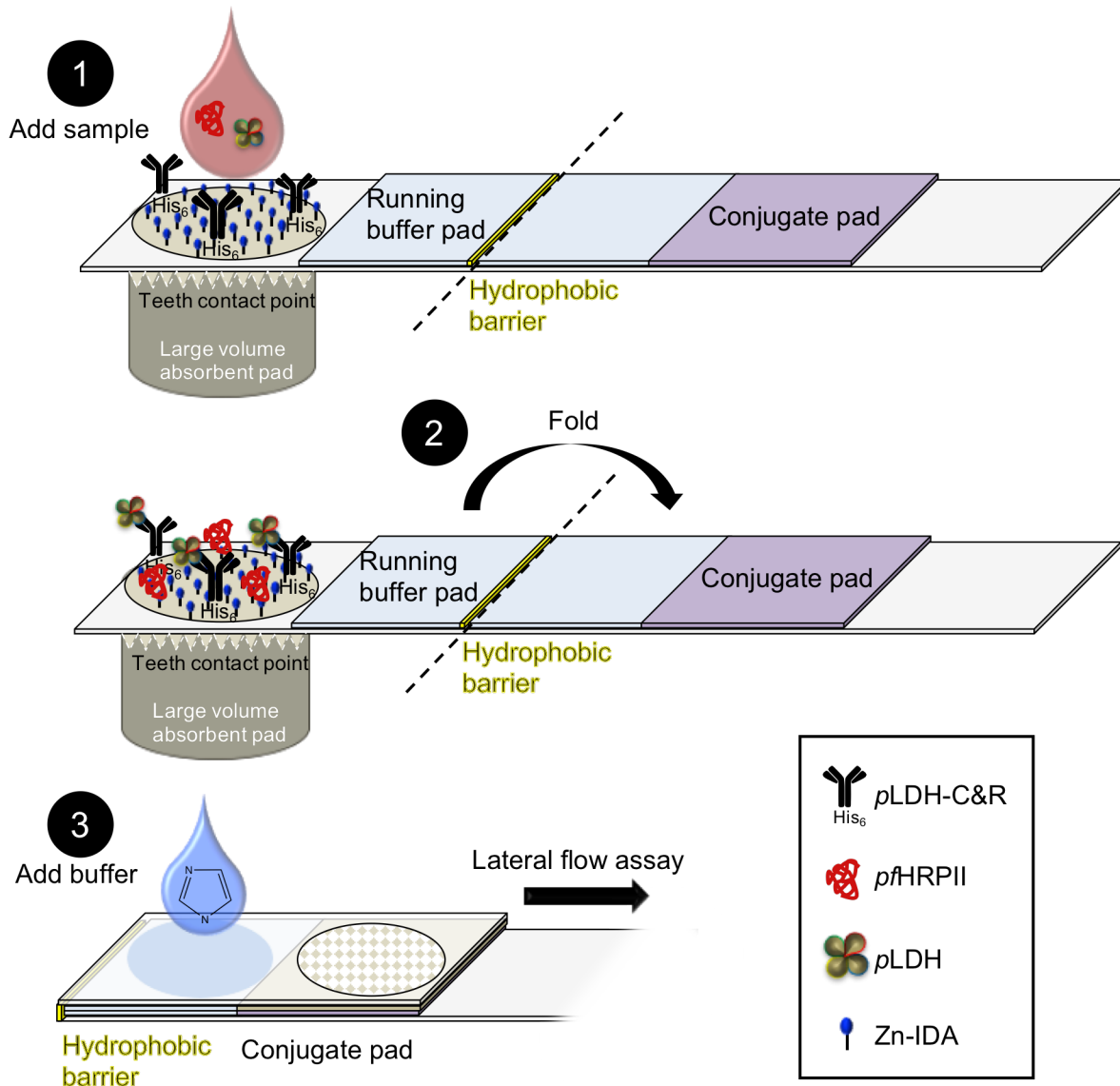


Figure VI.8. Workflow for the origami RDT, which combines a Zn-IDA functionalized membrane with a lateral flow assay, for sensitive detection of malaria. Malarial biomarker *pfHRP II* is captured directly on the membrane and *pLDH* is captured through a unique capture and release (C&R) reagent. Through a simple fold these biomarkers are presented to the lateral flow assay and released by imidazole. Figure graciously provided by Westley Bauer.

for low-resources settings. But, as has been fully discussed in this document, RDTs lack sensitivity. In Chapter III, a sample preparation method was presented that effectively used Ni-NTA magnetic beads to increase the sensitivity of commercially available RDTs. Unfortunately, the procedure was somewhat complex and required separate assay components. Thus, it was considered whether the Zn-IDA membranes could be incorporated into a lateral flow assay to provide the same enhancement as the magnetic beads but in a more simple format.

This thought led to the design of the origami RDT, which combines Zn-IDA membranes with a lateral flow assay. In this design, sample is flowed through a Zn-IDA membrane where the biomarker is captured and concentrated. A simple fold of the test then presents all of the captured biomarker to the lateral flow assay where a release buffer is added, freeing the biomarker for capture at the test line (Figure VI.8). The incorporation of the Zn-IDA membrane eliminates the sample volume limitation of RDTs, the major cause of their lack of sensitivity. Sample volume is no longer limited as large sample volumes can be added to the Zn-IDA membrane for biomarker capture and then through folding of the test, the biomarker from the large volume is presented to the test without the sample matrix. Thus, sample processing and the RDT are combined into one test, so no additional assay components are needed.

An obvious requirement of this diagnostic strategy is the ability to release the biomarker from the membrane in order for it to flow down the lateral flow assay for detection. Release of *pf*HRP_{II} was attempted by addition of imidazole, which at high concentrations out competes *pf*HRP_{II} for binding to the zinc atoms. Preliminary experiments showed that a 4 M imidazole solution (pH = 8) was able to release 85% of the *pf*HRP_{II} when the sample matrix was buffer and 50% when the sample matrix was whole blood (Figure VI.9). The reduced recovery observed from whole blood samples is likely due to the fact that it is a complex matrix and interactions

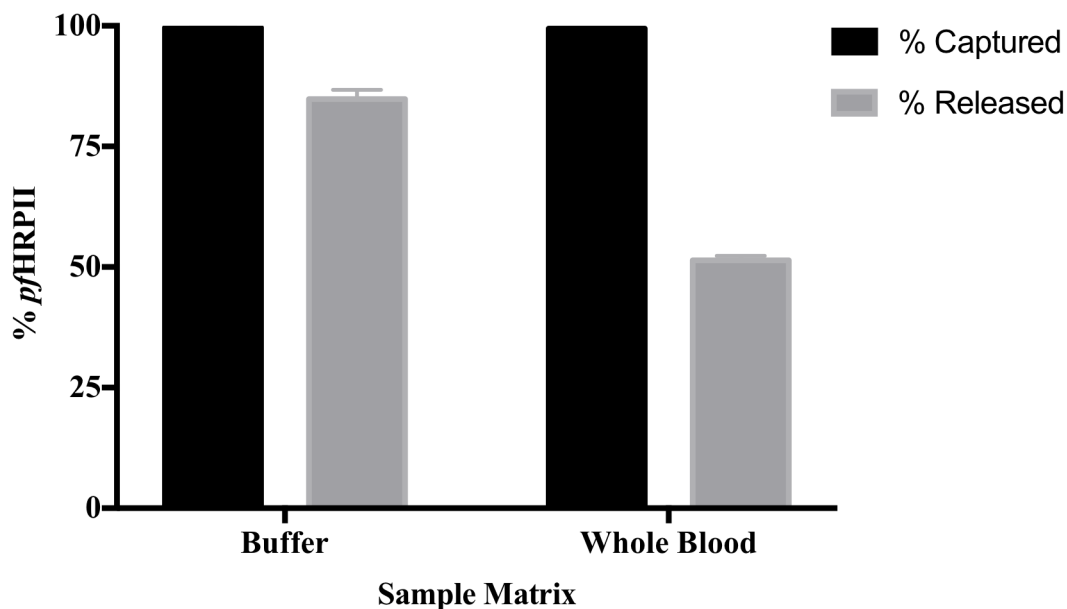


Figure VI.9. The amount *p/HRP II* captured, from buffer and whole blood sample matrices, by Zn-IDA membranes and subsequently released upon addition of imidazole.

with the components of the blood reduce the interaction of imidazole with the bound *p/HRP II*. Nonetheless, these results show great promise for the origami RDT as it was demonstrated that the biomarker can simply be released from the membrane through incorporation of imidazole into the release buffer. It is expected that amount of imidazole required for release could be lowered by decreasing the amount of zinc coordinated to the membrane, thus reducing the number of *p/HRP II* re-binding events.

Furthermore, this origami RDT design can be used for enhanced detection of biomarkers other than *p/HRP II* through the use of a unique capture and release reagent (C&R) developed in our lab.¹³⁵ This reagent is an antibody modified with a histidine peptide. The result is essentially a His-tagged antibody that can specifically bind to the Zn-IDA membrane. This process functionalizes the membrane with an antibody. As a result, whatever biomarker the antibody is against can also be captured on the Zn-IDA membrane (Figure VI.8). Since this binding is based upon interaction between histidine and zinc, just as with *p/HRP II*, this biomarker-antibody

complex can also be released by imidazole for subsequent detection on the lateral flow strip (Figure VI.10).

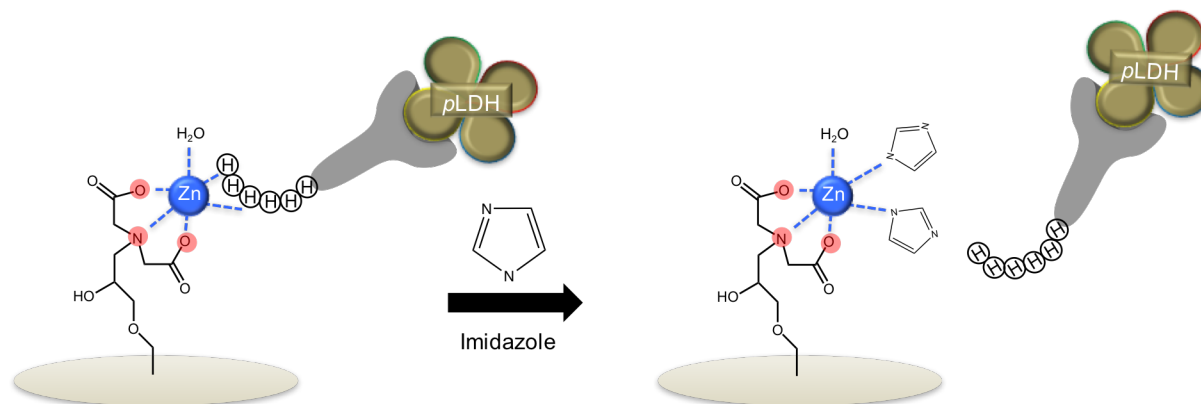


Figure VI.10. The catch and release reagent bound to a Zn-IDA functionalized membrane. This reagent allows for capture of *pLDH* on the membrane and subsequent elution results from addition of imidazole.

While this catch and release agent can be designed for a variety of biomarkers, it is specifically being developed for *pLDH*. This biomarker was mentioned in Chapter II as a good alternative to *pfHRP2*, as it is found in all species of malaria and also clears in the same time frame as the parasite. In the proposed origami RDT, the Zn-IDA membrane will be used to capture both *pfHRP2* and *pLDH* for subsequent release onto a dual RDT that can detect both biomarkers. The ability to detect these biomarkers produces a much more effective malaria RDT as detection of *pLDH* informs whether or not there is an active malaria infection, while the simultaneous presence of *pfHRP2* confirms a *falciparum* infection (Figure VI.11). The determination of species is important, as the treatment plan changes for *falciparum* vs. non-*falciparum* infections.¹³⁶

Thus, the development of the origami RDT from combination of a Zn-IDA flow-through membrane for capture of histidine-rich biomarkers or capture agents and a lateral flow assay for subsequent detection will produce an enhanced RDT for malaria. The incorporation of the Zn-

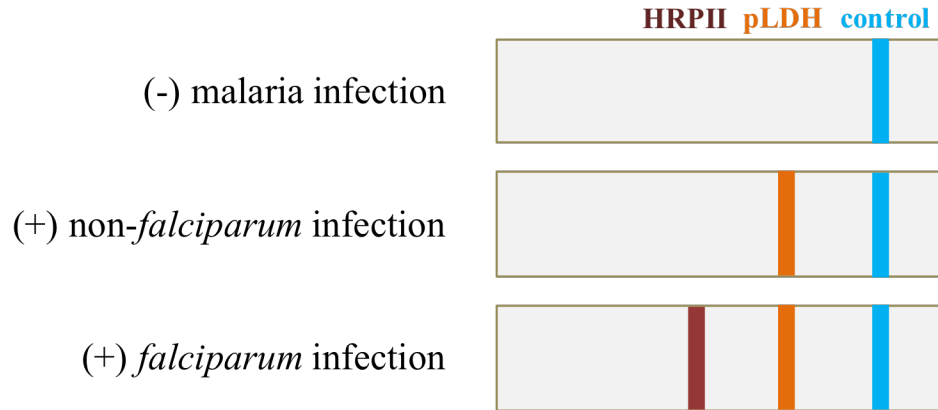


Figure V.11. Possible test outcomes for the origami RDT. Detection of both *pfHRPII* and *pLDH* allows for the user to distinguish between *falciparum* and *non-falciparum* infections.

IDA membrane produces a large volume RDT, which allows more biomarker to be presented to the test, increasing the ability of the test to detect low-infection level. It is expected that a sample volume of 500 μL will result in a 2-log enhancement in the limit of detection relative to commercially available RDTs. Furthermore, only a simple fold is required to achieve this result. This test has the potential to have a large impact on low-resource malaria diagnosis, as it will not only allow for the detection of low level infections but also provide information on the type of malaria infection. Thus, a new diagnostic will be developed that takes on the format of currently used RDTs, producing a more sensitive and accurate test with a workflow that will be familiar to healthcare workers.

In this work, many promising methods and designs for effective low-resource diagnostics have been presented. As these diagnostic strategies have been shown to effectually detect infectious diseases, the final challenge in diagnostic development arises: the translation of a diagnostic from the academic setting into a product that can be distributed throughout the world. This transition is a challenge that requires the collaboration of scholars in science, engineering and business, as well as academia and industry. It is only through such collaborations that these

diagnostic tools can actually be implemented. As I leave Vanderbilt, I am confident in the ability of the scientists that remain to carry on the development of the origami RDT. I also see an infrastructure forming that will bring together experts from a variety of backgrounds for the translation of these technologies into useful products. This outlook gives me great hope that the academic work presented here will move forward to impact the world.

Acknowledgments

Special thanks to Matthew Park for his work on the development of on-membrane *p/HRPII* detection and Thomas Scherr for his assistance with image analysis. Partial support for this work was provided by the Intellectual Ventures Laboratory and the Bill and Melinda Gates Foundation Grand Challenges in Global Health (OPP1161986). Further support was provided by Vanderbilt University through the Laboratories for Innovations in Global Health Technologies and the Mitchum E. Warren, Jr. Graduate Research Fellowship (L.E.G.).

REFERENCES

1. Hotez, P. J.; Kamath, A., Neglected Tropical Diseases in Sub-Saharan Africa: Review of Their Prevalence, Distribution, and Disease Burden. *PLOS Neglected Tropical Diseases* **2009**, *3* (8), e412.
2. Institute for Health Metrics and Evaluation: GBD Compare 2015. <http://vizhub.healthdata.org/gbd-compare/>.
3. Sharma, S.; Zapatero-Rodríguez, J.; Estrela, P.; O’Kennedy, R., Point-of-Care Diagnostics in Low Resource Settings: Present Status and Future Role of Microfluidics. *Biosensors* **2015**, *5* (3), 577-601.
4. Jamison, D. T.; Breman, J. G.; Measham, A. R.; Alleyne, G.; Claeson, M.; Evans, D. B.; Jha, P.; Mils, A.; Musgrove, P., *Priorities in Health*. World Bank: Washington, DC, USA, 2006.
5. Yager, P.; Edwards, T.; Fu, E.; Helton, K.; Nelson, K.; Tam, M. R.; Weigl, B. H., Microfluidic diagnostic technologies for global public health. *Nature* **2006**, *442* (7101), 412-418.
6. Peeling, R. W.; Mabey, D., Point-of-care tests for diagnosing infections in the developing world. *Clinical Microbiology and Infection* **2010**, *16* (8), 1062-1069.
7. Yager, P.; Domingo, G. J.; Gerdes, J., Point-of-Care Diagnostics for Global Health. *Annual Review of Biomedical Engineering* **2008**, *10* (1), 107-144.
8. Malkin, R. A., Design of Health Care Technologies for the Developing World. *Annual Review of Biomedical Engineering* **2007**, *9* (1), 567-587.
9. Bland, R. M.; Rollins, N. C.; Broeck, J. V. d.; Coovadia, H. M.; Child Health, G., The use of non-prescribed medication in the first 3 months of life in rural South Africa. *Tropical Medicine & International Health* **2004**, *9* (1), 118-124.
10. Urdea, M.; Penny, L. A.; Olmsted, S. S.; Giovanni, M. Y.; Kaspar, P.; Shepherd, A.; Wilson, P.; Dahl, C. A.; Buchsbaum, S.; Moeller, G.; Hay Burgess, D. C., Requirements for high impact diagnostics in the developing world. *Nature* **2006**, *SI*, 73-79.

11. Drain, P. K.; Hyle, E. P.; Noubary, F.; Freedberg, K. A.; Wilson, D.; Bishai, W. R.; Rodriguez, W.; Bassett, I. V., Diagnostic point-of-care tests in resource-limited settings. *The Lancet Infectious Diseases* **2014**, *14* (3), 239-249.
12. *World Malaria Report*; World Health Organization: 2016.
13. Cowman, A. F.; Healer, J.; Marapana, D.; Marsh, K., Malaria: Biology and Disease. *Cell* **2016**, *167* (3), 610-624.
14. Hill, A. V. S., Vaccines against malaria. *Philosophical Transactions of the Royal Society B: Biological Sciences* **2011**, *366* (1579), 2806.
15. *World Malaria Report*; World Health Organization: 2015.
16. Wu, L.; van den Hoogen, L. L.; Slater, H.; Walker, P. G. T.; Ghani, A. C.; Drakeley, C. J.; Okell, L. C., Comparison of diagnostics for the detection of asymptomatic Plasmodium falciparum infections to inform control and elimination strategies. *Nature* **2015**, *528* (7580), S86-S93.
17. Dondorp, A. M.; Yeung, S.; White, L.; Nguon, C.; Day, N. P. J.; Socheat, D.; von Seidlein, L., Artemisinin resistance: current status and scenarios for containment. *Nat Rev Micro* **2010**, *8* (4), 272-280.
18. Chen, I.; Clarke, S. E.; Gosling, R.; Hamainza, B.; Killeen, G.; Magill, A.; O'Meara, W.; Price, R. N.; Riley, E. M., "Asymptomatic" Malaria: A Chronic and Debilitating Infection That Should Be Treated. *PLOS Medicine* **2016**, *13* (1), e1001942.
19. Laban, N. M.; Kobayashi, T.; Hamapumbu, H.; Sullivan, D.; Mharakurwa, S.; Thuma, P. E.; Shiff, C. J.; Moss, W. J., Comparison of a PfHRP2-based rapid diagnostic test and PCR for malaria in a low prevalence setting in rural southern Zambia: implications for elimination. *Malaria Journal* **2015**, *14* (1), 25.
20. Bell, D.; Perkins, M., Malaria Diagnostics: Lighting the Path. In *Treatment and Prevention of Malaria*, Springer Basel: 2012; pp 293-307.
21. *Malaria Rapid Diagnostic Test Performance: Results of WHO product testing of malaria RDTs: Round 6 (2014-2015)*; World Health Organization: 2015.

22. Imwong, M.; Stepniewska, K.; Tripura, R.; Peto, T. J.; Lwin, K. M.; Vihokhern, B.; Wongsan, K.; von Seidlein, L.; Dhorda, M.; Snounou, G.; Keereecharoen, L.; Singhasivanon, P.; Sirithiranont, P.; Chalk, J.; Nguon, C.; Day, N. P. J.; Nosten, F.; Dondorp, A.; White, N. J., Numerical Distributions of Parasite Densities During Asymptomatic Malaria. *The Journal of Infectious Diseases* **2016**, *213* (8), 1322-1329.
23. Tiono, A. B.; Ouédraogo, A.; Diarra, A.; Coulibaly, S.; Soulama, I.; Konaté, A. T.; Barry, A.; Mukhopadhyay, A.; Sirima, S. B.; Hamed, K., Lessons learned from the use of HRP-2 based rapid diagnostic test in community-wide screening and treatment of asymptomatic carriers of *Plasmodium falciparum* in Burkina Faso. *Malaria Journal* **2014**, *13* (1), 30.
24. Cook, J.; Xu, W.; Msellem, M.; Vonk, M.; Bergström, B.; Gosling, R.; Al-Mafazy, A.-W.; McElroy, P.; Molteni, F.; Abass, A. K.; Garimo, I.; Ramsan, M.; Ali, A.; Mårtensson, A.; Björkman, A., Mass Screening and Treatment on the Basis of Results of a *Plasmodium falciparum*-Specific Rapid Diagnostic Test Did Not Reduce Malaria Incidence in Zanzibar. *The Journal of Infectious Diseases* **2015**, *211* (9), 1476-1483.
25. Tietje, K.; Hawkins, K.; Clerk, C.; Ebels, K.; McGray, S.; Crudder, C., The essential role of infection-detection technologies for malaria elimination and eradication. *Trends Parasitol.* **2014**, *30*.
26. Davis, K. M.; Swartz, J. D.; Haselton, F. R.; Wright, D. W., Low-Resource Method for Extracting the Malarial Biomarker Histidine-Rich Protein II To Enhance Diagnostic Test Performance. *Analytical Chemistry* **2012**, *84* (14), 6136-6142.
27. Davis, K. M.; Gibson, L. E.; Haselton, F. R.; Wright, D. W., Simple sample processing enhances malaria rapid diagnostic test performance. *Analyst* **2014**, *139* (12), 3026-3031.
28. Ricks, K. M.; Adams, N. M.; Scherr, T. F.; Haselton, F. R.; Wright, D. W., Direct transfer of HRPII-magnetic bead complexes to malaria rapid diagnostic tests significantly improves test sensitivity. *Malaria Journal* **2016**, *15* (1), 399.
29. Bauer, W. S.; Kimmel, D. W.; Adams, N. M.; Gibson, L. E.; Scherr, T. F.; Richardson, K. A.; Conrad, J. A.; Matakala, H. K.; Haselton, F. R.; Wright, D. W., Magnetically-Enabled Biomarker Extraction and Delivery System: Towards Integrated ASSURED Diagnostic Tools. *Analyst* **2017**, DOI: 10.1039/c7an00278e.
30. Bhamla, M. S.; Benson, B.; Chai, C.; Katsikis, G.; Johri, A.; Prakash, M., Hand-powered ultralow-cost paper centrifuge. *Nature Biomedical Engineering* **2017**, *1*, 0009.

31. Nunes Pauli, G. E.; de la Escosura-Muniz, A.; Parolo, C.; Helmuth Bechtold, I.; Merkoci, A., Lab-in-a-syringe using gold nanoparticles for rapid immunosensing of protein biomarkers. *Lab on a Chip* **2015**, *15* (2), 399-405.
32. Fu, E.; Liang, T.; Houghtaling, J.; Ramachandran, S.; Ramsey, S. A.; Lutz, B.; Yager, P., Enhanced Sensitivity of Lateral Flow Tests Using a Two-Dimensional Paper Network Format. *Anal. Chem. (Washington, DC, U. S.)* **2011**, *83* (20), 7941-7946.
33. Dirkzwager, R. M.; Liang, S.; Tanner, J. A., Development of Aptamer-Based Point-of-Care Diagnostic Devices for Malaria Using Three-Dimensional Printing Rapid Prototyping. *ACS Sensors* **2016**, *1* (4), 420-426.
34. Tong, S.; Ren, B.; Zheng, Z.; Shen, H.; Bao, G., Tiny Grains Give Huge Gains: Nanocrystal-Based Signal Amplification for Biomolecule Detection. *ACS Nano* **2013**, *7* (6), 5142-5150.
35. Badu-Tawiah, A. K.; Lathwal, S.; Kaastrup, K.; Al-Sayah, M.; Christodouleas, D. C.; Smith, B. S.; Whitesides, G. M.; Sikes, H. D., Polymerization-based signal amplification for paper-based immunoassays. *Lab on a Chip* **2015**, *15* (3), 655-659.
36. Markwalter, C. F.; Ricks, K. M.; Bitting, A. L.; Mudenda, L.; Wright, D. W., Simultaneous capture and sequential detection of two malarial biomarkers on magnetic microparticles. *Talanta* **2016**, *161*, 443-449.
37. McDade, T. W., Development and validation of assay protocols for use with dried blood spot samples. *American Journal of Human Biology* **2014**, *26* (1), 1-9.
38. Enderle, Y.; Foerster, K.; Burhenne, J., Clinical feasibility of dried blood spots: Analytics, validation, and applications. *Journal of Pharmaceutical and Biomedical Analysis* **2016**, *130*, 231-243.
39. Sample Collection Cards & Kits.
http://www.gelifesciences.com/webapp/wcs/stores/servlet/catalog/en/GELifeSciences-us/products/AlternativeProductStructure_21465/.
40. Demirev, P. A., Dried Blood Spots: Analysis and Applications. *Analytical Chemistry* **2013**, *85* (2), 779-789.

41. Tuailleon, E.; Mondain, A.-M.; Meroueh, F.; Ottomani, L.; Picot, M.-C.; Nagot, N.; Van de Perre, P.; Ducos, J., Dried blood spot for hepatitis C virus serology and molecular testing. *Hepatology* **2010**, *51* (3), 752-758.
42. Colson, K. E.; Potter, A.; Conde-Glez, C.; Hernandez, B.; Ríos-Zertuche, D.; Zúñiga-Brenes, P.; Collaborators, S. M.; Iriarte, E.; Mokdad, A. H., Use of a commercial ELISA for the detection of measles-specific immunoglobulin G (IgG) in dried blood spots collected from children living in low-resource settings. *Journal of Medical Virology* **2015**, *87* (9), 1491-1499.
43. Iroh Tam, P.-Y.; Hernandex-Alvarado, N.; Schleiss, M. R.; Hassan-Hanga, F.; Onuchukwu, C.; Umoru, D.; Obaro, S. K., Molecular Detection of *Streptococcus pneumoniae* on Dried Blood Spots from Febrile Nigerian Children Compared to Culture. *PLoS ONE* **2016**, *11* (3), e0152253.
44. Jain, P.; Chakma, B.; Patra, S.; Goswami, P., Potential Biomarkers and Their Applications for Rapid and Reliable Detection of Malaria. *BioMed Research International* **2014**, *2014*, 20 pages.
45. Bousema, T.; Okell, L.; Felger, I.; Drakeley, C., Asymptomatic malaria infections: detectability, transmissibility and public health relevance. *Nat Rev Micro* **2014**, *12* (12), 833-840.
46. Mukonka, V. M.; Chanda, E.; Haque, U.; Kamuliwo, M.; Mushinge, G.; Chileshe, J.; Chibwe, K. A.; Norris, D. E.; Mulenga, M.; Chaponda, M.; Muleba, M.; Glass, G. E.; Moss, W. J., High burden of malaria following scale-up of control interventions in Nchelenge District, Luapula Province, Zambia. *Malaria Journal* **2014**, *13* (1), 153.
47. Buderer, N. M. F., Statistical Methodology: I. Incorporating the Prevalence of Disease into the Sample Size Calculation for Sensitivity and Specificity. *Academic Emergency Medicine* **1996**, *3* (9), 895-900.
48. Hajian-Tilaki, K., Sample size estimation in diagnostic test studies of biomedical informatics. *Journal of Biomedical Informatics* **2014**, *48*, 193-204.
49. Scherr, T. F.; Ryskoski, H. B.; Sivakumar, A.; Ricks, K. M.; Adams, N. M.; Wright, D. W.; Haselton, F. R., A handheld orbital mixer for processing viscous samples in low resource settings. *Analytical Methods* **2016**, *8* (40), 7347-7353.
50. Adam, B. W.; Alexander, J. R.; Smith, S. J.; Chace, D. H.; Loeber, J. G.; Elvers, L. H.; Hannon, W. H., Recoveries of Phenylalanine from Two Sets of Dried-Blood-Spot Reference

Materials: Prediction from Hematocrit, Spot Volume, and Paper Matrix. *Clinical Chemistry* **2000**, *46* (1), 126.

51. Aydin-Schmidt, B.; Mubi, M.; Morris, U.; Petzold, M.; Ngasala, B. E.; Premji, Z.; Björkman, A.; Mårtensson, A., Usefulness of Plasmodium falciparum-specific rapid diagnostic tests for assessment of parasite clearance and detection of recurrent infections after artemisinin-based combination therapy. *Malaria Journal* **2013**, *12* (1), 349.

52. Grandesso, F.; Nabasumba, C.; Nyehangane, D.; Page, A.-L.; Bastard, M.; De Smet, M.; Boum, Y.; Etard, J.-F., Performance and time to become negative after treatment of three malaria rapid diagnostic tests in low and high malaria transmission settings. *Malaria Journal* **2016**, *15* (1), 496.

53. Bashir, I. M.; Otsyula, N.; Awinda, G.; Spring, M.; Schneider, P.; Waitumbi, J. N., Comparison of PfHRP-2/pLDH ELISA, qPCR and Microscopy for the Detection of Plasmodium Events and Prediction of Sick Visits during a Malaria Vaccine Study. *PLoS ONE* **2013**, *8* (3), e56828.

54. Hopkins, H.; Kambale, W.; Kanya, M. R.; Staedke, S. G.; Dorsey, G.; Rosenthal, P. J., Comparison of HRP2- and pLDH-Based Rapid Diagnostic Tests for Malaria with Longitudinal Follow-Up in Kampala, Uganda. *The American Journal of Tropical Medicine and Hygiene* **2007**, *76* (6), 1092-1097.

55. Desakorn, V.; Dondorp, A. M.; Silamut, K.; Pongtavornpinyo, W.; Sahassananda, D.; Chotivanich, K.; Pitisuttithum, P.; Smithyman, A. M.; Day, N. P. J.; White, N. J., Stage-dependent production and release of histidine-rich protein 2 by Plasmodium falciparum. *Transactions of The Royal Society of Tropical Medicine and Hygiene* **2005**, *99* (7), 517-524.

56. Hamainza, B.; Moonga, H.; Sikaala, C. H.; Kamuliwo, M.; Bennett, A.; Eisele, T. P.; Miller, J.; Seyoum, A.; Killeen, G. F., Monitoring, characterization and control of chronic, symptomatic malaria infections in rural Zambia through monthly household visits by paid community health workers. *Malaria Journal* **2014**, *13* (1), 128.

57. Tanner, M.; Greenwood, B.; Whitty, C. J. M.; Ansah, E. K.; Price, R. N.; Dondorp, A. M.; von Seidlein, L.; Baird, J. K.; Beeson, J. G.; Fowkes, F. J. I.; Hemingway, J.; Marsh, K.; Osier, F., Malaria eradication and elimination: views on how to translate a vision into reality. *BMC Medicine* **2015**, *13* (1), 167.

58. Plucinski, M. M.; Morton, L.; Bushman, M.; Dimbu, P. R.; Udhayakumar, V., Robust Algorithm for Systematic Classification of Malaria Late Treatment Failures as Recrudescence or

Reinfection Using Microsatellite Genotyping. *Antimicrobial Agents and Chemotherapy* **2015**, *59* (10), 6096-6100.

59. Yeka, A.; Tibenderana, J.; Achan, J.; D'Alessandro, U.; Talisuna, A. O., Efficacy of Quinine, Artemether-Lumefantrine and Dihydroartemisinin-Piperaquine as Rescue Treatment for Uncomplicated Malaria in Ugandan Children. *PLOS ONE* **2013**, *8* (1), e53772.

60. Mouatcho, J. C.; Goldring, J. P. D., Malaria rapid diagnostic tests: challenges and prospects. *Journal of Medical Microbiology* **2013**, *62* (10), 1491-1505.

61. Lindblade, K. A.; Steinhardt, L.; Samuels, A.; Kachur, S. P.; Slutsker, L., The silent threat: asymptomatic parasitemia and malaria transmission. *Expert Rev Anti Infect Ther.* **2013**, *11*.

62. Roh, M. E.; Oyet, C.; Orikiriza, P.; Wade, M.; Kiwanuka, G. N.; Mwanga-Amumpaire, J.; Parikh, S.; Boum, Y., Asymptomatic Plasmodium Infections in Children in Low Malaria Transmission Setting, Southwestern Uganda. *Emerging Infectious Diseases* **2016**, *22* (8), 1494-1498.

63. Ashley, E. A.; White, N. J., The duration of Plasmodium falciparum infections. *Malaria Journal* **2014**, *13* (1), 500.

64. Mukaka, M. M., A guide to appropriate use of Correlation coefficient in medical research. *Malawi Medical Journal : The Journal of Medical Association of Malawi* **2012**, *24* (3), 69-71.

65. Baker, J.; McCarthy, J.; Gatton, M.; Kyle, D. E.; Belizario, V.; Luchavez, J.; Bell, D.; Cheng, Q., Genetic Diversity of Plasmodium falciparum Histidine-Rich Protein 2 (PfHRP2) and Its Effect on the Performance of PfHRP2-Based Rapid Diagnostic Tests. *Journal of Infectious Diseases* **2005**, *192* (5), 870-877.

66. Martin, S. K.; Rajasekariah, G. H.; Awinda, G.; Waitumbi, J.; Kifude, C., Unified Parasite Lactate Dehydrogenase and Histidine-Rich Protein ELISA for Quantification of Plasmodium falciparum. *The American Journal of Tropical Medicine and Hygiene* **2009**, *80* (4), 516-522.

67. Rubach, M. P.; Mukemba, J.; Florence, S.; John, B.; Crookston, B.; Lopansri, B. K.; Yeo, T. W.; Piera, K. A.; Alder, S. C.; Weinberg, J. B.; Anstey, N. M.; Granger, D. L.; Mwaikambo, E. D., Plasma Plasmodium falciparum Histidine-Rich Protein-2 Concentrations Are Associated with Malaria Severity and Mortality in Tanzanian Children. *PLOS ONE* **2012**, *7* (5), e35985.

68. Tangpukdee, N.; Duangdee, C.; Wilairatana, P.; Krudsood, S., Malaria Diagnosis: A Brief Review. *Korean J Parasitol* **2009**, *47* (2), 93-102.
69. Murray, C. K.; Bennett, J. W., Rapid Diagnosis of Malaria. *Interdisciplinary Perspectives on Infectious Diseases* **2009**, *2009*, 415953.
70. Murray, C. K.; Gasser, R. A.; Magill, A. J.; Miller, R. S., Update on Rapid Diagnostic Testing for Malaria. *Clinical Microbiology Reviews* **2008**, *21* (1), 97-110.
71. Bell, D.; Peeling, R. W., Evaluation of rapid diagnostic tests: malaria. *Nature Reviews Microbiology* **2006**, *4* (9), S34.
72. Maltha, J.; Gillet, P.; Jacobs, J., Malaria rapid diagnostic tests in endemic settings. *Clinical Microbiology and Infection* **2013**, *19* (5), 399-407.
73. *Malaria Rapid Diagnostic Test Performance: Results of WHO product testing of malaria RDTs- Round 3*; World Health Organization: 2011.
74. Wongsrichanalai, C.; Barcus, M. J.; Muth, S.; Sutamihardja, A.; Wernsdorfer, W. H., A Review of Malaria Diagnostic Tools: Microscopy and Rapid Diagnostic Test (RDT). *The American Journal of Tropical Medicine and Hygiene* **2007**, *77* (6 Suppl), 119-127.
75. Bell, D.; Wongsrichanalai, C.; Barnwell, J. W., Ensuring quality and access for malaria diagnosis: how can it be achieved? *Nat Rev Micro* **2006**, *4* (9), 682-695.
76. Gubala, V.; Harris, L. F.; Ricco, A. J.; Tan, M. X.; Williams, D. E., Point of Care Diagnostics: Status and Future. *Analytical Chemistry* **2011**, *84* (2), 487-515.
77. Mudanyali, O.; Dimitrov, S.; Sikora, U.; Padmanabhan, S.; Navruz, I.; Ozcan, A., Integrated rapid-diagnostic-test reader platform on a cellphone. *Lab on a Chip* **2012**, *12* (15), 2678-2686.
78. Okell, L. C.; Bousema, T.; Griffin, J. T.; Ouedraogo, A. L.; Ghani, A. C.; Drakeley, C. J., Factors determining the occurrence of submicroscopic malaria infections and their relevance for control. *Nat Commun* **2012**, *3*, 1237.

79. Sturrock, H. J.; Hsiang, M. S.; Cohen, J. M.; Smith, D. L.; Greenhouse, B.; Bousema, T., Targeting asymptomatic malaria infections: active surveillance in control and elimination. *PLoS Med.* **2013**, *10*.
80. Laishram, D.; Sutton, P.; Nanda, N.; Sharma, V.; Sobti, R.; Carlton, J.; Joshi, H., The complexities of malaria disease manifestations with a focus on asymptomatic malaria. *Malaria Journal* **2012**, *11* (1), 29.
81. Shekalaghe, S.; Cancino, M.; Mavere, C.; Juma, O.; Mohammed, A.; Abdulla, S.; Ferro, S., Clinical performance of an automated reader in interpreting malaria rapid diagnostic tests in Tanzania. *Malaria Journal* **2013**, *12* (1), 1-9.
82. Feng, S.; Caire, R.; Cortazar, B.; Turan, M.; Wong, A.; Ozcan, A., Immunochromatographic Diagnostic Test Analysis Using Google Glass. *ACS Nano* **2014**, *8* (3), 3069-3079.
83. Saiki, R. K.; Scharf, S.; Faloona, F.; Mullis, K. B.; Horn, G. T.; Erlich, H. A.; Arnheim, N., Enzymatic amplification of beta-globin genomic sequences and restriction site analysis for diagnosis of sickle cell anemia. *Science* **1985**, *230* (4732), 1350-1354.
84. Engvall, E.; Perlmann, P., Enzyme-linked immunosorbent assay (ELISA) quantitative assay of immunoglobulin G. *Immunochemistry* **1971**, *8* (9), 871-874.
85. Van Weemen, B. K.; Schuurs, A. H. W. M., Immunoassay using antigen—enzyme conjugates. *FEBS Letters* **1971**, *15* (3), 232-236.
86. Drain, C. M.; Smeureanu, G.; Patel, S.; Gong, X.; Garno, J.; Arijeloye, J., Porphyrin nanoparticles as supramolecular systems. *New Journal of Chemistry* **2006**, *30* (12), 1834-1843.
87. Gong, X.; Milic, T.; Xu, C.; Batteas, J. D.; Drain, C. M., Preparation and Characterization of Porphyrin Nanoparticles. *Journal of the American Chemical Society* **2002**, *124* (48), 14290-14291.
88. Kruk, M. M.; Braslavsky, S. E., Structural volume changes upon triplet formation of water-soluble porphyrins depend on the resonant effect of the substituents. *Photochemical & Photobiological Sciences* **2012**, *11* (6), 972-978.
89. Hunter, C. A.; Sanders, J. K. M., The nature of .pi.-.pi. interactions. *Journal of the American Chemical Society* **1990**, *112* (14), 5525-5534.

90. Kasha M., R. H. R., Ashraf El-Bayoumi M., The exciton model in molecular spectroscopy. *Pure Appl. Chem.* **1965**, *11* (3-4), 371-392.
91. Rahman, M.; Harmon, H. J., Absorbance change and static quenching of fluorescence of meso-tetra(4-sulfonatophenyl)porphyrin (TPPS) by trinitrotoluene (TNT). *Spectrochimica Acta Part A: Molecular and Biomolecular Spectroscopy* **2006**, *65* (3-4), 901-906.
92. Blencowe, A.; Hayes, W., Development and application of diazirines in biological and synthetic macromolecular systems. *Soft Matter* **2005**, *1* (3), 178-205.
93. *Malaria Rapid Diagnostic Test Performance: Results of WHO product testing of malaria RDTs: Round 5*; World Health Organization: 2013.
94. Kifude, C. M.; Rajasekariah, H. G.; Sullivan, D. J.; Stewart, V. A.; Angov, E.; Martin, S. K.; Diggs, C. L.; Waitumbi, J. N., Enzyme-Linked Immunosorbent Assay for Detection of Plasmodium falciparum Histidine-Rich Protein 2 in Blood, Plasma, and Serum. *Clinical and Vaccine Immunology : CVI* **2008**, *15* (6), 1012-1018.
95. Veitch, N. C., Horseradish peroxidase: a modern view of a classic enzyme. *Phytochemistry* **2004**, *65* (3), 249-259.
96. Lequin, R. M., Enzyme Immunoassay (EIA)/Enzyme-Linked Immunosorbent Assay (ELISA). *Clinical Chemistry* **2005**, *51* (12), 2415.
97. Lin, Y.; Ren, J.; Qu, X., Catalytically Active Nanomaterials: A Promising Candidate for Artificial Enzymes. *Accounts of Chemical Research* **2014**, *47* (4), 1097-1105.
98. Deng, X.; Fang, Y.; Lin, S.; Cheng, Q.; Liu, Q.; Zhang, X., Porphyrin-Based Porous Organic Frameworks as a Biomimetic Catalyst for Highly Efficient Colorimetric Immunoassay. *ACS Applied Materials & Interfaces* **2017**, *9* (4), 3514-3523.
99. Zhang, W.; Ma, D.; Du, J., Prussian blue nanoparticles as peroxidase mimetics for sensitive colorimetric detection of hydrogen peroxide and glucose. *Talanta* **2014**, *120*, 362-367.
100. Sun, R.; Wang, Y.; Ni, Y.; Kokot, S., Spectrophotometric analysis of phenols, which involves a hemin-graphene hybrid nanoparticles with peroxidase-like activity. *Journal of Hazardous Materials* **2014**, *266*, 60-67.

101. Wang, L.; Yang, Q.; Ma, G.; Lin, W.; Wang, Z.; Huang, M.; Chen, S., Development of biocompatible PAMAM 'dendrzyme' to maintain catalytic activity in biological complex medium. *Journal of Materials Chemistry B* **2013**, *1* (34), 4259-4266.
102. Ahmed, S. R.; Kim, J.; Suzuki, T.; Lee, J.; Park, E. Y., Detection of influenza virus using peroxidase-mimic of gold nanoparticles. *Biotechnology and Bioengineering* **2016**, *113* (10), 2298-2303.
103. Gao, L.; Zhuang, J.; Nie, L.; Zhang, J.; Zhang, Y.; Gu, N.; Wang, T.; Feng, J.; Yang, D.; Perrett, S.; Yan, X., Intrinsic peroxidase-like activity of ferromagnetic nanoparticles. *Nat Nano* **2007**, *2* (9), 577-583.
104. Ye, H.; Yang, K.; Tao, J.; Liu, Y.; Zhang, Q.; Habibi, S.; Nie, Z.; Xia, X., An Enzyme-Free Signal Amplification Technique for Ultrasensitive Colorimetric Assay of Disease Biomarkers. *ACS Nano* **2017**, *11* (2), 2052-2059.
105. Jampaiah, D.; Srinivasa Reddy, T.; Coyle, V. E.; Nafady, A.; Bhargava, S. K., Co₃O₄@CeO₂ hybrid flower-like microspheres: a strong synergistic peroxidase-mimicking artificial enzyme with high sensitivity for glucose detection. *Journal of Materials Chemistry B* **2017**, *5* (4), 720-730.
106. Xia, X.; Zhang, J.; Lu, N.; Kim, M. J.; Ghale, K.; Xu, Y.; McKenzie, E.; Liu, J.; Ye, H., Pd-Ir Core-Shell Nanocubes: A Type of Highly Efficient and Versatile Peroxidase Mimic. *ACS Nano* **2015**, *9* (10), 9994-10004.
107. Wang, Z.; Yang, X.; Yang, J.; Jiang, Y.; He, N., Peroxidase-like activity of mesoporous silica encapsulated Pt nanoparticle and its application in colorimetric immunoassay. *Analytica Chimica Acta* **2015**, *862*, 53-63.
108. Gharibi, H.; Moosavi-Movahedi, Z.; Javadian, S.; Nazari, K.; Moosavi-Movahedi, A. A., Vesicular Mixed Gemini-SDS-Hemin-Imidazole Complex as a Peroxidase-Like Nano Artificial Enzyme. *The Journal of Physical Chemistry B* **2011**, *115* (16), 4671-4679.
109. Qu, R.; Shen, L.; Chai, Z.; Jing, C.; Zhang, Y.; An, Y.; Shi, L., Hemin-Block Copolymer Micelle as an Artificial Peroxidase and Its Applications in Chromogenic Detection and Biocatalysis. *ACS Applied Materials & Interfaces* **2014**, *6* (21), 19207-19216.
110. Dong, M.; Zhang, L.; Li, R.; Li, S.; Jiang, Y.; Qiao, Y.; Duan, Z.; Li, R.; Wang, Q.; Wang, H., Crosslinking catalysis-active center of hemin on the protein scaffold toward peroxidase mimic with powerful catalysis. *RSC Advances* **2016**, *6* (53), 47595-47599.

111. Perutz, M. F., Regulation of Oxygen Affinity of Hemoglobin: Influence of Structure of the Globin on the Heme Iron. *Annual Review of Biochemistry* **1979**, *48* (1), 327-386.
112. Tohjo, M.; Nakamura, Y.; Kurihara, K.; Samejima, T.; Hachimori, Y.; Shibata, K., Peroxidase activity of hemoproteins. IV. Hematin complexes as model enzymes of peroxidase. *Archives of Biochemistry and Biophysics* **1962**, *99* (2), 222-240.
113. Zhang, X.-Q.; Gong, S.-W.; Zhang, Y.; Yang, T.; Wang, C.-Y.; Gu, N., Prussian blue modified iron oxide magnetic nanoparticles and their high peroxidase-like activity. *Journal of Materials Chemistry* **2010**, *20* (24), 5110-5116.
114. Gibson, L. E.; Wright, D. W., Sensitive Method for Biomolecule Detection Utilizing Signal Amplification with Porphyrin Nanoparticles. *Analytical Chemistry* **2016**, *88* (11), 5928-5933.
115. Cole, K. A.; Ziegler, J.; Evans, C. A.; Wright, D. W., Metalloporphyrins inhibit β -hematin (hemozoin) formation. *Journal of Inorganic Biochemistry* **2000**, *78* (2), 109-115.
116. Morrison, D. B.; Williams, E. F., The Solubility and Titration of Hemin and Ferrihemic Acid. *Journal of Biological Chemistry* **1941**, *137* (2), 461-473.
117. Uno, T.; Takeda, A.; Shimabayashi, S., Effects of Imidazoles and pH on the Peroxidase Activity of the Hemin-Hydrogen Peroxide System. *Inorganic Chemistry* **1995**, *34* (6), 1599-1607.
118. Adamczyk, K.; Simpson, N.; Greetham, G. M.; Gumiero, A.; Walsh, M. A.; Towrie, M.; Parker, A. W.; Hunt, N. T., Ultrafast infrared spectroscopy reveals water-mediated coherent dynamics in an enzyme active site. *Chemical Science* **2015**, *6* (1), 505-516.
119. Bertini, I.; Gray, H. B.; Lippard, S. J.; Valentine, J. S., *Bioinorganic Chemistry*. University Science Books: Mill Valley, CA, 1994; pp 295-298.
120. Mazumdar, S.; Dugad, L. B.; Medhi, O. K.; Mitra, S., Proton nuclear magnetic resonance studies on haemin chloride in pyridine-water solution. *Journal of the Chemical Society, Dalton Transactions* **1988**, (11), 2797-2802.
121. Das, D. K.; Medhi, O. K., Aqua pyridine complex of protoporphyrinato IX iron (III): Effect of ligand binding, surfactant concentration and proton coupling on redox potential. **2005**.

122. Wilson, M. L., Malaria Rapid Diagnostic Tests. *Clinical Infectious Diseases* **2012**, *54* (11), 1637-1641.
123. Chiodini, P. L.; Bowers, K.; Jorgensen, P.; Barnwell, J. W.; Grady, K. K.; Luchavez, J.; Moody, A. H.; Cenizal, A.; Bell, D., The heat stability of Plasmodium lactate dehydrogenase-based and histidine-rich protein 2-based malaria rapid diagnostic tests. *Transactions of The Royal Society of Tropical Medicine and Hygiene* **2007**, *101* (4), 331-337.
124. Abba, K.; Deeks, J. J.; Olliaro, P.; Naing, C. M.; Jackson, S. M.; Takwoingi, Y.; Donegan, S.; Garner, P., Rapid diagnostic tests for diagnosing uncomplicated P. falciparum malaria in endemic countries. *Cochrane Database Syst Rev* **2011**, (7).
125. Deutsch-Feldman, M. Evaluating a Reactive Test-and-Treat Program for Sub-Patent Malaria in Macha, Zambia: Optimal Strategies to Achieve Elimination. Johns Hopkins University, 2016.
126. Wu, C.-Y.; Suen, S.-Y.; Chen, S.-C.; Tzeng, J.-H., Analysis of protein adsorption on regenerated cellulose-based immobilized copper ion affinity membranes. *Journal of Chromatography A* **2003**, *996* (1–2), 53-70.
127. Diekmann, S.; Siegmund, G.; Roecker, A.; Klemm, D. O., Regioselective Nitrilotriacetic Acid–Cellulose–Nickel-Complexes for Immobilisation of His6-Tag Proteins. *Cellulose* **2003**, *10* (1), 53-63.
128. Liu, Y.-C.; ChangChien, C.-C.; Suen, S.-Y., Purification of penicillin G acylase using immobilized metal affinity membranes. *Journal of Chromatography B* **2003**, *794* (1), 67-76.
129. Chan, W. H.; Lam-Leung, S. Y.; Fong, W. S.; Kwan, F. W., Synthesis and characterization of iminodiacetate cellulosic sorbent and its application in metal ion extraction. *Journal of Applied Polymer Science* **1992**, *46* (5), 921-930.
130. Ke, Y.-M.; Chen, C.-I.; Kao, P.-M.; Chen, H.-B.; Huang, H.-C.; Yao, C.-J.; Liu, Y.-C., Preparation of the immobilized metal affinity membrane with high amount of metal ions and protein adsorption efficiencies. *Process Biochemistry* **2010**, *45* (4), 500-506.
131. Gennaro, M. C.; Mentasti, E.; Sarzanini, C.; Baiocchi, C., Determination of traces of lead and copper after preconcentration on iminodiacetic acid-cellulose filters. *Analytica Chimica Acta* **1985**, *174*, 259-268.

132. Panton, L. J.; McPhie, P.; Lee Maloy, W.; Wellems, T. E.; Taylor, D. W.; Howard, R. J., Purification and partial characterization of an unusual protein of *Plasmodium falciparum*: histidine-rich protein II. *Molecular and Biochemical Parasitology* **1989**, *35* (2), 149-160.
133. Cretich, M.; Torrisi, M.; Daminelli, S.; Gagni, P.; Plavisch, L.; Chiari, M., Flow-through, viral co-infection assay for resource-limited settings. *Talanta* **2015**, *132*, 315-320.
134. Abdelwahed, W.; Degobert, G.; Stainmesse, S.; Fessi, H., Freeze-drying of nanoparticles: Formulation, process and storage considerations. *Advanced Drug Delivery Reviews* **2006**, *58* (15), 1688-1713.
135. Bauer, W. S.; Gulka, C. P.; Silva-Baucage, L.; Adams, N. M.; Haselton, F. R.; Wright, D. W., Development of a Magnetically-Enabled Multiplex Biomarker Enrichment Platform to Improve the Test Line Signals and Detection Limits of Rapid Diagnostic Tests. **2017**, *In preparation*.
136. *Guidelines for the Treatment of Malaria*; World Health Organization: 2015.
137. Chiodini, P. L., Malaria diagnostics: now and the future. *Parasitology* **2014**, *141* (14), 1873-1879.
138. Cordray, M. S.; Richards-Kortum, R. R., Emerging Nucleic Acid-Based Tests for Point-of-Care Detection of Malaria. *The American Journal of Tropical Medicine and Hygiene* **2012**, *87* (2), 223-230.
139. Jayasena, S. D., Aptamers: An Emerging Class of Molecules That Rival Antibodies in Diagnostics. *Clinical Chemistry* **1999**, *45* (9), 1628-1650.
140. Tan, W.; Donovan, M. J.; Jiang, J., Aptamers from Cell-Based Selection for Bioanalytical Applications. *Chemical Reviews* **2013**, *113* (4), 2842-2862.
141. Yang, X.; Bassett, S. E.; Li, X.; Luxon, B. A.; Herzog, N. K.; Shope, R. E.; Aronson, J.; Prow, T. W.; Leary, J. F.; Kirby, R.; Ellington, A. D.; Gorenstein, D. G., Construction and selection of bead-bound combinatorial oligonucleoside phosphorothioate and phosphorodithioate aptamer libraries designed for rapid PCR-based sequencing. *Nucleic Acids Research* **2002**, *30* (23), e132-e132.
142. He, W.; Elizondo-Riojas, M.-A.; Li, X.; Lokesh, G. L. R.; Somasunderam, A.; Thiviyanathan, V.; Volk, D. E.; Durland, R. H.; Englehardt, J.; Cavasotto, C. N.; Gorenstein, D.

G., X-Aptamers: A Bead-Based Selection Method for Random Incorporation of Druglike Moieties onto Next-Generation Aptamers for Enhanced Binding. *Biochemistry* **2012**, *51* (42), 8321-8323.

143. Garlick, R. L.; Kirschner Rj Fau - Eckenrode, F. M.; Eckenrode Fm Fau - Tarpley, W. G.; Tarpley Wg Fau - Tomich, C. S.; Tomich, C. S., Escherichia coli expression, purification, and biological activity of a truncated soluble CD4. *AIDS Research and Human Retroviruses* **2009**, *6* (4), 465-479.

144. Tobias, R.; Kumaraswamy, S., Application Note 14: Biomolecular Binding Kinetics Assays on the Octet Platform. Pall Life Sciences.

145. Jaffe, M., Uber den neideschlag, welchen pikrinsaure in normalen hrn erzeugt und uber eine neue reaction des kreatinins. *Z Physiol Chem* **1886**, *10*, 391-400.

146. Peake, M.; Whiting, M., Measurement of Serum Creatinine – Current Status and Future Goals. *Clinical Biochemist Reviews* **2006**, *27* (4), 173-184.

147. Spencer, K., Analytical Reviews in Clinical Biochemistry: The Estimation of Creatinine. *Annals of Clinical Biochemistry* **1986**, *23* (1), 1-25.

148. Hussain, I.; Tariq, M. I.; Siddiqui, H. L., Structure elucidation of chromogen resulting from Jaffe's reaction. *Journal of the Chemical Society of Pakistan* **2009**, *31* (6), 937-948.

149. Savory, D. J., Reference Ranges for Serum Creatinine in Infants, Children and Adolescents. *Annals of Clinical Biochemistry* **1990**, *27* (2), 99-101.

150. Ceriotti, F.; Boyd, J. C.; Klein, G.; Henny, J.; Queraltó, J.; Kairisto, V.; Panteghini, M., Reference Intervals for Serum Creatinine Concentrations: Assessment of Available Data for Global Application. *Clinical Chemistry* **2008**, *54* (3), 559.

APPENDIX A

SUPPORTING INFORMATION: CHAPTER II

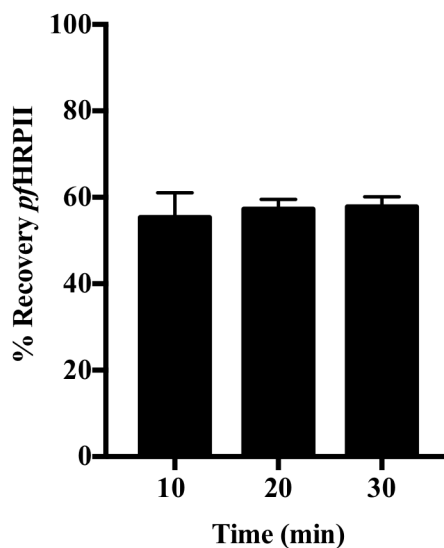


Figure SI II.1. The effect of vortex mixing time on *p/HRP II* recovery. No difference was observed between time points.

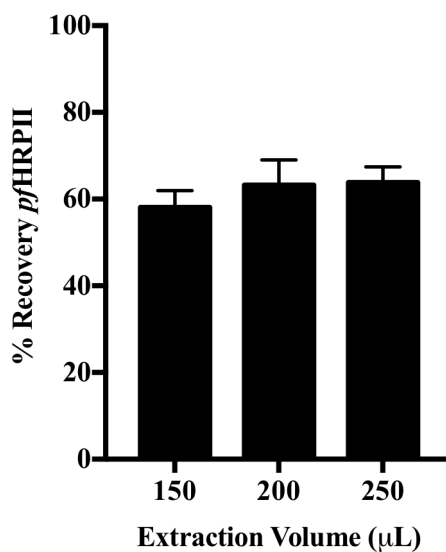


Figure SI II.2. The effect of the volume of extraction buffer on *p/HRP II* recovery. No difference was observed with different volumes.

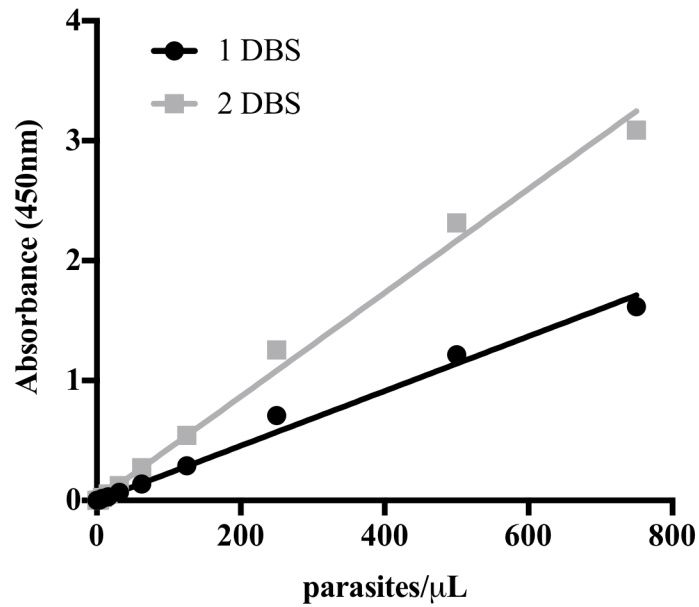


Figure SI II.3. A dried blood spot (DBS) ELISA standard curve was performed with one and two DBS samples in 300 μL of extraction buffer. As was expected, when two DBS were used the assay had twice the sensitivity. One DBS $y = 0.0023x$, two DBS $y = 0.0043x$.

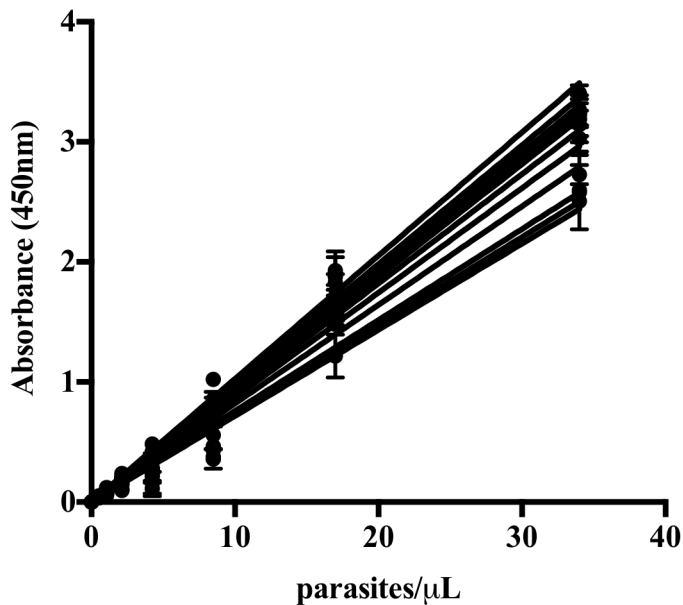


Figure SI II.4. *pfHRP II* ELISA standard curves performed at Macha Research Trust. Standards were made from parasite spiked diluted whole blood. These fourteen curves had an intra-assay variability of 6% and an inter-assay variability of 18% with a calculated LOD of 0.165 ± 0.003 pM *pfHRP II*.

Table SI II.1. *p*/HRP II levels found by *p*/HRP II DBS ELISA for patient samples from several of the first and last points in the time study. Values were not corrected for the inherent dilution that occurs upon DBS extraction. Microscopy results are also shown in parasites/ μ L (par/ μ L).

Patient Sample ID	Time Point (days)	Microscopy (par/ μ L)	<i>p</i> /HRP II DBS ELISA (pM)	Standard deviation (pM)	Patient Sample ID	Time Point (days)	Microscopy (par/ μ L)	<i>p</i> /HRP II DBS ELISA (pM)	Standard deviation (pM)
Patient 1	0.1	242000	1410	90	Patient 19	0.1	43440	230	70
	0.25	8000	570	40		0.25	21880	48	6
	0.5	840	227	5		0.5	10160	158	9
	0.75	0	52	3		0.75	3720	89	4
	37	0	0.12	0.03		35	0	1.04	0.06
Patient 2	0.1	145600	2490	80	Patient 20	0.1	3280	25	2
	0.25	24360	1400	200		0.25	50858	35	2
	0.5	22720	400	200		0.5	51556	64	4
	0.75	10080	300	100		0.75	66551	114	7
	38	0	-0.03	0.03		41	0	0.01	0.04
Patient 3	0.1	1440	670	40	Patient 21	0.1	17040	8	1
	0.25	3520	470	30		0.5	89875	145	7
	0.5	3680	170	10		0.75	40157	8.0	0.6
	0.75	1080	720	50		38	0	0.07	0.06
	31	0	-0.02	0.02					
	38	0	180	10					
Patient 4	0.1	1800	14	1	Patient 23	0.1	159600	600	30
	0.25	15280	29	2		0.25	12600	110	7
	0.5	14720	43	3		0.5	3640	36	2
	0.75	2120	37	4		0.75	840	25	2
	31	0	1.0	0.2		44	0	0.03	0.05
	38	0	1.1	0.1					
Patient 5	0.1	61680	670	30	Patient 24	0.1	92960	9.1	0.6
	0.25	29440	280	10		0.25	55136	66	3
	0.5	22469	300	100		0.75	3160	23	4
	0.75	1600	190	10		38	0	0.09	0.04
	35	0	0.48	0.08					
Patient 6	0.1	36400	200	10	Patient 26	0.1	3640	4600	400
	0.25	51239	45	2		0.25	4080	3400	200
	0.5	71016	31	2		0.5	1480	1400	100
	0.75	1560	71	4		0.75	128	1200	200
	40	0	0.66	0.03		28	0	0.13	0.07
					35	0	0.46	0.07	

Patient 7	0.1	23720	380	17	Patient 28	0.1	26980	11300	500
	0.25	14960	160	17		0.25	18760	10900	400
	0.5	560	72	3		0.5	1400	1700	200
	0.75	400	62	3		0.75	48	1829.514	700
	35	0	0.049	0.008		37	0	0.17	0.04
Patient 8	0.1	66400	350	40	Patient 31	0.1	10160	7500	600
	0.25	124160	1120	50		0.25	4800	500	200
	0.5	52045	249	6		0.5	2440	77	8
	0.75	1280	530	20		0.75	1360	110	6
	36	0	0.8	0.2		35	0	0.03	0.02
Patient 9	0.1	90080	240	10	Patient 32	0.1	4800	1200	50
	0.25	3640	250	10		0.25	1200	800	40
	0.5	3120	94	4		0.5	720	560	30
	0.75	272	38	3		0.75	0	880	40
	38	0	0.56	0.05		41	0	0.15	0.01
						48	0	0.18	0.02
Patient 10	0.1	29000	720	50	Patient 33	0.1	17040	3900	200
	0.25	37246	550	20		0.25	560	760	50
	0.5	39500	300	10		0.5	640	40	2
	0.75	480	51	2		0.75	520	40	10
	39	0	0.08	0.04		38	0	0.15	0.01
Patient 11	0.1	1120	6.7	0.8	Patient 34	0.1	3760	1200	100
	0.25	176	7	2		0.25	100652	100	20
	0.5	0	5.4	0.6		0.5	70788	54	3
	0.75	0	2	2		0.75	62725	72	4
	33	0	-0.06	0.008		44	0	0.05	0.01
	40	0	-0.049	0.008					
Patient 12	0.1	49960	630	90	Patient 35	0.1	6440	1800	500
	0.25	32836	930	40		0.25	4080	2100	400
	0.5	8240	240	10		0.5	1480	740	50
	0.75	1040	280	10		0.75	600	130	10
	42	0	-0.01	0.01		39	0	1.2	0.1
						46	0	0.07	0.01
Patient 13	0.1	13760	370	30	Patient 36	0.1	18440	1330	60
	0.25	6240	86	7		0.25	1160	2000	100
	0.5	64	19.0	0.8		0.5	480	3600	200
	0.75	0	8	2		0.75	176	3100	200
	41	0	-0.04	0.01		41	0	0	

Patient 14	0.1	5160	82	4	Patient 37	0.1	13120	1520	60
	0.25	173667	33	3		0.25	5080	115	2
	0.5	170667	200	20		0.5	1960	73	1
	0.75	28629	50	20		0.75	680	117	2
	38	0	-0.06	0.04		35	0	117	8
Patient 15	0.1	460200	540	30	Patient 38	0.1	82320	2900	100
	0.25	304000	330	10		0.25	7840	420	50
	0.5	152000	700	70		35	0	2.6	0.1
	0.75	4120	230	10					
	40	0	0.4	0.1					
Patient 16	0.1	81000	480	50	Patient 39	0.1	10560	520	40
	0.25	9240	64	7		0.25	21788	261	7
	0.5	17240	9.3	0.3		0.5	11240	90	10
	0.75	256	49	3		0.75	5720	78	3
	39	0	0.60	0.06		35	0	2.0	0.1
Patient 17	0.1	7200	10	20	Patient 40	0.1	22120	560	20
	0.25	117819	30	3		0.25	12640	104	4
	0.5	1280	140	10		0.5	11480	129	6
	0.75	5400	13	1		0.75	960	63	3
	39	0	0.3	0.2		35	0	2.2	0.1
Patient 18	0.1	6640	86	8					
	0.25	440	40	2					
	0.5	352	28	1					
	0.75	112	18	3					
	31	0	0.06	0.04					
	39	0	0.2	0.2					

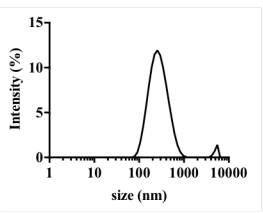
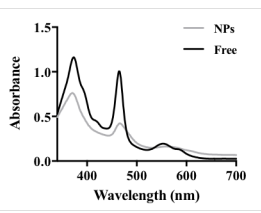
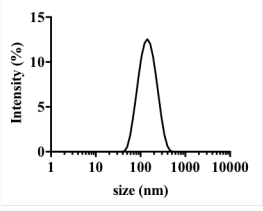
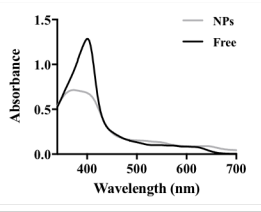
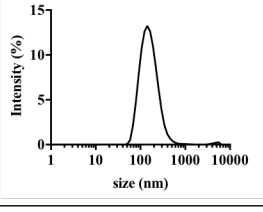
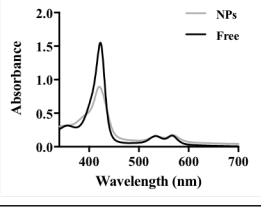
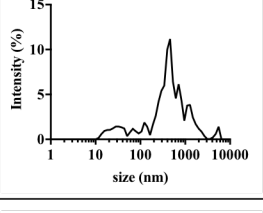
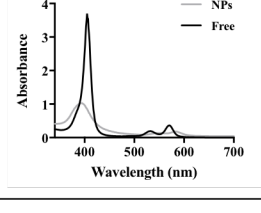
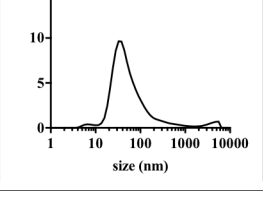
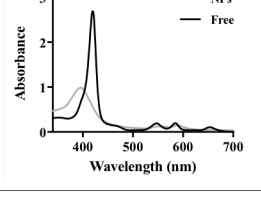
Acknowledgements

I would like to acknowledge Christine Markwalter, Danielle Kimmel, Lwiindi Mudenda, Saidon Mbambara, and Phil Thuma for their contributions to this work. Also, we thank the children and guardians who agreed to participate in the clinical aspect of this study, as well as Macha Research Trust for collection of the dried blood spot samples and for access to the samples and their on-site laboratories. This work was supported by the National Institute of Health/Fogarty International Center [D43 TW009348] and Vanderbilt University through Laboratories for Innovation in Global Health Technologies and the Mitchum E. Warren, Jr. Graduate Research Fellowship (L.E.G.). The clinical aspect of the study was supported by the National Institutes of Health as part of the International Centers of Excellence for Malaria Research (U19 AI089680).

APPENDIX B

SUPPORTING INFORMATION: CHAPTER V

Table SI V.1. Size and optical characterization of the nanoparticles synthesized from various metal protoporphyrin IX derivatives.

PPIX Derivative	Dynamic Light Scattering	Zavg (nm)		PDI		Absorbance Spectra	λ_{max} (nm)	
		Average	Std Dev	Average	Std Dev		Free	NP
Mn(III) PPIX		260	50	0.30	0.06		373	371
Fe(III) PPIX		118	4	0.18	0.02		400	373
Co(III) PPIX		140	9	0.20	0.03		423	420
Cu(II) PPIX		Stable particles not formed					405	393
Zn(II) PPIX		60	30	0.4	0.1		420	396

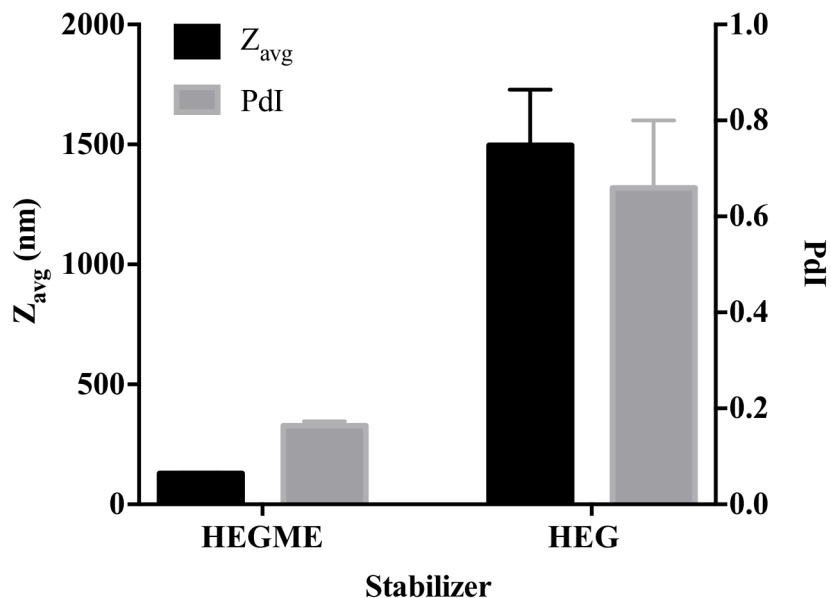


Figure SI V.1. The size and polydispersity of hemin nanoparticles synthesized with either hexaethylene glycol monomethyl ether (HEGME) or hexaethylene glycol (HEG) as the stabilizer. A stable nanoparticle sample was not produced when HEG was used as the stabilizer.

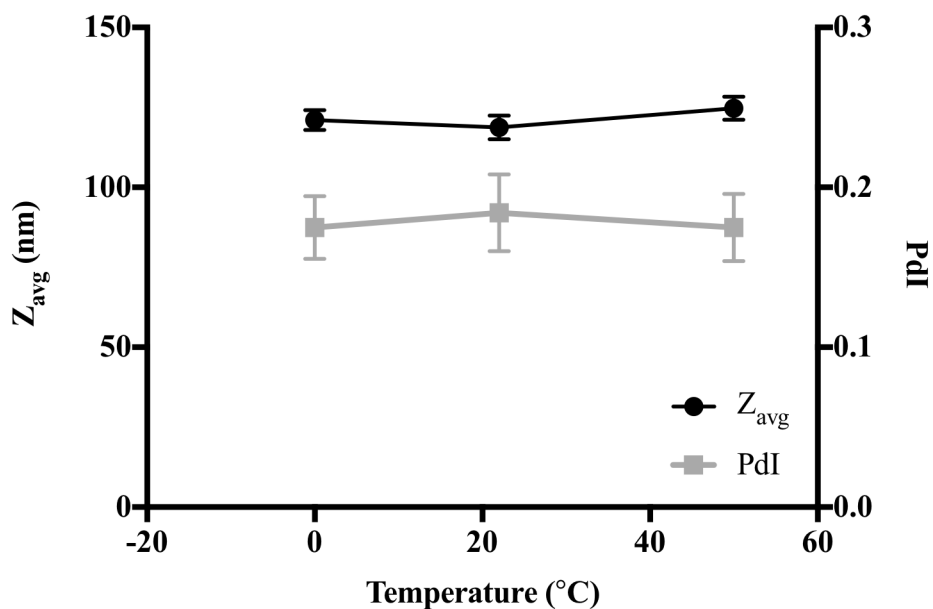


Figure SI V.2. Hemin nanoparticles were synthesized at different temperatures and no difference in nanoparticle size or polydispersity were seen.

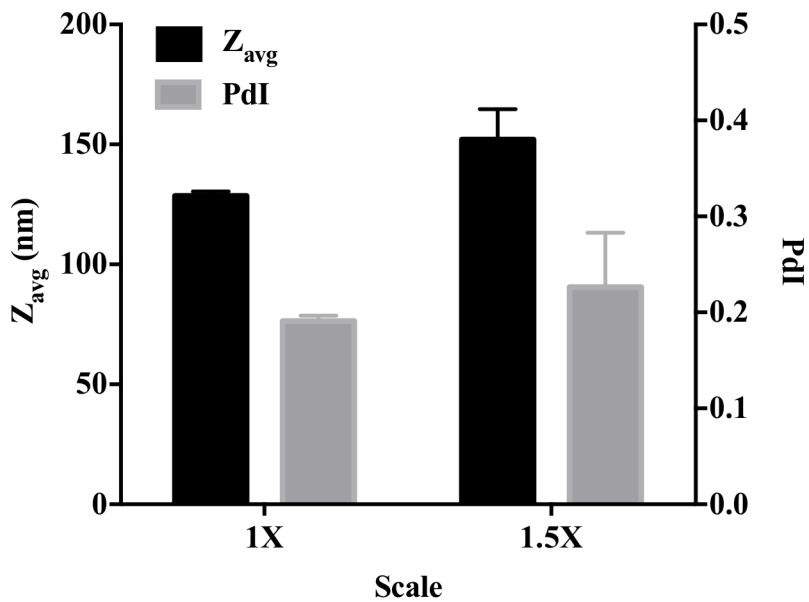


Figure SI V.3. The scale of the hemin nanoparticles synthesis was increased by 1.5X and an increase in particle size and polydispersity was observed.

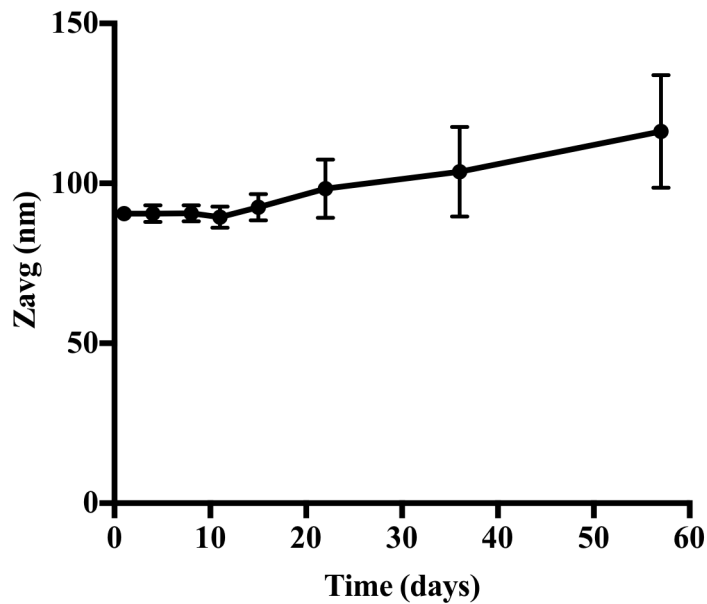


Figure SI V.4. The size stability of hemin nanoparticles, in solution, over time. The diameter of the particles remained around 100 nm for almost 2 months.

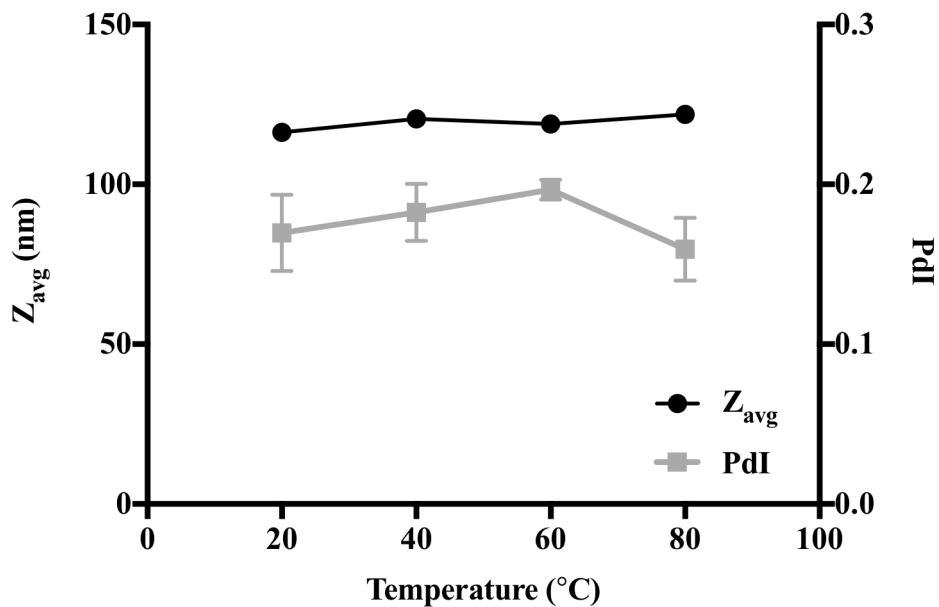


Figure SI V.5. The size of hemin nanoparticles remained constant even when exposed to temperatures of up to 80 °C for 20 minutes.

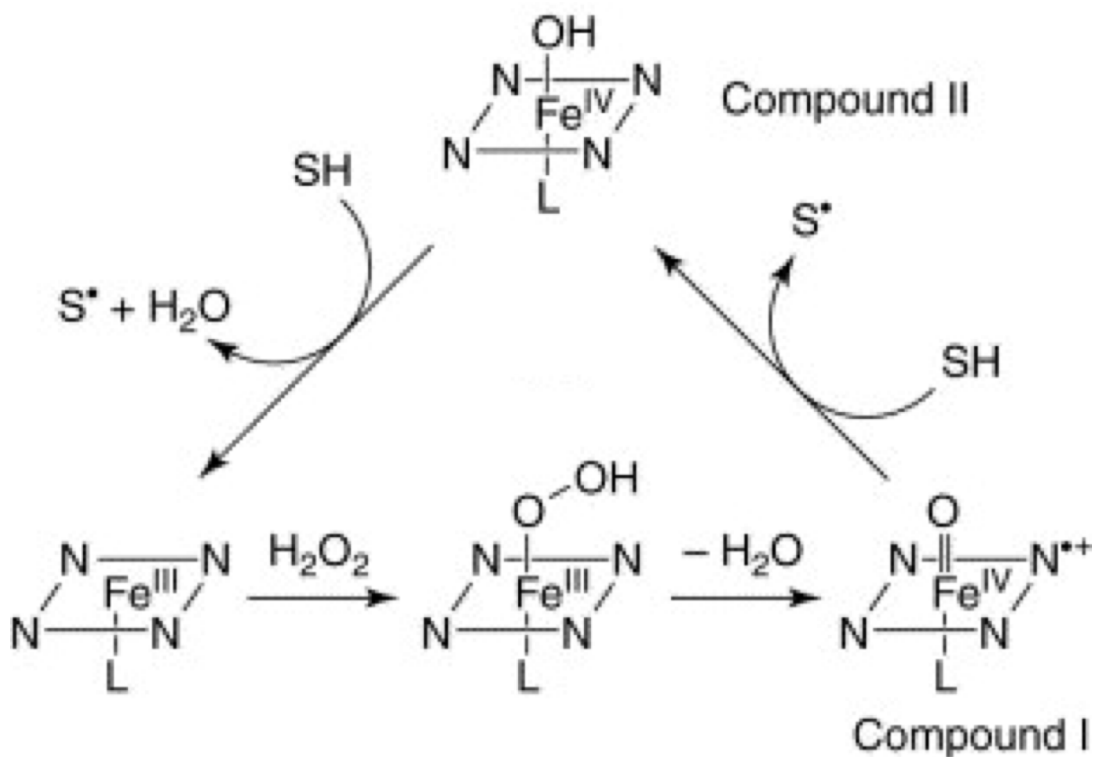


Figure SI V.6. The catalytic cycle of horseradish peroxidase. S = substrate, Ex. TMB (3,3',5,5'-tetramethylbenzidine). L = Ligand, Ex. histidine residue. Modified from Velde, F.; Rantwijk, F.; Sheldon, R. *Trends Biotechnol.* **2001**, *19* (2), 73-80.

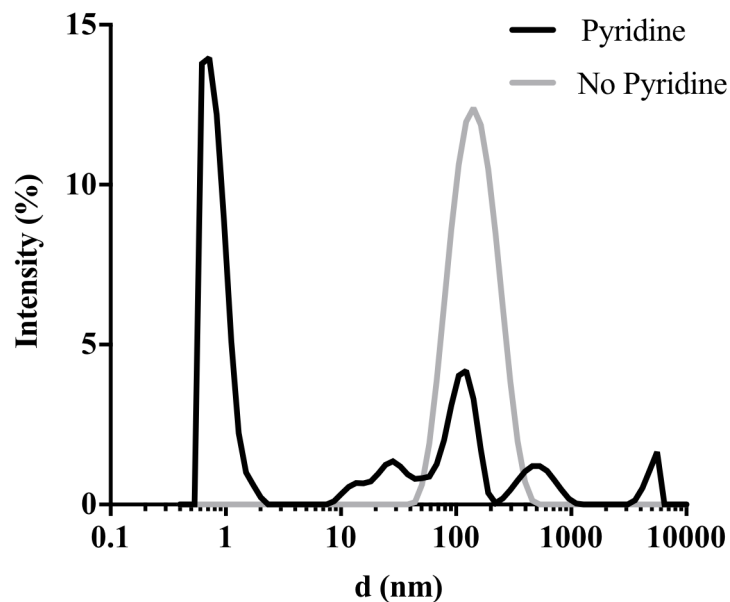


Figure SI V.7. The size distribution of hemin nanoparticles in 7.2% (0.9 M) pyridine. This is the concentration of pyridine added for hemin nanoparticle dissolution before addition of the colorimetric substrate (3,3',5,5'-tetramethylbenzidine). Nanoparticles are no longer observed after addition of pyridine.

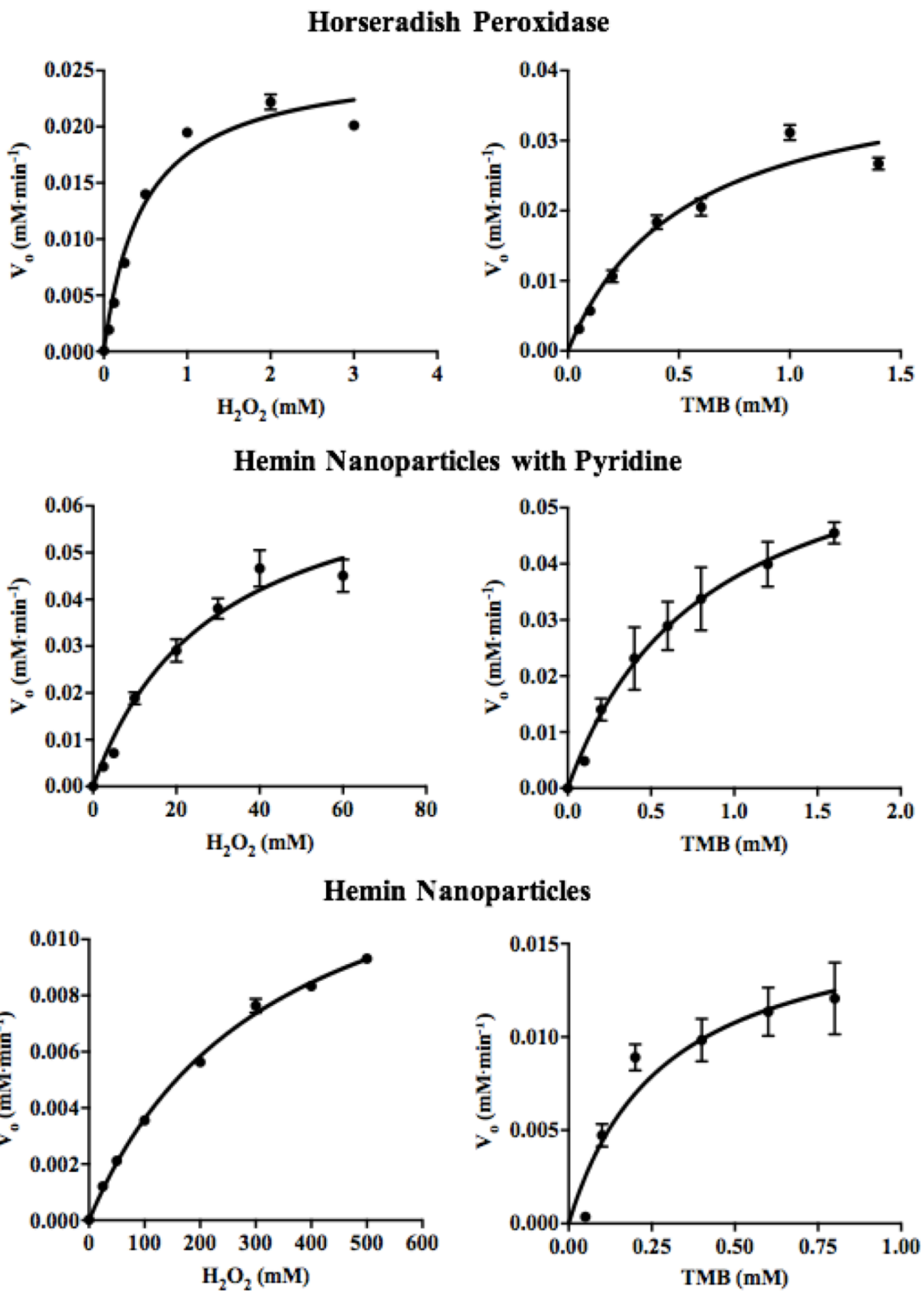


Figure SI V.8. Substrate vs. velocity curves for horseradish peroxidase and hemin nanoparticles with and without pyridine.

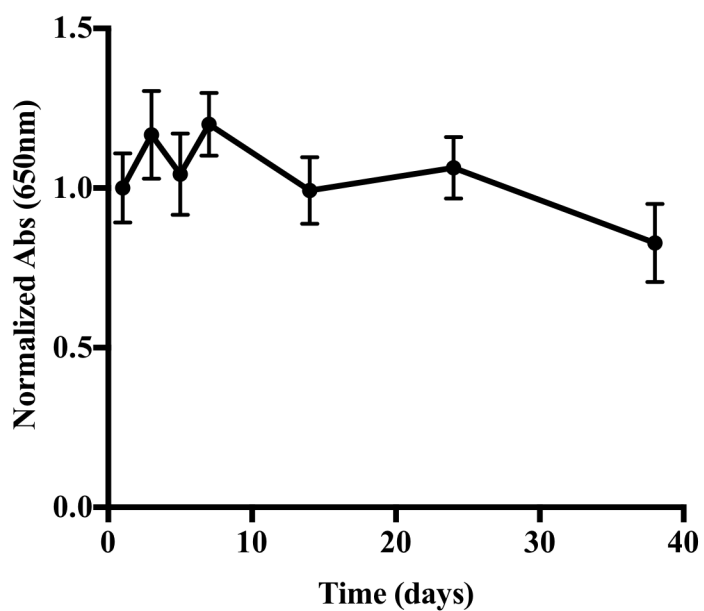


Figure SI V.9. The stability of the catalytic activity of hemin nanoparticles over time. No significant difference in signal was observed between Day 1 and Day 40.

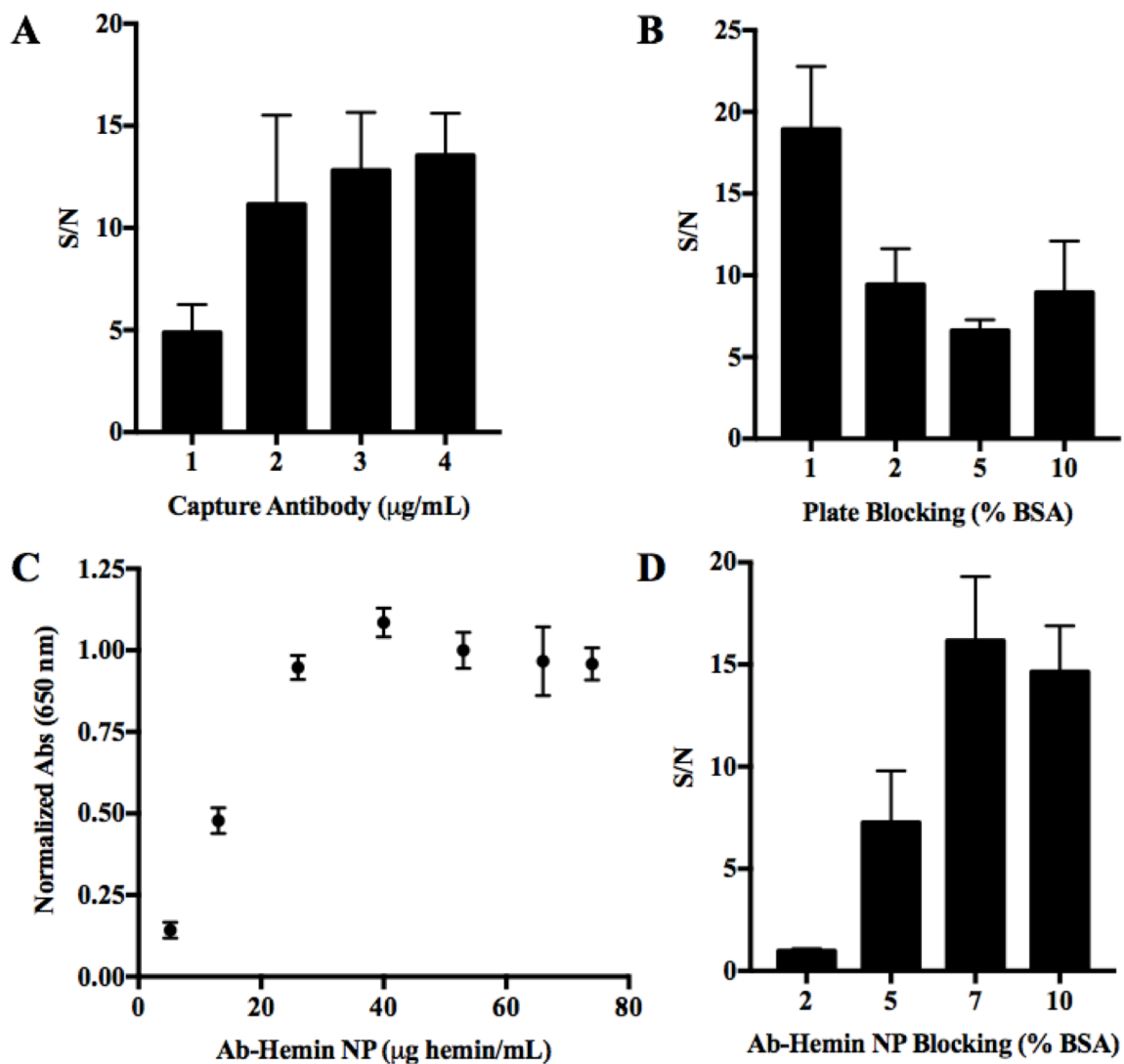


Figure SI V.10. Optimization experiments for the rabbit IgG detection assay using the hemin nanoparticle detection strategy (Ab-Hemin NPs). A) Capture antibody concentration of 4 $\mu\text{g/mL}$ was chosen. B) Plate blocking with 1% BSA was selected. C) Ab-Hemin NP concentration of 40 $\mu\text{g/mL}$ resulted in maximum assay signal. D) Ab-Hemin NPs were blocked with 7% BSA.

Negative

Positive

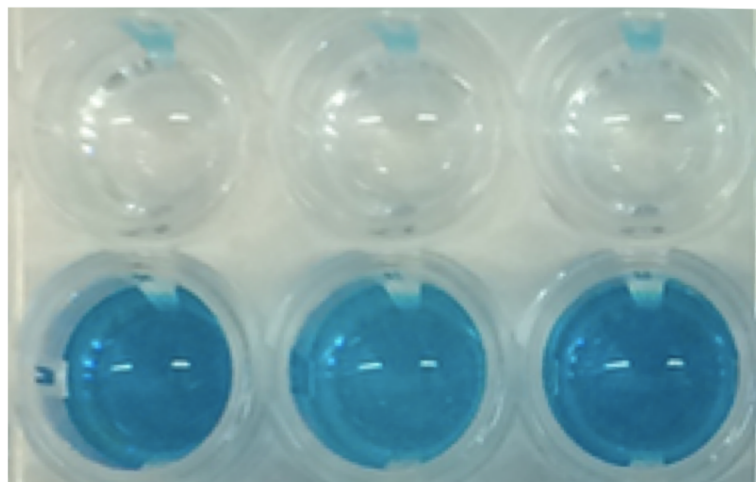


Figure SI V.11. The visual signal produced by the hemin nanoparticle detection strategy. Negative = 0 pM Rab-IgG, Positive = 100 pM Rab-IgG.

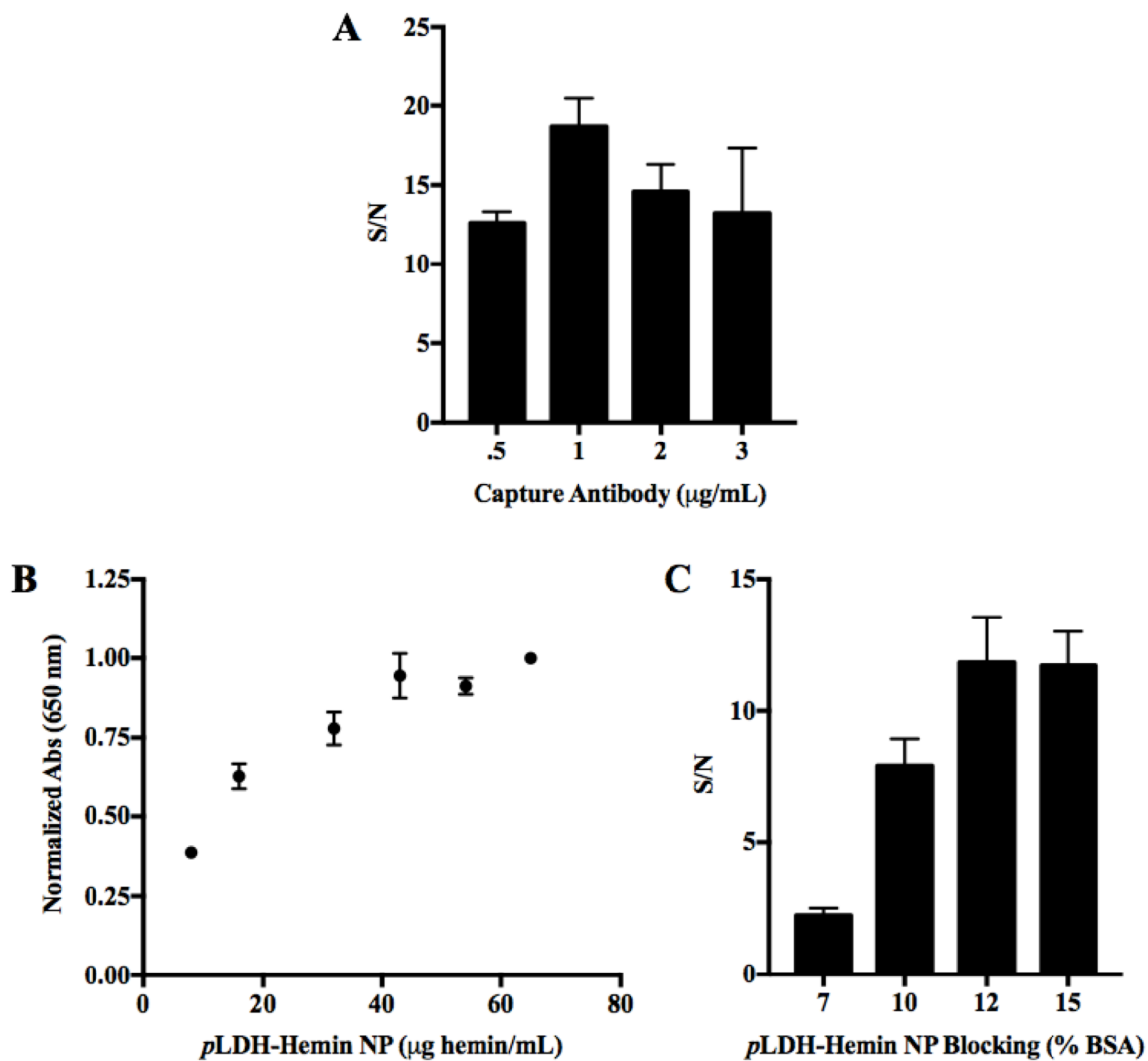


Figure SI V.12. Optimization experiments for the *p*LDH assay using the hemin nanoparticle detection strategy (*p*LDH Hemin NP). A) Capture antibody concentration of 1 $\mu\text{g/mL}$ was chosen. B) *p*LDH-Hemin NP concentration of 40 $\mu\text{g/mL}$ resulted in maximum assay signal. C) *p*LDH-Hemin NPs were blocked with 12% BSA.

Acknowledgements

Special thanks to Matthew Park for assistance with the nanoparticle synthesis optimization experiments, as well as Dr. Aren Gerden for performing the cyclic voltammetry study. Partial support for this work was provided by the Bill and Melinda Gates Foundation (OPP1123092) and the Mitchum E. Warren, Jr. Graduate Research Fellowship (L.E.G.). Additionally, we would like to thank the Vanderbilt Institute of Nanoscale Science and Engineering for access to DLS instrumentation and Dr. Alissa Weaver's lab for access to the ZetaView particle analyzer.

APPENDIX C

DETECTION OF MALARIAL DNA WITH HEMIN NANOPARTICLES

Introduction

The hemin nanoparticle (Hemin NP) detection strategy described in detail in Chapter V shows great promise for application in low-resource settings. This method has great stability but also employs multiple modes of signal amplification, resulting in a sensitive assay with a simple signal readout. In Chapters V and VI, this method was successfully used for the detection of protein biomarkers with limits of detection well within clinically relevant ranges. While protein detection is essential, there are also many nucleic acid biomarkers which are of interest for disease diagnosis. Particularly, in the diagnosis of malaria, not only is the extent of the infection important to diagnosis but also the species of *plasmodium* infecting the individual. This species differentiation is most effectively done through the use of nucleic acid biomarkers.^{137, 138} Taking this into consideration, a natural extension of the Hemin NP detection strategy is detection of nucleic acid biomarkers. In the following, we show a strategy for nucleic acid detection with Hemin NPs through biotin-streptavidin linkages. These particles are then used in a plate assay for the specific detection of malaria target DNA.

Experimental

Materials

Malaria target DNA and capture and detection DNA sequences were purchased from Integrated DNA Technologies (IDT). Specific sequences are detailed in Table 1. The capture and

detection sequences are thiolated, allowing for biotinylation through a maleimide-PEG2-biotin linker (catalog no. 21901BID). Manufacturer instructions were followed for this reaction. All other reagents are specified in Chapter V or were purchased from Sigma Aldrich or Fisher Scientific.

Name	Sequence
Malaria Target DNA	5'-ACA TGG CTA TGA CGG GTA ACG GGG AAT TAG AGT TCG ATT CCG GAG AGG GAG CCT GAG AAA TAG CTA CCA CAT CTA AGG AAG GCA -3'
Capture DNA	5'-CGT TAC CCG TCA TAG CCA TGT T ₁₀ -thio -3'
Detection DNA	5'-thio- T ₁₀ TGC CTT CCT TAG ATG TGG TAG CTA -3'

Table 1. Specific sequences of the target, capture and detection DNA used in the nucleic acid Hemin NP detection strategy.

Streptavidin-Conjugated Hemin Nanoparticles

Hemin NPs were synthesized as described in Chapter V and streptavidin was conjugated to the nanoparticles through the same diazirine-based photoreactive linker (Strep-Hemin NP). In the coupling reaction, 16 µg of streptavidin was added for every 100 µg of hemin. Successful conjugation was determined by using these Strep-Hemin NPs to detect biotinylated rabbit IgG (biotin-Rab-IgG). This assay was carried out by laying down various concentrations biotin-Rab-IgG in buffer (1X PBS) and incubating for two hours. The plate was then blocked with 1% BSA in PBST (1X PBS with 0.1% Tween-20) for two hours. Following this step, Strep-Hemin NPs were blocked with 10% BSA and added to the assay at a concentration of 25 µg/mL for one hour. The plate was washed between each step with PBST. After the last wash, 50 µL of 0.9 M

pyridine in borate buffer pH = 8 was added to each well, followed by 100 μ L of TMB-One substrate. Absorbance was read at 650 nm.

Detection of Malaria Target DNA

To detect malaria target DNA in a plate assay format, 100 μ L of 30 μ g/mL streptavidin was immobilized on a plate with a 1 hour incubation. Next, 100 μ L of 1 μ M capture DNA was added in DNA binding buffer (5 mM Tris-HCl, 0.5 mM EDTA, 1 M NaCl, 0.05% Tween-20) and incubated for 1 hour. The plate was then blocked for two hours with 2% BSA in PBST with 10 μ M biotin. The samples containing malaria target DNA and 500 nM detection DNA, were then added in 1X PBS and incubated for 1 hour. Finally, Strep-Hemin NPs were added at a concentration of 25 μ g hemin/mL, in 10% BSA, for 1 hour. This step was followed by the addition of pyridine and TMB-One for signal generation and absorbance was read at 650 nm. Molecular biology grade water was used in this assay to prevent DNA degradation. The plate was washed with PBST between each step.

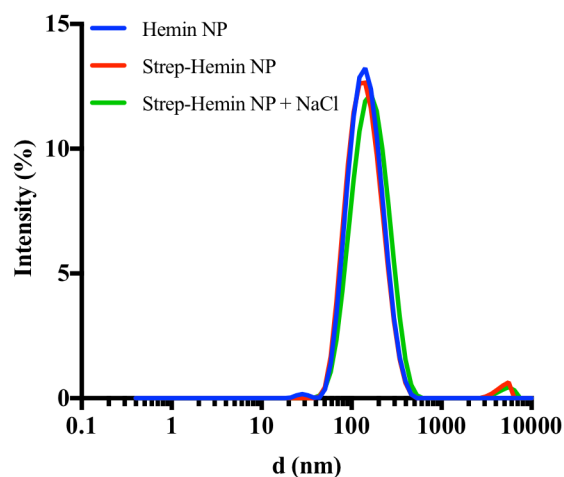


Figure 1. Size distribution of Hemin NP in various conditions. Hemin NPs: $d = 132 \pm 2$ nm (blue), Strep-Hemin NPs: $d = 132 \pm 1$ nm (red) and Strep-Hemin NPs in 150 mM NaCl: $d = 144 \pm 2$ nm (green). Hemin NP size remained consistent in between these conditions.

Results and Discussion

Characterization of Streptavidin-Conjugated Hemin Nanoparticles

Hemin NPs were characterized by dynamic light scattering (DLS) to determine their size and the stability of this size in different conditions. It was found that the conjugation of streptavidin did not significantly affect nanoparticle size, which would be expected since it is a relatively small protein (Figure 1). This observation also indicates that the Hemin NPs did not aggregate after conjugation, which shows the stability of the particles after conjugation. Additionally, the Hemin NPs were analyzed after the addition of 150 mM NaCl. This concentration of salt is necessary to facilitate DNA binding. It was thought that this amount of salt might interfere with the non-covalent interactions which hold the Hemin NPs together but DLS analysis showed that the Hemin NPs remained stable in these conditions (Figure 1).

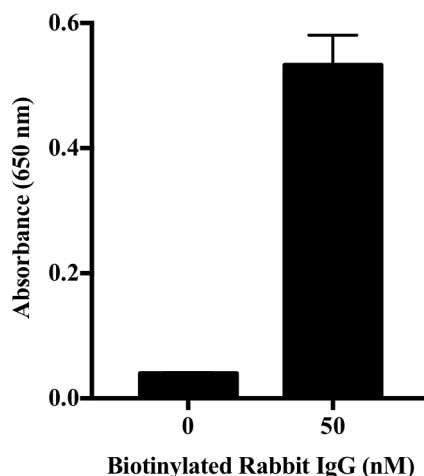


Figure 2. Detection of biotin-Rab IgG with Strep-Hemin NPs. This data proves effective conjugation of streptavidin to the nanoparticles.

Detection of Biotinylated Protein

The strategy chosen for modification of Hemin NPs for nucleic acid detection was conjugation of biotinylated detection DNA to streptavidin-conjugated Hemin NPs. The

conjugation of streptavidin to the particles was achieved through a photoreactive linker. To test whether this conjugation was successful and if the Hemin NPs would specifically bind to biotin, an assay for detection of biotinylated Rab-IgG was performed. In this assay, specific detection of the biotin-Rab-IgG was seen at nanomolar concentrations (Figure 2). Additionally, it was determined that a concentration of 25 μg hemin/mL of Strep-Hemin NPs was required to saturate the assay signal. This data was used to ensure sufficient Strep-Hemin NPs were added to this and future assays (Figure 3).

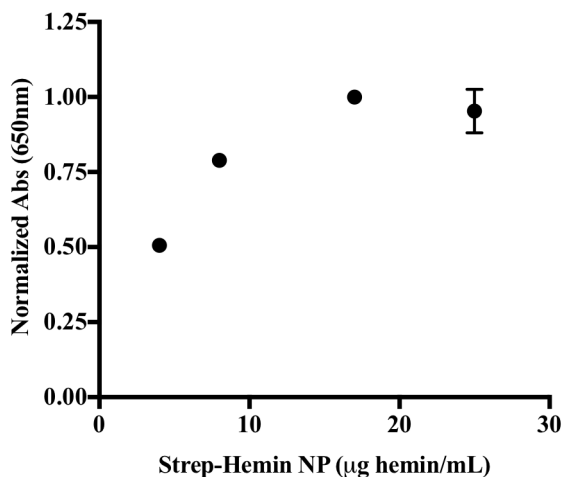


Figure 3. Concentration optimization of Strep-Hemin NPs for maximum assay signal in the detection of biotin-Rab IgG.

Detection of Malaria Target DNA

The goal of this project was to specifically detect a nucleic acid biomarker of malaria, as detection of these biomarkers allows for development of species-specific assays. To prove that specific detection could be achieved, a biotinylated capture DNA strand was immobilized on a streptavidin coated plate. Samples of target DNA, that had been pre-mixed with the biotinylated detection DNA, were then added followed by the Strep-Hemin NPs, which bind to the detection DNA (Figure 4).

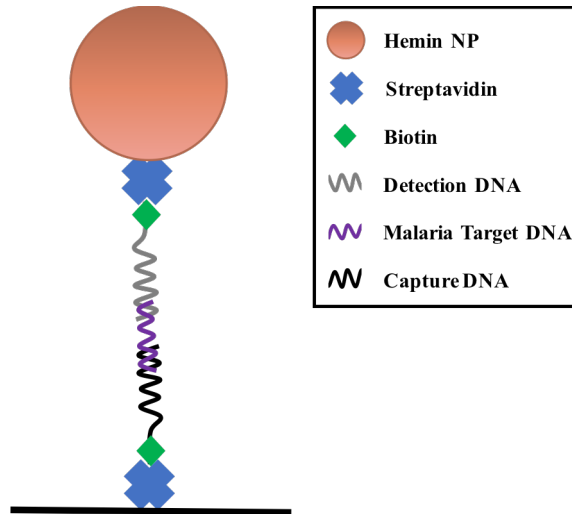


Figure 4. The detection scheme for malaria target DNA. Streptavidin is immobilized on the plate to anchor the capture DNA, which binds the malaria target DNA. Biotinylated detection DNA also binds the target sequence followed by binding of the Strep-Hemin NPs for signal generation.

The assay was optimized through determination of the amount of streptavidin required for immobilization of sufficient capture DNA on the plate. Also, the necessary blocking of the Strep-Hemin NPs with BSA was found. Using the optimized parameters, specific detection of the malaria target DNA was achieved with a signal-to-noise of 8 ± 3 (Figure 5). This result

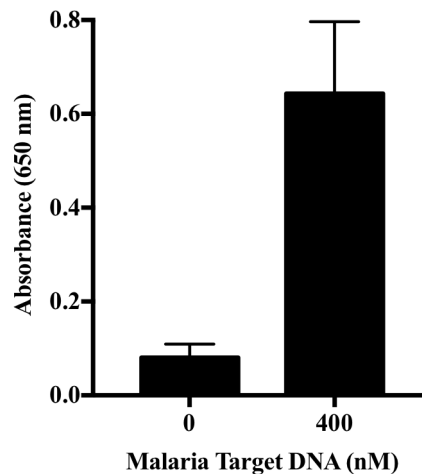


Figure 5. Specific detection of malaria target DNA with the Hemin NP detection strategy.

shows the versatility of the Hemin NP detection strategy in that it can be used to detect nucleic acids and proteins, as was described in Chapters V and VI. Additionally, this plate assay can be easily translated to a paper diagnostic, as it is known that streptavidin sticks to nitrocellulose allowing for immobilization on paper instead of the plate.

Conclusion

The Hemin NP detection strategy has been shown to specifically detect a malaria target DNA sequence. Detection was achieved through conjugation of streptavidin to the Hemin NPs for further conjugation to biotinylated DNA. This work shows the adaptability of the Hemin NP detection method to a wide range of biomarkers, making it a very flexible strategy. Future work will look to lower the limit of detection of the assay through additional optimization of the conjugation between the detection DNA and the Hemin NPs. Applications include low-resource, nucleic acid-based diagnostics for species differentiation and diagnosis of disease.

Acknowledgements

Special thanks to Christopher Stachurski for working on this project with much enthusiasm and Anna Bitting for assistance in experimental design. This work was supported by Vanderbilt University through Laboratories for Innovation in Global Health Technologies and the Mitchum E. Warren, Jr. Graduate Research Fellowship (L.E.G.).

APPENDIX D

SELECTION OF X-APTAMERS AGAINST INFECTION DISEASE BIOMARKERS

Introduction

In the development of a diagnostic, the selection of the molecular recognition element is one of the most integral steps. The molecular recognition element is the diagnostic component responsible for binding the biomarker and the specificity and affinity with which it binds greatly impacts the sensitivity and specificity of the resulting diagnostic. Antibodies are extensively employed as molecular recognition elements and are used in diagnostics from enzyme-linked immunosorbent assays to rapid diagnostics tests. Antibodies have many advantages including high affinity and specificity for the target and the ability to be generated for a wide variety of disease markers. Despite these advantages, antibodies lack stability and if denaturation occurs, it is irreversible. Furthermore, antibodies are produced *in vivo*, which can be difficult and expensive.¹³⁹ These downfalls are especially detrimental in low-resource settings where extreme environmental conditions often result in antibody degradation and diagnostic failure and high cost can prohibit diagnostic implementation.

As a result, additional molecular recognition elements of increased stability are of great interest. Aptamers are one such class of molecules. Aptamers are short, single stranded oligonucleotides that bind with high affinity to protein targets based upon 3-D confirmation.¹⁴⁰ Aptamers are much more stable than antibodies, allowing for easier and more reliable storage. Additionally, they are produced *in vitro* which is simple and cost effective.¹³⁹ Unfortunately, aptamers are not stable *in vivo* because they are susceptible to nucleases. To address this

problem, X-aptamers were developed. These aptamers are synthesized with a phosphorodithiolate backbone, preventing recognition of the aptamers by nucleases. Additionally, chemical modifications are introduced into the nucleotide bases of X-aptamers to produce a greater variety of structures resulting in more specific binding.^{141, 142}

In the following, a kit produced by AM Biotechnologies for selection of X-aptamers is tested. The X-aptamer library is bead-based. It is synthesized by a split-and-pool synthesis method and there is one aptamer sequence per bead. While the traditional method for aptamer selection, systematic evolution of ligands by exponential enrichment (SELEX), require 10-15 selection rounds, the bead-based method requires only two rounds. Furthermore, the bead-based selection method allows for incorporation of modifications into X-aptamers that are not compatible with SELEX.¹⁴² In this work, the X-aptamer kit was used to select aptamers against three infectious disease biomarkers: *Plasmodium falciparum* histidine-rich protein II (malarial biomarker), p24 capsid protein (human immunodeficiency virus (HIV) biomarker), and CD4 (biomarker for extent of HIV infection). After selection of the X-aptamers, resulting hits were analyzed by bio-layer interferometry (BLI) to determine the affinity of the X-aptamers for their targets. Discovery of X-aptamers against these targets could result in the development of more stable low-resource diagnostics where X-aptamers are used as the molecular recognition element in the place of antibodies.

Experimental

Materials

Recombinant HIV-1 p24, biotin labeled was acquired from ProSpec (catalog no. hiv-106). Recombinant *Plasmodium falciparum* histidine-rich protein II (rc-pfHRPII) was purchased

from CTK Biotech Inc. (catalog no. A3000). sCD4-183 (2-domain) was acquired from NIH AIDS Reagent Program (catalog no. 7356).¹⁴³ AM Biotechnologies, LLC X-Aptamer selection kit was obtained from AM Biotechnologies. EZ-Link Micro NHS-PEG₄-Biotinylation Kit was purchased from ThermoFisher Scientific (catalog no. 21955). Dynabeads M-280 Streptavidin (catalog no. 11205D), Dynabeads His-Tag Isolation (catalog no. 10103D) and 8% TBE gel (catalog no. EC62155BOX) were acquired from ThermoFisher Scientific. PCR reagents were purchased from Roche. Octet biosensors were acquired from Pall ForteBio.

X-Aptamer Selection Protocol

The X-aptamer selection was performed according to the manufacturer provided procedure. The following is a brief summary of this process (Figure 1). In the first step, a negative selection was performed which ensured any X-aptamers that non-specifically bound to other components in the selection process (such as magnetic beads) were eliminated. In this particular selection, both Dynabeads M-280 Streptavidin and Dynabeads His-Tag Isolation were used as p24 and CD4 were biotinylated and rc-*pfl*HRPII has many intrinsic histidines. Thus, a negative selection was performed using both of these bead types (300 μ L of each at the original concentration), where the beads were added to the aptamer library (typically 10^8 members), allowed to incubate, and then magnetically separated along with any other X-aptamers that were non-specifically bound to the magnetic beads.

Following this, the target proteins were bound to their respective magnetic beads and a positive primary selection was completed. This was done by combining all protein coupled magnetic beads with the X-aptamer library that remained after the negative selection. After incubation, the magnetic particles were again separated out along with any X-aptamers that were specifically bound to the target proteins. At this point, these aptamers were cleaved off the beads

through heat and basic conditions. Following this, the solution of cleaved oligonucleotides was neutralized for the secondary pull down selection. In this pull down, the cleaved X-aptamers were divided into five tubes and each target protein added to a different tube. The additional tubes were controls. Thus, each target was incubated individually with the library. After this incubation, the respective magnetic particles were added to magnetically separate the proteins and any bound X-aptamers.

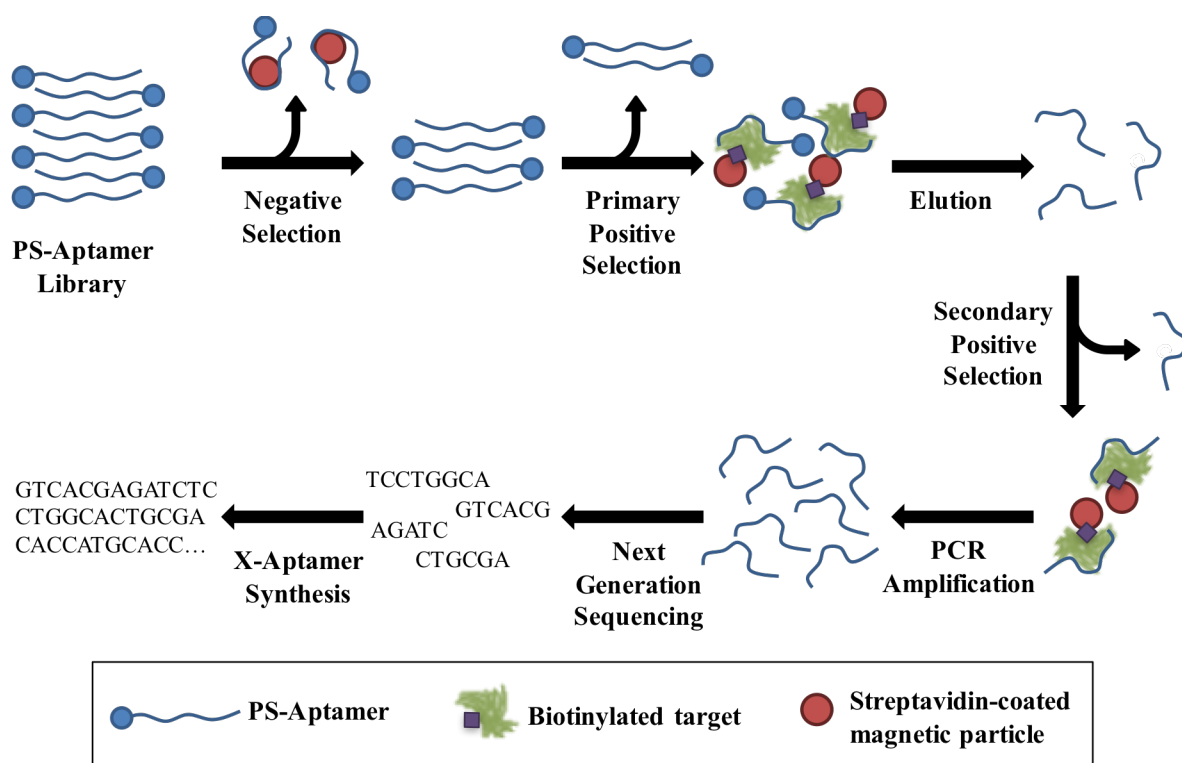


Figure 1. X-aptamer selection process with the AM Biotechnologies kit.

At this point the selection was completed and the resulting X-aptamers were amplified by polymerase chain reaction (PCR) with slight modification to the manufacturer’s protocol. For a 100 μ L PCR reaction, the following final concentrations of reagents were used: 1X PCR Buffer, 2.5 mM $MgCl_2$, 0.2 mM dNTP, 0.5 μ M forward primer, 0.5 μ M specified reverse primer, and 1.5 units Taq polymerase. Primers were provided by AM Biotechnologies. Thermal cycler

conditions were 94 °C for 1 minute, cycles of 94 °C for 30 seconds, 50 °C for 30 seconds, 72 °C for one minute and a final extension of 72 °C for 3 minutes. A PCR of 25 cycles was found to be sufficient. It was also found that SYBR green inhibited this PCR reaction.

After amplification with PCR, the resulting products were visualized on an 8% Tris-Borate-EDTA (TBE) gel with TBE running buffer. Sample (5 µL) was added to 2 µL of 5x non-reducing TBE sample buffer and 3 µL molecular biology grade water for analysis. The gel was run for 35-40 minutes at 200 V. SYBR green was used to stain the gel for 15 minutes before the gel was imaged on a UV-transilluminator. GeneRuler™ Ultra Low Range DNA Ladder was used and, as expected, the aptamer band was present around 75 base pairs. At this point, the amplified product was returned to AM Biotechnologies for next generation sequencing.

Bio-Layer Interferometry Protocol

All solutions were made in the PBSTM (1X PBS, 1 mM MgCl₂, 0.05% Tween-20). Analysis of the binding of CD4 and rc-*p*fHRPII X-aptamers was done by loading 100 nM biotinylated X-aptamer on streptavidin biosensors. These sensors were then blocked with 10 µg/mL of biocytin before the association step with the respective protein at the specified concentration. The experimental setup for the Octet instrument included a 300 second equilibration step, followed by 600 second aptamer load, 60 second biocytin quench, 300 second wash, 60-180 second baseline, 600 second protein association and 600 second dissociation steps. Parallel reference sensors were run in an identical manner but without aptamer loading. These tips were used for background subtraction, eliminating any non-specific signal. Since the p24 protein was purchased biotinylated it was loaded onto the tips instead of the X-aptamers. Originally, very little binding to the tips was observed so p24 was biotinylated further with the EZ-link biotin reagent. p24 was loaded at a concentration of 50 µg/mL. X-aptamers were

associated to p24 at a concentration of 5 μM . All other steps of the assay performed as specified above.

Results and Discussion

The X-aptamer selection produced 60 sequences that were synthesized by AM Biotechnologies for further analysis. Twenty-five of these sequences were against *rc-pfHRPII* (Table 1), twenty against CD4 (Table 2), and fifteen against p24 (Table 3). The affinity of these X-aptamers for their target proteins was then assessed using an Octet RED96. This instrument uses bio-layer interferometry (BLI) to measure binding and dissociation in real time. BLI is an optical technique where white light is passed down a fiber optic biosensor. This light is reflected back from two surfaces. One is a reflective reference surface and the other is a biocompatible layer at the end of the sensor. These two beams of light interfere with each other and this interference pattern changes upon binding. There is a change because when a molecule binds, the

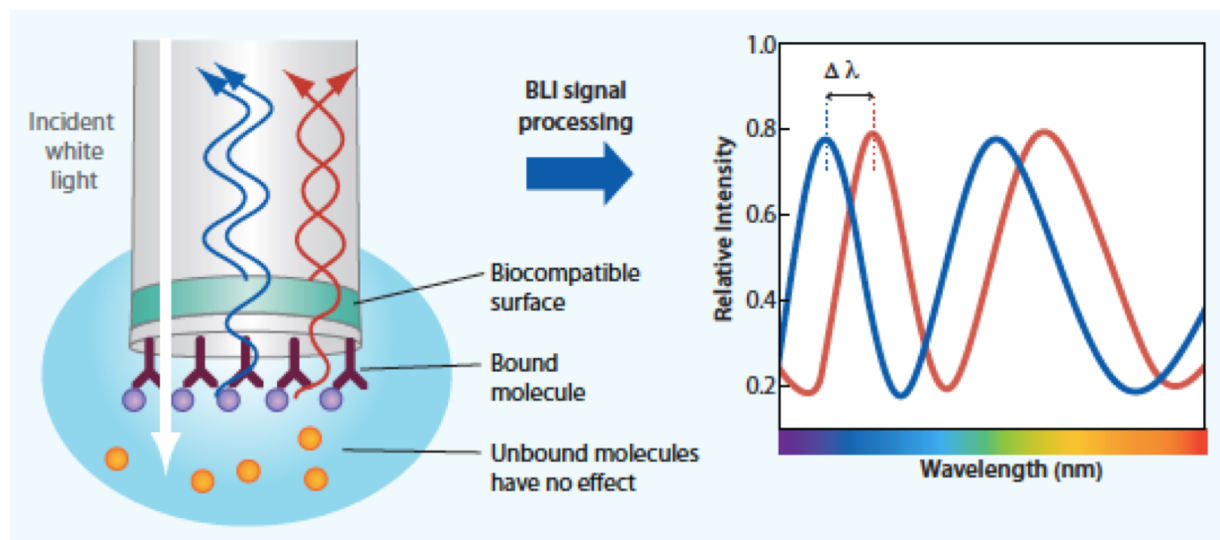


Figure 2. Bio-layer interferometry theory. This technique is used by the Octet RED96 to monitor binding events in real time.¹⁴⁴

distance between the two reflective surfaces changes causing the shift in the interference pattern, this is represented as a nm shift and is related to how many molecules bind to the biosensor (Figure 2). This data can then be used to determine the equilibrium dissociation constant, K_D , which is the ratio of off-rate to on-rate, producing a metric for how tightly two molecules bind. If two molecules have a very high affinity for each other, then the resulting K_D is low.¹⁴⁴

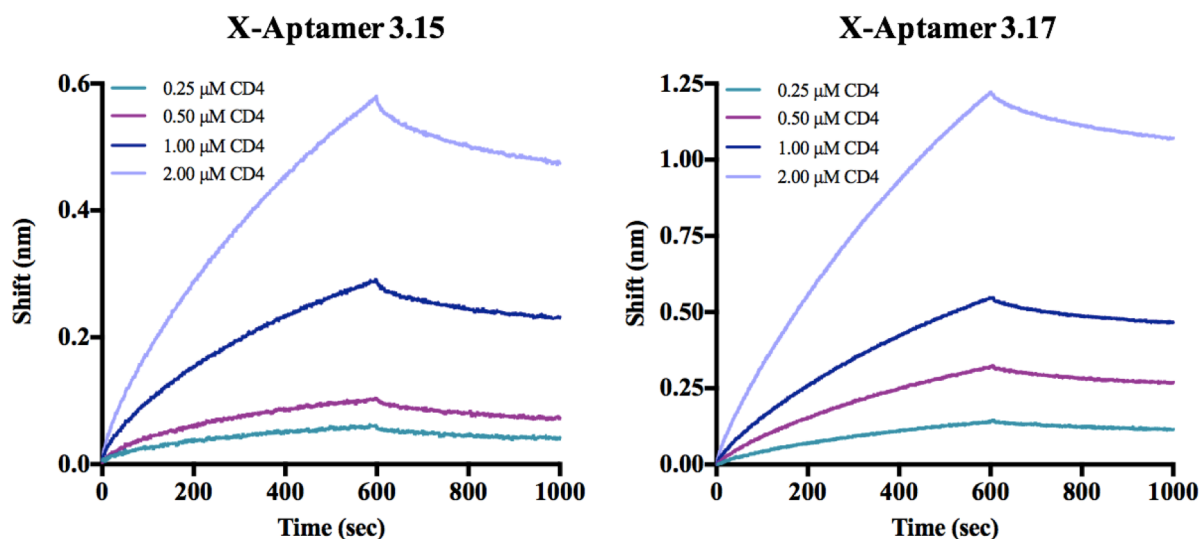


Figure 3. Association and dissociation curves for X-aptamers 3.15 and 3.17, two of the five selected aptamers that showed significant binding with low micromolar amounts CD4 target protein.

To discover the best X-aptamers that resulted from the selection, a screen was performed where each aptamer was tested for binding with 5 μM of protein target. This concentration was chosen because if binding was not observed with this amount of protein then the affinity of the aptamer and protein pair is not sufficient for implementation into a diagnostic. The screen for *p/HRPII* was done by immobilization of the biotinylated X-aptamers on a streptavidin biosensor and association of the protein. Only X-aptamer 2.19 showed any indication of binding and the amount of binding observed was not sufficient for a K_D below the micromolar range. A screen against CD4 resulted in five X-aptamers (3.05, 3.15, 3.16, 3.17, and 3.18b) that displayed

significant binding at 5 μM target protein. These aptamers were further analyzed at lower concentrations and were all found to have high nanomolar equilibrium dissociation constants (Figure 3). The aptamer with the best affinity was X-aptamer 3.05. Binding of this aptamer was analyzed at six CD4 concentrations and after fitting the data to a 1:1 kinetics model it was found to have a $K_D = 436 \pm 7 \text{ nM}$ with a $k_{\text{on}} = 10,100 \pm 100 \text{ (M}\cdot\text{sec)}^{-1}$ and a $k_{\text{off}} = 4.42 \times 10^{-3} \pm 2 \times 10^{-5} \text{ (sec)}^{-1}$ (Figure 4). Finally, the p24 screen was completed by loading the biotinylated protein onto the biosensor tips and then associating 5 μM of the aptamers. No binding was observed in this screen.

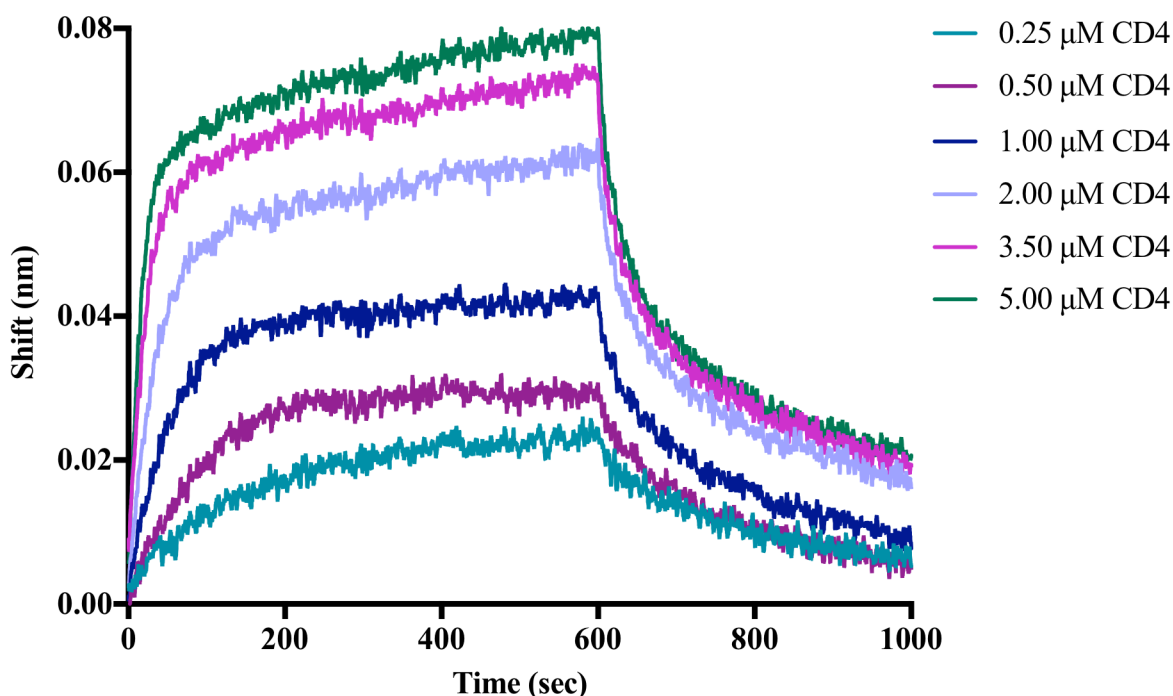


Figure 4. The association and dissociation curves for X-Aptamer 3.05 with CD4 target protein measured on the Octet RED96. The equilibrium dissociation constant (K_D) for this aptamer was found to be 436 nM.

There are several explanations for why binding was only observed for the X-aptamers selected against CD4. First, CD4 was the only target protein that was not tagged. The *rc-pfHRPII*

protein was tagged with Glutathione S-transferase (GST) and p24 was fused to beta-galactosidase. It could be that most of the aptamers selected for these proteins were against the tag instead of the protein and then these sequences were eliminated by the algorithm used by AM Biotechnologies for selection of the most promising aptamer sequences for synthesis. As a result, there could have been high-affinity X-aptamers selected against these specific target proteins. Furthermore, the complete lack of binding observed for any of the p24 X-aptamers could be a result of the change in the arrangement of the protein and aptamer when analysis was performed on the Octet. As was mentioned previously, the thickness of the layer on the end of the biosensor produces the nanometer shift measured by the instrument. As a result, large molecules cause a much greater shift than small ones. Aptamers are much smaller than proteins, so in the *rc-pfHRPII* and CD4 assay, we were looking for the association of the protein which should be easy to see. In the p24 assay, the protein was loaded, giving a big shift, followed by the aptamer, which would give a small shift. So, it is possible the shift caused by binding of the aptamers was not observed. As a result, for any future analyses the aptamer will be loaded on the tips first, followed by association of the protein.

Conclusion

The X-aptamer selection kit produced by AM Biotechnologies was found to be user-friendly with minimal time required for aptamer selection. This kit was used for the selection of X-aptamers against three infectious disease protein biomarkers: CD4, *rc-pfHRPII* and p24. The affinity of the resulting X-aptamers for their protein target was analyzed by BLI and the best aptamers were found to bind CD4 with high nanomolar affinity. A second, more targeted selection based upon the CD4 X-aptamers that were found in this work could result in the

discovery of an X-aptamer with a high affinity for CD4. This X-aptamer could then be incorporated into a diagnostic producing a more stable test for low-resource settings.

Acknowledgments

Partial support for this project was provided by AM Biotechnologies. We also thank AM Biotechnologies for technical assistance. The following reagent was obtained through the NIH AIDS Reagent Program, Division of AIDS, NIAID, NIH: sCD4-183 from Pharmacia, Inc.

<i>pf</i> HRPII X-Aptamers	Sequence
WRT.CA.2.01	TTTTT CA ACGA AGGGAwGGTTGwCCACwAATACTCATA TCGT TTTTT
WRT.CA.2.02	TTTTT CA TCGT AGCCA _w GGCCATCTGTTTC _z GATT _w GCAG _z TCGT TTTTT
WRT.CA.2.03	TTTTT CA ACGA zGTTCAACCCATCTACATCGAGTTCTCATA TCGT TTTTT
WRT.CA.2.04a	TTTTT CA ACGA zGGGCAACCTATTAC _z ATCGGATT _{Az} CACA TCGT TTTTT
WRT.CA.2.04b	TTTTT CA ACGA zGGGCAACCTATTAC _z ATCGGATT _{Az} CACA ACGA TTTTT
WRT.CA.2.05a	TTTTT CA TCGT CGGACAGGCTG _w CCGTTTC _z TACGA _z CACA TCGT TTTTT
WRT.CA.2.05b	TTTTT CA TCGT CGGACAGGCTG _w CCGTTTC _z TACGA _z CACA ACGA TTTTT
WRT.CA.2.06	TTTTT CA TCGT CGGGC _z TGTTATCCACATCGACAAA _z CATA TCGT TTTTT
WRT.GA.2.07	TTTTT GA ACGA ---GT _w AATGTGCCAG _y AACATCT _w GCCT ACGA TTTTT
WRT.GA.2.08	TTTTT GA ACGA GTATTAC _w TGCACC _w GTAGCCCTCATGCCA TCGT TTTTT
WRT.GA.2.09	TTTTT GA ACGA CGATTT _w A--GTGCGATACTCCAATA _w GAT TCGT TTTTT
WRT.GA.2.10	TTTTT GA ACGA CGCC--AATTGTTA _w GGGCTCAAGATCCCT TCGT TTTTT
WRT.GA.2.11	TTTTT GA ACGA ---yCAATTGGTACATAAACCAGT _w wGCT TCGT TTTTT
WRT.GA.2.12	TTTTT GA ACGA CGCC--AATGGTGCAGG _w CCCTCATGCAC TCGT TTTTT
WRT.GA.2.13	TTTTT GA ACGA TyATTAAACGCAGCT _w TA _w CCAAGTACCCT ACGA TTTTT
WRT.AC.2.14	TTTTT AC ACGA GyxCATACATA _{Ay} CGAGT _x GCT _x CGyTTG TCGT TTTTT
WRT.AC.2.15	TTTTT AC ACGA CCTATTGGCGACA _y CGACT _x GCT _x GTCCCTG ACGA TTTTT
WRT.AC.2.16	TTTTT AC ACGA CCGCTTAAATACA _y CGAGT _x CCCTCGyTGG ACGA TTTTT
WRT.AC.2.17	TTTTT AC TCGT CAGCATGGATACA _y CGACT _x AxAGAx _{CCTA} TCGT TTTTT
WRT.AC.2.18	TTTTT AC ACGA GyxCTTACATCCTCAA _y GAAGCGGCGCCTG TCGT TTTTT
WRT.AC.2.19	TTTTT AC ACGA CAACCTAATGACA _y CGAGAACCCTGTyTGT ACGA TTTTT
WRT.AC.2.20	TTTTT AC TCGT CC _x CTTACCAACA _y CGAGAACCCTGTGATG ACGA TTTTT
WRT.AC.2.21	TTTTT AC ACGA CCGCTTGATGACA _y CGACT _x GCCTCGCCTG TCGT TTTTT
WRT.AC.2.22	TTTTT AC ACGA GyxCTAATGCCTCCGACT _x AxCTCGyTTG ACGA TTTTT
WRT.AC.2.23	TTTTT AC TCGT CA--TTACCAACTCAA _{ACTx} CCT _x GTyTGG ACGA TTTTT

w=indole x=hydroxymethyl y=phenol z=boronic acid

Table 1. The sequences for the X-aptamers that were selected for *pf*HRPII. Only aptamer 2.19 showed binding with micromolar protein concentrations.

CD4 X-Aptamers	Sequence
WRT.AC.3.01	TTTTT AC TCGT GCGCCTAAATAGAyCGyGAAAxGGGTGCTG TCGT TTTTT
WRT.AC.3.02	TTTTT AC ACGA CCTATTGGCGACTCCCCTxGCTxCGyTTA ACGA TTTTT
WRT.AC.3.03	TTTTT AC TCGT GCGCCTAAATCCTCGAAGCTGCAGAACCTG TCGT TTTTT
WRT.AC.3.04	TTTTT AC TCGT GCGCCTAAATGTTCCGyAAAGCAGAxxyTTA TCGT TTTTT
WRT.AC.3.05	TTTTT AC TCGT GyGCCTAAATGTGCCGyGGAGCAGGTyTTG TCGT TTTTT
WRT.AC.3.06	TTTTT AC TCGT GyGCCTAAATGTGCCGAGGACCCTAxGCTA ACGA TTTTT
WRT.AC.3.07	TTTTT AC ACGA CCGCCTAAATGTAyCGyAAAAxGGCGyTTG ACGA TTTTT
WRT.AC.3.08	TTTTT AC ACGA CCGCCTAAATACGCGAACAAACCCTCGCCGT TCGT TTTTT
WRT.AC.3.09	TTTTT AC ACGA CCGCCTAAATACCTCCACTxAxAGAxGCTA ACGA TTTTT
WRT.AC.3.10	TTTTT AC TCGT GCxCTTGATGCCAyGAyGAAGCCT--CCTA ACGA TTTTT
WRT.AC.3.11	TTTTT AC TCGT GyGCCTAAATCCCTCGACTxGCTxGTyTGT TCGT TTTTT
WRT.AC.3.12a	TTTTT AC ACGA GyGCCTAAATGTAyGAyGTxGCTxGTyTTA ACGA TTTTT
WRT.AC.3.12b	TTTTT AC ACGA GyGCCTAAATGTAyGAyGTxGCCTGTyTTA ACGA TTTTT
WRT.AC.3.13	TTTTT AC TCGT GCTACTGAATACTCCGACTxCCAGCGyTTA ACGA TTTTT
WRT.AC.3.14	TTTTT AC TCGT GCxCAGACCAGTCTGAyATxGCTxCGCCTA TCGT TTTTT
WRT.AC.3.15	TTTTT GA ACGA CGATTACwATGGCCTwGGCTCATCATTCT TCGT TTTTT
WRT.AC.3.16	TTTTT GA ACGA --yG--CwATGTTAwGGyAACCAAGTAwGAC TCGT TTTTT
WRT.AC.3.17	TTTTT GA ACGA TyATTA--TG--GCwGGGwCCAAGTwGCAC TCGT TTTTT
WRT.AC.3.18a	TTTTT GA ACGA TyyGTAGCCGAGTAwGTAwCCATCATTCT TCGT TTTTT
WRT.AC.3.18b	TTTTT GA ACGA TyGCTAGCCGAGTAwGTAwCCATCATTCT TCGT TTTTT

w=indole x=hydroxymethyl y=phenol z=boronic acid

Table 2. The sequences for the X-aptamers that were selected for CD4. X-aptamers 3.05, 3.15, 3.16, 3.17 and 3.18b showed high nanomolar binding affinities (K_D).

Code	Sequence
WRT.AC.4.01	TTTTT AC ACGA CAGCCTAACACCTCCCAGTxCCCTAxxyTGT TCGT TTTTT
WRT.AC.4.02	TTTTT AC ACGA GCTATTACTGGTGCAAyACTAxAG--CCTA ACGA TTTTT
WRT.AC.4.03	TTTTT AC ACGA GyxCCTAAATCCTCAAyGAAGCAGAAGAGG TCGT TTTTT
WRT.AC.4.04a	TTTTT AC ACGA GyxCCTAACACCCTGAACCTCCCTAAGCGG TCGT TTTTT
WRT.AC.4.04b	TTTTT AC ACGA GyGCCTAACACCCTGAACCTCCCTAAGCGG TCGT TTTTT
WRT.AC.4.05	TTTTT AC TCGT GCTATTAATAGGCAAyAAAGCTxAxCCGT TCGT TTTTT
WRT.AC.4.06a	TTTTT AC ACGA GCxCTTGGATCCTCAAyGGAGCTxGTCCGT ACGA TTTTT
WRT.AC.4.06b	TTTTT AC ACGA GCTATTGGATCCTCAAyGGAGCTxGTCCGT ACGA TTTTT
WRT.AC.4.07	TTTTT GA ACGA --CC--AATTGGCCCCAGyCTCCTGATwGCT TCGT TTTTT
WRT.AC.4.08	TTTTT GA ACGA ----TAAAATGTTGwGGGAACCAATACCCT TCGT TTTTT
WRT.AC.4.09	TTTTT GA ACGA TyCCGTwATTGATGwGGyAACCTCGywGCT TCGT TTTTT
WRT.AC.4.10a	TTTTT CA TCGT CGGGTAACTTCATCACTCCGTATCwGCAAT TCGT TTTTT
WRT.AC.4.10b	TTTTT CA TCGT CGGGTAACTTCATCACTCCGTATCwGCATA TCGT TTTTT
WRT.AC.4.11a	TTTTT CA TCGT zGCCAwACCCAGCTCzATCzACTCAzACTA ACGA TTTTT
WRT.AC.4.11b	TTTTT CA TCGT zGGAAwACCCAGCTCzATCzACTCAzACTA ACGA TTTTT

w=indole x=hydroxymethyl y=phenol z=boronic acid

Table 3. The sequences for the X-aptamers that were selected for p24. No binding was observed.

APPENDIX E

SURFACE TENSION VALVES AS SEPARATION BARRIERS FOR A SERUM CREATININE ASSAY

Introduction

Low-resource areas around the world suffer from a lack of sensitive medical diagnostics, which is a result of limited monetary resources, environmental conditions that leave many assays ineffective, and a lack of trained personnel. In Chapter III, a simple sample processing step was introduced that increased the sensitivity of the commercially available low-resource diagnostics. The effectiveness of this technique led the Gates Foundation to provide further funding to develop this process into an automated, all-in-one diagnostic to minimize user error and required training. To achieved this goal, an instrument was designed by the Haselton laboratory that could automatically mix samples in the tube, eliminating the need for a handheld magnet. Additionally, a spectrophotometer was incorporated into the instrument to read the assay signal. Assays for measurement of proteins using an ELISA strategy and nucleic acids with PCR were developed for this instrument. In the following, this work was extended through the development of an assay for the analysis of a clinical chemistry marker. This assay for serum creatinine, an indicator of renal health, was developed using air valves as separation barriers within the tube. The combination of all of these analyses into one, cost-effective instrument, with minimal user steps, brings a diversity of sensitive diagnostic assays into a format that shows great potential for implementation at major health facilities in low-resource areas.

Experimental

Materials

Picric acid (catalog no. 197378) and creatinine (catalog no. C4255) were purchased from Sigma Aldrich. Square FEP Tubing (0.093" ID, 1/8" OD, 0.016" Wall Thickness) was acquired from Zeus (catalog no. 0000174799). Cha-seal tube sealant was used to seal the ends of the tube. Hardened 440C Stainless Steel Balls, 1.5 mm diameter were purchased from McMaster-Carr (catalog no. 1598K17). Steel sandblasting beads were also used to mix samples. Human serum was purchased from Bioreclamation IVT (catalog no. HMSRM).

Jaffe Reaction

The Jaffe reaction has been extensively used in clinical chemistry for the determination of creatinine for many years.^{145, 146} This reaction takes advantage of the fact that an alkaline picric acid solution turns from yellow to red in the presence of creatinine. The Jaffe reagent was made with 4 parts, 0.2 M sodium hydroxide (NaOH) and 1 part, 30 mM picric acid. This was mixed in a 10:1 ratio with the sample. As a result, the final concentrations after sample addition were 0.145 M NaOH and 5.45 mM picric acid. Samples were either creatinine standards (creatinine in 1X PBS) or human serum. Unless otherwise specified, the reaction was allowed to proceed for 12 minutes before absorbance was read at 500 nm.

Preparation of Clinical Chemistry Assay Tube

The assay tube for the Jaffe reaction was prepared by first cutting a 5 cm section of square FEP tubing. Next, 100 μ L of Jaffe reagent was added by pipette forming the reaction chamber. The end of the tube closest to this chamber was sealed and then 3 stainless steel balls were added to this chamber. Next, a 20 μ L sample was added at the unsealed end of the tube,

making sure it was separated from the reaction chamber by an air valve. Finally, this end of the tube was also sealed.

Magnetic Bead Selection

Magnetic beads were used in this assay to break the surface tension of the air valve within the tube and mix the reagents and sample. Two types of beads were tested, sandblasting beads and stainless steel beads. To test whether these magnetic particles would interfere with the reaction, the integrity of the beads in aqueous solution was tested over time. After 1 hour, the beads were visualized with a macro lens on cell phone camera. Additionally, the stainless steel beads were added to the Jaffe reagent and monitored over time to see if an increase in absorbance at 500 nm was observed. This observation would indicate non-specific turnover of the reagent by the beads.

Mixing Optimization

The time required for breaking the air valve and mixing the two chambers with stainless steel beads was also tested. The time required was determined on the instrument by rotating the cartridge in relation to a stationary magnet, causing the movement of the magnetic particles, for different lengths of time. The absorbance of the reaction product was measured after 15 minutes.

Automated Serum Creatinine Assay

The clinical chemistry assay tube was made as previously specified and then placed in the instrument cartridge, between the grooves, and over the area backed with copper tape. The cartridge was aligned such that the magnetic beads were directly next to the stationary magnet. Before mixing, an absorbance reading was taken in the reaction chamber as a reference value. The cartridge was then rotated sufficiently so that the magnetic beads traversed through the entire tube. A back and forth rotation was continued for 4 minutes and then the solution was

allowed to sit for 8 minutes before the final absorbance reading was taken. These absorbance values were compared to those measured on a plate reader by removing reagents from the tube and adding to a plate for analysis.

Results and Discussion

Plate Assay for Determination of Creatinine

Creatinine is an important clinical chemistry biomarker used to determine renal health. It is a small molecule formed irreversibly from creatine, which is a required for generation of adenosine triphosphate (ATP). Creatinine, a waste product of this reaction, is found in many biological fluids and is cleared through glomerular filtration. Thus, the rate of creatinine elimination is related to renal health. In serum, creatinine remains stable day-to-day but accumulates in the case of renal failure. So serum was chosen as the biological matrix for analysis.¹⁴⁷

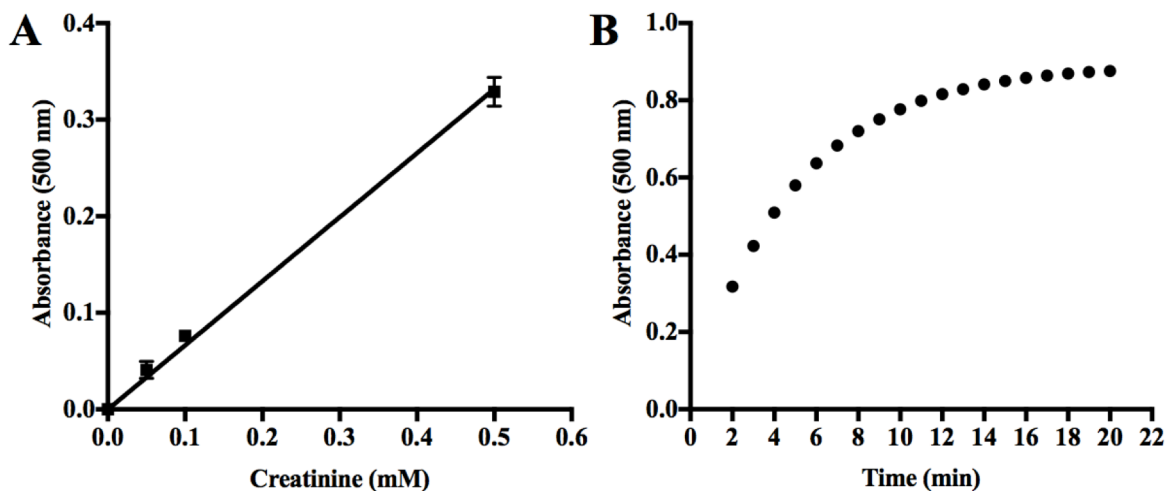


Figure 1. A) The standard curve for the detection of creatinine, using the Jaffe reaction, in a plate assay format. The linear regression was $y = 0.66x$ and the limit of detection was $7.4 \pm 0.2 \mu\text{M}$ creatinine. B) The time required for the Jaffe reaction to go to completion. It was found that with 1 mM creatinine the signal saturated around 12 minutes (right).

The Jaffe reaction was first reported over 100 years ago and has since been used extensively by clinical chemistry laboratories for the measurement of creatinine levels.^{145, 146} In this reaction, picric acid forms a red complex with creatinine in an alkaline solution.¹⁴⁸ This assay is sensitive and simple, so it was employed in this work. First, the Jaffe reaction was run in a plate assay with creatinine standards to determine the LOD of the assay (Figure 1A). The LOD was found to be $7.4 \pm 0.2 \mu\text{M}$ creatinine. The normal range of serum creatinine is $50 - 105 \mu\text{M}$ in adults and can be as low as $20 \mu\text{M}$ in young children.^{149, 150} Additionally, the concentration of creatinine increases with a decline in renal health. Thus, the LOD found for the Jaffe reaction is satisfactory for clinical analyses. In addition to determination of the LOD, the time required to reach the maximum signal was found. Thus, the progress of the reaction was monitored over time and it was found that the signal saturated after 12 minutes (Figure 1B).

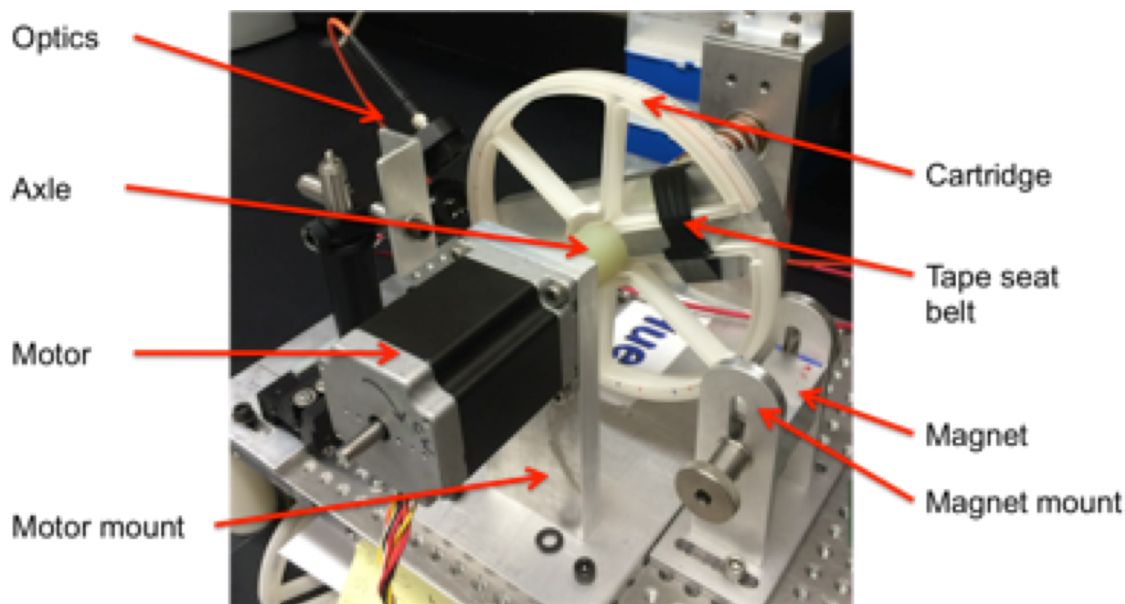


Figure 2. The major components of the automated, all-in-one instrument used for determination of serum creatinine.

Optimization of Automated Creatinine Assay

The goal of this project was to incorporate a clinical chemistry test into an all-in-one instrument that also performs PCR and ELISA assays in a relatively inexpensive, low-resource format. The goal was to create “one-touch” assays where an assay tube could simply be placed in the instrument cartridge, a button pushed and the test run automatically. This instrument was designed by our collaborators in the Haselton laboratory at Vanderbilt University (the specifics of this instrumentation will not be discussed in this dissertation). Briefly, the instrument consisted of circular cartridge that rotates relative to a stationary magnet. The rotation was programmed so that the magnet moved magnetic beads between specific chambers. A spectrophotometer is present on the other side of the cartridge for measurement of the absorbent signal produced by the assay (Figure 2). The expected commercial cost of the instrument is \$15,000, which is much cheaper than purchasing individual instrumentation for each of the assays. To incorporate the serum creatinine assay into a format that could be used with this instrumentation, the reagents and sample were loaded into a section of tubing, separated by an air

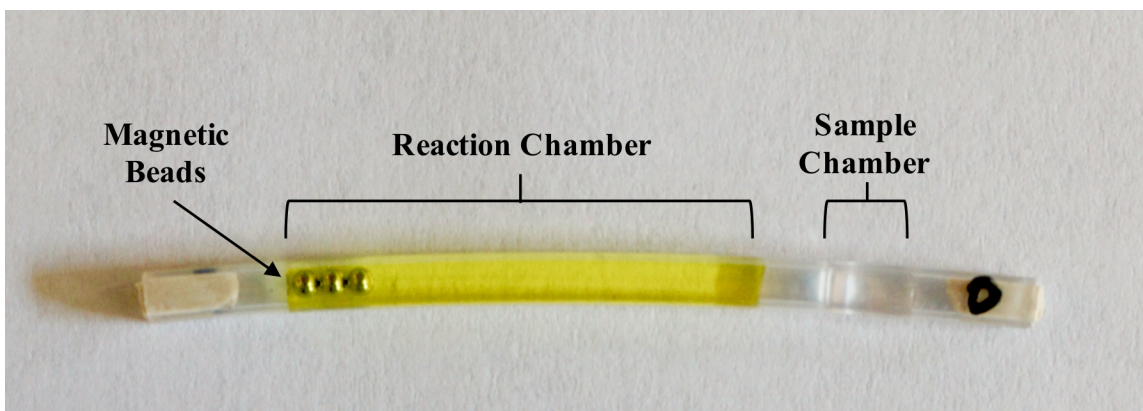


Figure 3. The clinical chemistry assay tube for analysis of serum creatinine. The reaction chamber contains the Jaffe reagent, which is separated from the sample chamber containing a creatinine sample by an air valve. The magnetic beads used to break the air valve and mix the two chambers are at the end of the tube and both ends of the tube are sealed. This tube is placed on the cartridge in the instrument.

(surface tension) valve. Magnetic beads were also added to the tube and the magnet was used to move these beads back and forth, breaking the surface tension valve and mixing the Jaffe reagent and sample. As a result, the reaction for analysis of serum creatinine began when mixing was initiated (Figure 3).

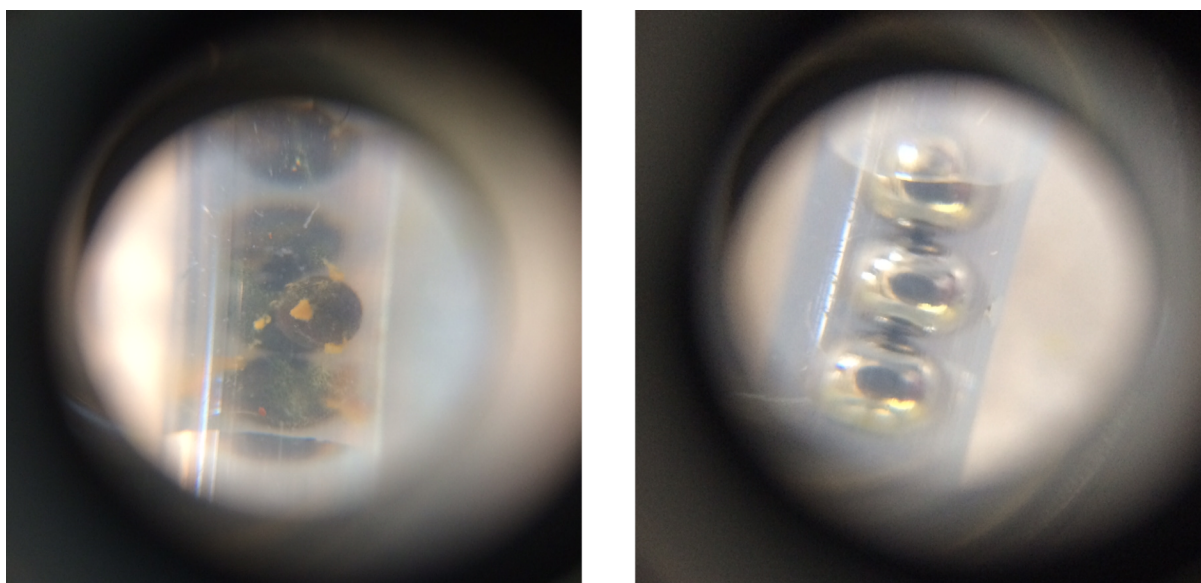


Figure 4. Magnetic beads were placed in aqueous solutions for 1 hour to determine their stability. The sandblasting beads (left) were found to corrode, while the stainless steel beads (right) retained their integrity.

The first step for incorporation of this assay into the tube was to determine the best bead type. It was discovered that beads with a diameter around 1 mm were sufficiently large to break the surface tension of the air valve. First, sandblasting beads were tested but they were found to corrode in aqueous solution after one hour. Thus, stainless steel beads were tested and after one hour, no corrosion was observed (Figure 4). This result would be expected because the sandblasting beads were made of steel, which is known to corrode much easier than stainless steel. Once the stainless steel beads were chosen, it was determined whether they caused the Jaffe reagent to turnover. To test this parameter, the stainless steel beads were incubated in this

reagent and the absorbance was monitored at 500 nm. No color change was observed (Figure 5A). Thus, the stainless steel beads were chosen for this assay.

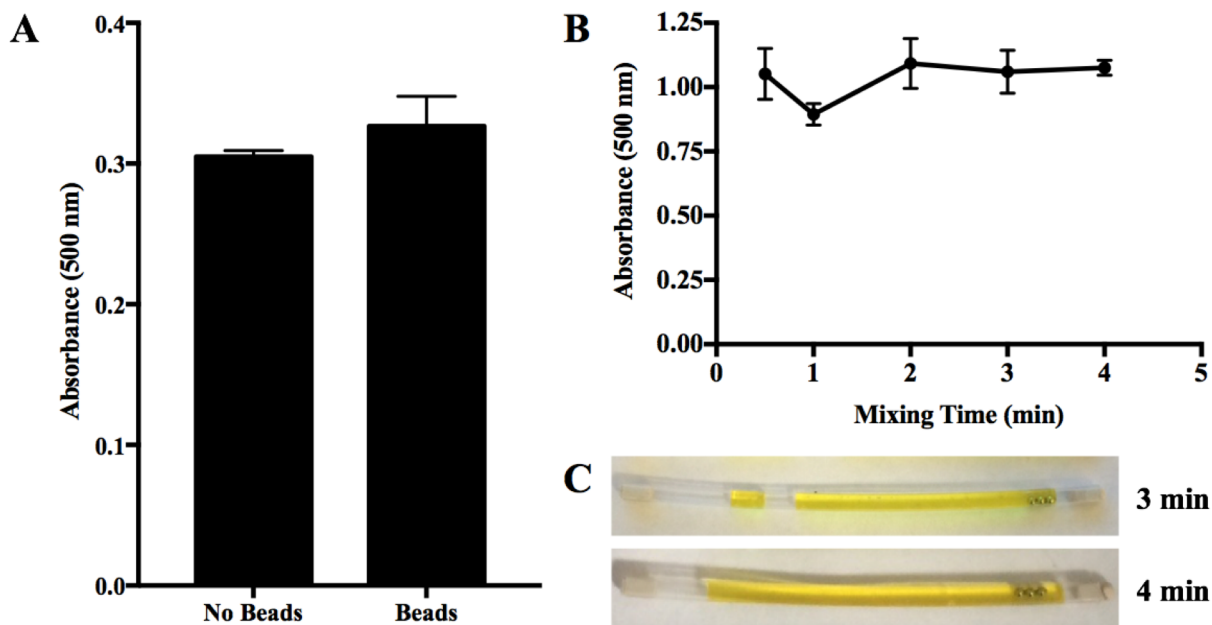


Figure 5. A) The absorbance of the Jaffe reagent without stainless steel beads and in the presences of the beads after one hour. No difference was observed. B) Optimization of the time required to break the air valve and mix the Jaffe reagent and sample. After two minutes, no significant difference in assay signal was observed. C) Visual observation of the mixing time showed that 4 minutes was required to fully eliminate the air valve.

An essential step in this assay is mixing, as no assay signal will be observed unless the air valve between the sample and reagent is broken. As a result, the mixing time required to consistently break this valve was determined. It was seen that similar assay signal was observed for all mixing times but the smallest error was observed after 4 minutes (Figure 5B). This aligned with visual observation which showed that the air valve was not consistently removed until the 4 minute time point (Figure 5C). It was also found that it was much easier to break the air valve when square tubing was used as opposed to round tubing. This observation is a result of lower surface tension with this geometry. Furthermore, the flat surface provided by the square tubing resulted in more reproducible optical measurements.

Automated Detection of Creatinine in Serum Samples

Once these assay parameters were optimized, the creatinine assay was run in the tube with automated mixing and absorbance readings on the instrument. First, creatinine standards in buffer were run. The resulting standard curve is shown in Figure 6A. The LOD ($3\sigma_{\text{blank}}/\text{slope}$) was $20.2 \pm 0.6 \mu\text{M}$ creatinine. After this, three human serum samples from individual donors were analyzed and all creatinine values were found to be within the normal clinical range (Figure 6B). Furthermore, these samples were also analyzed with a plate reader to confirm that the absorbance read by the automated instrument was correct. It was found that there was no difference between the measured values. Thus, the Jaffe method for determination of serum creatinine was effectively and reliably implemented in the tube assay design with a LOD comparable to that achieved in a plate assay.

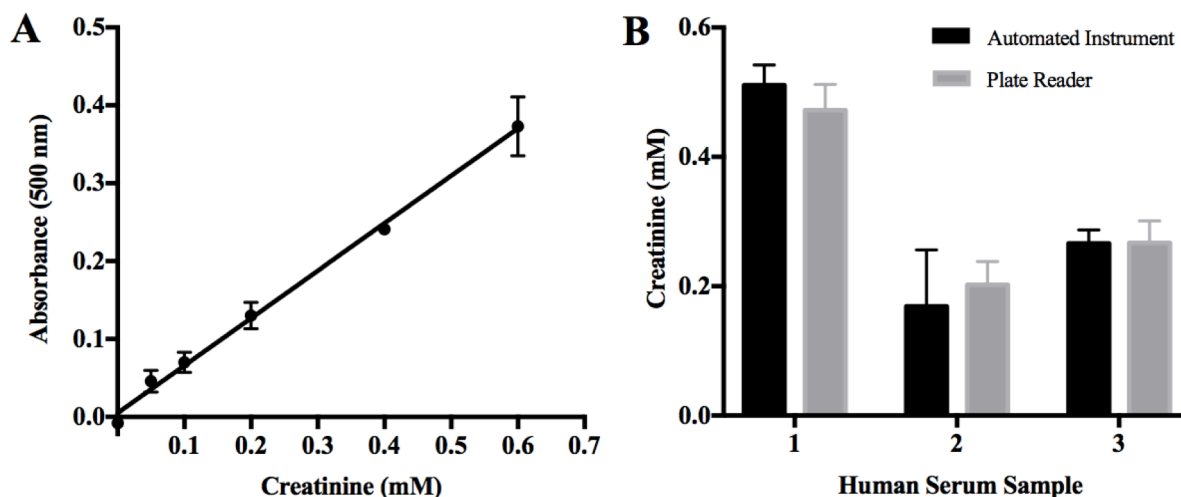


Figure 6. A) The creatinine standard curve acquired from analysis of standards on the automated instrument. The linear regression was $y = 0.61x + 0.005$ and the limit of detection $20.2 \pm 0.6 \mu\text{M}$ creatinine. B) Human serum samples from individual donors were analyzed for creatinine content. The same samples were also analyzed on the plate reader and the results were not statistically different.

Conclusion

In this work, it was shown that a serum creatinine assay could be effectively implemented in a tube-based format that employed air valves as separation barriers. To initiate the reaction these air valves were broken by magnetic beads, allowing the sample and Jaffe reagent to mix. An automated system designed for low-resource settings was used to both mix the reagents and read the resulting absorbent signal. This automated assay was found to detect clinically relevant concentrations of creatinine, from normal levels to levels observed in patients with renal failure. Finally, this assay was found to effectively detect creatinine in human serum samples. This instrument shows great versatility as it is able to perform the serum creatinine clinical chemistry assay in addition to ELISA and PCR. As a result, it shows great promise for implementation at major city or district level health clinics in low-resource areas of the world.

Acknowledgements

Special thanks to Thomas Scherr for assistance with instrument programming and the Haselton laboratory for design and construction of the automated instrument. Support for this work was provided by the Bill and Melinda Gates Foundation Grand Challenges in Global Health: Develop Technologies that Allow Assessment of Multiple Conditions and Pathogens at Point-of-Care (OPP1028749).

Lauren E. Gibson

Curriculum Vitae

512 Old Hickory Blvd
Apt. 2721
Nashville, TN 37209

Telephone: (270) 227-2751
Email: lauren.e.gibson@vanderbilt.edu

Education

Doctor of Philosophy, Chemistry **March 2017**
Vanderbilt University **Nashville, TN**
Advisor: Dr. David W. Wright
Dissertation: Development of Sensitive Biomolecule Detection Strategies for Low-Resource Settings

Bachelor of Science, Chemistry and Music Minor **May 2012**
Murray State University **Murray, KY**
GPA: 3.9, *Summa cum laude*

Research Experience

Graduate Research Assistant **2013-Present**
Vanderbilt University, Department of Chemistry **Nashville, TN**

Summary

Low-resource settings pose unique challenges for disease diagnostics. The uncontrolled environmental conditions and lack of clean water, resources, and trained personnel lead to a need for simple, stable, and inexpensive diagnostics. Currently, diagnostics which meet the above criteria lack sensitivity. To address this problem, we have designed new detection strategies that combine stability with sensitivity. Additionally, we have developed methods to enhance the sensitivity of current low-resource diagnostics and methods to better understand infectious disease biomarkers.

Fluorescent Nanoparticle-Based Signal Amplification Assay

- Developed and characterized porphyrin nanoparticle signal amplification method in which nanoparticles are broken apart into individual fluorescent porphyrin molecules. This method provides signal amplification without the use of an enzyme, increasing assay stability. Biomarker specificity is incorporated through an antibody.
- Optimized assay to detect low picomolar levels of IgG and malarial biomarker *Plasmodium falciparum* histidine-rich protein II (*pfHRP*II) in complex matrices, resulting in similar sensitivity to commercially available enzyme-based tests.

Catalytic Nanoparticle-Based Signal Amplification Assay

- Designed nanoparticle enzyme mimic based upon hemin, the molecule found in the active site of horseradish peroxidase. Signal amplification occurs through breaking hemin nanoparticles apart and subsequent catalytic turnover of a colorimetric substrate by hemin.
- Analyzed the optical, electrochemical and kinetic properties of the catalytic hemin complex.
- Detected picomolar levels of IgG and malarial biomarker *plasmodium* lactate dehydrogenase (*p*LDH) from complex matrices with a visual signal and increased stability relative to protein enzymes.

Enhancement of *Plasmodium falciparum* HRPII Rapid Diagnostic Tests (RDTs)

- Developed image analysis protocol for malaria RDTs and determined that a simple sample preparation technique improved RDT signal up to 14-fold with six RDT brands.

Dried Blood Spot ELISA for *Plasmodium falciparum* HRPII

- Developed extraction protocol for *pf*HRPII from dried blood spots samples and incorporated extracted samples into *pf*HRPII ELISA protocol with dried blood spot standard curve.
- Analyzed dried blood spot samples from rural Zambia.

Diagnostics Based on Zn-IDA Cellulose Flow Through Membranes

- Modified cellulose membranes with metal affinity ligands and evaluated *pf*HRPII capture and release from membrane.
- Optimized assay parameters for on-membrane detection of *pf*HRPII with horseradish peroxidase.
- Future work will combine membrane with nanoparticle-based signal amplification methods and with lateral flow assays producing a large volume RDT with increased sensitivity.

Undergraduate Research Assistant
Murray State University, Department of Chemistry
Advisor: Dr. R. Daniel Johnson

2011-2012
Murray, KY

Synthesis and Thermal Properties of Ionic Liquids

- Synthesized ionic liquids from phosphonium cations and alkyl sulfate anions.
- Characterized ionic liquids by TGA, DSC, NMR and ion chromatography.

Teaching and Mentoring Activities

Vanderbilt University, Department of Chemistry
Mentor for Undergraduate Research Assistant

Nashville, TN
2015 - 2016

- Designed undergraduate research project.
- Trained undergraduate in laboratory techniques and guided undergraduate through nanoparticle synthesis and flow-through diagnostic projects.

An Introduction to Evidence-Based Undergraduate STEM Teaching Fall 2015
• Completed requirements for graduate-level course that explores effective teaching strategies for college and university STEM classrooms.

Mentor for Visiting Scientists Summer 2015
• Trained Zambian scientists in laboratory techniques developed at Vanderbilt University

Head Teaching Assistant, General Chemistry Laboratory Spring 2013
• Managed TAs and grades for general chemistry laboratory.
• Taught laboratory section.

Teaching Assistant, General Chemistry Laboratory Fall 2012
• Instructed undergraduates in concepts relevant to laboratory experiments and directed laboratory.
• Graded laboratory reports and tests.

Murray State University, Department of Chemistry **Murray, KY**
Tutor and Teaching Assistant, General Chemistry 2010-2012
• Taught review sessions before exams.
• Guided undergraduates in laboratory experiments based upon concepts learned in lecture.
• Graded laboratory reports and homework.

Publications

Gibson, Lauren E., Wright, David W. Sensitive Biomolecule Detection Utilizing Signal Amplification with Porphyrin Nanoparticles. *Anal. Chem.* **2016**, 88 (11), 5928-5933.

Davis, Keersten M.*, **Gibson, Lauren E.***, Haselton, Frederick R., Wright, David W. Simple Sample Processing Enhances Malaria Rapid Diagnostic Test Performance. *Analyst* **2014**, 139, 3026-3031. *Selected as a HOT article in May 2014.*

*Authors contributed equally.

Bauer, Westley S.*, Kimmel, Danielle W.*, Adams, Nicholas M., **Gibson, Lauren E.**, Scherr, Thomas F., Richardson, Kelly A., Conrad, Joseph A., Matakala, Kalumbu, Haselton, Fredrick R., Wright, David W. Magnetically-Enabled Biomarker Extraction and Delivery System: Towards Integrated ASSURED Diagnostic Tools. *Analyst* **2017**, DOI: 10.1039/c7an00278e.

Publications in Preparation

Gibson, Lauren E., Markwalter, Christine F., Mudenda, Lwiindi, Kimmel, Danielle W., Mbambara, Saidon, Thuma, Philip E., Wright, David W. *Plasmodium falciparum* HRPII ELISA for Analysis of Dried Blood Spot Samples from Rural Zambia.

Gibson, Lauren E., Park, Matthew, Gerdon, Aren E., Wright, David W. Hemin Nanoparticle Signal Amplification for Detection of Biomolecules in Low-Resource Settings.

Markwalter, Christine F., **Gibson, Lauren E.**, Mudenda, Lwiindi, Kimmel, Danielle W., Mbambara, Saidon, Thuma, Philip E., Wright, David W. Detection of *p*LDH and *p*fHRPII from a Single Dried Blood Spot by On-bead ELISA.

Selected Presentations

Gibson, Lauren E., Wright, David W. Dual Mode Signal Amplification with Hemin Nanoparticles. Gordon Research Conference: Bioanalytical Sensors, Newport, RI, June 2016. Poster Presentation.

Gibson, Lauren E., Wright, David W. Sensitive Method for Biomolecule Detection Utilizing Porphyrin Nanoparticles. Area Collegiate Chemistry Meeting, Martin, TN, April 2016. Oral Presentation.

Gibson, Lauren E. Little Things Make a Big Difference: Using Nanoparticles to Diagnose Disease in the Developing World. 3 Minute Thesis Competition, Nashville, TN, February 2016. Oral Presentation.

Gibson, Lauren E., Wright, David W. Absorbent, Fluorescent, and Catalytic Signal Amplification with Porphyrins. 1st International Caparica Conference on Chromogenic and Emissive Materials. Lisbon, Portugal, September 2014. Poster Presentation.

Gibson, Lauren E., Wright, David W. Absorbent, Fluorescent, and Catalytic Signal Amplification with Porphyrins. Gordon Research Conference: The Chemistry and Biology of Tetrapyrroles. Newport, RI, July 2014. Poster Presentation.

Field Research Experience

Malaria Protein Biomarker Study

July 2016

Macha Research Trust

Macha, Zambia

- Analyzed over 350 dried blood spot samples for *pf*HRP II by ELISA.
- Evaluated biomarker levels in infected individuals and biomarker clearance after treatment.

Malaria mBEADs Pilot Field Study

Aug.-Sept. 2015

Macha Research Trust

Macha, Zambia

- Developed dried blood spot ELISA for the malarial biomarker *pf*HRP II.
- Assisted in the design and implementation of clinical field studies.
- Collected blood samples in rural Zambia and analyzed samples by rapid diagnostic tests, enhanced rapid diagnostic tests using mBEADs device, and dried blood spot ELISA.

Grant Writing Experience

Contributed to Gates Foundation Grand Challenges Explorations Grant (2016). Primary author for grant proposal: "Large Volume Origami RDT". PI: David W. Wright. Funded (\$100,000).

Honors and Awards

Mitchum E. Warren, Jr. Graduate Research Fellowship, Vanderbilt University	2016
2011-2012 Outstanding Chemistry Major, Murray State University	2012
ACS Undergraduate Award in Analytical Chemistry	2011
John W. Carr Scholarship, Murray State University	2008-2012